Nonequilibrium dynamics in constrained quantum many-body systems

Johannes Feldmeier

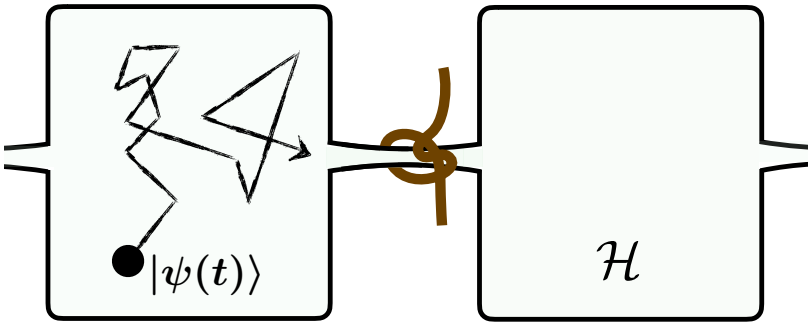

Technische Universität München
Fakultät für Physik

Nonequilibrium dynamics in constrained quantum many-body systems

Johannes Feldmeier

Vollständiger Abdruck der von der Fakultät für Physik der Technischen Universität München zur Erlangung des akademischen Grades eines

Doktors der Naturwissenschaften (Dr. rer. nat.)

genehmigten Dissertation.

Vorsitz:

Prof. Dr. Rudolf Gross

Prüfer*innen der Dissertation:

1. Prof. Dr. Michael Knap
2. Prof. Dr. Simone Warzel

Die Dissertation wurde am 06.07.2022 bei der Technischen Universität München eingereicht und durch die Fakultät für Physik am 05.08.2022 angenommen.

Nonequilibrium dynamics in constrained quantum many-body systems

Abstract

Symmetries and constraints constitute central concepts in physics and are vital tools for classifying equilibrium quantum phases of matter. In this thesis, we investigate the role of constraints in quantum many-body systems out of equilibrium. Using a combination of numerical and analytical techniques, we demonstrate that constraints can lead to unexpected and novel dynamical phenomena. In the first part of the thesis, we study how the presence of local gauge constraints – characteristic of exotic quantum phases of matter such as spin liquids – can induce slow dynamical relaxation to equilibrium and in certain cases even prevent such relaxation altogether. Dynamical properties of systems with gauge constraints can also serve as important signatures to identify them in experiment. In this context, we propose local dynamical probes as a way to detect the presence of topological edge states in the Kitaev honeycomb spin liquid. In the second part of the thesis, we go on to consider the dynamics of systems with novel types of mobility constraints – so-called fracton phases of matter – and show that the time evolution in such systems generally leads to the emergence of classical hydrodynamic transport at late times. Our analysis reveals novel, subdiffusively slow hydrodynamic universality classes in these fracton systems, in agreement with recent results from quantum simulation experiments. We further demonstrate how fracton constraints can also affect the dynamics of quantum information, as indicated by a significant slowing down of operator spreading. Certain mobility constraints can even lead to the emergence of tagged particle tracer motion in homogeneous quantum many-body systems. Using this connection we are able to greatly simplify the calculation of exact transport properties in several generic and even integrable systems.

Nichtgleichgewichtsdynamik in Quantenvielteilchensystemen mit Zwangsbedingungen

Zusammenfassung

Symmetrien und die sich daraus ergebenden Zwangsbedingungen stellen in der Physik zentrale Konzepte dar und fungieren als wichtige Werkzeuge für die Klassifizierung der Gleichgewichtsphasen von Quantenmaterie. In dieser Dissertation untersuchen wir die Rolle von Zwangsbedingungen außerhalb des thermischen Gleichgewichts. Durch eine Kombination aus numerischen sowie analytischen Methoden zeigen wir, dass Zwangsbedingungen zu überraschenden neuen dynamischen Phänomenen führen können. Im ersten Teil der Dissertation studieren wir wie lokale Eich-Zwangsbedingungen – charakteristisch für exotische Quantenphasen wie Spinflüssigkeiten – eine langsame Relaxationsdynamik ins thermische Gleichgewicht zur Folge haben können und diese in manchen Fällen sogar vollständig verhindern. Dynamische Eigenschaften von Systemen mit Eich-Zwangsbedingungen können zudem als wichtige Signaturen zu deren experimentellen Identifikation dienen. In diesem Zusammenhand schlagen wir lokale dynamische Protokolle als Möglichkeit vor, topologische Randzustände in der Kitaev Spinflüssigkeit auf dem Honigwabengitter zu detektieren. Im zweiten Teil der Dissertation untersuchen wir die Dynamik von Systemen mit neuen Arten von Zwangsbedingungen – sogenannte Fracton-Phasen – und zeigen, dass die Zeitentwicklung in solchen Systemen im Allgemeinen zur Emergenz von klassischem, hydrodynamischem Transport zu späten Zeiten führt. Unsere Untersuchung enthüllt neue, subdiffusiv langsame hydrodynamische Universalitätsklassen in Fracton-Systemen, in Übereinstimmung mit aktuellen Resultaten aus Quantensimulationsexperimenten. Wir zeigen darüber hinaus, wie Zwangsbedingungen in Fracton-Systemen die Dynamik von Quanteninformation beeinflussen können, angezeigt durch ein erhebliches Verlangsamen der Ausbreitung von Operatoren. Manche Zwangsbedingungen können emergent sogar zur Bewegung markierter, unterscheidbarer Teilchen in homogenen Quantensystemen führen. Diesen Zusammenhang nutzend gelingt es uns, die Berechnung von Transporteigenschaften in einigen generischen sowie integrablen Quantensystemen erheblich zu vereinfachen.

Contents

Listing of figures

Acknowledgments

The past four years have been a great experience made possible by an environment of great people that I had the fortune to be surrounded by.

First and foremost, I want to thank Michael for taking me on and supervising me as a PhD student. I am deeply grateful for the freedom and flexibility I got to enjoy as a member of your group and for the support and encouragement I received working on the topics I was interested in. Thank you for that, Michael, and thank you for your patience, your physical insight, your positive attitude, and your mentorship throughout the past four years!

I want to thank Frank Pollmann for many fruitful collaborations during my time as a PhD student. It was a great experience working with you and learning from your intuition and your approach to physics problems, which you always shared in the most instructive and enthusiastic ways.

I thank Johannes Knolle for our collaboration which I greatly enjoyed and through which I learned a lot about spin liquids.

I want to express my gratitude to Michael, Frank, Johannes and Sergej Moroz for running the TUM condensed matter theory group during the past four years. You created a great collaborative atmosphere and I look forward to working with you in the future.

I thank Matthias Punk for his support, his valuable advice, and our collaboration during my Master project. Thank you for introducing me to the physics of dimer models and for giving phenomenally good lectures that I learned so much from.

I thank Wilhelm Zwerger, who introduced me to so many aspects of physics over the past eight years, from my first lectures about quantum mechanics and condensed matter theory to non-equilibrium statistical mechanics and cold atoms. It was fascinating to hear so many interesting stories about science while being part of the Zwerger group during my Bachelor thesis and later during lunches at the IPP cantine.

The research presented in this thesis is the result of joint efforts and I thank the many people who I was fortunate to collaborate and discuss with. I thank William Witczak-Krempa for a great collaboration. I also thank Pablo Sala, Giuseppe De Tomasi, Alexander Schuckert, Ansgar Burchards and Willian Natori for all their efforts that they put into our collaborations. I thank Pablo Sala and Tibor Rakovszky for many long and insightful

discussions that have made working on constrained systems a great joy. I especially want to thank Ehud Altman for hosting me during my visit to Berkeley, for many insightful discussions, and for his great enthusiasm.

My great time as a PhD student would not have been possible without my companions in the condensed matter theory group. I want to thank my office mate Clemens Kuhlenkamp, who selflessly offered the desk next to the window to me when I first arrived in Michael's group. Thank you for being such a great office mate during the past four years, I immensely enjoyed and learned a lot from our long discussions about physics. I thank Alexander Schuckert for the many discussions about physics and science in general, his inspiring enthusiasm, and many great bike rides. I thank Annabelle Bohrdt for the teamwork while on teaching duty, for many insightful physics discussions and for organizing football games and many other sports activities. I thank Fabian Bohrdt for joining in on all these sports activities and providing valuable insights on all physics-related matters. I thank Simon Weidinger, my predecessor as IT-responsible person in Michael's group, who set things up in a way that made it easy for me take up the job. I also want to thank Johannes Hauschild and Sheng-Hsuan Lin for their expertise, their unbounded patience and their support on all IT-related matters. I thank Yujie Liu for his efforts in setting up the quantum computing theory practicals together. I want to thank the members of the wider condensed matter theory group who provided a great environment over the past years, especially Elisabeth Wybo, Kevin Hémery, Izabella Lovas, Umberto Borla, Claudio Benzoni, Johannes Lang and Bernhard Frank. I thank Karin Ramm for all her help in bureaucratic matters. I also thank my old office mates Dima Pimenov and Sebastian Huber. I am especially grateful to Sebastian for the many insightful discussions on the physics of dimer models. I thank the International Max Planck Research School for Quantum Science and Technology which I was fortunate to take part in and that allowed me to attend many great summer schools and workshops.

I am lucky to be able to thank my friends and family who helped me maintain balance and a good spirit throughout the years. I thank Michael Schmid for his friendship and the most insightful discussions. I thank Johannes Manner and Johannes Kässinger for keeping up our Stammtisch after eight years and counting. I thank the 'Alte Ofen'-Stammtisch around Vreni, Tom and Johannes for always providing me with food for thought. I thank Marianne for making the long way to Munich to go on hiking trips. I thank Lea and Timon for our expeditions into the climbing hall. I thank Marija and Pino for providing an open door and excellent food. I thank my sisters Martha and Sophie for always being on top of things. I thank my grandparents Maria and Johann, as well as Maria, for providing inspiration and support. I thank my parents Sabine and Gerhard for their enormous support, for always being there for me, and for always knowing the right course of action. Finally, I want to thank Marina for all her love and support. You provide me with a deep sense of happiness and calm, and that makes facing life a joyful task.

Publications

Parts of the content of this thesis have been published or uploaded to a preprint server in Refs. [1–7]. They contain large parts of the material presented here, partly with textual overlap. The author of this thesis has made significant and substantial contributions to these publications, ranging from the development of ideas, literature research, analytical calculations, design, development and implementation of numerical codes, data analysis, to the interpretation of results, and writing of the papers. In this thesis, when numerical data obtained by co-authors is shown, we indicate so at the beginning of the corresponding chapter.

- **Johannes Feldmeier**, Frank Pollmann, Michael Knap, Emergent Glassy Dynamics in a Quantum Dimer Model, Phys. Rev. Lett. 123, 040601 (2019) [1]
- **Johannes Feldmeier**, Pablo Sala, Giuseppe De Tomasi, Frank Pollmann, Michael Knap, Anomalous Diffusion in Dipole- and Higher-Moment-Conserving Systems, Phys. Rev. Lett. 125, 245303 (2020) [2]
- **Johannes Feldmeier**, Willian Natori, Michael Knap, Johannes Knolle, Local probes for charge-neutral edge states in two-dimensional quantum magnets, Phys. Rev. B 102, 134423 (2020) [3]
- **Johannes Feldmeier**, Frank Pollmann, Michael Knap, Emergent fracton dynamics in a nonplanar dimer model, Phys. Rev. B 103, 094303 (2021) (Editors' Suggestion) [4]
- **Johannes Feldmeier**, Michael Knap, Critically slow operator dynamics in constrained many-body systems, Phys. Rev. Lett. 127, 235301 (2021) [5]
- Ansgar Burchards, **Johannes Feldmeier**, Alexander Schuckert, Michael Knap, Coupled hydrodynamics in dipole-conserving quantum systems, Phys. Rev. B 105, 205127 (2022) [6]
- **Johannes Feldmeier**, William Witczak-Krempa, Michael Knap, Emergent tracer dynamics in constrained quantum systems, Phys. Rev. B 106, 094303 (2022) [7]

I think I can safely say that nobody understands quantum mechanics.

Richard P. Feynman

More is different.

Philip W. Anderson

1 Introduction

The Schrödinger equation, first introduced almost one hundred years ago [8], forms the foundation for our understanding of quantum physics at low energies. This 'theory of everything' – as it pertains to a condensed matter point of view – is swiftly stated: $i\hbar\partial_t |\psi\rangle = \hat{H} |\psi\rangle$, where $|\psi\rangle$ describes the quantum state of the system and $\hat{H}$ is the Hamiltonian that describes motion and interactions of particles. In principle, all that is left to do is to solve it. But as quick and precise as we may be in stating our goal, achieving it is tremendously challenging: The number of different states that need to be accounted for in the Schrödinger equation grows exponentially with the number of particles making up the system of interest. If we would like to describe the macroscopic properties of condensed matter systems, we are presented with a seemingly insurmountable task. This is the many-body problem.

How can progress be made? One approach is to approximate a given problem with a different one that is tractable, for example because the particles in the new problem do not interact with each other. This is the program of mean-field theory and its extensions. Often, apart from the dimensionality of the system, the success of mean field descriptions comes down to choosing the 'right' quasiparticles that can be approximated as being non-interacting. This highlights the fact that in practice we require physical insight beyond an (impossible) brute force application of the Schrödinger equation to correctly describe the behavior of many-body quantum systems, echoing the viewpoint of Anderson that "more is different" [9]. More rigorously, phases of matter and the transitions between them can often be captured by Ginzburg-Landau effective actions for the long length scale degrees of freedom [10, 11], treated within the renormalization group approach [12]. The Ginzburg-Landau action for a given microscopic system can be postulated purely on grounds of global symmetries and thus exhibits *universality*, which holds that the micro-

scopic details are qualitatively unimportant for the long wavelength physics. This immensely successful paradigm establishes global symmetry and its spontaneous breaking as a cornerstone of our understanding of equilibrium phases of matter.

However, over the last decades we have learned that this is not the full story. Ignited by the experimental discovery of the fractional quantum Hall effect [13] and the presence of high-temperature superconductivity in the cuprates [14], subsequent theory development has led to the realization that there exist topologically ordered quantum phases that cannot be distinguished by any local order parameter, thus falling outside the Landau paradigm of global symmetry breaking[1] [15]. Instead, novel quantum phases of matter such as fractional quantum hall states and spin liquids are characterized by topological ground state degeneracies, fractionalization and emergent gauge structures, the latter of which lead to *local* symmetries instead of global ones [15]. These insights, along with the development of powerful numerical tools such as the density matrix renormalization group (DMRG) [16–19], have led to flourishing and continuous theoretical progress in classifying the ground state quantum phases of matter over recent years [20].

At the same time, this immense success is built on the description of stationary quantum systems in equilibrium. In contrast, much less is known about the behavior of closed quantum many-body systems in nonequilibrium situations, as clear guiding principles such as the Landau paradigm are absent. In addition, numericals tools such as DMRG, while working wonders investigating ground states with low entanglement, start to hit the 'entanglement wall' out of equilibrium, as in general an exponential number of (highly entangled) eigenstates contributes to the time evolution. Once more, these issues seemingly render attempts to make general statements challenging. Nevertheless, some remarkable progress has been achieved, in particular with regards to the crucial question [21, 22]: Do quantum many-body systems prepared in nonequilibrium initial states eventually thermalize? The answer culminated in the formulation and numerical verification of the *eigenstate thermalization hypothesis* (ETH) [23–26], which provides a viable mechanism for thermalization in generic interacting quantum systems. However, important open questions remain. If a quantum system thermalizes, in which manner (e.g. how quickly) is the thermal state approached dynamically? How can we characterize or even classify such dynamical processes for different microscopic models and is there any universality to their dynamics in the spirit of Ginzburg-Landau? In addition, although it is expected that generic interacting systems thermalize, under which circumstances can exceptions to this rule occur? The phenomenon of many-body localization in systems with strong disorder provides an example for such an exception to thermalization [27–40], but are there more? Remarkably, current quantum simulation platforms can provide theorists with hints to where answers might be found.

Edging closer to Feynman's vision of a quantum simulator [41], control over isolated

[1] Whether and how such such phases may be realized in the cuprates is at present not fully understood and constitutes one of the major challenges in condensed matter.

quantum many-body systems has progressed impressively over recent years across a variety of platforms, such as cold atoms [42, 43], trapped ions [44–46], superconducting qubits [47, 48], certain condensed matter based setups [49], and others [50]. It is worth noting that machines performing quantum computing tasks inherently operate out-of-equilibrium. Understanding the nonequilibrium dynamics of closed quantum many-body systems is thus an integral part of making progress towards the long-term goal of building large-scale quantum computers and simulators. At the same time, currently available devices are already able to address some of the above questions. In particular, a 2017 investigation of quantum quench dynamics in an ensemble of 51 Rydberg atoms demonstrated the absence of thermalization for certain initial states [51]. This remarkable feature – termed quantum many-body scars [52–57] – was attributed to the presence of dynamical *constraints* in the Hamiltonian time evolution. Therefore, in part sparked by these experimental results, efforts surged attempting to develop a more general understanding of the role of symmetries, which act as dynamical constraints, in nonequilibrium quantum systems.

In this context, one key realization that arose in recent years is that the dynamics of generic interacting quantum many-body systems can often be understood within an effective hydrodynamic picture [58–66]. This is in fact an example of out-of-equilibrium universality and paves the way for using tools such as random unitary circuits, which are often simpler to handle theoretically than Hamiltonians, to characterize nonequilibrium dynamics [61–68]. Making use of such methods it was possible to establish the generic expectation that closed systems with a global $U(1)$ symmetry (i.e., a conserved charge) should exhibit emergent classical diffusion at late times of the nonequilibrium evolution. This result in turn leads to many interesting questions in the broader context of constrained systems. What happens if we go beyond conventional global $U(1)$ constraints? In particular, as outlined above, novel phases of matter are often characterized by local gauge constraints instead of global symmetries. We may thus wonder whether these lead to emergent hydrodynamics as well and if so, what their universality class turns out to be. Similar questions arise in the context of novel constrained fracton phases of matter [69, 70], such as systems conserving several multipole moments of a global $U(1)$ charge. There are many motivating factors to find answers to these questions. Aside from furthering our understanding of the quantum thermalization process more broadly, understanding the dynamics of constrained systems in particular might offer ways to characterize them in experiment, potentially driving the development of novel tools for quantum information processing.

The remainder of this thesis, addressing the questions outlined above, is structured as follows:

- In Chapter 2 we provide an introduction to the main concepts discussed in this the-

sis. In particular, the field of constrained dynamics is wide and we provide a guide to some of the dynamical phenomena that have been the focus of intense research in recent years and that appear throughout this thesis. We further introduce the constrained systems most relevant to this thesis and discuss how they are realized in quantum simulation platforms and quantum materials.

- Part I of this thesis investigates the dynamics of systems with local gauge constraints such as dimer models and spin liquids.

- In Chapter 3 we consider the dynamics of a two-dimensional quantum dimer model with local gauge constraints. We demonstrate numerically that after a quantum quench, most intial states show a rapid equilibration of local observables. However, there exists a low energy phase of the model in which the constraints lead to an effective standstill of the dynamics. We analytically argue for a lower bound on the thermalization time in this regime and find extremely slow glassy dynamics due to the presence of the gauge constraints.

- In Chapter 4 we investigate a dimer model in a non-planar bilayer geometry. We show that this model features a rich structure of conserved quantities beyond the local gauge constraints. These conserved quantities can lead to unconventionally slow hydrodynamics at late times and signatures of fracton-like dynamics. For certain initial states, the presence of non-local conserved winding numbers can even prevent local thermalization altogether.

- In Chapter 5 we consider the Kitaev honeycomb spin liquid which features a $\mathbb{Z}_2$ gauge structure. We propose a scheme to extract local dynamical signatures of the presence of topological edge states using spin-polarized scanning tunneling microscopy. Such an approach can also be used to detect edge states in other novel quantum phases such as topological magnon insulators.

- In Part II of this thesis we focus on the dynamics of fractonic systems in which the mobility of charges is constrained by the conservation of higher multipole moments.

- In Chapter 6 we find novel subdiffusive hydrodynamic universality classes associated with the conservation of higher multipole moments, which we verify numerically in one dimension using random circuit tools. Our results are in qualitative agreement with results from cold atom quantum simulation experiments.

- In Chapter 7 we consider Hamiltonian systems with conserved charge and dipole moment. We formulate a theory of classical linear fluctuating hydrodynamics that describes the coupled dynamics of charge and energy density in the presence of

dipole conservation. It is demonstrated that this effective description is in agreement with nonequilibrium quantum field theory results for a dipole-conserving Bose-Hubbard model.

- In Chapter 8 we consider the dynamics of operators in dipole-conserving systems. We show that the presence of dipole-constraints can significantly slow down the generically expected ballistic growth of operators. In particular, using a combination of analytical arguments and random automaton circuits, we demonstrate the emergence of sub-ballistic operator spreading at the critical point of a density-driven localization transition.

- In Chapter 9 we show how the presence of constraints can lead to the emergence of tracer dynamics in quantum many-body systems of indistinguishable particles. We use this connection to provide exact transport coefficients in a number of generic as well as integrable quantum systems. We further demonstrate how the combination of these constraints with fracton constraints can give rise to novel universality classes of emergent hydrodynamics.

- To conclude, we provide a summary and an outlook in Chapter 10.

- Appendix A contains an overview of the (numerical) methods used throughout this thesis

- Appendix B contains a number of supplemental analytical calculations for the bilayer dimer setup of Chapter 4.

2
Preliminaries

In this introductory chapter, we discuss concepts around thermalization and constraints that are central to this thesis. After an overview of nonequilibrium dynamics and the eigenstate thermalization hypothesis, we go on to provide a brief guide to some of the key phenomena in constrained dynamics that have been the focus of much interest in recent years. We close with a discussion of experimental platforms that can be used to realize the constrained systems discussed in this thesis.

2.1 Thermalization in classical and quantum systems

The central questions of this thesis revolve around the dynamics of interacting quantum many-body systems. Generically, we expect that such systems *thermalize*: At late times, expectation values of local observables equal those of an equilibrium macrostate that can be characterized by only a few conserved quantities. Much of our discussions will be centered around how this approach to equilibrium occurs in detail. Before plunging into these investigations, we discuss how it is possible in the first place that an initial microstate gives rise to such an equilibrium macrostate despriction, even though the underlying microscopic evolution is symmetric under time reversal, a question which has been a topic of much discussion ever since the inception of statistical mechanics. More recently, the question of how thermalization occurs in the context of quantum many-body systems has received a lot of interest [21, 23, 26, 71]. In this introductory section, we provide a brief overview of attempts to explain how statistical mechanics can emerge in the time evolution of classical systems before discussing how these concepts can be extended to the quantum domain within the context of the eigenstate thermalization hypothesis. Much of the following discussion follows the reviews of Refs. [21, 22].

2.1.1 Ergodicity and thermalization in classical systems

The question how many-particle systems reach an equilibrium state characterized by only a handful of properties such as energy or particle number lies at the heart of justifying statistical mechanics. Let us consider an isolated classical system of N particles whose state at time t is characterized by a point $\Gamma(t) = (\boldsymbol{q}_1(t), ..., \boldsymbol{q}_N(t), \boldsymbol{p}_1(t), ..., \boldsymbol{p}_N(t))$ in phase space. Statististical mechanics poses that equilibrium expectation values $\langle O \rangle_{eq}$ of an observable O *as measured in experiment* in this system are equal to phase space averages taken with respect to a microcanonical ensemble:

$$\langle O \rangle_{eq} = \frac{\int_S d\Gamma O(\Gamma)}{\int_S d\Gamma}. \tag{2.1}$$

Here, the integral over the phase space variables Γ runs over a microcanonical shell S of constant energy in phase space. Eq. (2.1) weights all microstates within this shell *equally*. This relation between experiments and ensemble averages is an empirical fact, although highly non-trivial: There is only a single physical system present in the experiment, not an ensemble. So why does Eq. (2.1) apply to outcomes of experiments on equilibrium systems? One way of justifying Eq. (2.1) resorts to the textbook ergodic hypothesis [72].

Ergodic hypothesis

The ergodic hypothesis poses that the ensemble average on the right hand side of Eq. (2.1) emerges due to a time average over the system's trajectory in phase space: Experiments are performed over a finite time scale, and so the experimental output corresponds to an average of the instantaneous value of the observable O over this time scale. The ergodic hypothesis then argues that since the experimental time scale is larger than the characteristic time scale of the system's dynamics, the expectation value of an observable as measured in experiment should be given by

$$\langle O \rangle_{eq} = \lim_{T\to\infty} \frac{1}{T} \int_0^T dt\, O(t). \tag{2.2}$$

Here, $O(t)$ is the value of the observable for the microscopic state of the system at time t. It is now further assumed that the dynamics of the system is *ergodic*, meaning it has a dense trajectory in phase space. According to Liouville's theorem, the system will then spend equal time in all parts of the phase space shell S. This implies that the time average on the right hand side of Eq. (2.2) indeed turns into the ensemble average of Eq. (2.1), i.e.,

$$\lim_{T\to\infty} \frac{1}{T} \int_0^T dt\, O(t) = \frac{\int_S d\Gamma O(\Gamma)}{\int_S d\Gamma}. \tag{2.3}$$

In practice, establishing ergodicity, i.e. Eq. (2.3), rigorously for a given system is a very challenging task that has been accomplished only in a limited number of cases [73–76].

If a system's trajectory is ergodic in phase space, Eq. (2.3) holds and infinite time averages are equal to ensemble averages. However, in practice the explanatorial power of the ergodic hypothesis is limited by the applicability of Eq. (2.2): The amount of time needed for the trajectory of an ergodic system to densely cover all of phase space is exponentially large in the number of constituents. The time scale over which an observable is averaged in an experiment is certainly short compared to such an enormous time, and therefore the experimental outcome $\langle O \rangle_{eq}$ cannot simply be set equal to the infinite time average in Eq. (2.2). Put differently, it is observed empirically that systems thermalize on much shorter than exponential time scales, questioning the role of the ergodic hypothesis in explaining the emergence of statistical mechanics.

Typicality

The ergodic hypothesis is very ambitious in its attempt to provide a mechanism for the emergence of statistical mechanics, leading to averages over exponentially long times. Notably, the ergodic hypothesis makes no reference to the nature of the observables O, it applies to *all* observables in a closed system by virtue of ergodic phase space trajectories. However, experiments do not have access to all possible observables but usually refer to macroscopic sums of local quantities. One can then attempt to explain the emergence of statistical mechanics for this subset of observables only. As a consequence, the requirement of an average over a dense phase space trajectory can be dropped. Starting from a microscopic initial state, the system then only needs to reach a *typical* state for which the observables of interest take values already close to the microcanonical ensemble average of statistical mechanics. In other words, the values of such macroscopic observables are almost constant across the energy shell, such that a single typical state already returns the ensemble average. It is then argued that because typical states are much more numerous than atypical ones, this process generally need not take an exponentially long amount of time.

Chaos

Closely related to these ideas of ergodicity and typicality is the concept of chaos in classical systems [77]. It asserts that in chaotic systems the time evolution is exponentially sensitive to the chosen initial conditions. In particular, for two initially close phase space points $\Gamma_1(0)$ and $\Gamma_2(0)$, the growth of the difference $|\delta\Gamma(t)| = |\Gamma_1(t) - \Gamma_2(t)| \sim e^{\lambda_L t}$ of their phase space coordinates is governed by a finite Lyapunov exponent λ_L. This sensitivity results from the non-linearity of the classical equations of motion and is known as the butterfly effect. It is then intuitive to assume that a system originally in an atypical initial state will quickly evolve to a typical configuration due to the chaotic nature of the dynamics. However, we point out that precise connections between typicality, chaos and thermalization in classical systems are lacking. In particular, the typicality argument

does not distinguish between thermalizing dynamics and integrable systems that do not thermalize, a clear drawback compared to the mathematically sharp ergodic hypothesis. Remarkably however, when attempting to extend the concept of thermalization to the quantum case, it is the arguments of typicality that reap the most reward. In particular, the above issue of lacking mathematical clarity is resolved in the quantum case.

2.1.2 Eigenstate thermalization in closed quantum systems

Can the above considerations about thermalization be extended to quantum many-body systems? At first sight the two questions of thermalization in classical and quantum systems appear quite different. We relied on a phase space description in the classical scenario, a description which does not generalize to quantum systems. Furthermore, direct attempts to extend the concept of chaos to quantum systems fail, as the Schrödinger equation that governs the dynamics of quantum systems is linear. Finally, the arguments on which the classical ergodic hypothesis rests cannot apply to the quantum case: Consider a quantum system with Hamiltonian $\hat{H}$ and eigenstates $|m\rangle$ with associated eigenenergies $\hat{H}\,|m\rangle = E_m\,|m\rangle$. The eigenstates $|m\rangle$ are invariant under the time evolution, i.e., $e^{-i\hat{H}t}\,|m\rangle = e^{-iE_m t}\,|m\rangle$ up to a global phase, and thus the dynamics starting from $|m\rangle$ clearly cannot explore the entire energy shell of eigenstates in a small window ΔE around the energy E_m. As we discuss in the following, the resolution to these issues lies in the structure of the eigenstates $|m\rangle$ themselves, which have to be typical in a similar spirit as discussed above.

Random matrix theory and quantum chaos

The dynamics of a Hamiltonian quantum system is uniquely determined by its eigenstates and eigenenergies $|m\rangle$ and E_m. Attempts to extend the concept of chaos to quantum systems thus naturally refer to the properties of $|m\rangle$ and E_m. The central idea of quantum chaos holds that for chaotic systems, these eigenstates and eigenvectors effectively appear as if the Hamiltonian were a random matrix. This is known as random matrix theory (RMT) [78], forming the cornerstone of quantum chaos and the eigenstate thermalization hypothesis.

Random matrix theory was originally advanced by the works of Wigner [79–81] and Dyson [82] on the energy spectra of large nuclei, realizing that the statistical properties of the distribution of nuclear energy levels match those of ensembles of random matrices. In particular, the distribution

$$P(\hat{H}) \sim \exp\Big\{-\frac{1}{2a^2}\mathrm{Tr}(\hat{H}^2)\Big\}, \tag{2.4}$$

with an energy scale a defines the Gaussian orthogonal ensemble (GOE) for real symmet-

ric matrices $\hat{H}$[1]. Crucially, for Hamiltonians randomly drawn from Eq. (2.4), the probability distribution of the spacing ω of consecutive energy levels in the spectrum ($\omega \geq 0$), known as Wigner-Dyson distribution, can be approximated by

$$P(\omega) = A\omega \exp\{-B\omega^2\}. \tag{2.5}$$

Here, A and B are determined by normalization and the overall energy scale. The main qualitative feature of Eq. (2.5) is $P(\omega \to 0) = 0$, which indicates that two consecutive energy levels are highly unlikely to be very close to each other, a feature known as *level repulsion*. Level repulsion in the spectrum of Hamiltonians is a form of correlation that can be attributed to couplings between nearby energy levels due to interactions. One of the central insights of RMT holds that chaotic quantum many-body Hamiltonians[2] show the same level statistics Eq. (2.5) as random matrices[3]. Notably, it suffices that the Hamiltonian looks like a random matrix in a generic basis, even though there exist special basis choices in which the Hamiltonian of a physical system is sparse and does not look random[4]. The emergence of Wigner-Dyson energy level statistics in the spectrum of quantum many-body Hamiltonians is now a commonly accepted definition of quantum chaos.

Crucially, this characterization of quantum chaos is able to distinguish non-integrable systems from integrable ones. Integrable systems feature an extensive number of conserved quantities, thus avoiding level repulsion through vanishing coupling between nearby eigenstates. According to the Berry-Tabor conjecture [84], integrability leads to uncorrelated, independently distributed energy levels described by Poisson statistics. The associated distribution of the spacings between consecutive levels is given by

$$P(\omega) = \exp\{-\omega\}, \tag{2.6}$$

normalized to an average spacing of unity. For a given quantum many-body Hamiltonian, we expect to see the emergence of either Eq. (2.5) or Eq. (2.6) in the statistics of level spacings as we approach the thermodynamic limit. This provides a key indication for presence or absence of quantum chaos. In practice, attempts to extract signatures of quantum chaos include investigations of the spectral form factor [67, 68, 85–87] or dynamical consequences of level repulsion [88, 89].

[1]The GOE applies to systems with time-reversal symmetry. Similarly defined ensembles exist for systems without time-reversal symmetry, the Gaussian unitary ensemble (GUE), as well as for systems with time-reversal but without rotational symmetry, the Gaussian symplectic ensemble (GSE).

[2]In the absence of additional symmetries such as lattice point groups, global charges, etc. If such symmetries are present, the energy spectrum may still display RMT behavior within the symmetry-resolved sectors of the Hilbert space.

[3]Bohigas, Giannoni and Schmit formulated the conjecture that all quantum systems with chaotic classical analog follow RMT level statistics [83]

[4]For example, physical Hamiltonians usually exhibit a notion of locality that is absent in purely random matrices. The matrix elements of such Hamiltonians in any local basis are sparse.

While the statistics of the distribution of energy levels E_m of a Hamiltonian constitutes the most direct indication of quantum chaos, RMT also makes important statements about the structure of the eigenstates $|m\rangle$ of quantum chaotic systems [71]. In a nutshell, according to RMT the eigenstates of random matrices are simply random unit vectors in Hilbert space[5]. Using this property, the matrix elements of a given local observable $\hat{O} = \sum_i O_i |i\rangle \langle i|$ between two eigenstates $|n\rangle$ and $|m\rangle$ of a random matrix can be evaluated as

$$O_{mn} = \langle m| \hat{O} |n\rangle \approx \langle \hat{O} \rangle \delta_{mn} + \sqrt{\frac{\langle \hat{O}^2 \rangle}{\mathcal{D}}} R_{mn}, \tag{2.7}$$

where $\mathcal{D}$ is the dimension of the Hilbert space and R_{mn} is a random variable with mean zero and unit variance. $\langle \hat{O} \rangle = \sum_i O_i$ is the 'infinite temperature' average of the operator $\hat{O}$ over the entire Hilbert space and provides the leading (in $1/\mathcal{D}$), diagonal contribution to the matrix element of Eq. (2.7). Crucially, Eq. (2.7) does not hold for *all* operators $\hat{O}$, as is manifest for projectors $\hat{O} = |\ell\rangle \langle \ell|$ on specific eigenstates. The result that the expectation value of an operator with respect to a single random pure state equals the infinite temperature ensemble average is called *typicality* [91–95][6]. RMT then predicts that Eq. (2.7) also applies to eigenstates from the middle of the energy spectrum of quantum chaotic Hamiltonians. We thus see how this notion of typicality ties in with our previous discussion of classical systems: A single eigenstate $|n\rangle$ is already sufficient to reproduce ensemble averages of relevant observables, up to small corrections decaying as $1/\mathcal{D}$.

Since (mid spectrum) eigenstates of quantum chaotic Hamiltonians are essentially random states, their precise form is expected to depend sensitively on the precise parameters of the Hamiltonian. This sensitive dependence can be viewed as analogous to the sensitive dependence of trajectories on initial conditions in classical chaotic systems and has recently been formalized as an additional probe of quantum chaos [98, 99].

Eigenstate thermalization hypothesis

In general, the expectation values of relevant observables depend on the system's energy. Such a dependency is not part of the RMT approach which thus requires some extension. This has led to the *eigenstate thermalization hypothesis* (ETH), a statement about matrix el-

[5] For eigenstates of quantum systems with a chaotic classical counterpart in the semi-classical limit, this is Berry's conjecture [90].

[6] Typicality has also practical implications that allow to perform numerical calculations with pure states rather than ensembles. It can be extended to finite temperatures using imaginary time evolution [96, 97]. We use this approach in Chapter 3 to evaluate thermal expectation values without having to determine all eigenstates of the Hamiltonian.

ements of physical observables[7] first formulated by Srednicki [23–25][8],

$$O_{mn} = O(E)\delta_{mn} + e^{-S(E)/2} f_O(E,\omega) R_{mn}, \tag{2.8}$$

where $E = \frac{1}{2}(E_m + E_n)$ is the average and $\omega = E_n - E_m$ is the difference in energy of the two eigenstates $|n\rangle$ and $|m\rangle$. $O(E)$ is assumed to be a *smooth* function of the energy E, $f_O(E,\omega)$ is smooth in both E and ω, $S(E)$ is the thermodynamic entropy, and R_{mn} is a random variable with vanishing mean and unit variance. We see that the ETH of Eq. (2.8) is quite similar to the RMT result Eq. (2.7). Indeed, since both $O(E)$ and $f_O(E,\omega)$ are smooth, they will be approximately constant in a small neighborhood around a given energy E. Within energy intervals of a certain scale, called the Thouless energy, chaotic systems described by the ETH exhibit RMT behavior[9] in an effective Hilbert space of size proportional to the density of states $\exp\{S(E)\}$. Using the Ansatz of Eq. (2.8), we can investigate the thermalization of observables under the dynamics of a quantum chaotic Hamiltonian starting from an initial state $|\psi(t=0)\rangle = \sum_m C_m |m\rangle$,

$$\langle\psi(t)|\,\hat{O}\,|\psi(t)\rangle = \sum_m |C_m|^2 O_{mm} + \sum_{m\neq n} C_m^* C_n e^{-i(E_n - E_m)t} O_{mn}. \tag{2.9}$$

If we concentrate on the long time average of this expectation value, the second, oscillating term drops out and we obtain

$$\frac{1}{T}\int_0^T \langle\psi(t)|\,\hat{O}\,|\psi(t)\rangle \to \sum_m |C_m|^2 O(E_m). \tag{2.10}$$

This expression a priori still depends on the initial state through the constants C_m. To see that the right hand side of Eq. (2.10) is indeed equal to the expected microcanonical ensemble average, let us assume that the inital state $|\psi(t=0)\rangle$ is short-range correlated. The expectation value of the system's energy then becomes (for short-range models) an extensive sum over independent local contributions. As a consequence, by the central limit theorem, relative flucuations in energy are suppressed as $\sim 1/\sqrt{N}$ in system size. Accordingly, the C_m contributing to Eq. (2.10) will be restricted to eigenstates from a very small window around the energy expectation value $E = \langle\psi(0)|\hat{H}|\psi(0)\rangle$ of the initial state. Using the ETH Eq. (2.8), all contributing states then have the same expectation

[7] Again, highly non-local multibody terms such as projectors on individual eigenstates are not included. In general it is not entirely clear to which operators the ETH applies. As general rule, we expect all observables that refer to small subsystems are within the scope of the ETH.

[8] A first observable-centric approach to ergodicity in quantum systems was provided by von Neumann's ergodic theorem [100], which can be connected to RMT [101].

[9] Reciprocally, there exists a so-called Thouless time after which the dynamics of the system follows RMT predictions. In systems with conservation laws this timescale is expected to go as $\tau_{\mathrm{Th}} \sim L^z$, where z is the dynamical transport exponent. Many recent efforts have been devoted to confirming this picture using the so-called spectral form factor [67, 68, 87, 102–105].

value $O(E_m) = O(E)$, such that indeed

$$\sum_m |C_m|^2 O(E_m) = O(E) \sum_m |C_m|^2 = \sum_{|E_m - E| < \Delta E} \frac{O(E_m)}{\sum_{|E_m - E| < \Delta E}} = \langle \hat{O} \rangle_{\text{microcan.}} \tag{2.11}$$

Due to the suppressed off-diagonal matrix elements O_{mn}, fluctuations of $\langle \psi(t) | \hat{O} | \psi(t) \rangle$ around this average will be exponentially small at sufficiently late times, guaranteeing that the system is thermal at any instance. However, ETH cannot predict how long this approach to equilibrium takes for a given model, observable, and initial state. In principle, the energy differences in Eq. (2.9) are exponentially small in system size, such that exponentially long thermalization times are possible. On the other hand, the off-diagonal matrix elements are small, such that dephasing of the second term in Eq. (2.9) might quickly bring the system into equilibrium. Numerical work has demonstrated that thermalization can indeed occur on small timescales already for small numbers of particles [26]. Today, there exists a large body of numerical evidence that the ETH is indeed generically valid in interacting quantum many-body systems [106–115]. For large parts of this thesis we will be invested in determining the time scale and the manner in which quantum many-body systems relax towards equilibrium.

2.1.3 Exceptions to eigenstate thermalization

The ETH puts the concept of thermalization in quantum many-body systems on a firm footing. Nonetheless, while generic interacting quantum many-body systems are expected to exhibit quantum chaos and show eigenstate thermalization, there are very notable exceptions for which the ETH does not hold. We have already briefly mentioned *integrable* quantum systems, which exhibit an extensive number of local conserved quantities and equilibrate to a generalized Gibbs ensemble rather than thermal equilibrium [116–119]. Violation of the ETH and absence of thermalization also occurs in disordered quantum systems, via mechanisms known as Anderson localization [120, 121] for non-interacting systems and many-body localization (MBL) as its counterpart in the presence of interactions [27–36, 38–40]. In particular, MBL is believed to be stable with respect to general local perturbations (unlike integrable systems) for sufficently large disorder strength. This robustness of MBL can be used as a tool to stabilize interesting phases of matter such as symmetry-protected topological phases at finite energy densities [122–124] or discrete time crystals [125–130]. Notably, even below (but close to) the critical disorder strength required for localization, the approach to equilibrium in disordered systems can remain unconventionally slow [131–137]. MBL is widely believed to be stable only in one spatial dimension (although this is still a matter of debate, see e.g. [27, 138–141]) and is unstable to the presence of external noise [142–148]. We will see additional examples of exceptions to eigenstate thermalization that have been considered in the literature as we go through the remainder of this chapter.

2.2 Constraining the approach to equilibrium: Motivation and dynamical phenomena

As we have seen, the ETH provides a mechanism by which quantum many-body systems can reach thermal equilibrium. However, the existence of many-body localization demonstrates that ETH and thermalization do not apply to all quantum systems[10]. This 'exception to the rule' naturally inspires two fundamental questions that have been the focus of much interest in recent years. On the one hand:

> (1) *Are there novel ways by which violations of the ETH and absence of thermalization can occur also in translationally invariant systems without disorder?*

And on the other hand, similar to the phenomenology of MBL systems below the critical disorder strength:

> (2) *Can there be circumstances under which quantum systems eventually thermalize but do so in a slow fashion?*

If we can find such systems, natural follow-up questions concern their realization in experimental settings and whether their special properties may be of practical use in areas such as quantum information processing. These questions constitute our central motivation and will guide our thinking throughout this thesis. In particular, both questions allude to the prospect that the nonequilibrium dynamics of many-body systems should be *constrained* in one way or another as to evade a quick relaxation to thermal equilibrium. This leads us to the study of *constrained quantum many-body systems*.

In order to appreciate how the presence of constraints can lead to slow dynamics in many-body systems (classical and quantum), let us echo the following perspective from the theory of kinetically constrained models of Ref. [149]: Consider a classical lattice gas of N sites with binary local state space $|0\rangle$ and $|1\rangle$ and energy function $H(c)$ which depends on the configuration $|c\rangle = |c_1 ... c_N\rangle$ of the system. A stochastic approach to thermal equilibrium at inverse temperature β can be modelled in a Monte Carlo fashion through transitions in configuration space:

$$|c\rangle \to |c'\rangle\,, \quad \text{at rate} \quad \gamma(c \to c'). \tag{2.12}$$

Here, $\gamma(c \to c')$ is the rate (or acceptance probability) for the update $c \to c'$. Importantly, the rates should statisfy the detailed balance condition

$$\frac{\gamma(c \to c')}{\gamma(c' \to c)} = \exp\big\{-\beta[H(c') - H(c)]\big\}. \tag{2.13}$$

[10] We often use the terms 'ergodic', 'thermalizing' and 'obeys the ETH' synonymously unless additional context is provided.

If the set of possible updates is ergodic, the system will thermalize to the canonical ensemble. Crucially, there are many ways to choose the updates such that detailed balance is fulfilled, all of which lead to thermalization of local observables. This freedom of choice is usually taken advantage of in Monte Carlo simulations in order to reduce autocorrelation times and reach thermal equilibrium – in the form of a typical state that reproduces ensemble predictions for sums of local observables – as quickly as possible. However, in the present context we can reverse this line of reasoning and imagine that constraining the set of updates without affecting detailed balance can lead to a much slower approach to such a typical state. In particular, in stochastic lattice gases or systems with cellular automaton-type dynamics, we can interpret the Monte Carlo steps as part of a *real time* dynamical evolution. From this perspective, the much-dreaded 'local minima' of Monte Carlo simulations are viewed as features of slow dynamical relaxation which can be enhanced through the presence of constraints. Similar questions can then be formulated for natural quantum versions of such kinetic constraints, obtained by allowing only for certain constrained off-diagonal terms in the quantum Hamiltonian.

In the following, we provide a brief overview of several relevant examples of novel phenomena in constrained dynamics that have been uncovered over the past years and that will be relevant in the remainder of this thesis.

2.2.1 Glassy dynamics

The reasoning presented in the previous paragraphs, see Ref. [149], originates from the physics of classical kinetically constrained models [150–153]. These can exhibit extremely long relaxation times and therefore glassy dynamics at low temperatures within the framework of dynamical facilitation theory [154][11]. Naturally, the question arises whether similarly, long relaxation times can be found in kinetically constrained closed quantum systems. This has been found to be the case in a number of quantum systems with kinetic constraints, showing metastable states, slow relaxation of local observables, and suppressed growth of the entanglement entropy [1, 149, 158–161]. In addition, slow glass-like relaxation also at elevated temperatures has been found in heavy-light particle mixtures in which heavy particles act as effective disorder potential for light particles on prethermal time scales [162–173]. This is similar in spirit to systems with 'disorder-free localization' which generate their own static disorder potential [174–180].

We can formulate an illustrative argument to see how the quantum counterpart of a kinetically constrained classical system can feature slow dynamics. Let us assume, as suggested below Eq. (2.13), that a classical constrained Monte Carlo type evolution indeed features slow relaxation at low temperatures due to the presence of local energy minima. These minima may not necessarily be very deep, but since only a constrained set of up-

[11] This is in contrast with thermodynamic explanations of the glass transition [155–157], whose complete theoretical characterization remains an active challenge.

dates is available they will be far apart (in configuration space). We can then promote the allowed classical updates $c \to c'$ to (weak) off-diagonal terms in a quantum Hamiltonian while keeping the energy function $H(c)$ as diagonal terms,

$$\hat{H} = \sum_c H(c) \left|c\right\rangle \left\langle c\right| + \sum_{c,c':\, \gamma(c\to c')\neq 0} \Delta_{c,c'} (\left|c\right\rangle \left\langle c'\right| + \left|c'\right\rangle \left\langle c\right|). \tag{2.14}$$

If the $\Delta_{c,c'}$ are sufficiently weak (we could for example set $\Delta = 1/\beta$ at low temperatures), the local minima will persist. However, they can now only be connected through quantum tunneling processes, which are suppressed not only in the height of the energy barrier between minima, but also their hamming distance in configuration space. In that sense we might even expect 'quantum glasses' to be slower than their classical counterparts. We illustrate this line of arguments in Fig. 2.1. The challenge is then to determine which relevant models feature scenarios as outlined above. In particular, we will show that glassy quantum dynamics does occur for a two-dimensional constrained quantum dimer model in Chapter 3.

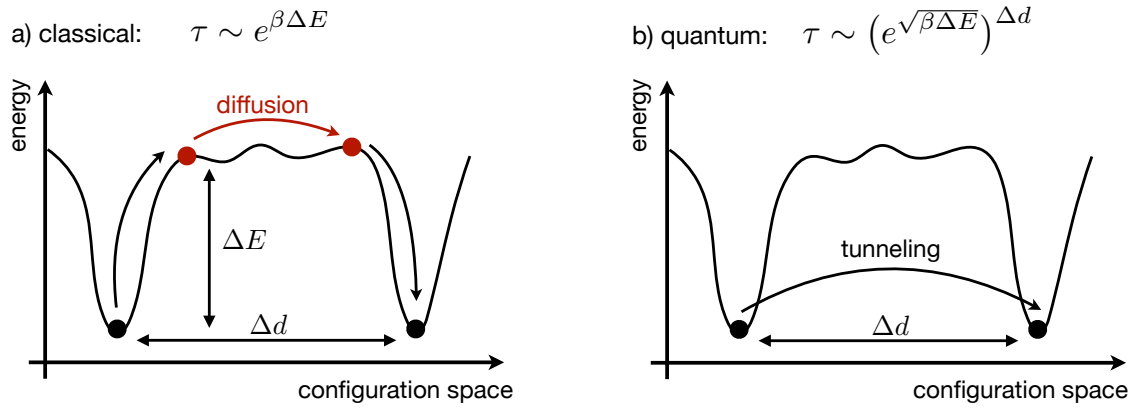

Figure 2.1: Glassy dynamics in classical and quantum constrained models. **a)** For classical stochastic Monte Carlo updates, the time τ to cross an energy barrier between two minima is dominated by the height ΔE of the barrier. In between the two minima, the system performs a diffusion process in configuration space. **b)** In closed quantum systems with small off-diagonal hopping terms $\sim 1/\beta$, the tunneling rate through the barrier is suppressed in both its height *and* width. This is indicated here by a simple WKB result for the tunneling amplitude.

2.2.2 Emergent hydrodynamics

In a sense, the simplest constraint to occur in quantum many-body systems is a global conserved $U(1)$ charge[12]. This could be the total number of particles or simply the energy (in a closed system) itself. Nonetheless, even such elementary constraints have important consequences for quantum dynamics. In particular, the presence of a conserved charge prevents a rapid relaxation to thermal equilibrium since charge inhomogeneities cannot

[12] That is, an extensive sum over local charges, such as the total particle number $\hat{N} = \sum_x \hat{n}_x$

decay locally. Instead, charge has to be transported through the system until a spatially homogeneous density is reached eventually. It is then an important task to determine in which manner this transport proceeds. Non-interacting or integrable systems are characterized by stable quasiparticles and thus generally exhibit ballistic propagation of charge excitations[13] [181–183]. However, ballistic transport is a consequence of phase coherence in systems that avoid thermalization. In generic interacting quantum many-body systems, we rather expect interactions to quickly induce many-body dephasing, destroying ballistic quasiparticle propagation. Therefore, it is now generally believed that the unitary time evolution leads to an emergent hydrodynamic regime of *diffusive* transport at late times [58–60, 65, 66, 184]. We provide an illustration of the associated thermalization process in the presence of conserved charges in Fig. 2.2: After an initial early time regime, the system will first equilibrate *locally*. From the point of view of local observables, which cannot access details of the initial state that have been scrambled quickly throughout the system, the state is then characterized by a course-grained local charge density $n(x,t)$. Accordingly, the final approach to global equilibrium can be described by an *effective* evolution equation for $n(x,t)$. By symmetry, the simplest equation allowed in a linear hydrodynamic expansion (in the absence of additional conserved quantities) is a diffusion equation[14],

$$\partial_t n(x,t) = D\,\partial_x^2 n(x,t), \tag{2.15}$$

where the details of the underlying unitary quantum time evolution enter the value of the effective diffusion constant D. We emphasize that the emergence of hydrodynamic transport from unitary quantum dynamics is highly non-trivial and difficult to establish rigorously. In particular, a controlled evaluation of transport coefficients such as the diffusion constant is extremely challenging in general. Establishing systematic algorithms that can achieve this goal is subject of several recent theoretical efforts [186–192]. As experimental capabilities to probe the emergence of hydrodynamics progress rapidly [193–204], the computation of transport coefficients could become a benchmark for quantum simulators in the future. Later in this thesis, in Chapter 9, we consider a special class of quantum many-body systems where transport properties can be extracted exactly.

On a more qualitative level, we emphasize that the emergence of diffusion in quantum many-body systems is an example of out-of-equilibrium universality. That is to say, irrespective of microscopic details, the general form of the diffusion equation Eq. (2.15) applies. We can then pose the question whether the presence of constraints beyond conventional global conserved charges can exhibit novel dynamical universality classes. This will be the subject of large parts of Chapters 4,6,7,9. In particular, our task is twofold: 1)

[13] Similarly, ballistic transport is expected on small to intermediate timescales at low energies where quasiparticle lifetimes are long.

[14] Throughout this thesis we will work with lattice systems where Umklapp-scattering processes ensure the absence of *momentum-conservation*. For momentum-conserving systems the hydrodynamic structure becomes richter, leading, in particular, to KPZ universality in one dimension [185].

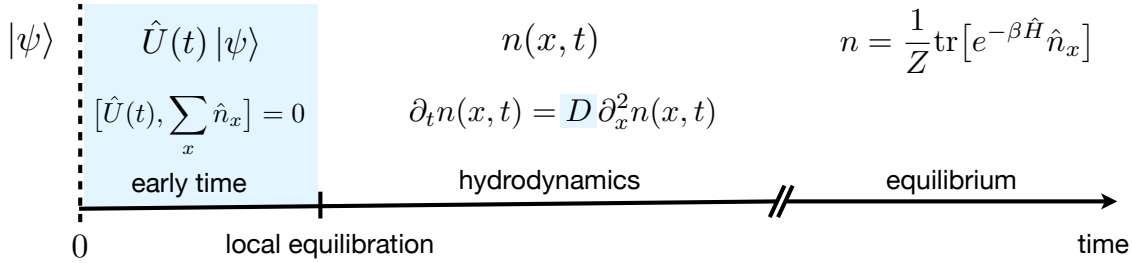

Figure 2.2: Thermalization process in systems with conserved quantities. First line: The state of the system from the point of view of *local observables*. At early times, knowledge of the full quantum state is required to characterize the system. At hydrodynamic timescales, the system is characterized by a coarse-grained local charge density $n(x,t)$. Equilibrium is characterized by the average charge density n. **Second line:** The dynamics of the system. At early, times the full unitary evolution $\hat{U}(t)$ needs to be considered. At hydrodynamic time scales the system follows an emergent, effectively classical hydrodynamic equation (here: the diffusion equation). Microscopic details merely enter the numerical value of the diffusion constant. In equilibrium, the system has reached a static state up to thermal fluctuations. **Third line:** The thermalization process of the system can thus be characterized by early time dynamics until local equilibration, an emergent hydrodynamic regime, and equilibrium.

Establishing the (potentially novel) hydrodynamic universality classes of constrained systems. 2) Demonstrating that such hydrodynamics indeed emerges from a unitary closed quantum evolution. Importantly, step 1) can often be achieved by considering random unitary circuit dynamics [65, 66] or effectively classical counterparts of constrained quantum systems instead of closed system quantum Hamiltonians [2, 205–207], similar to the perspective of kinetically constrained models we presented previously. However, we emphasize that we will investigate hydrodynamic relaxation at *high* temperatures; unconventionally slow transport in constrained models is thus not due to the presence of local energy minima. Instead, constraints can restrict the entropic forces that lead to hydrodynamics (loosely speaking: charge gradients decay for entropic reasons in conventional diffusive systems), modifying the eventual universality class of transport.

2.2.3 Operator dynamics and entanglement growth

So far, we have mostly considered the dynamics of simple local observables, which can indicate glassy behavior or slow hydrodynamic transport. What other dynamical measures of thermalization and quantum chaos are there? One common approach is to study the scrambling of quantum information throughout the system due to the unitary time evolution [208–211]. This process corresponds to the growth of operators in the Heisenberg picture from initially local objects to large superpositions of long Pauli operator strings. A way to quantify this spread of operators is offered by out-of-time-ordered correlation functions (OTOCs) between two operators [208–212],

$$C_{\mathcal{O}_1\mathcal{O}_2}(t) = \left\langle \left| [\hat{\mathcal{O}}_1(t), \hat{\mathcal{O}}_2] \right|^2 \right\rangle , \tag{2.16}$$

see also Fig. 2.3 for an illustration. For generic systems, the spatial support of an operator $\hat{\mathcal{O}}_1(t)$ grows linearly in time, leading to a ballistic light-cone structure in the OTOC of Eq. (2.16). Conceptually, OTOCs can be introduced as canonically quantized versions of a classical quantity that probes the exponential divergence of trajectories with slightly different initial conditions [212, 213]. However, this property persists only close to a classical limit, while in general the growth of the OTOC in quantum systems is bounded and saturates to a constant value [60, 63, 64, 213–217]. Nonetheless, OTOCs serve as useful measures of information scrambling and linear spreading of quantum chaos. In particular, OTOCs can distinguish between generic systems, integrable systems [218], and many-body-localized systems where the light cone moves logarithmically slow [219–223]. We will investigate novel ways in which the spreading of operators can be qualitatively slowed down in Chapter 8. In addition, the spreading of operators also serves as a bound for the growth of quantum entanglement, which can be quantified e.g. through the subsystem Rényi entropies

$$S_n(t) = \frac{1}{1-n} \log\big(\mathrm{tr}[\rho_A^n(t)]\big), \tag{2.17}$$

where $\rho_A(t)$ is the reduced density matrix of the subsystem A. Such entanglement entropies generically grow linearly in time in thermalizing systems, with a velocity upper-bounded by the ballistic spreading of operators [61, 64].

It has previously been established that both the dynamics of operators [63–66, 189, 224] as well as entanglement [61, 62, 225–227] in thermalizing systems can be captured within an effective hydrodynamic description. Accordingly, the presence of conservation laws can have qualitative impact on those processes. This has been verified explicitly in random circuit models with a global $U(1)$ charge conservation law [65, 66], which leaves clear signatures in the profile of certain OTOCs[15] and leads to a slow growth of Rényi entanglement entropies $S_n(t)$ for $n > 1$ [62, 228, 229]. Again, we can pose the question how such features generalize to the presence of additional constraints beyond conventional $U(1)$ charges.

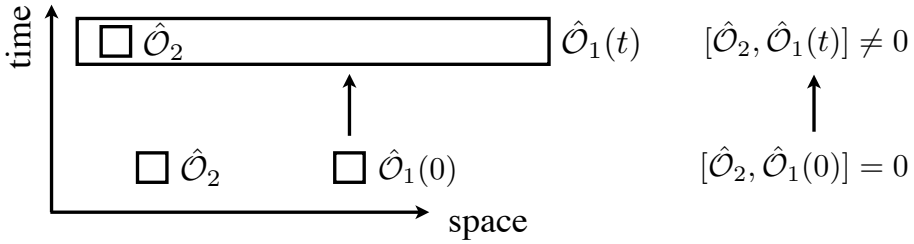

Figure 2.3: Operator growth. Under unitary time evolution, the spatial support of an operator $\hat{\mathcal{O}}_1(t)$ in the Heisenberg picture grows. This growth can be captured by out-of-time-ordered correlation functions: While at early times $\hat{\mathcal{O}}_1(t)$ commutes with a spatially distant operator $\hat{\mathcal{O}}_2$, at later times the spatial support of $\hat{\mathcal{O}}_1(t)$ overlaps with $\hat{\mathcal{O}}_2$, leading to non-trivial commutation relations.

[15] In particular, those OTOCs in which at least one of the operators $\hat{\mathcal{O}}_{1/2}$ has finite overlap with the charge conservation law.

2.2.4 Quantum many-body scars

One of the main driving forces behind the large interest in the dynamics of constrained quantum systems in recent years has been the discovery of *quantum many-body scars* [51–57]. These can be defined as eigenstates with low (i.e. sub-volume law) entanglement at high energies in the many-body spectrum[16]. Notably, these special eigenstates coexist with a vast majority of highly entangled eigenstate that fulfill the ETH. Systems with quantum many-body scars thus exhibit weak violations of the eigenstate thermalization hypothesis[17]. Although the number of such eigenstates is exponentially small compared to the size of the Hilbert space, they are relevant to experiments whenever their overlap with experimentally preparable states is large. The most well-known model exhibiting such quantum many-body scars is the so-called 'PXP' model,

$$\hat{H} = \sum_x \hat{P}_{x-1}\hat{X}_x\hat{P}_{x+1}, \qquad \hat{P}_x = 1 - \hat{n}_x, \tag{2.18}$$

which is approximately realized in Rydberg atom quantum simulators [51]. The model Eq. (2.18) operates on a binary local Hilbert space $\hat{n}_x \in \{0, 1\}$ and $\hat{X}_x$ corresponds to the x-Pauli matrix. The experiments of Ref. [51] revealed very slow relaxation tied to the presence of quantum many-body scars starting from specific initial states. From a theoretical perspective, there exist a number of known mechanisms that can lead to the emergence of scars in the spectrum of quantum many-body systems. Among them are so-called spectrum-generating algebras [57, 230, 231] or projector embedding constructions [232]; see the recent reviews of Refs. [233, 234] and references therein for an overview of the many examples of such scarring-mechanisms that have emergent in recent years.

2.2.5 Hilbert space fragmentation

We have discussed a number of dynamical phenomena in constrained quantum many-body systems: Glass-like and hydrodynamic relaxation to an eventual thermal state, which is unconventionally slow, but does not violate the ETH. Secondly, the presence of special 'scarred' eigenstates in the many-body spectrum, which corresponds to a weak violation of ETH. Notably however, constraints also offer novel ways to achieve *strong* violations of the ETH, where a finite ratio of all eigenstates of the Hamiltonian are non-thermal. One route to obtain localization of observables (similar to MBL) in this way leads to the concept of Hilbert space fragmentation [235–238]. This concept is best approached from the perspective of kinetically constrained models in Eq. (2.12). We consider a set of updates sufficiently constrained such that the space of possible configurations splits into

[16] For comparison, we can note that RMT predicts eigenstates in the middle of the spectrum to be random states, which exhibit volume-law entanglement.

[17] As opposed to the strong violation of the ETH in many-body-localized systems, where all eigenstates are believed to escape the ETH.

disjoint partitions. In the language of kinetically constrained models this is known as *reducibility* [150]. The partitioning of configuration space can become strong enough such that local observables do not relax towards their expected thermal value even at infinite times. Consequently, thermalization is absent also in quantum Hamiltonians subject to the same constraints on their off-diagonal terms[18], *cf.* Eq. (2.14). There, the dynamics of the system becomes reducible in Hilbert space, which is said to be 'fragmented' if it splits into an exponentially large number of disjoint subsectors [235]. Again, if this exponential fragmentation becomes sufficiently strong, local observables remain stuck at non-thermal values. We emphasize that it is difficult in general to infer whether a given fragmentation of Hilbert space is strong enough to cause absence of thermalization.

Formally, see Refs. [233, 238, 239], Hilbert space fragmentation can be introduced by considering a basis $\{|\psi_j\rangle\}$ of the Hilbert space $\mathcal{H}$, as well as the associated Krylov spaces

$$\mathcal{K}_j = \text{span}\{|\psi_j\rangle\,, \hat{H}\,|\psi_j\rangle\,, \hat{H}^2\,|\psi_j\rangle\,, ...\}. \tag{2.19}$$

In generic, ergodic many-body systems without (conventional) symmetries[19] we expect that $\mathcal{K}_j = \mathcal{H}$ for all j, i.e. the state $|\psi\rangle$ explores the entire Hilbert space $\mathcal{H}$ under applications of the Hamiltonian. Fragmentation of the Hilbert space can then be defined by $\mathcal{K}_j \neq \mathcal{H}$, with $\mathcal{H}$ becoming a direct sum of *exponentially* many disjoint Krylov spaces. Defined in this way, unlike reducibility in classical kinetically constrained models, fragmentation is a *basis-dependent* concept. Importantly, for thermalization of local observables to be absent, a strong fragmentation should exist in a sufficiently simple, local basis[20]. Hilbert space fragmentation was initially introduced in the context of fractonic constrained models with dipole conservation [235, 236]. Therein, fragmentation occurs in a classical, i.e., unentangled basis, equivalent to reducibility. In certain examples it is even possible to provide explicit expressions for the 'quantum numbers' that label the disjoint subspaces [237]. We will study the properties of such models beyond fragmentation in the second part of this thesis. Recently, an example of strong Hilbert space fragmentation which requires an entangled set of basis states was provided in the context of Temperley-Lieb chains in Ref [239].

2.3 Constrained quantum systems in theory and experiment

Up until this point, we have provided an overview over the concept of thermalization in quantum many-body systems and some of the exciting phenomena that may occur when a many-body system's approach to equilibrium is constrained. However, so far we have

[18] Considering a closed quantum system only adds yet another constraint: energy conservation.

[19] Or with symmetries such as lattice transformations, particle number, etc. already resolved, such that $\mathcal{H}$ is the Hilbert space associated to one symmetry sector.

[20] The Hilbert space is always entirely disconnected in the eigenbasis of the Hamiltonian, which, however, is not a simple, local basis.

(mostly) avoided referencing specific systems. In this section, we introduce some of the physical constraints that we will be occupied with on a theoretical level throughout this thesis. We then proceed to give a brief account of several experimental platforms that potentially allow for realizations of these models.

2.3.1 Emergent gauge theories

Part I of this thesis studies the dynamics of many-body systems with local gauge constraints. Gauge theories are central to our modern understanding of physics as they lie at the heart of fundamental particle physics [240] and hold the promise of valuable applications in quantum information processing [241]. Gauge theories in quantum many-body systems such quantum spin liquids are usually thought of as *emergent* low energy descriptions. Here we discuss briefly some of the most relevant aspects of gauge constraints for this thesis.

Dimer Models

In Chapters 3,4 we consider the dynamics of quantum dimer models [242]. Such models originate from Anderson's idea to use the resonating valence bond state as a means to describe the high temperature cuprates [243]. In this scenario, a 'dimer' is a local singlet formed between two spins and one assumes that the low energy subspace of the relevant Hubbard model is well-captured by restricting to the dimer basis. One can then write down a corresponding quantum dimer Hamiltonian in this new basis. From this perspective, quantum dimer models are emergent low-energy descriptions of interacting electron or spin systems. However, we may also consider the properties of dimer models in their own right once the restriction to dimer coverings is made. Putting aside the origin story of dimers as spin singlets, this presents a good starting point to introduce the central concepts of gauge theory as relevant for this thesis. Let us consider close-packed, nearest neighbor dimer coverings of a square lattice as shown in Fig. 2.4 and let $\hat{d}^\dagger_{i,\mu}\hat{d}_{i,\mu} = \hat{n}_{i,\mu} \in \{0,1\}$ denote the dimer occupation number on the bond between sites i and $i+\hat{e}_\mu$, $\mu \in \{x,y\}$. The Hilbert space of valid dimer coverings is characterized by the constraints

$$\hat{\tilde{G}}_i := \hat{n}_{i,x} + \hat{n}_{i-\hat{e}_x,x} + \hat{n}_{i,y} + \hat{n}_{i-\hat{e}_y,y} = 1. \tag{2.20}$$

Eq. (2.20) expresses that there is exactly one dimer emanating from each lattice site. Let us note that within this geometry, there exist non-local winding numbers W_x (W_y) defined as

$$W_x = \sum_{i_x} (-1)^{i_x} \hat{n}_{(i_x,i_y),y}, \tag{2.21}$$

and analogous for W_y. Eq. (2.21) is independent of i_y and is invariant under *any* local rearrangement of the dimer configuration [242] that is consistent with the constraints

Eq. (2.20). A concrete Hamiltonian in the dimer basis that preserves the constraints Eq. (2.20), the famous Rokhsar-Kivelson model that we consider in Chapter 3 [244], is given by

$$\begin{aligned}\hat{H} &= -J\sum_i(\hat{d}^\dagger_{i,x}\hat{d}^\dagger_{i+\hat{e}_y,x}\hat{d}_{i,y}\hat{d}_{i+\hat{e}_x,y}+h.c.)+V\sum_i(\hat{n}_{i,x}\hat{n}_{i+\hat{e}_y,x}+\hat{n}_{i,y}\hat{n}_{i+\hat{e}_x,y}) = \\ &= -J\sum_{\text{plaq.}}\left(|\square\rangle\langle\square|+|\square\rangle\langle\square|\right)+V\sum_{\text{plaq.}}\left(|\square\rangle\langle\square|+|\square\rangle\langle\square|\right),\end{aligned} \tag{2.22}$$

where the ellipses in the pictorial representation correspond to dimers occupying the bonds. We see explicitly how this model maps to a theory with $U(1)$ gauge structure by introducing the 'electric fields' [245, 246]

$$\hat{E}_{i,\mu} = (-1)^{i_x+i_y}\left(\hat{n}_{i,\mu}-\frac{1}{2}\right), \tag{2.23}$$

which correspond to spin-1/2 variables $\hat{E}_{i,\mu}\in\{\pm 1/2\}$ on the bonds of the lattice. The constraint Eq. (2.20) then becomes (Δ_μ denotes a discretized lattice derivative)

$$\hat{G}_i := (-1)^{i_x+i_y}\left(\hat{\tilde{G}}_i-2\right) = \hat{E}_{i,x}-\hat{E}_{i-\hat{e}_x,x}+\hat{E}_{i,y}-\hat{E}_{i-\hat{e}_y,y} = \Delta_\mu\hat{E}_{i,\mu} = -(-1)^{i_x+i_y}. \tag{2.24}$$

Eq. (2.24) takes the conventional form of a Gauss law for a static staggered charge distribution $\rho_i = -(-1)^{i_x+i_y}$. Upon introducing the ladder operators $\hat{U}_{i,\mu}$ with $[\hat{U}_{i,\mu},\hat{E}_{j,\nu}] = \delta_{ij}\delta_{\mu\nu}\hat{U}_{i,\mu}$ for the electric fields, the Hamiltonian Eq. (2.22) reads

$$\begin{aligned}\hat{H} &= -J\sum_i(\hat{U}^\dagger_{i,y}\hat{U}^\dagger_{i+\hat{e}_y,x}\hat{U}_{i+\hat{e}_x,y}\hat{U}_{i,x}+h.c.)+V\sum_i(\hat{U}^\dagger_{i,y}\hat{U}^\dagger_{i+\hat{e}_y,x}\hat{U}_{i+\hat{e}_x,y}\hat{U}_{i,x}+h.c.)^2 \\ &= -J\sum_{\text{plaq.}}\left(|\square\rangle\langle\square|+|\square\rangle\langle\square|\right)+V\sum_{\text{plaq.}}\left(|\square\rangle\langle\square|+|\square\rangle\langle\square|\right),\end{aligned} \tag{2.25}$$

where in the pictorial representation, thick lines correspond to bonds with $E_{i,\mu} = +1/2$. We notice that the first term in Eq. (2.25) takes the form of the Kogut-Susskind Hamil-

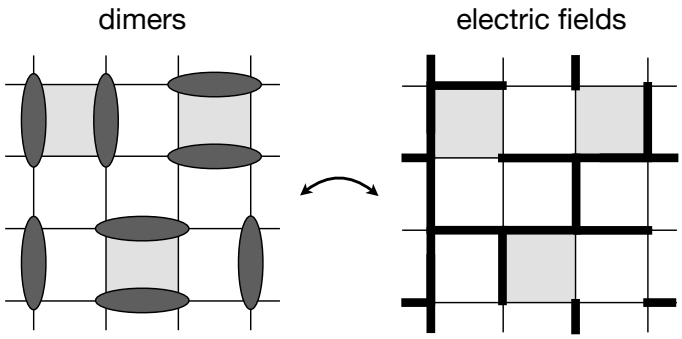

Figure 2.4: Dimer model - gauge theory duality. Mapping between close-packed nearest neighbor dimer occupations and eletric field configurations according to Eq. (2.24). The flippable plaquettes are marked in light gray.

tonian for lattice quantum electrodynamics [247]. The usual contribution of the electric field $\hat{E}_{i,\mu}^2 = 1/4$ provides only a constant shift and is omitted. This is a consequence of truncating the electric field to just two possible values, making Eq. (2.25) a quantum link model [246, 248–250]. The $\hat{U}_{i,\mu} \sim e^{i\hat{a}_{i,\mu}}$ are Wilson operators associated to a compact gauge field $a_{i,\mu}$, which acts as the canonically conjugate phase variable to the electric field. As expected, Eq. (2.25) is then invariant under the local $U(1)$ gauge transformations

$$\hat{U}_{i,\mu} \to e^{i\theta_{i+\hat{e}_\mu}} \hat{U}_{i,\mu} e^{-i\theta_i} \tag{2.26}$$

for an arbitrary lattice function θ_i, corresponding to $a_{i,\mu} \to a_{i,\mu} + \Delta_\mu \theta_i$. The present discussion shows that the quantum dimer model on the square lattice indeed corresponds to a $U(1)$ lattice gauge theory, and there exists a large body of works detailing its ground state phase diagram [251–257]. However, much less is known about the dynamics in such systems. In this thesis, we explore the role of the gauge constraints Eqs. (2.20,2.24) for nonequilibrium dynamics. In Chapter 3 we uncover the presence of glassy dynamics as discussed previously, and we investigate unconventional hydrodynamics and novel forms of ergodicity breaking due to the non-local winding numbers Eq. (2.21) in Chapter 4.

Spin liquids

In the previous paragraph, we restricted our discussion to a Hilbert space with $U(1)$ gauge structure from the get-go. Naturally, the question arises how such gauge constraints can effectively emerge as low energy theories of realistic many-body spin systems. This is believed to be the case in quantum spin liquids [258–262], where *fractionalization* of spin excitations into new particles gives rise to emergent gauge fields at low energies. Spin liquids are novel topological quantum phases of matter of local spin Hamiltonians in which the ground state breaks neither spin rotation nor lattice symmetries. They fall outside the conventional symmetry-breaking classification of quantum phases of matter. Instead, spin liquids are characterized by their long-range entanglement and topological properties. In particular, due to the presence of anyons in two dimensions they present potential platforms for fault-tolerant topological quantum computation [241]. However, due to the absence of a conventional order parameter, identifying spin liquids in current experiments is challenging. In Chapter 5 we study how probing local dynamical properties of spin liquid states might aid in their experimental identification.

Some key concepts of spin liquid states can be illustrated within a parton mean field description. Therein, the usual spin-$1/2$ operators $\hat{\boldsymbol{S}}_i$ on site i can be expressed in terms of auxilliary bosons[21] [265],

$$\hat{\boldsymbol{S}}_i = \frac{1}{2} \sum_{\alpha,\beta} \hat{d}_{i,\alpha}^\dagger \boldsymbol{\sigma}_{\alpha\beta} \hat{d}_{i,\beta}, \tag{2.27}$$

[21] It is also possible to use fermions[263]. In that case, the resulting gauge structure will be $SU(2)$ instead of $U(1)$[264].

where $\alpha, \beta \in \{\uparrow, \downarrow\}$ and the $\sigma^{a=x,y,z}$ are the Pauli matrices. Importantly, the description Eq. (2.27) enlarges the local Hilbert space dimension. In order to describe a physical spin wave function, one should thus introduce the constraints

$$\sum_{\alpha} \hat{d}^{\dagger}_{i,\alpha} \hat{d}_{i,\alpha} = 1, \tag{2.28}$$

i.e., there is exactly one boson at each site. Again, we encounter local constraints that naturally lead to an emergent gauge structure. In particular, given an antiferromagnetic Heisenberg-type lattice spin model $\hat{H} = \sum_{ij} J_{ij} \hat{\boldsymbol{S}}_i \cdot \hat{\boldsymbol{S}}_j$ and inserting the decomposition Eq. (2.27), a mean field decoupling in $Q_{ij} = \langle \hat{d}^{\dagger}_{i,\alpha} \hat{d}_{j,\alpha} \rangle$ yields[22] [15]

$$\hat{H} = -\frac{1}{2} \sum_{ij} J_{ij} \left[(\hat{d}^{\dagger}_{i,\alpha} \hat{d}_{j,\alpha} Q_{ij} + h.c.) - |Q_{ij}|^2 \right] + \sum_{i} \lambda_i (\hat{d}^{\dagger}_{i,\alpha} \hat{d}_{i,\alpha} - 1), \tag{2.29}$$

where λ_i is a chemical potential that fixes the constraint Eq. (2.28) on average. We see that Eq. (2.29) is invariant under the $U(1)$ gauge transformations

$$\begin{aligned} Q_{ij} &\to e^{i\theta_i} Q_{ij} e^{-i\theta_j} \\ \hat{d}_{i,\alpha} &\to \hat{d}_{i,\alpha} e^{-i\theta_i}, \end{aligned} \tag{2.30}$$

and thus describes spinons moving in the presence of a compact $U(1)$ gauge field, which is static at the mean field level. In practice, a careful analysis of the stability of a given self-consistent mean field Ansatz upon including fluctuations of the gauge field is required [259] [23]. In a spin liquid phase, the spinons are deconfined and appear as stable low energy excitations along with the excitations of the gauge field. In addition, the gauge structure may be broken down from $U(1)$ to $\mathbb{Z}_2$ via the Higgs mechanism [267, 268]. In Chapter 5 we consider the spin liquid state of the Kitaev honeycomb model [241], where the emergent gauge field is static and the mean field parton construction solves the model *exactly*. In that case, the employed partons are Majorana fermions $\hat{b}_{i,\alpha}$ instead of complex bosons or complex fermions, which renders the mean fields $Q_{ij} = i \langle \hat{b}_{i,\alpha} \hat{b}_{j,\alpha} \rangle$ real since $(\hat{b}_{i,\alpha} \hat{b}_{j,\alpha})^2 = -1$. This condition induces a $\mathbb{Z}_2$ gauge structure as only $\theta_i = 0, \pi$ remain as viable gauge transformations in Eq. (2.30).

2.3.2 Fracton models

In recent years, novel types of constrained quantum systems that are known as 'fracton models' have attracted much interest [69, 70, 269–277]. Loosely speaking, such systems are characterized by elementary excitations – called fractons – with restricted mobility (see e.g. Fig. 2.5). An early example was provided in the form of a solvable lattice model in

[22] Of course, there are other mean field channels in which the Hamiltonian can be decoupled.
[23] For example, pure compact $U(1)$ gauge theory is confining in two dimensions [266].

Ref. [269], which aptly characterized the system's low energy properties as 'topological overprotection', as elementary excitations cannot diffuse locally, leading to long relaxation times. Relatedly, fracton models can feature an *exponential*[24] number of degenerate ground states, which cannot be distinguished locally. This is in contrast with other topologically ordered states, which have constant (or algebraic) ground state degeneracy. Fracton models generally come in two different types, named type I and type II. In models of type I, such as the X-cube code [273], there exist mobile objects composed of multiple fractons that can move along subdimensional manifolds such as lines or planes, even though single fractons are immobile. In type II models on the other hand, such as Haah's cubic code [270], there are no dispersive quasiparticles and excitations sit at the corners of a fractal structure. Moving an excitation leads to the creation of new excitations and thus costs energy. These exactly sovable three-dimensional lattice examples of fracton models are gapped.

Notably however, there also exist gapless fracton models that can be understood as symmetric tensor gauge theories (or multipole gauge theories) [274, 275, 278, 279]. In the simplest case, such a gauge theory is a rank-2 generalization of (compact) $U(1)$ quantum electrodynamics[25]. That is to say, instead of a usual vector potential $A_i(x)$ ($i = 1, ..., d$, where d is the spatial dimension) and its conjugate electric field $E_i(x)$, one works with a two-indices tensor $A_{ij}(x)$ and its conjugate variables $E_{ij}(x)$. Demanding invariance under the gauge transformation $A_{ij}(x) \to A_{ij}(x) + \partial_i\partial_j\theta(x)$ and including potential charge degrees of freedom, this leads to a modified Gauss law (the generator of such gauge transformations)

$$\sum_{ij} \partial_i\partial_j E_{ij} = \rho, \tag{2.31}$$

with the local charge density $\rho(x)$. Such a Gauss law naturally implies conservation not only of the total charge, but also of the dipole moment of the charge density, since

$$\int d^dx \boldsymbol{x}\rho(x) = \int d^dx \boldsymbol{x} \sum_{ij} \partial_i\partial_j E_{ij} \sim \text{boundary terms}. \tag{2.32}$$

If the dipole moment is conserved, single charges are immobile and thus become fractons. Only composite objects, such as dipole excitations, acquire non-trivial mobility, see Fig. 2.5. Similar constraints are relevant in certain models of the fractional quantum Hall effect [280–285]. While at first sight this approach appears very different to the gapped lattice models mentioned above, it has been shown that multipole gauge structures can incorporate e.g. the gapped fracton phase of the X-cube model by Higgsing the gauge excitations [286, 287]. Furthermore, the multipole gauge description offers an exciting duality to elasticity theory in two dimensions [288–290], in which immobile fractons, mobile dipoles and gapless gauge excitations map to disclinations, dislocations and phonons

[24] Exponential in the linear spatial extent of the system

[25] Such fracton theories can be viewed as higher rank generalizations of $U(1)$ spin liquids [274]

Figure 2.5: Fractons in dipole-conserving systems. In systems with dipole-conservation, single charges are immobile and correspond to fractons. In contrast, dipole objects composed of two fractons can move freely.

of the lattice, respectively.

In this thesis our interest in fractonic systems is twofold: On the one hand we will demonstrate in Chapters 3,4 that the more conventional $U(1)$ gauge theories of quantum dimer models can exhibit dynamical features similar to fractons, such as glassy dynamics at low energies and the emergence of mobility along subdimensional manifolds [291]. On the other hand, while above we introduced the concept of fractons in the language of low energy field theory, in this thesis we consider the thermalization dynamics of fracton lattice models with multipole conservation laws at high energies, see in Chapters 6-9.

2.3.3 Experimental platforms: Synthetic quantum systems and quantum materials

Loosely speaking, experimental realizations of constraints in quantum many-body systems require one of two things: a high degree of control over a synthetic quantum system or a natural material realization. Both of these areas have seen immense progress over recent years [43–46, 50, 292, 293]. Here, we provide a brief overview of several experimental platforms that (potentially) realize the constrained systems introduced above.

Synthetic quantum systems

The central idea of synthetic quantum systems is to arrange a large set of quantum mechanical degrees of freedom while maintaining control and being able to manipulate its quantum state, in conjuction with tools to characterize the properties of this state. In the spirit of Feynman [41], this would allow for efficient simulation of quantum many-body problems on such devices. The main challenge is to overcome the apparent conflict between large system sizes and maintaining full control: The device needs to be isolated from environmental noise, while at the same time being steered externally towards a desired time evolution of the quantum state. We sketch the progress that has been achieved in several platforms over recent years and how constrained systems can be implemented in them. We emphasize that the following selection of platforms is not exhaustive and we refer to the literature for more information [50].

Rydberg atoms

A quantum simulation platform that lends itself very naturally to the study of constrained systems is based on Rydberg atoms in which an electron is excited to high principal quantum number [51, 292, 294, 295]. Rydberg atoms feature strong repulsive van der Waals interactions that scale as $V_{ij} \sim C/R_{ij}^6$ with the distance between two atoms. The atoms can be trapped in optical tweezers and arranged in essentially any desirable configuration, providing a high degree of control. The quantum dynamics of an ensemble of Rydberg atoms is controlled by the distances between the atoms as well as by laser driving the transition between ground state $|g\rangle$ and Rydberg excited state $|r\rangle$. This gives rise to an effective spin-$1/2$ many-body Hamiltonian [51]

$$\hat{H} = \Omega \sum_i \hat{\sigma}_i^x + \Delta \sum_i \hat{n}_i + \sum_{ij} V_{ij} \hat{n}_i \hat{n}_j, \tag{2.33}$$

where Ω and Δ are the Rabi frequency and detuning of the ground state - Rydberg transition and $\hat{n}_i = |r\rangle \langle r|_i$[26]. When two atoms are sufficiently close, the strong interaction V_{ij} prevents simultaneous excitation of both atoms into the Rydberg excited state. This is known as the Rydberg blockade, which serves as a tool to implement robust two-qubit gates in the context of gate-based quantum computation [296, 297] and naturally implements a constraint in the quantum simulation of the Hamiltonian Eq. (2.33). The state of the atomic ensemble can be measured in a site-resolved manner through imaging the fluorescence of ground state atoms.

In recent years, the many-body Hamiltonian Eq. (2.33) has been implemented to study for example quantum phase transitions between symmetry breaking phases [298, 299] as well as quantum dynamics [51]. The latter has led to the discovery of quantum many-body scars in the PXP model of Eq. (2.18), which is realized by Eq. (2.33) in the nearest-neighbor blockade regime. There exist also proposals to use the blockade to implement local gauge constraints [295, 300, 301]. Recently, a Kagome lattice quantum dimer state that corresponds to a $\mathbb{Z}_2$ spin liquid phase [302] was implement in a Rydberg platform [303]. In this experiment, the spin liquid is constructed directly in the dimer basis. Rydberg atoms have recently even been used to tackle certain classical graph problems of finding maximal independent sets, whose solution can naturally be encoded in the ground state of Eq. (2.33) [304].

Cold atoms in optical lattices

Cold atoms in optical lattices have proven to be an extremely versatile quantum simulation platforms over the past decades [42, 43]. The geometry of the setup is controlled by trapping the atoms inside an external confining potential, which can be used to

[26] It is also possible to encode spin-$1/2$ qubit degrees of freedom in hyperfine ground state levels or in two different Rydberg levels [292].

engineer the dimensionality of the system. On top of the trap, an optical lattice can be imposed by interference of counterpropagating laser beams, which generates an optical standing wave that acts as a periodic lattice potential for the trapped atoms. This allows one to study Hamiltonians relevant in the context of condensed matter systems. The associated tight-binding tunneling matrix element of atoms in the optical lattice is controlled (with stretched-exponential sensitivity, *cf.* Fig. 2.1) by tuning the lattice depth. The contact interaction between atoms can be controlled independently via Feshbach resonances, which allow for a tuning of the scattering length. This degree of control provides access to strongly interacting systems that can realize correlated phases of matter, the paradigmatic example being the Fermi-Hubbard model [305, 306]. There are several probes for measuring correlations in a given quantum state in cold atomic setups. One possibility is to perform time-of-flight measurements that map the momentum distribution of an expanding atomic cloud to a real space distribution which can subsequently be measured. This method was instrumental in verifying the creation of a Bose-Einstein-condensate [307, 308] as well as the superfluid-Mott insulator transition [309]. More recently, the development of quantum gas microscopes [310, 311] allows for single-site resolved snapshots of the many-body state. Such microscopy provides access to high-order correlations that can be vital in characterizing strongly correlated phases of matter [312–315]. Over the past years, this toolset has also provided insights into nonequilibrium properties of quantum many-body systems, shedding light on many of the concepts discussed above: Thermalization after a quench [316] and emergence of hydrodynamics [193–197, 317], as well as non-thermal behavior such as integrable quantum dynamics [199, 200] and observation of many-body localization [141, 318, 319].

In the context of constrained systems relevant for this thesis, cold atoms in optical lattices have recently been used to realize models with fractonic dipole conservation laws as described above. This can be achieved by imposing a linearly tilted potential in addition to the optical lattice. The Hamiltonian implemented in such a setup is the Fermi-Hubbard model with linear potential along the x-direction,

$$\hat{H} = -t \sum_{i,\sigma,\mu} (\hat{c}^\dagger_{i+\hat{e}_\mu,\sigma} \hat{c}_{i,\sigma} + h.c.) + U \sum_{i,\sigma} \hat{n}_{i,\sigma} \hat{n}_{i,\bar{\sigma}} + F \sum_{i,\sigma} i_x \hat{n}_{i,\sigma}. \tag{2.34}$$

This model has been realized in two dimensions in Ref. [197] and later in one dimension in Refs. [320, 321]. The relation to the dipole-conserving fracton systems introduced above can be established most directly in the latter case in the regime of strong tilts $F \gg t, U$. Eq. (2.34) couples directly to the fermion center of mass, which we thus expect to act as an emergent dipole conservation law, at least on prethermal time scales (that is, exponentially long in the tilt strength). Indeed, moving a single fermion one site up the tilt (which is suppressed as t/F) yields a large energy penalty for strong F, and so a second fermion needs to move down the tilt at the same time in order to arrive back on energy shell. The

movement of the two fermions thus needs to be correlated and this correlation is mediated by the Hubbard interaction term U. We then naturally expect the emergence of a dipole/center of mass-conserving correlated hopping term at order $U\,(t/F)^2$. Formally, this is indeed found after a Schrieffer-Wolff-transformation[27], which yields an effective Hamiltonian (on a one-dimensional lattice), see Refs. [320–322],

$$\hat{H}_{\text{eff}} = U\frac{t^2}{F^2}\sum_i(\hat{c}^\dagger_{i-1,\sigma}\hat{c}_{i,\sigma}\hat{c}_{i,\bar{\sigma}}\hat{c}^\dagger_{i+1,\bar{\sigma}} + h.c.) + U\sum_{i,\sigma}\hat{n}_{i,\sigma}\hat{n}_{i,\bar{\sigma}} + F\sum_{i,\sigma} i\hat{n}_{i,\sigma} + \mathcal{O}\big(Ut^2/F^2\big), \tag{2.35}$$

where the remaining terms of order $\mathcal{O}(Ut^2/F^2)$ all commute with the local density $\hat{n}_i = \hat{n}_{i,\uparrow} + \hat{n}_{i,\downarrow}$. It should be noted that the effective Hamiltonian Eq. (2.35) acts within the basis obtained from the Schrieffer-Wolff transformation, not the original fermions. The experiments of Refs. [320, 321] investigated signatures of localization in linear potentials [323, 324] as well as the Hilbert space fragmentation that occurs in dipole-conserving models such as Eq. (2.35). Ref. [197] on the other hand investigated the relaxation dynamics of the tilted setup Eq. (2.34) in two dimensions, where it was found that the system does thermalize, albeit in a subdiffusively slow manner. In chapters 6,7 we relate this slow subdiffusive relaxation dynamics to the hydrodynamic theory of dipole-conserving many-body systems.

Trapped ions

An alternative to neutral atoms uses ions as elementary building blocks for quantum simulation [44–46]. The ions can be trapped in confining harmonic potentials where they form a crystal structure due to Coulomb repulsion; spin-$1/2$ qubit degrees of freedom can again be encoded in internal levels and can be locally addressed using focused lasers. The quantum dynamics is controlled by global laser beams which couple the spin-$1/2$ degrees of freedom to the ions' motional degrees of freedom. Due to the long-range nature of the Coulomb interaction (which governs these motional degrees of freedom), this results in effective long-range, i.e. power-law decaying, spin interactions. In addition, tightly focused laser beams can be used to engineer local magnetic fields for the spins. State detection can be performed with single-site resolution using fluorescence imaging.

Trapped ions have proven to be a versatile platform for probing the dynamics of quantum many-body systems over recent years, including investigations of many-body localization [325] and dynamical quantum phase transitions[28] [326]. Recently, experiments in trapped ion platforms have also explored localization in tilted systems similar to Eq. (2.34)[29] [327]. Another experiment has demonstrated the emergence of hydrody-

[27] The Schrieffer-Wolff-transformation is equivalent to a high frequency expansion in a rotating frame with respect to the tilted potential part of the Hamiltonian.

[28] We will investigate dynamical quantum phase transitions in a constrained system in Chapter 3

[29] Due to the presence of the linear potential, the long-range spin interactions become exponentially suppressed, yielding an effectively short-range system.

namics in a long-range interacting spin chain [198].

Quantum computers

The previously presented schemes fall under the category of *analog* quantum simulation, where the model of interest is naturally implemented in the constituents of the respective platform and dynamics ensues by letting the system evolve under its many-body Hamiltonian. In contrast, in *digital* approaches one first devises a scheme to encode the relevant degrees of freedom of a quantum many-body system within a predefined set of isolated qubits. The quantum state of the qubits is then evolved in a discrete manner by sequential application of few-qubit quantum gates. The selection of gates is taylored to the problem of interest in such a way that the encoded degrees of freedom evolve according to a desired Hamiltonian. The Hamiltonian time evolution is thus represented as a quantum circuit. In practice such a representation can be achieved by Trotterization of the time evolution into small steps. The advantage of digital quantum simulation in universal quantum computers [328] comes with its programmability; given a universal gate set, in principle any Hamiltonian can be realized. This is in contrast with analog platforms that typically realize very specific Hamiltonians. However, this programmability naturally has its costs, imposing challenging requirements on gate-fidelity and coherence times.

Despite these challenges, much progress on the road towards programmable quantum computation has been achieved throughout a variety of different platforms. Among them are superconducting qubit architectures [47, 48], based on non-linear LC electric circuits with a Josephson junction as inductance. Notably, Ref. [329] announced a quantum advantage over classical supercomputers performing a sampling task with superconducting qubits, and recently, the topological toric code ground state has been implemented in this platform [330]. A relevant solid state platform are nitrogen-vacancy (NV) centers in diamond, which provide effective two-level systems with very long coherence times that can be addressed optically. They are also valuable platforms for quantum simulation and sensing and have been demonstrated to show thermalization and the emergence of hydrodynamics [204], as well as discrete time crystalline order [331]. We emphasize that there exist many other promising platforms for quantum computing, including electron semiconductor qubits [49], linear optics [332], and others [50]; we refer to the literature for details on those approaches.

Quantum materials

Andersons's original idea to describe the high temperature superconducting cuprates as a spin liquid [243] sparked the search for realizations of spin liquids in other materials. Today, the list of candidate materials for spin liquids is long [258–262, 293, 333] and here we do not attempt to provide a comprehensive survey. Instead, in the context of Chapter 5, let

us highlight the presence of candidate materials believed to be well described by effective spin Hamiltonians with strong Kitaev interactions $\sum_{\langle ij \rangle_\gamma} \hat{S}_i^\gamma \hat{S}_j^\gamma$ [293, 333–335]. The earliest example of such candidates is the family of iridiates, and more recently $\alpha - \mathrm{RuCl_3}$. Both exhibit a Mott-insulating state of partially filled t_{2g} orbitals with layered honeycomb structure. Common to these materials is the presence of strong spin-orbit coupling which is necessary to induce the anisotropy of the Kitaev term [336]. Under realistic circumstances, the projected Hamiltonian also contains interactions of the Heisenberg-type, which spoils the exact solvability of the pure Kitaev model and narrows the parameter range for which a spin liquid ground state is expected [259]. Experimentally, neutron scattering on α-$\mathrm{RuCl_3}$ has demonstrated signs of *proximate* spin liquid behavior [337, 338] at elevated energies above an eventual magnetic zig-zag ordering at sufficiently low temperatures [339, 340]. Remarkably, the magnetic order can be suppressed by the presence of a magnetic field [341, 342]. In accord with this finding, thermal Hall measurements of α-$\mathrm{RuCl_3}$ in a magnetic field revealed a half-quantized thermal Hall conductivity [343], indicating the presence of Majorana edge modes in a field-induced spin liquid phase. However, the latter result is still under debate [344, 345], which renders alternative probes of the spin liquid highly desirable. In this context it has recently become possible to exfoliate $\alpha - \mathrm{RuCl_3}$ down to monolayer thickness [346–348], which could pave the way for novel, tunneling junction-based probes of the potential spin liquid phase [3, 349–351]. In Chapter 5 we investigate how such a setup might reveal the presence of localized edge modes through probes of local dynamical response functions. We further note that there exist also materials, the pyrochlore oxides, which realize a classical version of a spin liquid – spin ice [352]. The spin ice model can be treated within an emergent gauge theory description [353] and we use a similar construction in Chapter 4 to describe the conserved quantities in a non-planar dimer model.

Part I

Nonequilibrium dynamics in systems with local gauge constraints

3

Emergent glassy dynamics in a two-dimensional quantum dimer model

This chapter is based on the publication

> Johannes Feldmeier, Frank Pollmann, Michael Knap, *"Emergent glassy dynamics in a two-dimensional quntum dimer model"*, Phys. Rev. Lett. 123, 040601 (2019)

Structure, text and figures have been adapted for the purposes of this thesis.

As we have outlined in our introductory chapter, far-from equilibrium states of strongly interacting and non-integrable quantum many-body systems are generally believed to quickly relax to a local thermal equilibrium at infinite temperature. By contrast, the experiment of Ref. [51] with one-dimensional ultracold atoms in the Rydberg blockade regime has found that certain highly-excited states feature long-lived coherent oscillations of local observables. Due to the Rydberg blockade [51, 354–360], a constrained quantum many-body system is realized featuring exceptional eigenstates, entitled quantum many-body scars [52–55, 361–363].

Interestingly, the one-dimensional Rydberg chain in the regime of nearest neighbor blockade that was realized in these experiments admits a direct mapping to yet another constrained model: the close-packed dimer coverings that we have introduced in Sec. 2.3.1, but on a two-rung ladder geometry. The mapping between these two models is given in Ref. [364][1]. This motivates our first example of constrained dynamics that

[1] This also establishes a connection between the Rydberg model and the presence of gauge con-

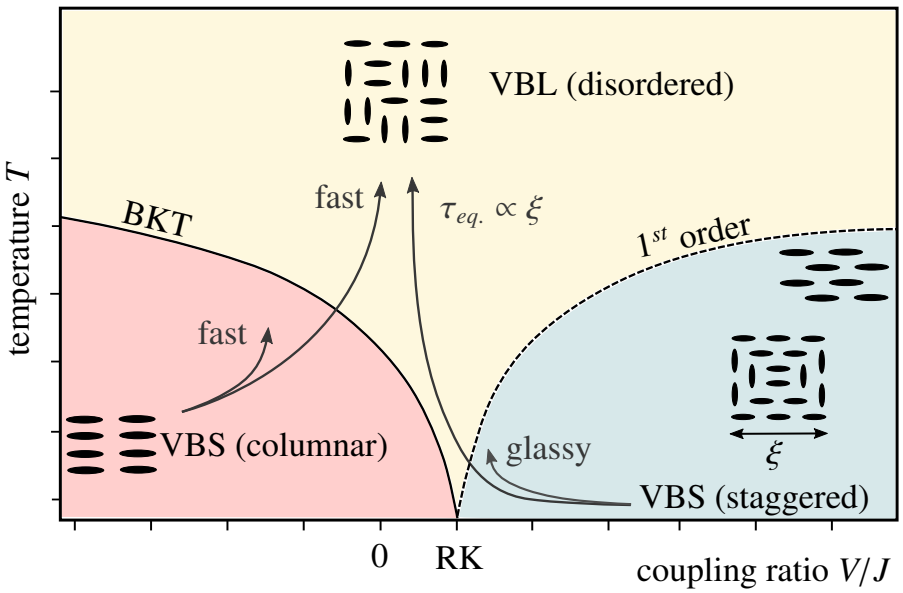

Figure 3.1: Dynamical phase diagram of the QDM (schematic). Quenches within and across the columnar phase are accompanied by fast relaxation of local observables to thermal expectation values, with a rate that is fixed by the microscopic parameter J. Quenches across the 1^{st}-order transition show a 'melting' character, with thermalization times $\sim \xi$ given by the length scale of the staggered domains. Within the staggered phase, the dynamics appears glassy with relaxation times bounded by $\tau_{\text{eq.}} \gtrsim \exp(c \log(V/J)\, \xi^4)$. Arrows are indicative of the different quench protocols considered.

we consider in this chapter, the far-from-equilibrium time evolution of a quantum dimer model (QDM) in *two spatial dimensions*; see also Refs. [160, 366]. We determine the rich dynamical phase diagram upon quenching the model far from thermal equilibrium (see Fig. 3.1 for an overview) and identify initial states at finite energy density whose dynamical relaxation is obstructed as a consequence of kinematic constraints. Moreover, for such initial states consisting of a set of staggered dimer domains of length scale ξ, we analytically derive a lower bound on the local thermalization timescale that scales exponentially in ξ^4. This effect is induced by highly detuned processes involving 'defects' seperated by a distance ξ, which surprisingly reveals a mechanism of slow dynamics that is in fact similar to proposals of fractonic systems at low temperatures [269, 291]. We find arrested quantum dynamics at $T = 0$ and extremely slow relaxation at finite energy densities, reminiscent of the physics of classical glasses [149].

3.1 Model

We start by introducing again the QDM on the square lattice, where a hard-core constraint enforces each site to be occupied by exactly one singlet dimer, see insets in Fig. 3.1 for the illustration of a few dimer configurations. The dynamics is generated by the following

straints which we have described for the dimer model. Another gauge formulation of the Rydberg chain in terms of a 1D $U(1)$ link model has been provided in [365]

Hamiltonian, originally introduced by Rokhsar and Kivelson (RK) [244],

$$\begin{aligned} \hat{H} &= \hat{H}_V + \hat{H}_J \\ \hat{H}_V &= V \sum_{\text{plaq.}} \left(|\square\rangle\langle\square| + |\square\rangle\langle\square| \right) \\ \hat{H}_J &= -J \sum_{\text{plaq.}} \left(|\square\rangle\langle\square| + |\square\rangle\langle\square| \right) . \end{aligned} \tag{3.1}$$

Here, $\hat{H}_V$ gives a constant energy-offset to each pair of parallel dimers, while the off-diagonal kinetic term $\hat{H}_J$ flips a pair of resonant singlets. Importantly, the dimer model features non-local conservation laws represented by winding numbers W_x and W_y, see Eq. (2.21), which provide a staggered count of the number of dimers intersecting a given straight line through the sample [242]. For the remainder of this work, we restrict to the zero-winding sector $W_x = W_y = 0$, which constitutes the largest part of the full Hilbert space.

The nature of the equilibrium phase diagram of the square-lattice QDM remains a matter of high interest, but seems to converge to a framework similar to the one depicted in Fig. 3.1 [251–257]. In particular, for $T = 0$, the model possesses an RK-point at $V = J$, where the exact ground state wave function can be constructed as an equal weight superposition of all dimer coverings within each winding number sector [244]. The RK-point separates two crystalline VBS phases, that show columnar order for $V < J$ and staggered order for $V > J$. Both VBS phases exist up to certain finite temperatures, before the transition to a disordered VBL phase, which is conjectured to extend all the way to the RK-point at $T = 0$ [256, 367]. While the columnar-VBL transition is expected to be of BKT-form, and thus continuous, the staggered-VBL transition is of 1$^{\text{st}}$-order [252, 254].

3.2 Columnar states: Thermalization

The BKT-transition can be captured by introducing an order parameter that detects the spontaneous breaking of C_4-rotational lattice symmetry,

$$\hat{\phi}_c = \frac{2}{L^2} \sum_{\text{plaq.}} \left(|\square\rangle\langle\square| - |\square\rangle\langle\square| \right) , \tag{3.2}$$

which counts the imbalance between horizontal and vertical plaquettes on an $L \times L$ square lattice. Restricting to the zero momentum sector on periodic boundary conditions (PBCs), $\hat{\phi}_c$ distinguishes the two translational invariant columnar ground states $|c_A\rangle$ and $|c_B\rangle$, related by a $\pi/2$-rotation and $\hat{\phi}_c |c_{A/B}\rangle = \pm |c_{A/B}\rangle$.

To study thermalization in our system, we compute the relaxation of order parameters in a quench protocol to their corresponding thermal expectation values. We thus consider

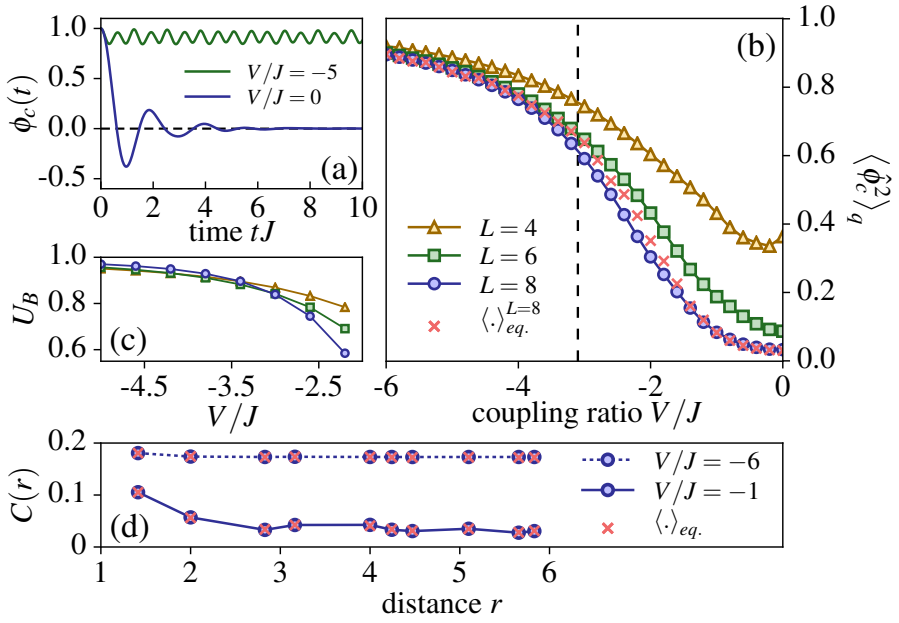

Figure 3.2: Thermalization of columnar initial states. **(a)** Relaxation of the columnar order parameter $\hat{\phi}_c$ both within and across the columnar phase. **(b)** Long-time averaged values of $\hat{\phi}_c^2$ for different system sizes, starting from a columnar inital state and quenched to finite values of V/J. Included are the corresponding thermal values for $L = 8$. Agreement between the two becomes less accurate around the phase transition at $V_c/J \approx -3.1$, but is excellent deep within the phases. **(c)** The crossing in the long-time averaged Binder cumulant U_B of $\hat{\phi}_c$ marks the corresponding finite-T phase transition. **(d)** The time-averaged dimer correlation functions $C(r)$, starting from a columnar initial state, agree well with the corresponding equilibrium values, even deep within the VBS phase.

the long-time averaged values

$$\left\langle \hat{O} \right\rangle_q := \lim_{t\to\infty} \frac{1}{t} \int_0^t dt' \left\langle \psi(t') \right| \hat{O} \left| \psi(t') \right\rangle \tag{3.3}$$

of a given observable $\hat{O}$ following a quench from an initial state $|\psi(t=0)\rangle = |\psi_0\rangle$ on systems of linear size $L \in \{4, 6, 8\}$, which we choose as a columnar state on PBCs, $|\psi_0\rangle = |c_A\rangle$. The averages of Eq. (3.3) are to be compared with the corresponding thermal expectation values

$$\left\langle \hat{O} \right\rangle_\beta = \mathrm{Tr}\left\{ e^{-\beta \hat{H}} \hat{O} \right\}, \quad \left\langle \hat{H} \right\rangle_\beta \stackrel{!}{=} \left\langle \psi_0 \right| \hat{H} \left| \psi_0 \right\rangle, \tag{3.4}$$

where the effective inverse temperature β is chosen to match the energy of the initial state. For $L = 8$, the system cannot be diagonalized fully, so we use the typicality approach [368] where the expectation values of Eq. (3.4) are drawn from random (infinite temperature) initial states, which are subsequently evolved in imaginary time up to $\tau = \beta$ such that the rightmost relation in Eq. (3.4) is fulfilled. We provide more detialed comments on the effective temperatures obtained from Eq. (3.4) in Sec. 3.4.

As displayed in Fig. 3.2 (a+b), the columnar order parameter shows efficient relaxation to thermal values for all values of the ratio V/J after the quench, less accurate only in the

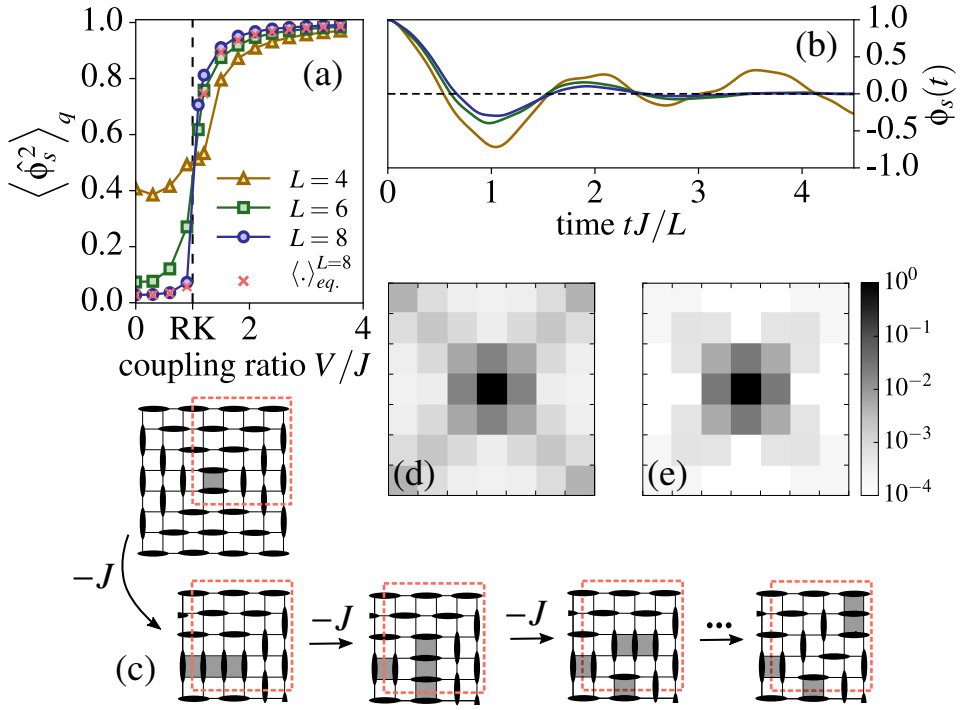

Figure 3.3: Localization of staggered initial states. **(a)** Long-time averaged values of the staggered order parameter $\hat{\phi}_s^2$ starting from a staggered initial state. **(b)** In a quench across the transition to the disordered regime (here: $V/J = 0$), the dynamics of $\hat{\phi}_s$ scales with L^{-1}. **(c)** The state $|p_A\rangle$. Excitations from this state containing four plaquettes are expected to delocalize along the diagonals of the system. **(d)** The thermal expectation value of the potential energy landscape at an energy matching the quench in (e). **(e)** The late-time plaquette densities obtained after quenching $\frac{1}{\sqrt{2}}(|p_A\rangle + |p_B\rangle)$ to $V/J = 3$ differ strongly from the thermal values in (d) at large distances from the center.

vicinity of the arising phase transition. The thermalization of order parameters allows for the determination of finite-temperature phase transitions via finite size scaling arguments, as has been done for ground state phases of the model [251]. Even though the exact transition point between columnar and disordered phase may turn out quite inaccurate in such small systems [251, 256], the qualitative picture is expected to hold, nonetheless. As shown in Fig. 3.2 (c), the Binder cumulant $U_B \propto 1 - \left\langle \hat{\phi}_c^4 \right\rangle_q / 3 \left\langle \hat{\phi}_c^2 \right\rangle_q^2$ shows a crossing at $V/J \approx -3.1$, which signals the transition to the C_4-symmetry-breaking columnar phase. Time-averages were converged at times $tJ = 300$ on $L = 8$, which supports a quick thermalization of $\hat{\phi}_c$ in a wide range of model parameters.

This fast thermal relaxation can be substantiated by investigating the behavior of local observables. For this purpose, we define the dimer-dimer correlation functions $C(r)$ as

$$C(r) = \langle \hat{n}_0 \hat{n}_{\boldsymbol{r}} \rangle - \langle \hat{n}_0 \rangle \langle \hat{n}_{\boldsymbol{r}} \rangle , \tag{3.5}$$

where $\hat{n}_{\boldsymbol{r}}$ is the dimer occupation number at bond $\boldsymbol{r}$. Quenches from $|c_A\rangle$ even deep inside the columnar phase are accompanied by fast relaxation of $C(r)$, save for spontaneous symmetry breaking. The latter can be accounted for by choosing a rotationally invariant

initial state $|\psi_0\rangle = \frac{1}{\sqrt{2}}(|c_A\rangle + |c_B\rangle)$, which leads to the results of Fig. 3.2 (d). The fast thermalization is due to the kinetic part $\hat{H}_J$ of the Hamiltonian (3.1) being able to effectively explore the phase space starting from the columnar initial state.

3.3 Staggered states

Having established efficient thermal relaxation for quenches from columnar initial states, we now move on to consider the quench dynamics of staggered initial states. We first note that the fully staggered state is part of a maximum-winding sector and entirely frozen. Therefore, we construct instead the exact ground state in the limit $V/J \to \infty$ within the zero-winding sector, which yields a state of 'pyramid'-like shape, where the tip of the pyramid serves as a dynamically active defect between extended areas of staggered configurations, see Fig. 3.1 inset. In the thermodynamic limit on periodic boundaries, the staggered ground state contains four such pyramidic domain walls [257]. For a quench from the staggered phase to the disordered regime however, the dynamics will mainly be governed by the behavior of individual pyramid states, which we can effectively capture by considering a single pyramid on open boundary conditions (OBCs). This choice allows us to double the length scale ξ of the initial state, given our finite size limitations. On an OBC-geometry, there exist two pyramidic ground states $|p_A\rangle$ and $|p_B\rangle$, from which we construct a $\mathbb{Z}_2$ order parameter to distinguish them:

$$\hat{\phi}_s := \frac{2}{L^2}\left\{\sum_{l_A}\hat{n}_{l_A} - \sum_{l_B}\hat{n}_{l_B}\right\}. \tag{3.6}$$

Here, the indices l_A denote the bonds occupied in the $|p_A\rangle$-state, $\hat{n}_{l_A}|p_A\rangle = |p_A\rangle$, and correspondingly for l_B, such that again $\hat{\phi}_s|p_{A/B}\rangle = \pm|p_{A/B}\rangle$. Even though the Hilbert space is somewhat restricted on OBCs, we still expect the dynamics of the 1$^{\text{st}}$-order transition to be well captured in our approach, as the dynamics is initiated in the center of the pyramid.

As it turns out, our quench protocol starting from the pyramid ground state crosses a phase transition at an infinitesimal distance from the RK point at $V = J$, see Fig. 3.3 (a). This is due to the vanishing energy density of the pyramidic initial state; we explain this feature in Sec. 3.4. As a result, the dynamics of $\hat{\phi}_s$ signals a 1$^{\text{st}}$-order transition at the RK-point, with a sharp rise of $\left\langle \hat{\phi}_s^2 \right\rangle_q$ for larger systems. Quenching across the transition to the disordered phase, the dynamical order parameter in Fig. 3.3 (b) shows an approximate collapse of its zero-crossings and extrema upon rescaling time $t \to t/L$. This characterizes the melting dynamics proliferating around the initial dynamical center and implies a timescale $\tau_{eq.}$ of thermalization that is effectively set by the length scale ξ of the initial staggered domain. Interestingly, this scale also impacts the Loschmidt return rate that can be used to characterize dynamical phase transitions [369]. We investigate the consequences of the exotic dynamics in this model for the presence of dynamical phase transitions in

Sec. 3.5.

3.3.1 Localization

While monitoring the order parameter suggests thermal behavior also within the staggered phase, Fig. 3.3 (a), this is not the case for local observables which indicate the absence of thermalization for such quenches. This can be demonstrated by mapping out the potential energy landscape, i.e., the plaquette density, following a quench. Here, we start from a symmetrized staggered state $|\psi_0\rangle = \frac{1}{\sqrt{2}}(|p_A\rangle + |p_B\rangle)$, quenching to $V/J = 3$. We find the thermal potential energy landscape to include delocalized plaquettes along the system diagonals, Fig. 3.3 (d). In sharp contrast, the distribution of plaquettes following the quench, averaged up to $tJ = 300$ on $L = 8$, remains localized around the center, see Fig. 3.3 (e). An analysis on $L = 6$, where the system may be diagonalized fully, also shows no signs of thermalization at later times.

To understand this property, we can consider the large-V/J dynamics around, say, $|p_A\rangle$ as an effective single-particle problem on a finite, one-dimensional lattice. Shifting the plaquettes along the 2D diagonal in Fig. 3.3 (c) corresponds to a quantum particle moving in 1D, where the position x of the particle relates to the position of the plaquettes, see Fig. 3.4. Therefore, $x = 0$ corresponds to $|p_A\rangle$, $x = 1$ labels the second state of Fig. 3.3 (c) with three flippable plaquettes, and all states with $x \geq 2$ have four plaquettes. The particle then moves in an effective potential $U(x)$ that is given by

$$U(x) = \begin{cases} V, & x = 0 \\ 3V, & x = 1 \\ 4V, & x \geq 2 \end{cases}, \tag{3.7}$$

which will host at least one bound state for finite $V > 0$. It is then apparent that the single-particle nature of the effective model induces the non-thermal behavior. In particular, in a formal thermal average, all particle positions with $x \geq 2$ contribute equally, leading to the observed delocalization along the diagonal. In constrast, the wave function for a particle starting at $x = 0$ will decay within the potential barrier. We note that we have similarly observed dynamical arrest in columnar states containing string-like excitations, composed of finite columns aligned perpendicular to the background state. These states are strongly repulsively bound, leading to large relaxation time scales. It would be interesting to consider these states in more detail in the future. In either case, constraints are essential for the emergent slow quantum dynamics.

3.3.2 Thermodynamic limit

A natural question arising in the context of localization is its stability in the thermodynamic limit, and whether the apparent localization on our finite systems has to be inter-

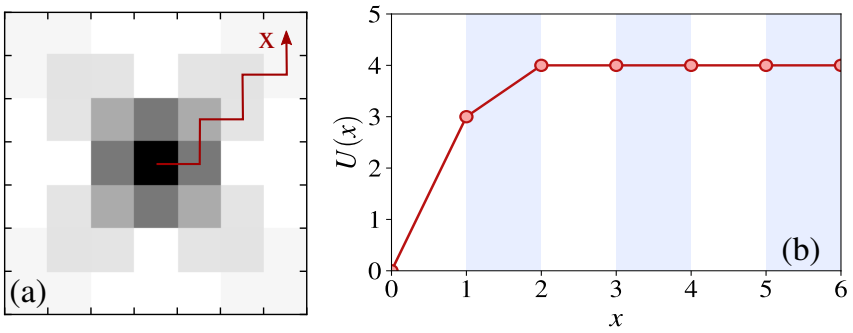

Figure 3.4: Effective 1D system. (a) Shifting plaquettes along the diagonal of the square lattice can be interpreted as an effective 1D model, with a potential well located around the origin, **(b)**.

preted rather as a long-lived, prethermal plateau. In this regard, we distinguish two ways to take the thermodynamic limit: (A) We take $L, \xi \to \infty$ such that $L/\xi \to \text{const.}$, which corresponds to a finite number of pyramids in the initial state and hence a vanishing energy density for $V/J > 1$. (B) We let $\xi = \text{const.}$ such that $L/\xi \to \infty$, which leaves us with a finite density of pyramids and thus a finite energy density in the thermodynamic limit. We consider both cases seperately in the following

Case (A): Vanishing energy density

Case (A) is captured by the numerical results for small systems, where the appearance of bound states within each pyramid ensures the localization around its respective center. The independence of the pyramids with respect to each other is ensured by their diverging lengthscale ξ, effectively protecting them against melting. This last point can be made more specific by arguing that the matrix elements between certain states with different ξ in a given energy shell are highly suppressed compared to their level spacing, similar in spirit to arguments employed in the context of MBL [138]. In particular, there exist states that are close in energy, yet not exactly degenerate, which can only be connected via $\mathcal{O}(L^2)$ consecutive plaquette flips that are off-resonant from the starting energy shell. For example, in a system of size $L \times L$, a state consisting of pyramids of fixed average length ξ_1, thus hosting $(L/\xi_1)^2$ active defects, is close in energy to a state with different length scale $\xi_2 > \xi_1$, which in turn has already melted up $\xi_2^2/\xi_1^2 - 1$ plaquettes per pyramid (on average) in its interior. Since we have chosen $\xi_1 \sim L$ of order system size, we need to make $\mathcal{O}(L^2)$ local plaquette flips in order to connect the two states. All of these plaquette flips are off-resonant, and we can therefore estimate the matrix element connecting the two states in perturbation theory,

$$\Delta \sim J \left(\frac{J}{V}\right)^{\mathcal{O}(L^2)} = \exp\{-\log(V/J) \times \mathcal{O}(L^2)\}. \tag{3.8}$$

At the same time, the many-body level spacing between the two states is certainly bounded by the total number of dimer configurations on the square lattice, which asymptotically goes as

$$\epsilon \gtrsim J \exp\{-\frac{G}{\pi} L^2\}, \tag{3.9}$$

where G is the Catalan's constant [370]. Whether the two states under consideration can hybridize is determined by which of the energy scales in Eqs. (3.8,3.9) is dominant. In particular, since both scales decay exponentially in L^2, we can always find a value of J/V such that $\Delta/\epsilon \to \exp\{-\mathcal{O}(L^2)\}$, leading to non-hybridized states and thus, arrested quantum dynamics at $T = 0$. This argument directly shows that the pyramid structure of the initial state will be preserved in the post-quench dynamics, implying the existence of localized eigenstates just above the ground state.

To illustrate these argument further numerically, at least within the bounds of finite size limitations, we can investigate the supposed rearrangement $\xi_1 = 4 \to \xi_2 = 8$ on $L = 8$. Fig. 3.5 shows the potential energy landscape, as well as the dimer-density $\langle \hat{n}_l \rangle$ on the bonds l of the lattice for selected eigenstates in the rotationally invariant sector at $V/J = 5$. The eigenstates of Fig. 3.5 are adjacent in the spectrum of $\hat{H}$, chosen at an energy that corresponds approximately to the presence of $(L/\xi_1)^2 = 4$ plaquettes in the system. Consistent with the argument presented above, we find that states with different ξ_1, ξ_2 are *not* hybridized. We can extend these numerical considerations by changing from OBCs to fixed boundaries that correspond to a staggered background of $\xi = 4$. In this scenario, we envisage the 8×8 system as a patch of a larger system prepared at $\xi = 4$. As shown in Fig. 3.6, the *lowest* energy eigenstate, with $\xi = 4$, has not hybridized with any states of different ξ, consistent with our analytical arguments.

Case (B) Finite energy density

In case (B), at finite energy densities, we can provide similar arguments that now yield a lower bound on the thermalization timescales of local observables. To this end, we start from an initial state with a small, but *finite* energy density $\varepsilon \sim 1/\xi^2$, distributed equally over pyramids of length ξ, see Fig. 3.7 (a). The thermalization time $\tau_{\text{eq.}}$ is then bounded by the largest matrix element Δ that hybridizes states with equal energies but locally different ξ, which in turn is bounded from above by the lowest order in perturbation theory at which such states of similar energy can be reached.

Given the initial state of homogeneous energy density, we ask at which timescale local inhomogeneities can arise, leading to relaxation of local observables. In terms of the staggered initial state, this time corresponds to the time needed in order to break up the pyramids. To keep the overall energy balanced, all processes that lead to states of similar energy necessarily need to break up pyramids of size ξ and reassemble them as pyramids of larger size ξ', thereby reducing the local energy density. As shown in Fig. 3.7 (b), this will create a number of defects along the boundary of this new formed pyramid in the

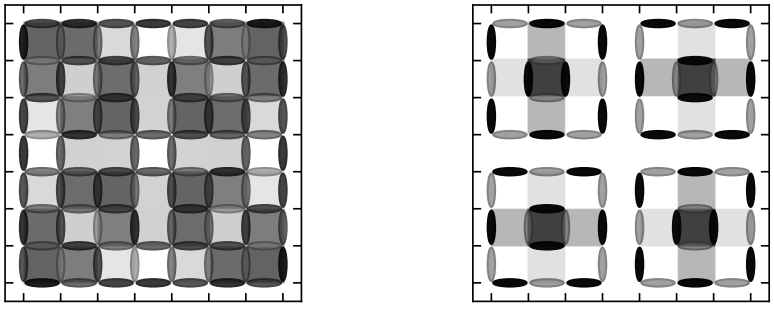

(a) $E = 19.498$ (b) $E = 19.599$

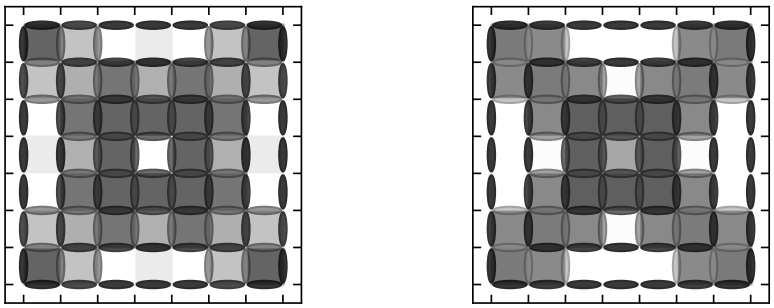

(c) $E = 19.682$ (d) $E = 19.877$

Figure 3.5: Localization at vanishing energy densities. Illustration of both plaquette-density and dimer-density for rotationally invariant eigenstates on $L = 8$ at large $V/J = 5$. All states (a)-(d) are taken at energies E dominated by the presence of about four parallel plaquettes. (a),(c),(d) clearly show the structure of a large pyramid with $\xi = 8$ and the corresponding delocalization along the system diagonal as discussed previously. On the other hand, (b) is localized around pyramids of size $\xi = 4$.

background of the original staggered lengthscale ξ. The total energy difference of this process can then be estimated by the difference in the number of parallel dimer plaquettes,

$$\Delta E/V \simeq \left\{1 - \left(\frac{\xi'}{\xi}\right)^2\right\} + \left[\frac{\xi'}{\xi}\left(\xi - 1\right)\right], \tag{3.10}$$

where the term in the curly brackets originates from the reduced number of plaquettes within the larger pyramid, while the term in the square brackets is caused by the defects along the new boundary. To reach states of similar energy, we set $\Delta E = 0$ and obtain $\frac{\xi'}{\xi} = \xi + \mathcal{O}(1/\xi)$. The minimum size of the new pyramid is therefore given by

$$\xi' \sim \xi^2. \tag{3.11}$$

Due to the staggered nature of the system, this state can only be reached via un- and refolding the area of the new pyramid, which requires $\sim \xi'^2$ plaquette flips, all off-resonant from the starting energy. The matrix element can thus be shown to be at most proportional to

$$\boxed{\Delta \sim J\left(\frac{J}{V}\right)^{c\xi'^2} = J\exp\left\{-c\log\left(\frac{V}{J}\right)\xi^4\right\},} \tag{3.12}$$

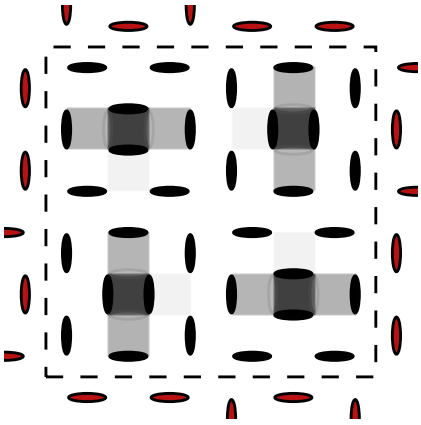

Figure 3.6: Staggered boundary conditions. Dimers on the outer side of the boundary (marked in red) are fixed in a staggered configuration of scale $\xi = 4$. The plaquette- and dimer-densities of the lowest eigenstate at $V/J = 5$ demonstrate the continuation of $\xi = 4$ on the inner side of the boundary.

where c is a constant of order $\mathcal{O}(1)$. We observe that the implied lower bound for the time scale $\tau_{\text{eq.}} \sim 1/\Delta$ grows extremely fast with the staggered scale ξ of the inital state for $V/J > 1$. The system sizes required to observe the slow relaxation of Eq. (3.12) at large V/J are numerically out of reach. Accordingly, small scale simulations of systems up to L=8 sites with pyramids of size $\xi \sim 4$ show the absence of relaxation, as predicted by our analytical formula and demonstrated numerically above. Eq. (3.12) should be regarded as a lower bound for the relaxation time, which is why formally we cannot exclude full localization.

Finally, let us remark that there is actually an intermediate case between (A) and (B) when the number of pyramids is infinite, but the energy density is still vanishing. In this case, starting from a length scale ξ between pyramids and using the same arguments as above, the new length scale ξ' at which we can first reach states of similar energy becomes

$$\xi' \sim \min\{L, \xi^2\}. \tag{3.13}$$

However, we have already seen above in case (A) that for $\xi' \sim L$ the system localizes due to the competition between matrix elements and level spacings. Therefore, we expect localization in the thermodynamic limit even for an infinite amount of plaquettes in the initial state so long as

$$\xi L^{-1/2} \neq 0, \tag{3.14}$$

which does however still correspond to vanishing energy densities.

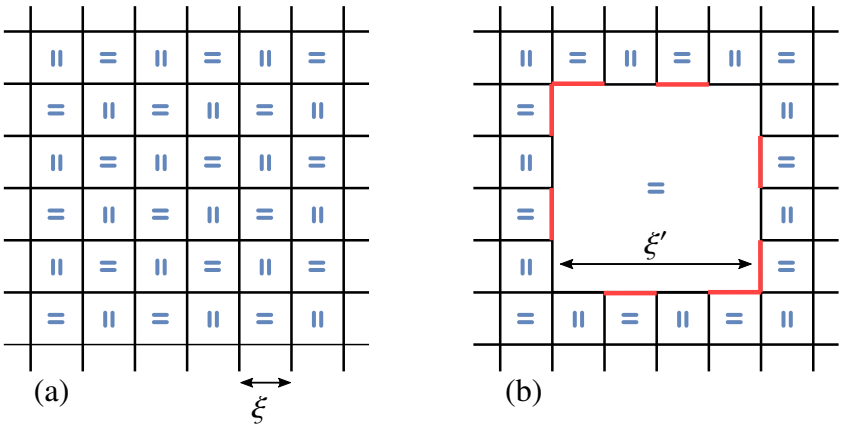

Figure 3.7: Cost for local equilibration. (a) Starting configuration of pyramids of length ξ, with the orientation of the central plaquettes indicated in blue. **(b)** Thermalization of local observables requires the formation of larger pyramids of size ξ', which creates defects (red) with respect to the original background at the boundaries.

3.4 Effective temperature

To gain a better understanding of the quenches indicated in the schematic dynamical phase diagram of Fig. 3.1, we investigate the effective temperatures as obtained from Eq. (3.4). In the limit of $V/J \to \mp\infty$, both the columnar and staggered initial states yield $T = 0$, as each of them correspond to the ground states in the respective case. By contrast, at $V/J = 0$, $\left\langle \mathrm{col/pyr} \middle| \hat{H}_{V/J=0} \middle| \mathrm{col/pyr} \right\rangle = 0$ for both states. Since the spectrum of $\hat{H}$ is symmetric at this point, both states (just as every other product state) correspond to infinite temperature. Varying V/J in between can give rise to finite T.

While for the columnar initial state, the temperature will rise strictly monotonously from 0 to ∞ when lowering $|V|/J$, the same is not true for the staggered ground state. In particular, we show that for $V/J > 0$, the energy of a given state $|\psi\rangle$ can be written as

$$\langle \hat{H} \rangle_\psi = \langle \hat{H}_{RK} \rangle_\psi + (V - J) \langle \hat{H}_V \rangle_\psi \geq (V - J) \langle \hat{H}_V \rangle_\psi \,, \tag{3.15}$$

where $\hat{H}_{RK}$ denotes the Hamiltonian at the RK-point $V/J = 1$, and we have used that $\hat{H}_{RK}$ is positive definite as it can be written as a sum of projectors. From Eq. (3.15) we infer that for all $V/J > 1$, the system's ground state cannot have an extensive amount of flippable plaquettes. This follows from the energy of such a state being extensive, while the pyramid state only has finite energy V for all system sizes and ratios V/J. The energy difference between the exact ground state at a general coupling ratio within the staggered phase and the maximally staggered product initial state is thus only intensive, which means that in the quench protocol to finite $V/J > 1$, the effective temperature is only lifted infinitesimally.

At the RK-point, the ground state is the equal weight superposition of all dimer coverings in the zero-winding sector and contains an extensive amount of plaquettes. Thus,

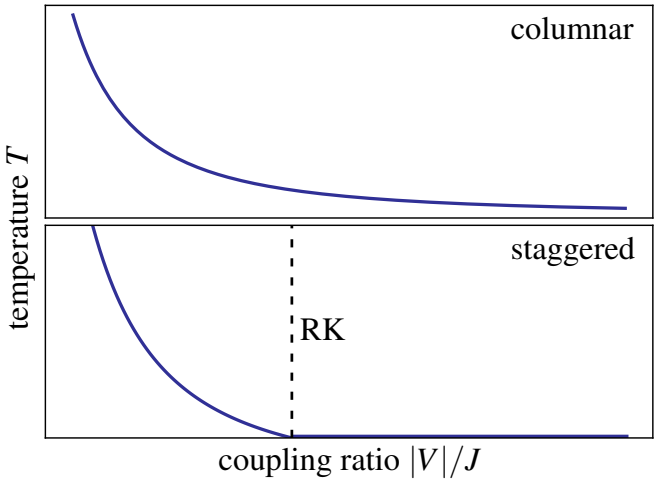

Figure 3.8: Effective temperatures following a quantum quench. Schematic of the effective temperature in the thermodynamic limit of the columnar and pyramidic initial states at the corresponding quench parameters. Along $V/J > 1$, the staggered initial state carries only an intensive amount of energy with respect to the ground state, and thus corresponds to an infinitesimal temperature.

upon crossing the RK point, i.e., for $V/J < 1$, the ground state energy is bounded from above by

$$E_{\mathrm{gs}}(V/J < 1) \leq -|V - J| \, \langle \hat{H}_V \rangle_{\psi=\mathrm{RK}} \,, \tag{3.16}$$

and is thus extensive. Hence, once the RK-point is crossed in the quench, the amount of energy inserted into the system by the quench is extensive, and corresponds to finite temperatures. This shows directly that the transition at the RK-point to the staggered phase is discontinuous within the zero-winding sector.

Beyond these considerations, the effective temperature can in principle be extracted numerically from Eq. (3.4) of the main text. A schematic of the effective temperature is shown in Fig. 3.8.

As a final remark for this section, we stress that although quenches inside the staggered phase starting from the pyramidic ground state add only infinitesimally to the temperature in the thermodynamic limit, quenches from an initial state with finite staggered scale ξ do add an extensive amount of energy to the system and correspond to finite temperatures. Therefore, the non-thermal dynamical properties of the quantum dimer model found numerically above indeed correspond to a dynamical arrest at $T = 0$, characteristic of structural glasses.

3.5 Dynamical phase transitions

As we have already indicated briefly in Sec. 3.3, we can use the theory of dynamical phase transitions (DPTs) [369, 371] to further characterize and compare the BKT- and the 1^{st}-order transitions. A hallmark in the study of DPTs is the emergence of non-analytic, kink-like structures in the return amplitude to the original ground state manifold following a

quench, the Loschmidt rate, defined as

$$\lambda(t) = -\frac{2}{L^2} \log \left(\sum_{n \in \{gs\}} |\langle n \,|\, \psi(t) \rangle|^2 \right). \tag{3.17}$$

Here, the manifold $\{gs\}$ consists of $\{|c_A\rangle, |c_B\rangle\}$ for the BKT, and $\{|p_A\rangle, |p_B\rangle\}$ for the 1^{st}-order transition. The behavior of $\lambda(t)$ upon quenching across the BKT-transition is shown in Fig. 3.9 (a), where an initial columnar state is taken to the VBL phase at $V = 0$. The time evolution of $\phi_c(t)$ has already converged reasonably well for $L = 6, 8$, while $\lambda(t)$ exhibits significant finite size fluctuations which dominate the Loschmidt rate at late times. This is evidenced by the suppressed magnitude of oscillations at late times on $L = 8$ as compared to $L = 6$. Nonetheless, there exist two systematic crossings of the individual ground state weights $\lambda_{A/B}(t) = -2/L^2 \log |\langle c_{A/B} | \psi(t) \rangle|^2$, at which sharp kinks are expected to form for $L \to \infty$. The critical times of the kinks are in rough agreement with the zeros of the order parameter $\phi_c(t)$, Fig. 3.9 (b), linking the dynamical phase transitions in the order parameter and the Loschmidt echo [372].

An analogous analysis carried out for the 1^{st}-order DPT yields vastly different results, shown in Fig. 3.10 (a), where the rate $\lambda(t)$ is given for $L = 4, 6, 8$, in a quench of $|p_A\rangle$ to $V = 0$. Here, we can identify the following: First, the sharp features visible in $\lambda(t)$, marked by black stars in Fig. 3.10 (a), correspond to resonances specific to the point $V = 0$. They can be understood in a simplified picture of the pyramid tip as a single plaquette embedded in a staggered, and thus anisotropic, mean field background. The dynamics of the central plaquette is then described by an effective two-level Hamiltonian $H_{\text{eff}} \propto -J\sigma_x + V\sigma_z$, which, for $V \neq 0$, sustains a finite population of the inital ground state at any time. For $V = 0$, the background becomes isotropic and the central plaquette undergoes coherent Rabi-oscillations, which depopulate the ground state with period π/J, roughly corresponding to the separation of the black stars in Fig. 3.10 (a). The temporal positions of the resonances are similar on all system sizes L, which indicates that the short-time dynamics following the quench is dominated by only small regions around the central plaquette. This again characterizes the melting dynamics proliferating around the dynamical center of the initial state, which successively has to work its way to the outside.

The scaling of this process is revealed by the dynamical order parameter $\phi_s(t)$ in Fig. 3.10 (b), which shows an approximate collapse of the zero-crossings and extrema of $\phi_s(t)$ upon rescaling $t \to t/L$. Therefore, considering an initial state not composed of a single pyramid covering the lattice, but rather multiple pyramids of average size ξ, the timescale $\tau_{eq.}$ of thermalization is effectively set by ξ. Relating to the phase diagram of Fig. 3.1, this corresponds to a quench across the transition not from the ground state at $V/J \to \infty$, but an initial state with energy corresponding to a finite-T state at a finite ratio V/J.

Finally, letting $L \to \infty$ and $\xi \to \infty$, the $\propto L$-scaling of the relaxation dynamics also

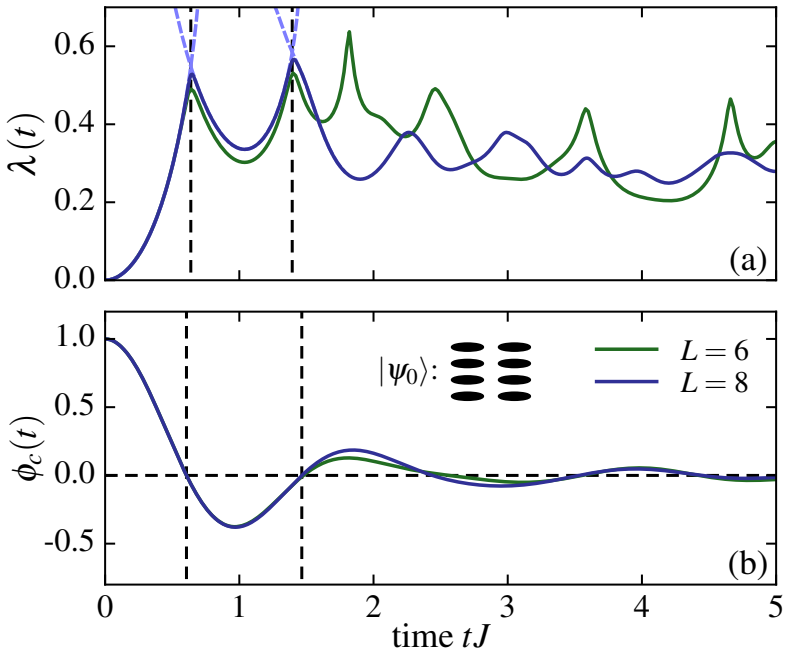

Figure 3.9: Dynamical Phase Transitions: Columnar states (a) Loschmidt rate $\lambda(t)$ for $L = 6, 8$ following a quench from of a columnar product state to $V = 0$. The light blue dashed lines indicate the weights $\lambda_{A/B}$ of the individual ground states $|c_{A/B}\rangle$. **(b)** Columnar order parameter dynamics for the same quench. The dashed lines mark the zero-crossings of $\phi_c(t)$ and kinks of $\lambda(t)$, respectively.

shifts the crossing of $\lambda_{A/B}(t)$ to increasingly late times. Hence, while $L \to \infty$ can be shown to yield $\lambda(t) = \min(\lambda_A(t), \lambda_B(t))$, thus developing sharp features, the angle at which $\lambda_{A/B}(t)$ cross becomes increasingly flat. If, based on the scaling of the order parameter, we conjecture a corresponding $\propto 1/L$-scaling of this angle, a simple scaling analysis for $\lambda(t)$ shows the cancellation of both effects and interestingly, no discontinuity develops in $\partial_t \lambda(t)$ for $\xi \sim L \to \infty$ for quenches across .

3.6 Conclusion & outlook

In this chapter, we have examined the dynamical phase diagram of the square lattice quantum dimer model. We have found that inside the staggered phase, local relaxation is lower bounded by an extraordinarily large time scale characteristic for glassy systems, valid even in the thermodynamic limit for quench dynamics initiated at finite energy densities. The associated mechanism employs emergent non-dispersing defects at low energies, which are reminiscent to the physics of fracton models. It would be interesting to see whether these connections can in fact be made more rigoros. In addition, we have demonstrated how the structure of the low energy states in the staggered phase affects the phenomenology of dynamical phase transitions.

Future lines of investigation may also address similar physics for quantum dimer models on different lattice geometries or in different winding sectors. In particular, dimer constraints that can be implemented in Rydberg quantum simulators are interesting in this

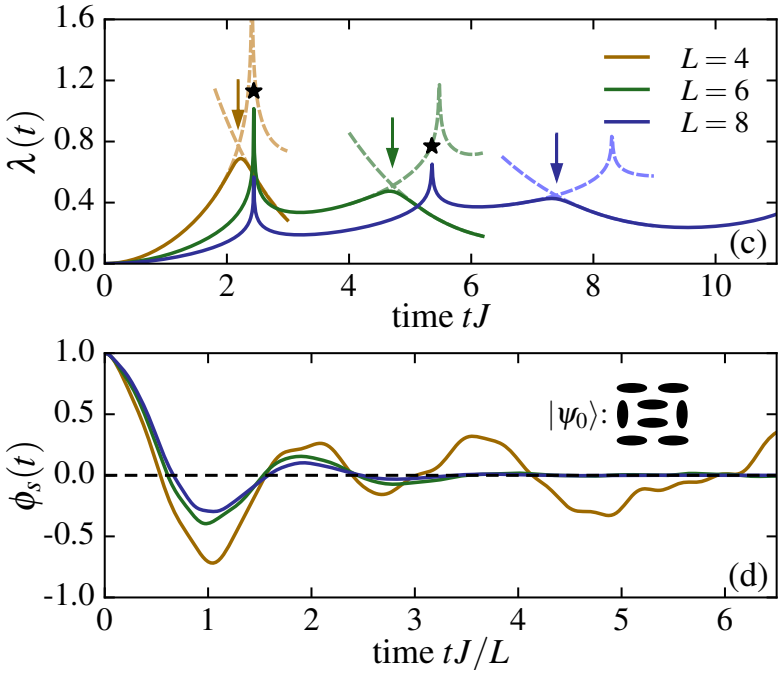

Figure 3.10: Dynamical Phase Transitions: Staggered states (a) Loschmidt rate $\lambda(t)$ for $L = 4, 6, 8$ starting from a staggered initial state, with light dashed lines corresponding to the weights $\lambda_{A/B}(t)$ of $|p_{A/B}\rangle$ in the vicinity of their crossing points, marked by arrows. Black stars mark resonances. **(b)** shows t/L-scaling of the staggered order parameter dynamics.

respect. We will consider a different geometry in the following chapter, although therein we are mostly interested in dynamics at high instead of low energies.

4

Emergent fracton dynamics in a non-planar dimer model

This chapter is based on the publication

> Johannes Feldmeier, Frank Pollmann, Michael Knap, *"Emergent fracton dynamics in a non-planar dimer model"*, Phys. Rev. B. 103, 094303 (2021) (Editors' Suggestion)

Structure, text and figures have been adapted for the purposes of this thesis. Sec. 4.2.1 contains material not included in the publication.

In this chapter we continue our analysis of nonequilibrium dynamics in dimer models, which, as we saw in Sec. 2.3.1, can be mapped to lattice gauge theories in which a local Gauss law constrains the system dynamics. In the previous chapter we have already experienced that, in general, understanding the effects of such gauge constraints on nonequilibrium properties is a challenging task. In addition to the extremely slow glassy dynamics derived in Chapter 3, recent efforts in this context have e.g. pointed out the possibility of strict localization in coupled gauge-matter and pure gauge theories [174, 175, 178, 373], through mechanisms akin to many-body localization (MBL) [27, 30, 31, 34]. As an immediate related question, we can ask whether the presence of local gauge constraints can also have a qualitative effect on the relaxation towards equilibrium even if the constraints are not sufficiently strong to localize the system. In particular, pure gauge theories with a *static* electric charge background, which can often be mapped to equivalent loop or dimer models, lack an obvious choice of suitable observables (other than the local energy density) to probe the late-time relaxation dynamics due to the absence of charge transport.

In this chapter, we study a particular $U(1)$ gauge theory at high energies, a bilayer

dimer model, where this limitation can be circumvented due to the presence of topological soliton configurations formed by the gauge fields. These solitons correspond to so-called 'Hopfions' that exist more generally in the cubic dimer model [374–376]. We show that the associated soliton conservation assumes the form of a usual $U(1)$ conservation law in the bilayer geometry, and thus provides a way to define a notion of transport via suitably chosen local correlation functions. Due to its universality, the late-time emergent hydrodynamic relaxation can be studied qualitatively using numerically feasible classically simulable circuits, as has recently been applied in other constrained systems [2, 205–207], see also chapters 6,8,9 as well as Sec. A.3. Many of the results described below can thus alternatively be viewed through the lense of lattice gases or cellular automata, but extend to the late time behavior of quantum systems as well.

After introducing the bilayer dimer model and deriving the abovementioned global $U(1)$ conservation law in Sec. 4.1, we divide the analysis of its associated dynamics into two parts: In the first part, Sec. 4.2, we consider the model with full quasi-two-dimensional extension and study the dynamics of initial states hosting a finite density of conserved fluxes. Most strikingly, the local charges associated to the global soliton conservation law display fracton-like dynamics: While they are immobile as single particle objects, composites of these charges are effectively confined to diffuse along one-dimensional tubes within the quasi-2D system. We provide an explanation of these results in terms of a large class of conserved quantities that exist in the system. Notably however, the confinement to such effective 1D tubes is not due to subsystem symmetry constraints. Rather, the timescale necessary for charges to escape the 1D tubes diverges with increasing system size, providing an intriguing instance of non-ergodic behavior induced by the local gauge constraints. In the second part, Sec. 4.3, we then go on to study the dynamics of the model in a quasi-one-dimensional limit on an open-ended cylinder. In this case, the Hilbert space is fragmented into an exponential (in system size) number of disjoint subspaces and hosts statistically localized integrals of motion (SLIOMs) that where introduced recently for constrained systems [237]. We determine the generic hydrodynamics exhibited by such SLIOMs and find subdiffusive decay of local correlations that can be understood analytically through the mapping to a classical tracer diffusion problem, which we will investigate in much more detail in Chapter 9. Having analyzed the dynamics of the bilayer dimer model, we conclude with Sec. 4.4 by demonstrating explicitly that the global $U(1)$ charge is equivalent to a topological soliton conservation law in the form of Hopfions.

4.1 Model and conservation laws

4.1.1 Hamiltonian

The bilayer dimer model we consider is depicted in Fig. 4.1 (a): It is given by two coupled layers of a square lattice, with bosonic hard-core dimers residing on the bonds, subject to a close-packing conditions of exactly one dimer touching each lattice site. If $\hat{n}^{(d)}_{\boldsymbol{r},\alpha} \in \{0,1\}$ denotes the dimer occupation on a bond $(\boldsymbol{r},\alpha)$ with $\alpha \in \{\pm x, \pm y, \pm z\}$, this condition can be phrased as

$$\sum_{\alpha \in \{\text{vertex } \boldsymbol{r}\}} \hat{n}^{(d)}_{\boldsymbol{r},\alpha} = 1 \quad \text{for all } \boldsymbol{r}, \tag{4.1}$$

where the sum extends over five nearest neighbor sites in Eq. (4.1) on the bilayer lattice. The Hilbert space of the system is then given by the set of all configurations satisfying Eq. (4.1) at every site. The close-packing condition Eq. (4.1) can also be interpreted as a local gauge constraint, which explicitly turns into a Gauss law in a dual formulation of the quantum dimer model as an instance of a $U(1)$ quantum link model [250, 377]. Details on the associated mapping for the planar case, which can easily be generalized to the (hyper)cubic geometry, can be found in Chapter 2.3.1 and the references therein.

With the Hilbert space at hand, we again consider the standard Rokhsar-Kivelson (RK) model of elementary plaquette resonances between pairs of parallel dimers, which takes the pictorial form

$$\hat{H}_J = -J \sum_p \hat{h}_p = -J \sum_p \left(|\,\square\,\rangle\langle\,\square\,| + h.c. \right). \tag{4.2}$$

Here, the sum extends over all elementary plaquettes p of the bilayer lattice. We can further allow for a constant potential term yielding an energy offset for each parallel dimer pair,

$$\hat{H}_V = V \sum_p \left(\hat{h}_p\right)^2 = V \sum_p \left(|\,\square\,\rangle\langle\,\square\,| + |\,\square\,\rangle\langle\,\square\,| \right), \tag{4.3}$$

such that the full Hamiltonian is given by $\hat{H} = \hat{H}_J + \hat{H}_V$.

4.1.2 Transition graph mapping and flux sectors

We want to analyze the structure of the Hilbert space under the dynamics of Eq. (4.2) and to this end introduce a description in terms of an effective loop model. Such a description is known as 'transition graphs', which we generalize here to the bilayer case. In this mapping, we take the two dimer configurations on the upper and lower layer and form their transition graph by projecting them on top of each other, see Fig. 4.1 (a). This yields a model of closed, non-intersecting loops in the resulting projected two-dimensional layer. The smallest possible loop of length two consists of two horizontal dimers in both layers directly on top of each other. Notice that the loops can be assigned a chirality, which is inverted upon exchanging the configurations of upper and lower layer.

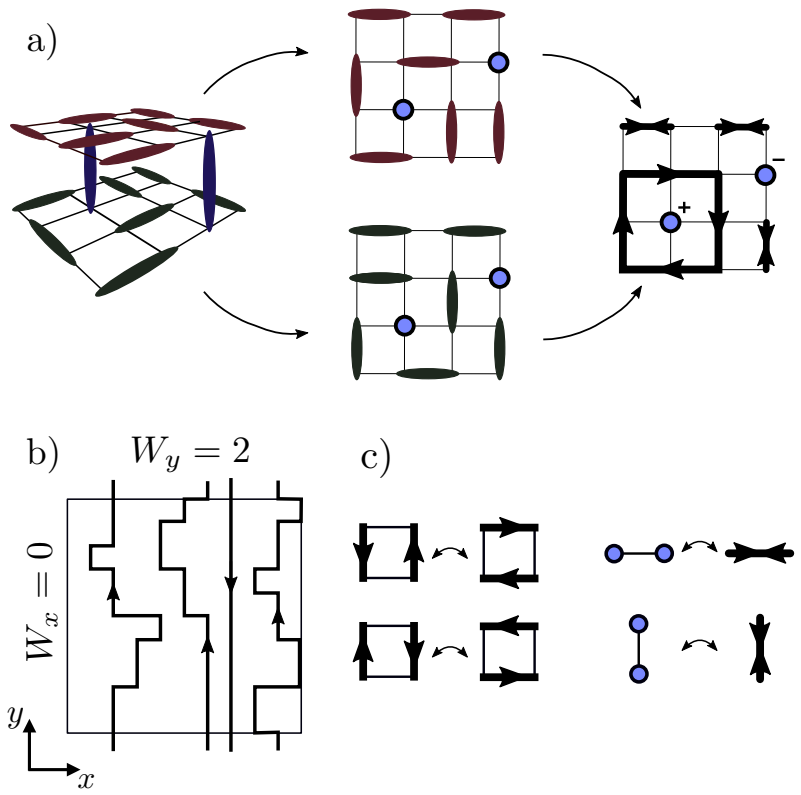

Figure 4.1: Construction of transition graphs. a) The dimer configuration on the bilayer geometry is seperated into upper and lower layer, with interlayer dimers connecting the two marked as dots. The two configurations are then projected on top of each other from a bird's eye view to give rise to a directed loop model as explained in the main text. The interlayer dimers are assigned charges corresponding to their sublattice. The shown configuration is also the simplest one hosting a single Hopfion. **b)** Configurations with non-trivial fluxes W_x and W_y contain loops winding around the boundaries (other loops/interlayer charges not shown to avoid cluttering). **c)** Loop-moves originating from the elementary dimer plaquette flips.

The directed loop segments can be described formally by new occupation numbers $\hat{n}^{(l)}_{\boldsymbol{r},\alpha} \in \{0,1\}$, which indicate the presence of a loop segment pointing from site $\boldsymbol{r}$ to $\boldsymbol{r}+\boldsymbol{e}_\alpha$, where $\boldsymbol{r}$ is now a *two-dimensional* vector and $\alpha \in \{\pm x, \pm y\}$. A full loop $\mathcal{L}$ of length $|\mathcal{L}|$ is then characterized by an ordered set $\{\boldsymbol{r}_0, \boldsymbol{r}_1, ..., \boldsymbol{r}_{|\mathcal{L}|-1}\}$ of lattice sites, with $\boldsymbol{r}_{n+1} = \boldsymbol{r}_{\boldsymbol{n}} + \boldsymbol{e}_\alpha$. By convention, we choose the direction of a loop running through a site $\boldsymbol{r} = (r_x, r_y)$ as the orientation of the original dimer that occupies the site $\boldsymbol{r}' = (\boldsymbol{r}, r_z)$ with r_z such that $\boldsymbol{r}'$ is on the even (or A) sublattice, see Fig. 4.1 (a). The dimers between the two layers now appear as on-site particles for which we define the corresponding number operators $\hat{n}^{(h)}_{\boldsymbol{r}}$. We then assign a *charge* to these particles depending on the sublattice they occupy, i.e. particles on sublattice $A(B)$ carry a charge $+1(-1)$. The total charge in the system is then given by $\sum_{\boldsymbol{r}} (-1)^{r_x+r_y}\, \hat{n}^{(h)}_{\boldsymbol{r}} = 0$, and we refer to the $\hat{n}^{(h)}_{\boldsymbol{r}}$ as 'interlayer charges' in the following. A simple example of this construction is displayed in Fig. 4.1 (a).

Importantly, on periodic boundary conditions, there can exist non-local loops winding around the system boundaries, see Fig. 4.1 (b) and Eq. (2.21). We can thus define global

winding numbers or *fluxes* (these terms will be used interchangeably in this work) W_x and W_y for a given configuration by summing up the windings of all individual loops along both the x- and y-direction, respectively, see Fig. 4.1 (b). The fluxes W_x and W_y are independently conserved under the dynamics of $\hat{H}_J$ and divide the Hilbert space into disconnected subspaces. In later sections, we will mainly be concerned with the additional structure of the Hilbert space on top of these flux sectors.

Finally, we can also translate the elementary plaquette flips of Eq. (4.2) to the loop picture, which take the form $\hat{H}_J = \hat{H}_J^{(l)} + \hat{H}_J^{(h)}$, where

$$\hat{H}_J^{(l)} = \sum_p \Big[|\quad\rangle\langle\quad| + |\quad\rangle\langle\quad| + h.c. \Big], \tag{4.4}$$

and

$$\hat{H}_J^{(h)} = \sum_{\langle \boldsymbol{r},\boldsymbol{r}'\rangle} \Big[|\quad\rangle\langle\quad| + h.c. \Big]. \tag{4.5}$$

$\hat{H}_J^{(l)}$ describes the dynamics involving loop segments only, while $\hat{H}_J^{(h)}$ corresponds to the creation/annihilation of a $\pm$ interlayer charge pair on neighbouring sites, annihilating/creating a length-two loop on the same sites. In the pictorial representation of Eq. (4.5), the charges from interlayer dimers are marked as blue circles in the transition graph.

4.1.3 A global $U(1)$ conservation law

The transition graph picture provides an intuitive starting point for deriving a global conserved charge $\hat{\mathcal{Q}}$ that we later, in Sec. 4.4, associate with the presence of topological solitons. Here, we first notice that under the loop dynamics of Eq. (4.4), the difference in the number of A– and B–sublattice sites enclosed by a particular loop stays constant as long as that loop does not split or merge with another loop. If such a split or merger occurs, then *the sum* of the differences of A and B sites enclosed by the involved loops stays constant. Thus, if $v_{\mathcal{L}} \subset \mathbb{Z}^2$ denotes the interior of a loop $\mathcal{L}$, see Fig. 4.2, then we can infer the global conserved quantity

$$\hat{\mathcal{Q}} = \sum_{\mathcal{L}} \Delta N_{AB}(v_{\mathcal{L}}), \tag{4.6}$$

where the sum extends over all loops $\mathcal{L}$ in the transition graph of a given dimer configuration and $\Delta N_{AB}(v_{\mathcal{L}})$ is the difference between the number of A and B sites contained in the set $v_{\mathcal{L}}$. We note that due to the Gauss law Eq. (4.1), each site in the transition graph is either part of a loop or occupied by an interlayer charge. Since loops always contain an equal number of A and B sites, $\Delta N_{AB}(v_{\mathcal{L}})$ is just the total interlayer charge enclosed by $\mathcal{L}$.

Since the loops $\mathcal{L}$ can become arbitrarily extended, Eq. (4.6) is not in the form of a

sum over local terms. However, for *any* directed, closed, and non-intersecting loop $\mathcal{L} = \{\boldsymbol{r}_0, \boldsymbol{r}_1, ..., \boldsymbol{r}_{|\mathcal{L}|-1}\}$ on the square lattice, the difference in the number of A/B sites within $v_\mathcal{L}$ can be expressed as (see Appendix B.1 for a proof)

$$N_{AB}(v_\mathcal{L}) = \frac{1}{4}\sum_{n=0}^{|\mathcal{L}|-1}(-1)^{x_n+y_n}\Big(\boldsymbol{\ell}_o(\boldsymbol{r}_n)\wedge\boldsymbol{\ell}_i(\boldsymbol{r}_n)\Big), \tag{4.7}$$

where $\boldsymbol{\ell}_o(\boldsymbol{r}_n) = \boldsymbol{r}_{n+1}-\boldsymbol{r}_n$ and $\boldsymbol{\ell}_i(\boldsymbol{r}_n) = \boldsymbol{r}_n-\boldsymbol{r}_{n-1}$ are the directions of the out- and ingoing loop segments at $\boldsymbol{r}_n$. The symbol '$\wedge$' denotes the wedge product $\boldsymbol{a}\wedge\boldsymbol{b} = a_xb_y - a_yb_x$. Eq. (4.7) is illustrated in Fig. 4.2 (a) with a specific example. Using Eq. (4.7) in Eq. (4.6), the

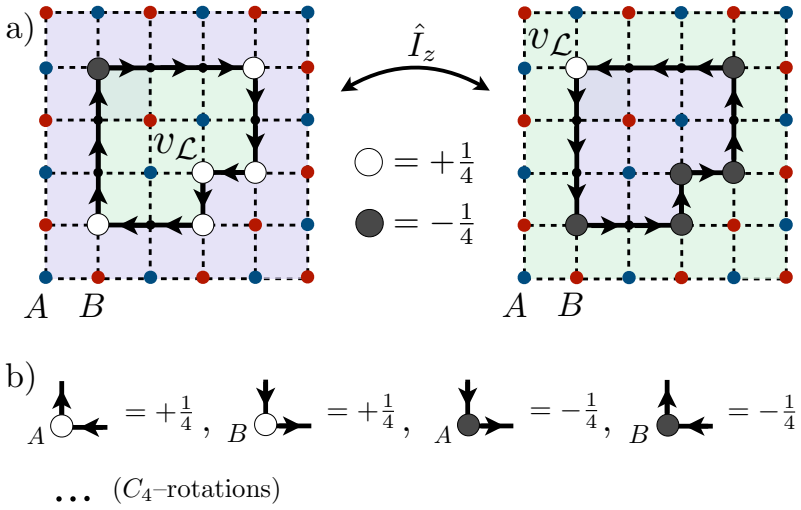

Figure 4.2: Loop interior and corner charges. a) The interior $v_\mathcal{L}$ of a loop $\mathcal{L}$ contains all sites within the green shaded area, and turns into the complement upon inverting the chirality. In transition graphs, the loop chirality can be inverted via the inversion operator $\hat{I}_z$ which exchanges top and bottom layer of the original dimer lattice. White and gray circles illustrate the corner charges $\hat{\mathcal{C}}_{\boldsymbol{r}} = \pm\frac{1}{4}$ from Eq. (4.8). The validity of Eq. (4.7) can directly be verified for this example. **b)** Dictionnary for the corner charges $\hat{\mathcal{C}}_{\boldsymbol{r}}$, modulo lattice C_4–rotations.

quantity $\hat{\mathcal{Q}}$ can finally be expressed as

$$\boxed{\hat{\mathcal{Q}} = \frac{1}{4}\sum_{\boldsymbol{r}}(-1)^{r_x+r_y}\Big(\hat{\boldsymbol{\ell}}_o(\boldsymbol{r})\wedge\hat{\boldsymbol{\ell}}_i(\boldsymbol{r})\Big) =: \sum_{\boldsymbol{r}}\hat{\mathcal{C}}_{\boldsymbol{r}},} \tag{4.8}$$

with the vector-valued operators

$$\begin{aligned}\hat{\boldsymbol{\ell}}_o(\boldsymbol{r}) &= \sum_{\alpha\in\{\pm x,\pm y\}}\boldsymbol{e}_\alpha\,\hat{n}^{(l)}_{\boldsymbol{r},\alpha}\\ \hat{\boldsymbol{\ell}}_i(\boldsymbol{r}) &= \sum_{\alpha\in\{\pm x,\pm y\}}\boldsymbol{e}_\alpha\,\hat{n}^{(l)}_{\boldsymbol{r}-\boldsymbol{e}_\alpha,\alpha}.\end{aligned} \tag{4.9}$$

Eq. (4.8) assumes a particularly useful form, as $\hat{\mathcal{Q}}$ is now a sum over local terms $\hat{\mathcal{C}}_{\boldsymbol{r}}$. Since $\hat{\mathcal{C}}_{\boldsymbol{r}} \neq 0$ only when there is a corner of some loop at $\boldsymbol{r}$, we refer to the $\hat{\mathcal{C}}_{\boldsymbol{r}}$ as *corner charges*,

see Fig. 4.2 (b) for the specific relation between loop corners and the corresponding charge values. A more direct proof of $[\hat{H}_J, \hat{\mathcal{Q}}] = 0$, regardless of the boundary conditions, is provided in Appendix B.2. Moreover, inspecting Fig. 4.2 (a), we see that a local excess of corner charges is directly connected to a local excess of interlayer charges. Finally, we notice that the corner charges carry only a fractional charge of $\pm 1/4$ and cannot move as independent particles, thus featuring fracton-like mobility constraints.

4.1.4 Conserved chiral subcharges

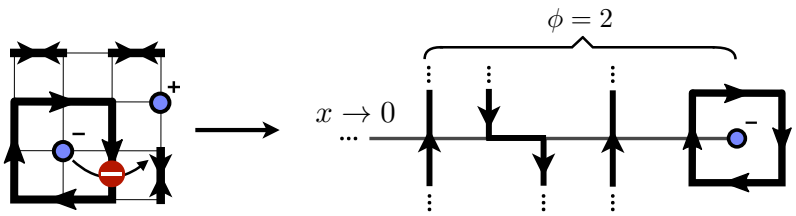

Figure 4.3: Construction of chiral subcharges. An interlayer charge enclosed by a chiral loop cannot escape the loop under the dynamics of the Hamiltonian. We can then attach a string to an interlayer charge which extends all the way to the system boundary and determine the total chirality ϕ of all loops enclosing the charge. The sum of all interlayer charges with a fixed chirality ϕ then presents a conserved quantity.

As it turns out, there exists an even larger set of additional conserved quantities on top of the charge $\hat{\mathcal{Q}}$. To see this, let us recall that according to the previous considerations, an interlayer charge enclosed by a loop cannot exit the loop under the dynamics generated by Eqs. (4.4),(4.5), see Fig. 4.3. To each interlayer charge, we can then associate a chirality via the total chirality of all loops enclosing it. Formally, we attach a string to the interlayer charge which extends all the way to the left system boundary and count the directed number of loop segments crossing it. For this purpose, we define the string operator

$$\hat{\phi}_{\boldsymbol{r}} = \sum_{r_x'=0}^{r_x-1} \left[\hat{n}^{(l)}_{(r_x', r_y), y} - \hat{n}^{(l)}_{(r_x', r_y+1), -y} \right], \tag{4.10}$$

that performs this counting, see Fig. 4.3. We further define an associated chiral interlayer charge operator

$$\hat{q}_{\boldsymbol{r}}(\phi) = \hat{n}^{(h)}_{\boldsymbol{r}} \, \delta\big(\hat{\phi}_{\boldsymbol{r}} - \phi\big), \tag{4.11}$$

that measures whether a given site $\boldsymbol{r}$ is occupied by an interlayer charge with chiral index ϕ.

As a given interlayer charge cannot exit the loops enclosing it, it cannot interact with interlayer charges outside these loops. Thus, the only way to annihilate the interlayer charge is via the interaction with an opposite interlayer charge carrying *the same* chiral

index. Formally, in the notation introduced above, the following set of quantities are then *independently* conserved under the Hamiltonian dynamics,

$$\boxed{\hat{Q}_\phi = \sum_{\boldsymbol{r}} (-1)^{r_x+r_y}\, \hat{q}_{\boldsymbol{r}}(\phi)\ ; \qquad \phi \in \Big\{-L_x, ..., L_x\Big\}.} \tag{4.12}$$

We call the quantities $\hat{Q}_\phi$ 'conserved chiral subcharges'. The formal proof of the invariance of Eq. (4.12), by direct computation of the commutator $[\hat{H}_J, \hat{Q}_\phi]$, is given in Appendix B.3. Importantly, the (non-local) chiral subcharges $\hat{Q}_\phi$ can also be related to the global quantity $\hat{\mathcal{Q}}$ via

$$\hat{\mathcal{Q}} = \sum_\phi\ \phi\ \hat{Q}_\phi, \tag{4.13}$$

which we proof in Appendix B.4. The presence of these conserved subcharges will be crucial to understanding the resulting dynamics of corner charges both in Sec. 4.2 and Sec. 4.3.

A few remarks are in order. While the above construction of the $\hat{Q}_\phi$ relied on open boundary conditions (at least in the x–direction), similar arguments proceed essentially analogously for periodic boundaries, where one can define relative instead of absolute chiralities of interlayer charges. We further note that the conservation of the quantities $\hat{Q}_\phi$ and $\hat{\mathcal{Q}}$ does depend on the dynamics being generated by elementary plaquette flips through Eq. (4.2) and, in general, does not persist in the presence of longer-range updates. However, such longer range updates are generally perturbatively small, and we may speculate that key features of the discussed physics still remain even in the presence of such terms.

4.2 Emergent fracton dynamics in the 2D bilayer dimer model

Having derived the conserved quantity $\hat{\mathcal{Q}}$ in the form of Eq. (4.8), we are interested in how the associated local corner charges $\hat{\mathcal{C}}_r$ are transported through the system under a generic time evolution. Notice that any nonequilibrium dynamics within the dimer Hilbert space, either from $e^{-i\hat{H}t}$ or some other unitary evolution built up by elementary plaquette flips, depends in general on the chosen initial state. In the following, we will focus on the real time dynamics emerging from initial states that host a finite density $|W_x|/L = |W_y|/L > 0$ of fluxes, see Fig. 4.5. We remark that such initial states can also be generated thermodynamically at low energies of a classical dimer model with energy function $\hat{H}_V$, which we verify in the following using Monte Carlo simulations.

4.2.1 Phase diagram of the classical model

Any nonequilibrium dynamics within the dimer Hilbert space, either from $e^{-i\hat{H}t}$ or some other unitary evolution built up by elementary plaquette flips, is in general dependent on

the chosen initial state. In later parts of this section we will focus mostly on the real time dynamics emerging from initial states that host a finite density of fluxes W_x andW_y. A relevant question then concerns how such initial states can best be prepared. A convenient way of achieving this task arises when the initial states of interest, or at least their most relevant feature of a finite flux density, can be prepared in the low energy phase of some local Hamiltonian. Here, we show that this is indeed possible in the bilayer dimer model: For $J = 0$, $V = 1$ there exists a low energy phase that stabilizes a finite density $W_x/L = W_y/L > 0$ of fluxes.

Numerical approach: Directed loop Monte Carlo.

We notice that for the chosen parameters, $\hat{H}_J = 0$ vanishes whereas $\hat{H}_{V=1}$ provides an energy function that makes the model amenable to a classical Monte Carlo study of its finite temperature phase diagram. We employ a directed-loop Monte Carlo scheme following Refs. [378–382], which is ideally suited to treat classical constrained models like dimer models, spin ice, or vertex models [367, 383], see also Appendix A.5 for further details. In this approach, one randomly breaks up a dimer into two monomers and moves one of the monomers through the system. The probabilities for the direction of the monomer's next respective step are chosen according to a local detailed balance rule defined via the Boltzmann weights $e^{-\beta \hat{H}_{V=1}}$. This is done in a fashion that minimizes 'bounces', i.e. the monomer retracing its previous path, thus improving the efficiency of the algorithm. When the two monomers meet again, they recombine into a dimer and the loop closes. We refer to the abovementioned literature for details on the implementation of this algorithm.

Importantly, the loop updates can be non-local and are thus able to explore different flux sectors. In numerical practice, the emergence of a low energy phase with finite flux density restricts the accessible system sizes to some degree, as the associated autocorrelation times at low temperatures become large. This is due to the non-local updates necessary to escape 'local minima' of the energy function. Nonetheless, the phase diagram of the model can be resolved accurately as demonstrated in the following.

Results for the phase diagram.

The main results of the Monte Carlo simulations, performed on system sizes up to $L := L_x = L_y = 80$, are displayed in Fig. 4.4. In Fig. 4.4 (a) we present the temperature-dependent expectation value $\langle E \rangle_T$ of the energy function $E = \hat{H}_{V=1}$, which simply counts the number of flippable plaquettes in the system. We clearly see a sharp, discontinuous drop in the energy at a critical temperature $T_c = 0.457$, indicative of a first order transition. This is confirmed both by the associated specific heat shown in Fig. 4.4 (b), which exhibits a sharp spike at the critical temperature, as well as a bimodal energy distribution at T_c characteristic for first order transitions [384].

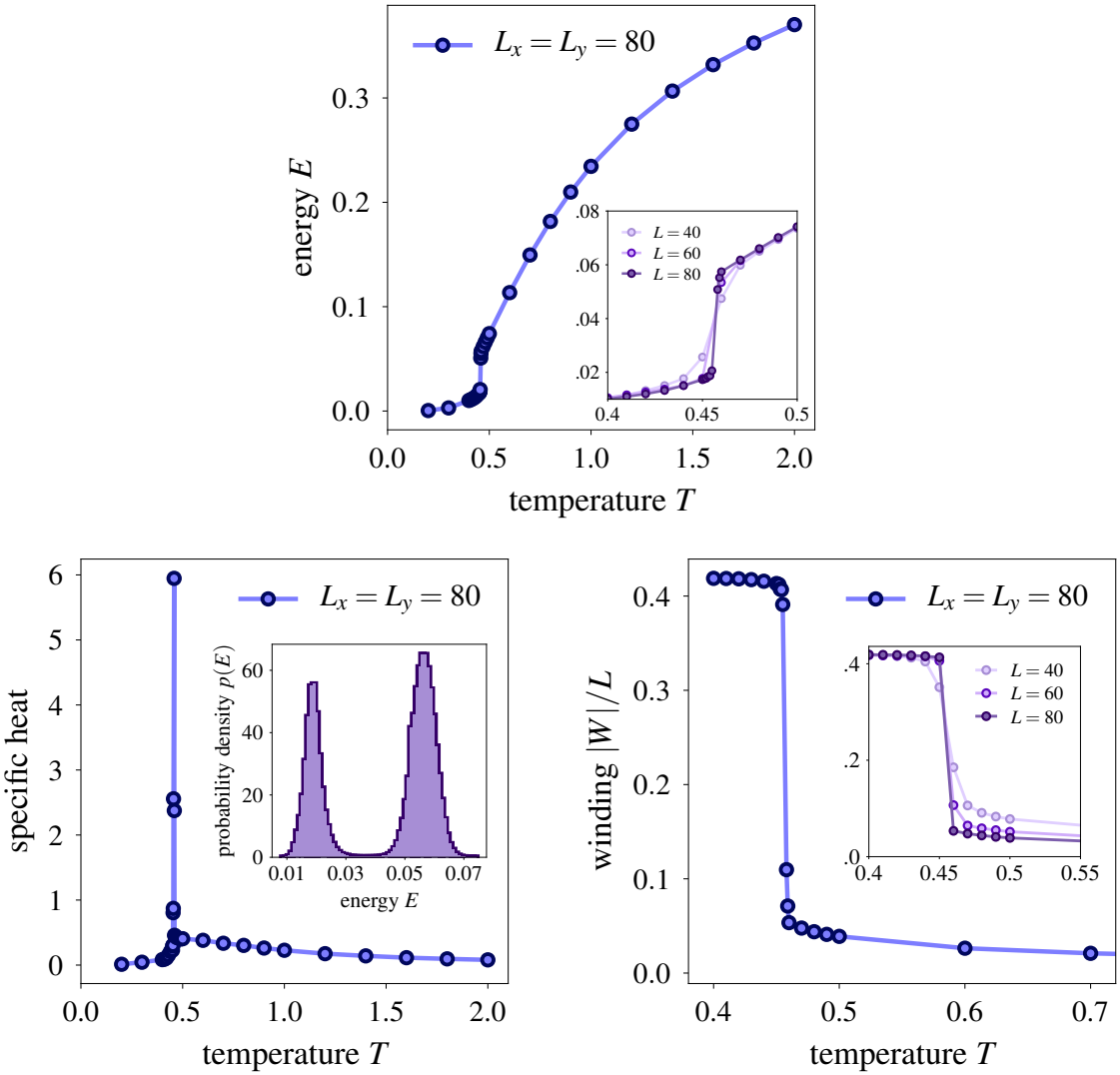

Figure 4.4: Phase transition in the classical limit $J = 0$. We investigate the phase diagram of the dimer model at $\hat{H}_J = 0$ via a classical directed-loop Monte Carlo scheme for systems up to $L = L_x = L_y = 80$. **a)** The temperature-dependent energy E displays a discontinuous drop at $T_c = 0.457$. Inset: The discontinuity sharpens for increasing system sizes. **b)** The associated specific heat has a sharp spike at the critical temperature, indicative of a first order transition. This agrees with the typical, bimodal energy distribution obtained for Monte Carlo simulations at T_c as shown in the inset. **c)** The flux density $|W|/L = |W_x|/L = |W_y|/L$ exhibits a jump at T_c, leading to a low temperature phase with finite winding density. Inset: Again, the discontinuity sharpens for increasing system sizes.

Most interestingly, this phase transition is accompanied by a discontinuous jump in the flux density, which we here define as $|W|/L = |W_x|/L = |W_y|/L$. While for $T > T_c$, $|W|/L \to 0$ approaches zero in the thermodynamic limit, we find $|W|/L > 0$ for $T < T_c$, with $|W|/L \approx 0.42$ for $T \to 0$, see Fig. 4.4 (c). We show local snapshots of typical examples of equilibrium configurations in the transition graph picture for both $T > T_c$, $T < T_c$ in Fig. 4.5.

While we established the presence of a finite temperature phase with finite flux density

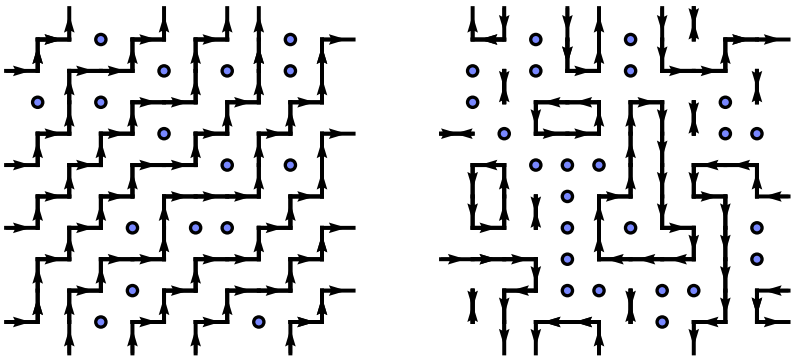

Figure 4.5: Initial states. Local snapshots of typical example configurations within the transition graph picture, both for finite ($W_x/L_x = W_y/L_y > 0$) and vanishing ($W_x/L_x = W_y/L_y = 0$) flux densities, corresponding to $T > T_c$ and $T < T_c$ respectively.

numerically only for $J = 0$, one might expect that this transition survives the onset of finite $J > 0$ due to continuity. As the Hamiltonian $\hat{H} = \hat{H}_J + \hat{H}_{V>0}$ is positive definite as long as $|J| \leq V$, every frozen state containing no flippable plaquettes is an exact ground state of the quantum model in that parameter regime, in analogy to the 2D QDM. Therefore, since ground states in the quantum model are equivalent to those in the classical model, it appears reasonable to speculate that also the finite temperature transition will survive in the quantum case.

4.2.2 Time evolution

Let us now introduce the unitary time evolution that allows us to study the dynamics of corner charges. Ideally, one would like to consider the full quantum time evolution $e^{-i\hat{H}t}$ for the closed system dynamics. This, however, is a challenging task due to the large Hilbert space in our quasi-2D system. Instead, we use that for conserved quantities such as $\hat{\mathcal{Q}}$, an effectively classical hydrodynamic picture at late times is expected to emerge [58–60, 65, 66, 184, 189, 385]. Due to this universal late time decay, every sufficiently ergodic time evolution that respects the system's conservation laws is expected to result in the same qualitative hydrodynamic tail. Details of the short time quantum coherent dynamics would therefore merely enter the numerical value of an effective diffusion constant. Thus, in order to capture only the qualitative aspects of the charge dynamics at late times, we can construct an alternative, classically simulable unitary evolution built up by elementary plaquette flips. This approach follows recent works on automaton circuits [205, 386–388], that have been applied to study the transport properties of fracton models [2, 197, 205–207, 389], and can even be connected to the dynamics of more conventional random unitary quantum circuits [103]. We refer to App. A.3 for an overview of this method.

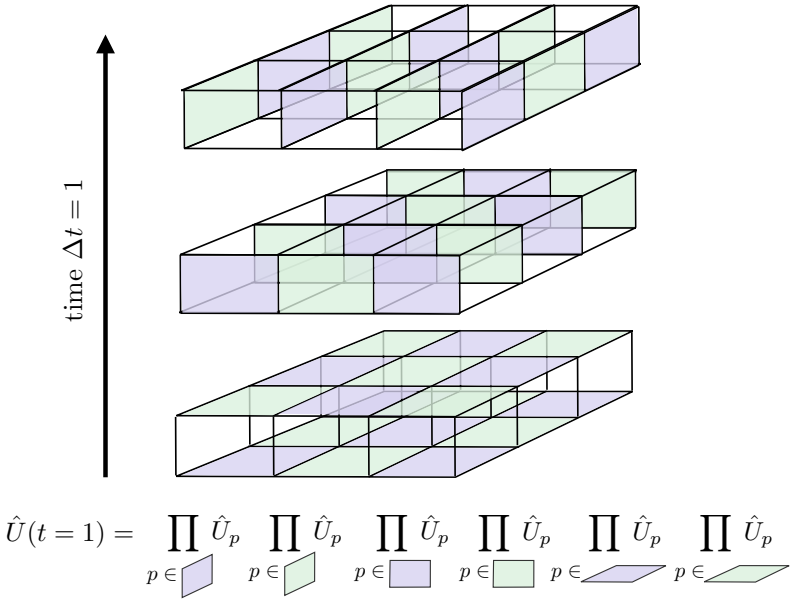

Figure 4.6: Time evolution. A single time step of the deterministic unitary evolution, built on the elementary plaquette updates $\hat{U}_p$ of Eq. (4.14). Within a fixed plaquette color, all associated local updates commute.

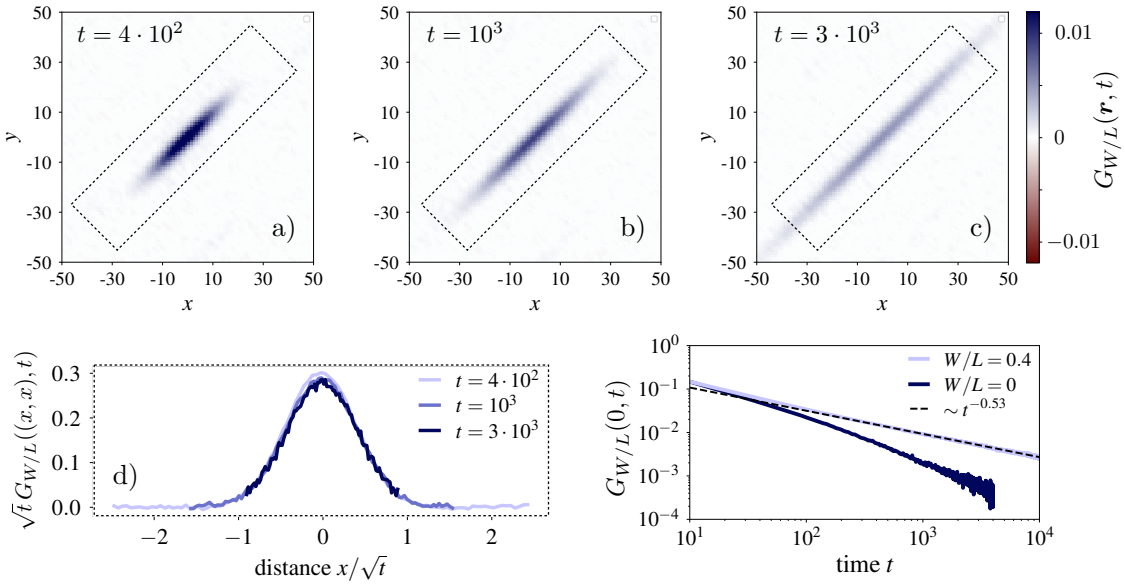

Figure 4.7: Relaxation dynamics of corner charge correlations. a)+b)+c) The spatially resolved corner charge correlation function $G_{W/L}(\boldsymbol{r}, t) = \langle \hat{\mathcal{C}}_0(0)\, \hat{\mathcal{C}}_{\boldsymbol{r}}(t) \rangle_{W/L}$ at different times t. The initial states in the average $\langle ... \rangle_{W/L}$ are sampled from random states within the fixed winding sector $W_x/L = W_y/L = 0.4$. We observe a clear restriction of the charge dynamics to an effective one-dimensional 'tube' along the diagonal. **d)** The dynamics along the diagonal is diffusive, demonstrated by the scaling collapse to a one-dimensional (Gaussian) diffusion kernel. **e)** The return probability $\langle \hat{\mathcal{C}}_{\boldsymbol{r}}(0)\, \hat{\mathcal{C}}_{\boldsymbol{r}}(t) \rangle_{W/L}$ is anomalously slow for a two-dimensional system with $W/L = 0.4$. In contrast, for a vanishing winding density $W/L = 0$, the correlations decay fast. The system sizes are $L_x = L_y = 200$ and $L_x = L_y = 1000$ for $W/L = 0.4$ and $W/L = 0$, respectively.

The elementary local unitary corresponding to a plaquette flip update is given by

$$\hat{U}_p = \left[\mathbb{1} - \left(\hat{h}_p\right)^2\right] + \hat{h}_p, \tag{4.14}$$

with $\hat{h}_p$ from Eq. (4.2). The action of Eq. (4.14) on a given dimer configuration $|\psi\rangle$ (represented as a product state) is easily understood: If $|\psi\rangle$ has a flippable plaquette at p, then $\hat{U}_p |\psi\rangle = \hat{h}_p |\psi\rangle$, i.e. the plaquette is flipped and we obtain a new product state. If, however, $|\psi\rangle$ has no flippable plaquette at p, then $\hat{U}_p |\psi\rangle = |\psi\rangle$, i.e. the state remains unchanged. We can then use the elementary updates from Eq. (4.14) as building blocks for defining a discrete time evolution scheme that can be simulated as a classical cellular automaton. To this end, we can define a deterministic Floquet time evolution, where

$$\hat{U}(t) = \left(\prod_{i=1}^{4L_xL_y} \hat{U}_{p_i}\right)^t, \tag{4.15}$$

and the plaquettes p_i are kept *fixed* throughout different instances of the time evolution. Furthermore, the p_i should be such that for $i \in \{1, ..., 4L_xL_y\}$, each plaquette appears exactly once within a Floquet period. We emphasize that alternative choices of update schemes, such as stochastic updates, yield a qualitatively equivalent late time relaxation, and throughout this work we employ a fixed deterministic evolution that is illustrated in Fig. 4.6.

Using these unitary evolution operators, we can then compute e.g. the correlation function of the previously introduced corner charges,

$$G_S(\boldsymbol{r}, t) := \langle \hat{\mathcal{C}}_{\boldsymbol{r}}(t)\, \hat{\mathcal{C}}_0(0) \rangle_{S \subseteq \mathcal{H}}\,, \tag{4.16}$$

where the average $\langle ... \rangle_{S \subseteq \mathcal{H}}$ is taken over dimer occupation number product initial states within some predefined subset $S \subseteq \mathcal{H}$ of the full Hilbert space.

4.2.3 Reduced mobility of corner charges

Having defined a proper time evolution, we move on to study to dynamics of corner charges via the correlations defined in Eq. (4.16). In particular, we will focus on averages over randomly chosen initial states hosting a finite flux density $W/L = W_x/L_x = W_y/L_y = 0.4$. The associated correlations are then denoted as $G_{W/L}(\boldsymbol{r}, t)$. The dynamics within such flux sectors is particularly interesting: As we saw in the construction of conserved quantities in Sec. 4.1, loops act as obstacles to the dynamics of both interlayer- and corner charges. The presence of non-contractible loops carrying a finite winding number should thus essentially trap charges in between two such winding loops. However, the loops themselves are dynamical objects as well, and we require the time evolution introduced above to resolve the ensuing system dynamics. We note that the resulting late time

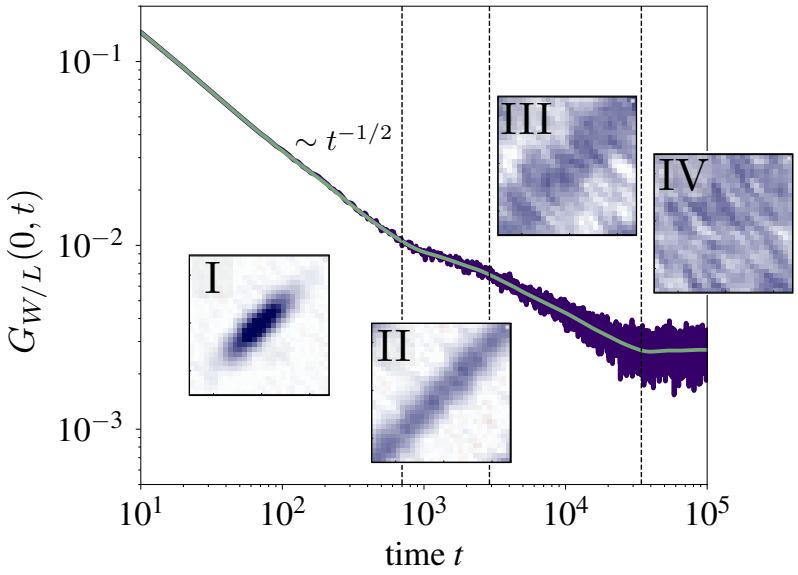

Figure 4.8: Thermalization process. The way to equilibrium, i.e. full delocalization of corner charges across the 2D system, can be split into four distinct stages that are reflected in local correlation functions: I: A stage of diffusive dynamics along effective one-dimensional tubes, with $G \sim t^{-1/2}$. II: A plateau where the charge is fully delocalized along the tube. III: The delocalization along the second direction sets in. IV: The charge is fully delocalized across the whole system. The system size in this example is $L_x = L_y = 30$ and the green curve corresponds to the moving average. This demonstrates that the formation of 1D tubes is not due to disconnectivities, but rather *bottlenecks* in the Hilbert space structure.

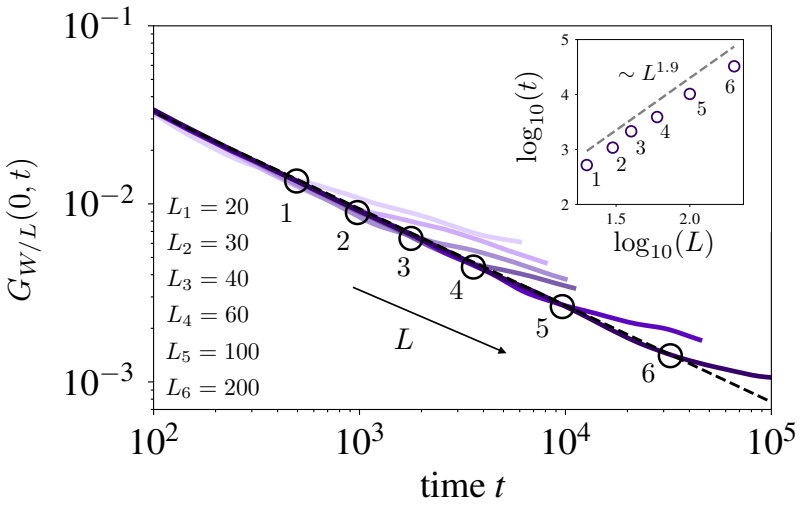

Figure 4.9: Finite size scaling. For increasing system size, the correlations follow the diffusive decay for increasingly long times, approximately scaling as $\sim L^2$ as shown in the inset. Therefore, the one-dimensional tubes are expected to persist up to infinite time in the thermodynamic limit. The displayed lines correspond to the moving average of the numerically sampled correlations.

relaxation should then be qualitatively equivalent to the closed system quantum dynamics for $\hat{H}_V = 0$, which, for product initial states at zero energy, corresponds to infinite temperature due to the symmetric spectrum of $\hat{H}_J$ (see Appendix B.5).

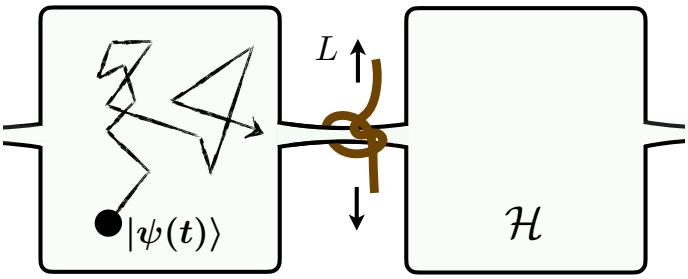

Figure 4.10: Origin of reduced dimensional mobility. The numerical results presented in Sec. 4.2 can be understood intuitively in terms of *bottlenecks* in the Hilbert space structure: As the system size increases, the bottlenecks become narrower, and the time needed to eventually pass through the bottleneck in order to explore the full Hilbert space diverges.

Our main numerical results for a system of size $L_x = L_y = 200$ are presented in Fig. 4.7. Inspecting the spatially resolved $G_{W/L}(\boldsymbol{r}, t)$ in Fig. 4.7 (a-c), we find diffusion of corner charges along effective, one-dimensional *tubes* within the 2D system. The diagonal direction of these tubes within the system corresponds to the winding order of the initial states, cf. Fig. 4.5. In Fig. 4.7 (d), we show the correlations $G_{W/L}(\boldsymbol{r} = (x, x), t)$ along the tube direction. These follow a 1D diffusion kernel

$$G_{W/L}(\boldsymbol{r} = (x, x), t) = \frac{1}{\sqrt{Dt}} e^{-x^2/Dt} \tag{4.17}$$

From the viewpoint of the site-local return probability $G_{W/L}(0, t) \sim 1/\sqrt{t}$, this leads to anomalous slow decay of local correlation functions, which would generically be expected to relax as $\sim 1/t$ for usual diffusion in two dimensions. This is demonstrated in Fig. 4.7 (e), where we compare $G_{W/L}(0, t)$ to the faster decaying correlations within the zero flux sector.

Remarkably, although the winding loops are dynamical as well and should in principle be able to move throughout the entire system, the effective 1D tubes do not appear to broaden within the times shown in the correlations of Fig. 4.7 (a-c). Therefore, an important question concerns whether in the thermodynamic limit, there exists a finite (but potentially very large) timescale at which the localization of corner charges within stationary 1D tubes eventually breaks down. To this end, we consider the return probability $G_{W/L}(0, t)$ within a smaller system of size $L_x = L_y = 30$ in Fig. 4.8, which reveals a multistage thermalization process in this finite size system: First (see (I) in Fig. 4.8), charges diffusive along the effective one-dimensional tubes. Then (see (II) in Fig. 4.8), the system reaches an intermediate plateau where the charges are fully delocalized along the 1D tube, but still remain localized with respect to the perpendicular direction. Eventually (see (III) and (IV) in Fig. 4.8), the 1D tubes start to broaden, and charges are delocalized across the entire 2D system. These results demonstrate that the winding loops are indeed in principle able to move through the system. To answer our question about the thermodynamic

limit posed above, we then need to study how the different timescales involved in the multistage thermalization process of Fig. 4.8 change as we increase the system size.

This analysis is perfomed in Fig. 4.9, where we show $G_{W/L}(0,t)$ for a range of system sizes $L \in \{20, 30, 40, 60, 100, 200\}$. As we increase L, the return probability follows the 1D diffusive decay for increasingly long times. In particular, the largest system size $L = 200$ still follows purely 1D relaxation at times when smaller systems have already fully delocalized. This suggests that in the thermodynamic limit, the time scale required to move the winding loops through the system indeed diverges. As a consequence, the system exclusively exhibits effectively 1D dynamics in the thermodynamic limit, failing to delocalize perpendicular to the winding direction. Intuitively, the diverging timescale of eventual 2D delocalization can be understood by the fact that non-local winding loops have to be moved as a whole for such a process to occur. Since the length of these loops diverges with system size, the timescale of these processes diverges as well.

We emphasize that the reduced dimensionality found for the charge dynamics – a hallmark of fracton–like excitations – comes without the presence of subsystem symmetries that would fundamentally restrict the charges to only move along one dimension, as is evidenced by the eventual 2D decay in finite size systems. As the corner charges can in principle move through the entire system, the generator of the dynamics is not 'reducible' in the language of classically constrained models [150]. Thus, instead of the Hilbert space falling into disconnected parts in the form of symmetry sectors, the fractonic behavior in the bilayer dimer model is rather due to bottlenecks in the Hilbert space, which become narrower as the system size is increased, see Fig. 4.10 for a symbolic depiction of the situation. It would be interesting to see how such a Hilbert space structure effects the validity of the eigenstate thermalization hypothesis (ETH) with respect to the Hamiltonian $\hat{H}$.

4.3 The quasi 1D bilayer model

In the previous section we have numerically demonstrated the emergence of reduced dimensional mobility for the corner charges of Eq. (4.8) in translationally invariant 2D systems. In this section, we change the geometry and consider a *quasi-one-dimensional*, cylindrical system. There, we encounter a strong fragmentation of the Hilbert space into an exponential in system size number of disconnected subsectors. In addition, the associated conserved quantities that label the different Hilbert space sectors fulfill a recently introduced concept of statistical localization [237]. We determine the algebraic long time decay of the corner charge correlations by mapping to a classical problem of tracer diffusion in a 1D system with hard core interacting particles.

4.3.1 Hilbert space fragmentation for large flux

We consider a quasi-1D system on a cylinder of length L_x with open boundaries, whose circumference L_y is kept finite. In order to analyze the structure of the Hilbert space

within this geometry, we investigate the relative size of the different disconnected subspaces that each can be labelled by a set of values $\{Q_\phi\}_{\phi\in[-L_x,L_x]}$ (with $Q_\phi \in \mathbb{Z}$) of the conserved chiral subcharges of Eq. (4.12). Implicitly assuming the flux number W_y to be fixed, we denote the relative size of the $\{Q_\phi\}$–subspace compared to the full Hilbert space at flux W_y by $P(\{Q_\phi\})$. We note that $P(\{Q_\phi\})$ is a probability distribution, i.e. $\sum_{\{Q_\phi\}} P(\{Q_\phi\}) = 1$, which can be sampled numerically by randomly drawing states from the full W_y–subspace. In addition, we can define the individual probabilities

$$P(Q_\phi) = \sum_{\{Q_{\phi'}\}_{\phi'\neq\phi}} P(\{Q_{\phi'}\}) \tag{4.18}$$

for the ϕ–th subcharge $\hat{Q}_\phi$ to assume a value Q_ϕ. It can be verified numerically through Monte Carlo sampling that different $\hat{Q}_\phi$ are essentially uncorrelated, i.e. $\langle \hat{Q}_\phi \hat{Q}_{\phi'} \rangle \propto \delta_{\phi,\phi'}$, which allows us to approximate $P(\{Q_\phi\}) \approx \prod_\phi P(Q_\phi)$ for the following arguments.

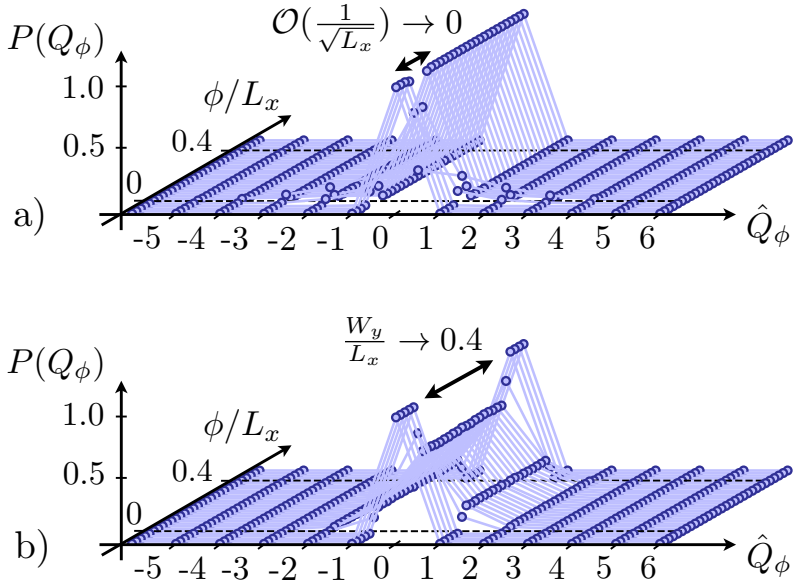

Figure 4.11: Hilbert space fragmentation in a quasi-1D geometry. We display the probability distributions $P(\hat{Q}_\phi)$ of the charges $\hat{Q}_\phi$ for randomly chosen states on a $L_x = 100$, $L_y = 6$ open-ended cylinder. **a)** For vanishing flux $W_y = 0$, almost all $\hat{Q}_\phi$ are statistically fixed to zero, i.e. $P(Q_\phi) = \delta_{Q_\phi,0}$. Thus, a small number of large sectors dominates the Hilbert space, which is only weakly fragmented. **b)** In contrast, for a finite winding density $W_y/L_x = 0.4$, there is an extensive amount ($0 \lesssim \phi \lesssim W_y$) of charges $\hat{Q}_\phi$ with a finite width probability distribution. As a result, the Hilbert space is strongly fragmented.

Choosing the flux-free sector $W_y = 0$ at first, we plot the distributions $P(Q_\phi)$ in Fig. 4.11 (a). We see that for almost all values of ϕ, the values Q_ϕ of the subcharges are statistically fixed to zero, i.e. $P(Q_\phi) = \delta_{Q_\phi,0}$. This holds for all ϕ outside a range of order $\mathcal{O}(\sqrt{L_x})$ around $\phi = 0$, which is expected from generic fluctuations of the distribution of winding loops even within the $W_y = 0$ – sector. Therefore, although an extensive number of conserved quantities $\hat{Q}_\phi$ exist, most of the associated subspaces are small, and

the Hilbert space is instead dominated by a small number of very large sectors. In the terminology of Ref. [235], the Hilbert space is only *weakly fragmented*.

In contrast, for a finite flux density $W_y/L_x > 0$ around the cylinder, the probability distributions $P(Q_\phi)$ obtain a finite width for an extensive number of ϕ between $0 \lesssim \phi \lesssim W_y$, see Fig. 4.11 (b). As a consequence, the relative size of *every* $\{Q_\phi\}$–subsector is exponentially suppressed with respect to the full Hilbert space: $P(\{Q_\phi\}) \approx \prod_\phi P(Q_\phi) \sim e^{-c\,L_x}$, since an extensive number of the $P(Q_\phi)$ in the product over ϕ is smaller than one. In particular, also the largest sector, $\{Q_\phi = 0\}$ for all ϕ, is exponentially suppressed, which is seen intuitively by multiplying all the probabilities $P(Q_\phi = 0)$ along the ϕ–axis in Fig. 4.11 (b). According to the definition provided in Ref. [235] the Hilbert space is thus *strongly fragmented*.

4.3.2 Statistical localization of chiral subcharges

Having identified the strong fragmentation of the Hilbert space in the previous section, we now turn to determine some of its consequences. In particular, the previous results imply the applicability of the recently introduced concept of statistical localization [237]. Let us shortly describe this concept in a hands-on way: The conserved chiral subcharges are given by $\hat{Q}_\phi = \sum_{\boldsymbol{r}} (-1)^{r_x+r_y}\, \hat{q}_{\boldsymbol{r}}(\phi)$, where $\hat{q}_{\boldsymbol{r}}(\phi)$ checks whether there is an interlayer charge at site $\boldsymbol{r}$ that is encircled by ϕ loops in total. Notice that within the cylindrical geometry, the definition of the $\hat{Q}_\phi$ remains well-defined. As there is a finite density of winding loops, we would then generally expect the main contributions to $\hat{Q}_\phi$ to come from interlayer charges located around the position of the ϕ^{th} winding loop. Where in turn is the ϕ^{th} winding loop located at along the cylinder? To get an estimate, let us assume there to be exactly W_y winding loops and let us further ascribe a one-dimensional position x_ϕ to the ϕ^{th} such loop. Then the probability $p_\phi(x_\phi)$ of finding this loop at x_ϕ is approximated by a simple count of the number of possibilities,

$$p_\phi(x_\phi) \approx \frac{\binom{x_\phi}{\phi-1}\binom{L_x-x_\phi-1}{W_y-\phi-1}}{\binom{L_x}{W_y}}, \tag{4.19}$$

i.e. the number of possibilities to have $\phi - 1$ winding loops to the left of x_ϕ times the number of possibilities to have the remaining $W_y - \phi - 1$ loops to the right of x_ϕ, divided by the overall number of possibilities to distribute the one-dimensional positions of all W_y loops across the system of length L_x [237]. For a winding loop in the bulk of the system, $p(x_\phi)$ is a peaked distribution of width $\sqrt{L_x}$ centered around $\phi L_x/W_y$. Via the line of arguments just provided, we then expect a very similar distribution $p_\phi(x_\phi)$ to describe the locations of the operators $\hat{q}_{\boldsymbol{r}}(\phi)$. Therefore, the $\hat{q}_{\boldsymbol{r}}(\phi)$ that constitute the $\hat{Q}_\phi$ are localized to a *subextensive* region of size $\sqrt{L_x}$, a feature termed statistical localization in Ref. [237].

To confirm this line of reasoning, we show in Fig. 4.12 (a) the numerically determined probability distributions $p_\phi(x_\phi)$ of the $x_\phi = r_x$ - positions of the operators $\hat{q}_{\boldsymbol{r}}(\phi)$, for different ϕ. More precisely, $p_\phi(x_\phi)$ is defined as

$$p_\phi(x_\phi) := \frac{\langle \hat{q}_{(x_\phi,0)}(\phi) \rangle_{W_y/L_x}}{\sum_{x'_\phi} \langle \hat{q}_{(x'_\phi,0)}(\phi) \rangle_{W_y/L_x}}. \tag{4.20}$$

We indeed find the expected localization to a $\sqrt{L_x}$ subregion within the system, for all ϕ scaling with system size. For ϕ not scaling with system size, the corresponding conserved quantities $\hat{Q}_\phi$ are instead localized close to the boundary, shown in Fig. 4.12 (a) for $\phi = 0$.

From Fig. 4.12 (a) we also clearly see that the average positions $\sum_{x_\phi} x_\phi \, p_\phi(x_\phi) =: \overline{x_\phi} < \overline{x_{\phi+1}}$ of the chiral subcharges are spatially ordered. This spatial ordering becomes even more apparent when realizing that the probability distributions $p_\phi(x_\phi)$ for different ϕ are not independent: We can compute the probability distribution $\tilde{p}_{\phi',\phi}(x'_{\phi'} - x_\phi)$ of the distance between two chiral interlayer charges for independent ϕ, ϕ'. Formally, we define $\tilde{p}_{\phi',\phi}(x'_{\phi'} - x_\phi)$ via

$$\tilde{p}_{\phi',\phi}(x'_{\phi'} - x_\phi) := \frac{\sum_x \langle \hat{q}_{(x,0)}(\phi) \, \hat{q}_{(x+x'_{\phi'}-x_\phi,0)}(\phi') \rangle_{W_y/L_x}}{\sum_{x,x'} \langle \hat{q}_{(x,0)}(\phi) \, \hat{q}_{(x',0)}(\phi') \rangle_{W_y/L_x}}. \tag{4.21}$$

We then consider the associated probability $P_{\phi',\phi}(x'_{\phi'} > x_\phi) = \sum_{x \geq 0} \tilde{p}_{\phi',\phi}(x)$ of finding the chiral interlayer charge associated to ϕ' to the right of the one associated to ϕ. In Fig. 4.12 (b), we see that there is a system-size-independent sharp step in $P_{\phi',\phi}(x'_{\phi'} > x_\phi) \approx \theta(\phi' - \phi)$ as a function of $\phi' - \phi$. Therefore, the SLIOMs $\hat{Q}_\phi$ are sharply ordered along the cylinder and thus form a conserved spatial charge pattern. Intuitively, this is understood from the fact that the $\hat{q}_{\boldsymbol{r}}(\phi)$ that contribute to $\hat{Q}_\phi$ are predominantly located between the ϕ^{th} and $(\phi+1)^{th}$ loop, counting from the left end of the system. In addition, the sharply peaked probability distribution $\tilde{p}_{\phi,\phi}(x'_\phi - x_\phi)$ of the distance between two interlayer charges contributing to the same $\hat{Q}_\phi$ shows that in a given state, the $\hat{Q}_\phi$ can be assigned a sharp position along the cylinder, see Fig. 4.12 (c).

Having confirmed the presence of the statistically localized integrals of motion (SLIOMs) $\hat{Q}_\phi$, a number of results obtained in Ref. [237] directly carry over to our situation. First, we notice that the inversion operator $\hat{I}_z$ that exchanges the dimer configurations of upper and lower layer induces the inversion of the chirality of all loops in the projected transition graph picture. Therefore, $\{\hat{I}_z, \hat{\phi}_{\boldsymbol{r}}\} = 0$ and hence also $\{\hat{I}_z, \hat{Q}_\phi\} = 0$ for all ϕ. Since also $[\hat{I}_z, \hat{H}] = 0$, this implies that the spectrum of all Hilbert space sectors (except for the sector with $\hat{Q}_\phi = 0$ for all ϕ) is doubly degenerate.

We further notice that in particular, also $\{\hat{I}_z, \hat{Q}_{\phi=0}\} = \{\hat{I}_z, \hat{Q}_{\phi=W_y-1}\} = 0$, i.e. both leftmost and rightmost chiral subcharges are inverted by $\hat{I}_z$. These conserved quanti-

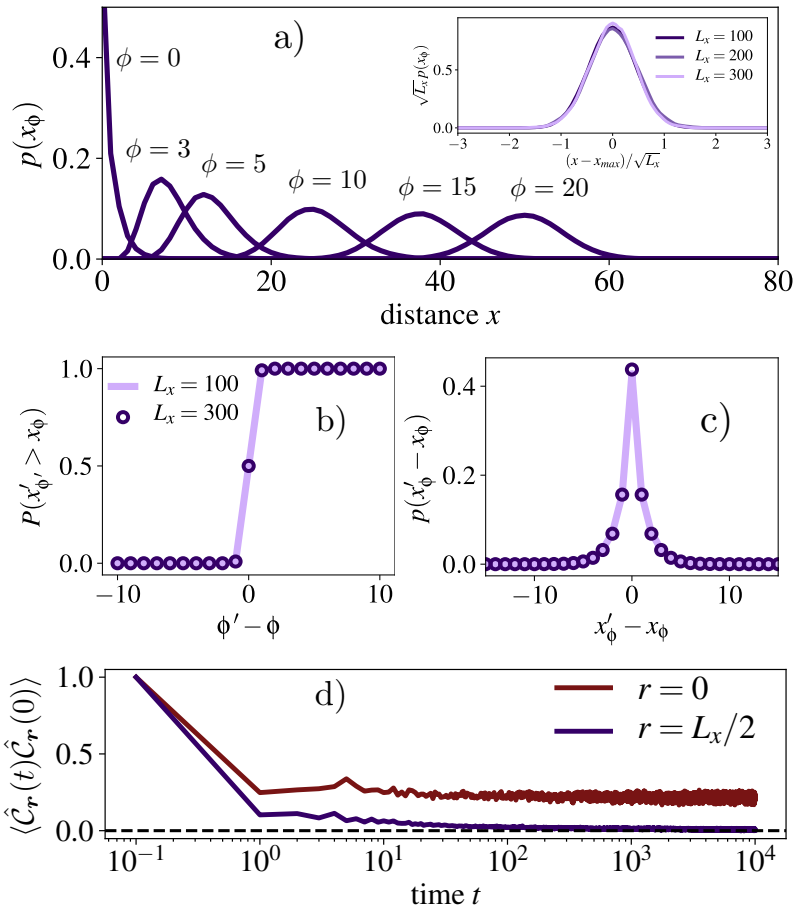

Figure 4.12: Statistically localized integrals of motion (SLIOMs). a) Probability distribution of the x-value $x_\phi = r_x$ of the position of the chiral interlayer charges $\hat{q}_{\boldsymbol{r}}(\phi)$ for fixed ϕ. The system size used for Monte Carlo simulations is $L_x = 100$, $L_y = 6$, as well as $W_y/L_x = 0.4$. For a given ϕ in the bulk, the $\hat{q}_{\boldsymbol{r}}(\phi)$ are generally localized to a subextensive region of size $\sim \sqrt{L}$, see Inset. In addition, there exist modes localized exponentially on the boundary, shown here for $\phi = 0$. These results demonstrate that the $\hat{Q}_\phi$ are statistically localized integrals of motion (SLIOMs) according to Ref. [237]. **b)** Probability of finding a chiral interlayer charge $\hat{q}_{(x'_{\phi'},0)}(\phi')$ to the right of another such charge $\hat{q}_{(x_\phi,0)}(\phi)$. The system-size-independent sharp step demonstrates the spatial ordering pattern of the $\hat{q}_{\boldsymbol{r}}(\phi)$ along the cylinder. **c)** Probability distribution of the distance between two interlayer charges $\hat{q}_{\boldsymbol{r}}(\phi)$ of the same ϕ. The sharply peaked distribution shows that the SLIOMs $\hat{Q}_\phi$ can be assigned 1D positions along the cylinder. **d)** The corner charge correlation function remains finite at the boundary due to the presence of edge modes, while decaying in the bulk.

ties (as well as all other $\hat{Q}_\phi$ with ϕ not scaling with system size) are localized close to the boundary as seen in Fig. 4.12 (a), and the formal similarity to so-called strong edge modes [390–395] were pointed out in [237]. As a results of these edge modes, corner charge correlation functions at the boundary will not decay but retain a finite memory, e.g. $\lim_{t\to\infty} \langle \hat{\mathcal{C}}_{(0,y)}(t)\, \hat{\mathcal{C}}_{(0,y)}(0)\rangle_{W_y/L_x} \neq 0$, see Fig. 4.12 (d).

In contrast to the correlations on the boundary, the bulk corner charge correlations do decay as shown in Fig. 4.12 (d). Therefore, the strong Hilbert space fragmentation due to SLIOMs is not in general enough to prevent the system from thermalizing [237]. Exactly

how the decay of bulk correlations ensues will be treated in the following paragraph.

4.3.3 Subdiffusive relaxation

As demonstrated in the previous section and in Fig. 4.12 (d), the bulk correlations in our cylindrical geometry decay even in the presence of a strong fragmentation of the Hilbert space due to SLIOMs. This induces the question of *how* these correlations decay qualitatively, and in particular how the presence of SLIOMs influences this decay process.

To answer this question, we present a (non-rigorous) analytical argument that yields a prediction for the form of the quasi-1D correlation functions

$$G^{(1d)}_{w_y}(x,t) := \langle \hat{\mathcal{C}}_{(x,0)}(t)\, \hat{\mathcal{C}}_{(0,0)}(0)\rangle_{W_y/L_x}\,, \tag{4.22}$$

evaluated for finite flux densities $w_y = W_y/L_x > 0$. For simplicity of notation, we assume $x = 0$ to be located in the bulk here. As demonstrated in the previous section, the SLIOMs $\hat{Q}_\phi$ obey a notion of locality, i.e. they form a conserved pattern of charges along the cylinder, as was similarly the case for the SLIOMs discussed in Ref. [237]. This pattern conservation can alternatively be interpreted as a hard core constraint, in that two different $\hat{Q}_\phi$ can never exchange relative positions along the cylinder. If $|\psi\rangle$ denotes some initial product state in the dimer occupation basis, we can then label this state $|\psi\rangle = |\{Q_\phi, x_\phi\}, \alpha\rangle$ by the values of its conserved quantities Q_ϕ and their 1D-positions x_ϕ ($x_\phi < x_{\phi+1}$), as well as a remaining set of parameters α containing microscopic details. Of course, the $\hat{Q}_\phi$ are not actually site-local objects, but rather composed by all the $\hat{q}_{\boldsymbol{r}}(\phi)$. Nonetheless, from a 'course-grained' point of view, we can ascribe a single x-position x_ϕ to each Q_ϕ, see Fig. 4.12 (c). In the following, we assume the microscopic details encoded by the parameters α not to be essential for the transport of conserved quantities at late times, thus omiting them from the notation, i.e. $|\psi\rangle \simeq |\{Q_\phi, x_\phi\}\rangle$. The corner-charge operator $\hat{\mathcal{C}}_{(x,0)}$ will then be sensitive to the SLIOM $\hat{Q}_\phi$ that is located at $x_\phi = x$, i.e. we assume

$$\hat{\mathcal{C}}_{(x,0)}\,|\psi\rangle \to \hat{\mathcal{C}}_{(x,0)}\,|\{Q_\phi, x_\phi\}\rangle \sim \sum_\phi \delta_{x_\phi,x}\, Q_\phi\; |\{Q_\phi, x_\phi\}\rangle\,. \tag{4.23}$$

Inserting this assumption into the expression Eq. (4.22) yields

$$\begin{aligned}
G^{(1d)}_{w_y}(x,t) &= \sum_\psi \langle\psi|\hat{\mathcal{C}}_{(x,0)}(t)\, \hat{\mathcal{C}}_{(0,0)}(0)|\psi\rangle_{W_y/L_x} \\
&\sim \sum_{\{Q_\phi, x_\phi\}} \langle\{Q_\phi, x_\phi\}|\hat{\mathcal{C}}_{(x,0)}(t)\, \hat{\mathcal{C}}_{(0,0)}|\{Q_\phi, x_\phi\}\rangle \\
&\sim \sum_{\{Q_\phi, x_\phi\}} \sum_\phi \delta_{x_\phi,0}\, Q_\phi\, \langle\{Q_\phi, x_\phi(t)\}|\hat{\mathcal{C}}_{(x,0)}|\{Q_\phi, x_\phi(t)\}\rangle \\
&\sim \sum_{\{Q_\phi, x_\phi(0)\}} \sum_{\phi,\phi'} \delta_{x_\phi(0),0}\, \delta_{x_{\phi'}(t),x}\, Q_\phi\, Q_{\phi'}\,,
\end{aligned} \tag{4.24}$$

where we have substituted $\sum_{\psi} \to \sum_{\{Q_\phi, x_\phi\}}$ and shifted the time dependence to the states in the last two lines. We now assume further that the position $x_\phi(t)$ of $\hat{Q}_\phi$ at time t does not depend on the value of Q_ϕ, thus again neglecting certain microscopic details. We can then directly carry out the average $\sum_{\{Q_\phi\}} Q_\phi Q_{\phi'} \sim \delta_{\phi,\phi'}$ to obtain

$$G_{w_y}^{(1d)}(x,t) \sim \sum_{\{x_\phi(0)\}} \sum_{\phi} \delta_{x_\phi(0),0}\, \delta_{x_\phi(t),x}. \tag{4.25}$$

Eq. (4.25) has an intuitive interpretation: $G_{w_y}^{(1d)}(x,t)$ describes the tracer motion of individual SLIOMs $\hat{Q}_\phi$, which move from $x_\phi(0) = 0$ at time $t = 0$ to $x_\phi(t) = x$ at time t. Notice that the $\hat{Q}_\phi$ become effectively *distinguishable* particles due to the (initial state) average $\sum_{\{Q_\phi\}}$.

Recalling that the $\hat{Q}_\phi$ obey an effective hard core constraint, we recognize that due to Eq. (4.25), the motion of SLIOMs should effectively be described by the tracer diffusion of hard core particles in one dimension. This problem has been studied within more direct setups in the mathematical literature and admits an exact solution for the asymptotic probability distribution of hard core tracer particles at long times [396–398] (see in particular Ref. [398] and references therein for an overview of the history of this problem). This probability distribution directly carries over to the correlations $G_{w_y}^{(1d)}(x,t)$ via Eq. (4.25), and we thus predict

$$G_{w_y}^{(1d)}(x,t) = (Dt)^{-1/4} \exp(-x^2/\sqrt{Dt}), \tag{4.26}$$

for the long time hydrodynamic decay of correlations in systems hosting SLIOMs in general, and our bilayer dimer setup specifically. For the latter, we can immediately verify the validity of Eq. (4.26) numerically, as shown in Fig. 4.13. Notice that the correlations assume a Gaussian shape, but decay *subdiffusively* slow, with $G_{w_y}^{(1d)}(0,t) \sim t^{-1/4}$ for the return probability (cf. $G(0,t) \sim t^{-1/2}$ for normal diffusion in 1D).

To conclude this section, we note that we expect the result Eq. (4.26) to be an *a priori* consequence of the presence of SLIOMs in arbitrary systems under a sufficiently ergodic time evolution. While we have explicitly used in Eq. (4.24) that at each point in time, the system is in a product state in the automaton evolution, a similar reasoning in terms of hard core tracer diffusion should apply equally well for any generic plaquette dynamics. It would be interesting to verify this prediction explicitly in the future, e.g. for systems such as the $t - J_z$-model discussed in Ref. [237].

4.4 Connections to topological solitons

As announced above in Sec. 4.1, the global conserved quantity $\hat{\mathcal{Q}}$, whose exotic associated transport properties we have investigated in the main body of this work, can be interpreted as a topological soliton conservation law. More specifically, we will show in this section that the total chiral charge $\hat{\mathcal{Q}}$ corresponds to the bilayer version of a con-

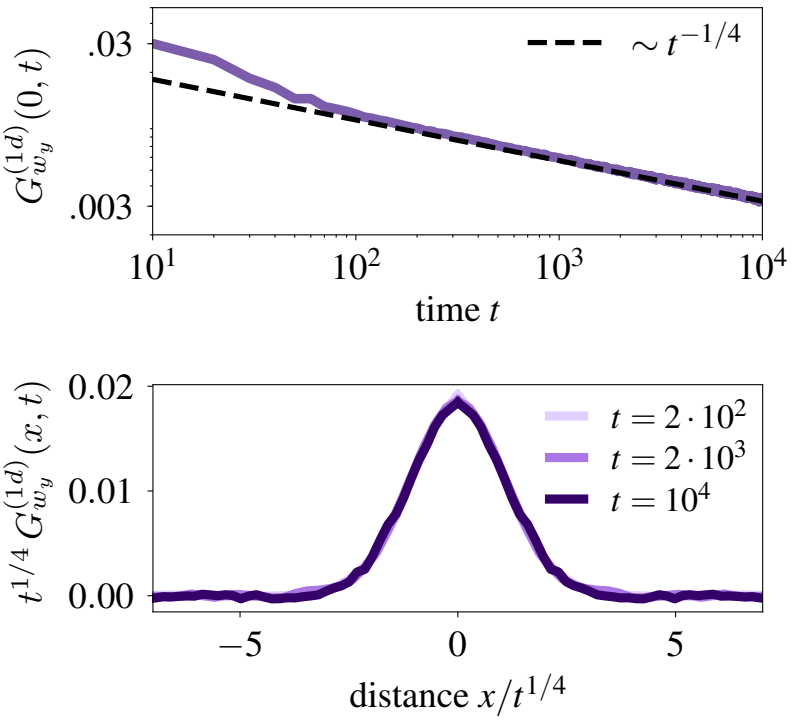

Figure 4.13: Relaxation of corner charges in 1D. Local correlations of the corner charge relax subdiffusively in an effective 1D geometry (cylinder with finite circumference). The exponent of the decay is $1/4$ and the correlations assume a Gaussian form. This is in full agreement with the probabilty distributions of hard-core tracer particles, expected to describe the late time decay of SLIOM correlation functions.

served *Hopf-invariant* that exists more generally in the cubic lattice dimer model as derived in Refs. [374, 375]. The correlation functions we considered previously can thus be interpreted as characterizing the dynamics of *Hopfions* (i.e. three-dimensional topological solitons) within the bilayer geometry.

4.4.1 Hopfions: A brief introduction

Before specifically analyzing the abovementioned reformulation of $\hat{\mathcal{Q}}$ as a conserved Hopf-number, let us first take a small detour to introduce the concept of Hopfions more generally: Hopfions are three-dimensional topological solitons, originally introduced in Ref.[399]. They can be defined in terms of the homotopy classes of maps between 3- and 2-spheres, $\boldsymbol{n} : \mathcal{S}^3 \to \mathcal{S}^2$. As $\mathcal{S}^3$ is isomorphic to $\mathbb{R}^3 \cup \{\infty\}$ by stereographic projection, we can think of $\boldsymbol{n}(\boldsymbol{r})$ as a unit vector field in $\mathbb{R}^3$ with a uniform limit $\boldsymbol{n}(|\boldsymbol{r}| \to \infty) = \boldsymbol{n}_0$. The fibres of this vector field, defined as the preimages $\boldsymbol{n}^{-1}(\boldsymbol{q}) \subset \mathbb{R}^3$ of given points $\boldsymbol{q} \in \mathcal{S}^2$ on the 2-sphere, form closed loops in $\mathbb{R}^3$. The linkage number $N_{\mathcal{H}}(\boldsymbol{n})$ of two such fibres under the map $\boldsymbol{n}$ yields the directed number of times two such loops are winding around each other, thereby providing an integer homotopy classification of $\boldsymbol{n}$. Within this interpretation of linking numbers of preimages, the necessity of a three-dimensional setting in

order to provide a non-trivial Hopf-invariant is evident.

For practical computational purposes, the Hopf invariant $N_{\mathcal{H}}(\boldsymbol{n})$ can be expressed as an integral,

$$N_{\mathcal{H}}(n) = \int d^3r\, \boldsymbol{B}(\boldsymbol{r}) \cdot \boldsymbol{A}(\boldsymbol{r}), \tag{4.27}$$

where the 'magnetic field' is given by $B_i = \epsilon_{ijk}\, \boldsymbol{n} \cdot (\nabla_j \boldsymbol{n} \times \nabla_k \boldsymbol{n})$ and the implicit vector potential $\boldsymbol{B} = \nabla \times \boldsymbol{A}$. The expression of Eq.(4.27) is typically applied to classical field theories where $\boldsymbol{n}(\boldsymbol{r})$ can be interpreted as a magnetization vector field in a solid state system. As opposed to their two-dimensional Skyrmion counterparts [400, 401], the stabilization of magnetic configurations with non-trivial Hopf-numbers have so far eluded experimental detection in solid state systems, and are subject to active research also in the context of topological phases of matter [402–404].

4.4.2 Hopfions in the dimer model

For the present lattice dimer model, the connection to the Hopf invariant of Eq.(4.27) can be made in two ways: Either by a suitable continuum limit which allows for a direct use of Eq.(4.27) [374]. Or, by providing a discrete lattice version of the invariant Eq.(4.27) [375], which is the approach we will adopt in the following. We emphasize that in order to define a Hopf number, we have to assume OBCs (therefore, in the end, the quantity $\hat{\mathcal{Q}}$ reduces to the Hopf number upon choosing open boundaries).

Following Refs. [375, 380], we first have to choose a lattice magnetic field description of our dimer model. For this purpose, we define a field on the bonds of the lattice,

$$B_\alpha(\boldsymbol{r}) = (-1)^{r_x+r_y+r_z} \left[\hat{n}^{(d)}_{\boldsymbol{r},\alpha} - \delta_{\alpha,z}\, \delta_{(-1)^{r_z},1}\right], \tag{4.28}$$

with $\alpha \in \{x, y, z\}$, that can be verified to satisfy a zero divergence condition

$$\nabla \cdot \boldsymbol{B}(\boldsymbol{r}) = \sum_\alpha \left[B_\alpha(\boldsymbol{r}) - B_\alpha(\boldsymbol{r} - \boldsymbol{e}_\alpha)\right] = 0, \tag{4.29}$$

see Fig. 4.14 for an example. Using Eq. (4.28), every dimer configuration maps uniquely to a magnetic field configuration. We can then think of our $L_x \times L_y \times 2$ bilayer-system with OBCs as being embedded within an infinite cubic lattice. Outside the bilayer system we fix the dimers to a trivial configuration $\hat{n}^{(d)}_{\boldsymbol{r},\alpha} = \delta_{\alpha,z}\, \delta_{(-1)^{r_z},1}$ for $\boldsymbol{r} \notin [0, L_x] \times [0, L_y] \times [0, 1]$, which implies a vanishing magnetic field $\boldsymbol{B}(\boldsymbol{r}) = 0$ on all bonds not part of the finite bilayer system. Notice that this property is consistent with the condition $\boldsymbol{n}(|\boldsymbol{r}| \to \infty) = const.$ required in the usual continuum definition of the Hopf number mentioned above.

With a magnetic field living on the *bonds* $(\boldsymbol{r}, \alpha)$ of the lattice at hand, the associated discrete vector potential $\boldsymbol{A}(\boldsymbol{r})$ is defined on its *plaquettes*. If $A_\gamma(\boldsymbol{r})$ denotes the vector potential on the plaquette whose center lies at $\boldsymbol{r} + \boldsymbol{e}_\alpha/2 + \boldsymbol{e}_\beta/2$ $((\alpha, \beta, \gamma) \in \mathrm{Perm}(x, y, z))$ with normal vector $\boldsymbol{e}_\gamma$, the relation between magnetic field and vector potential can be

expressed as

$$B_\alpha(\boldsymbol{r}) = (\nabla \times \boldsymbol{A}(\boldsymbol{r}))_\alpha = \epsilon_{\alpha\beta\gamma}\left[A_\gamma(\boldsymbol{r}) - A_\gamma(\boldsymbol{r}-\boldsymbol{e}_\beta)\right]. \tag{4.30}$$

Hence, once the values of the vector potential are known, the corresponding magnetic field values can simply be determined via a 'right-hand-rule', see Fig. 4.14 (c) for an illustration.

Equipped with these lattice definitions, the corresponding discrete equivalent to the Hopf number Eq.(4.27) for a given dimer configuration was given in Ref.[375] as

$$\begin{aligned} N_{\mathcal{H}} &= \frac{1}{8}\sum_{\boldsymbol{r}} \boldsymbol{A}(\boldsymbol{r})\cdot\bar{\boldsymbol{B}}(\boldsymbol{r}) = \frac{1}{8}\sum_{\boldsymbol{r},\alpha} A_\alpha(\boldsymbol{r})\,\bar{B}_\alpha(\boldsymbol{r}) = \\ &= \frac{1}{8}\sum_{\boldsymbol{r},\alpha} A_\alpha(\boldsymbol{r})\Big[B_\alpha(\boldsymbol{r}) + B_\alpha(\boldsymbol{r}+\boldsymbol{e}_\beta) + B_\alpha(\boldsymbol{r}+\boldsymbol{e}_\gamma) + \\ &+ B_\alpha(\boldsymbol{r}+\boldsymbol{e}_\beta+\boldsymbol{e}_\gamma) + B_\alpha(\boldsymbol{r}-\boldsymbol{e}_\alpha) + B_\alpha(\boldsymbol{r}-\boldsymbol{e}_\alpha+\boldsymbol{e}_\beta) + \\ &+ B_\alpha(\boldsymbol{r}-\boldsymbol{e}_\alpha+\boldsymbol{e}_\gamma) + B_\alpha(\boldsymbol{r}-\boldsymbol{e}_\alpha+\boldsymbol{e}_\beta+\boldsymbol{e}_\gamma)\Big], \end{aligned} \tag{4.31}$$

where the term $\bar{B}_\alpha(\boldsymbol{r})$ in brackets can be considered as the average magnetic field adjacent to the plaquette $A_\alpha(\boldsymbol{r})$, providing an analogy to the form of Eq.(4.27). The invariance of Eq.(4.31) either under gauge transformations of the vector potential,

$$A_\alpha(\boldsymbol{r}) \to A_\alpha(\boldsymbol{r}) + f(\boldsymbol{r}) - f(\boldsymbol{r}-\boldsymbol{e}_\alpha) \tag{4.32}$$

with some scalar function f, leaving the magnetic field invariant, as well as under elementary plaquette flips

$$A_\alpha(\boldsymbol{r}) \to A_\alpha(\boldsymbol{r}) \pm 1 \tag{4.33}$$

with a correspondingly transforming B-field according to Eq.(4.30), was demonstrated in Ref.[375].

4.4.3 Hopf-charge of conserved quantities

To show that in the bilayer geometry, $N_{\mathcal{H}}$ is indeed the total chiral charge $\mathcal{Q}$ from Eq. (4.8), we first recognize that according to Eq. (4.28), the magnetic field is non-zero only on bonds that are part of loops within the transition graph picture (as well as on the interlayer z-bonds along such loops), see Fig. 4.14b for an illustration. If we characterize a certain dimer configuration via the collection $\{\mathcal{L}\}$ of loops contained within its transition graph, we can show that $N_{\mathcal{H}}(\{\mathcal{L}\}) = \sum_{\mathcal{L}\in\{\mathcal{L}\}} N_{\mathcal{H}}(\mathcal{L})$ can be expressed as a sum over the Hopf numbers of individual loops: If a vector potential $\boldsymbol{A}_{1/2}(\boldsymbol{r})$ and its induced field $\boldsymbol{B}_{1/2}(\boldsymbol{r})$ lead to the (non-overlapping) loops $\mathcal{L}_{1/2}$ in the transition graph respectively, then $\boldsymbol{A}(\boldsymbol{r}) = \boldsymbol{A}_1(\boldsymbol{r}) + \boldsymbol{A}_2(\boldsymbol{r})$ contains both $\{\mathcal{L}\} = \{\mathcal{L}_1, \mathcal{L}_2\}$ in its induced transition graph. According to Eq. (4.31), the Hopf number of the dimer configuration described by $\boldsymbol{A}(\boldsymbol{r})$ is then given

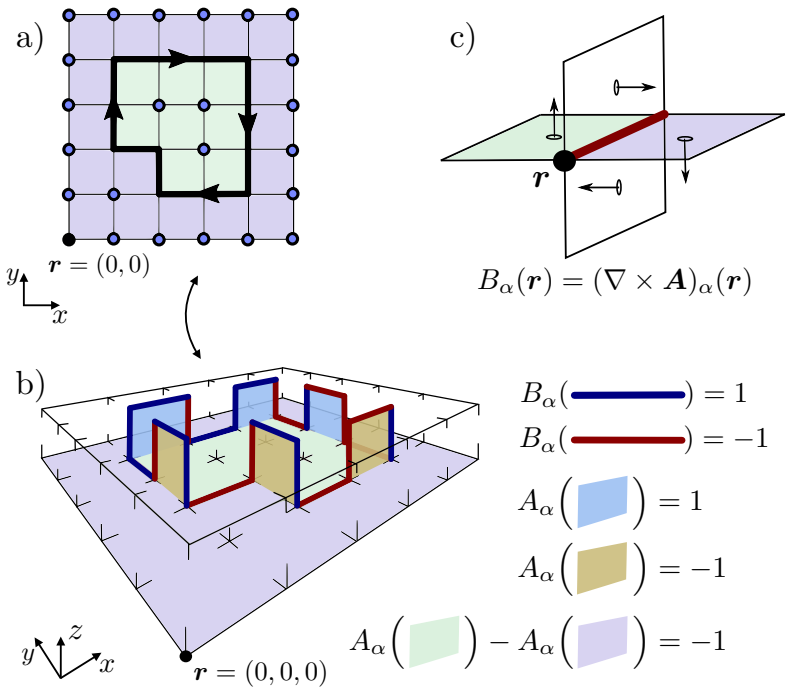

Figure 4.14: Lattice magnetic field description. A given dimer configuration containing a certain loop in its transition graph in a) can be mapped to a lattice magnetic field $B_\alpha(\boldsymbol{r})$ on the bonds of the bilayer lattice according to Eq. (4.28) in b). The magnetic field can be derived from an associated vector potential $A_\alpha(\boldsymbol{r})$ living on the plaquettes of the lattice, see c). The values of the vector potential for the example in b) where chosen according to Eq. (4.35) and Eq. (4.36). It can directly be verified that this choice leads to the correct dimer occupation numbers, as well as a Hopf number $N_{\mathcal{H}}$ from Eq. (4.31) that agrees with the total chiral charge $\hat{\mathcal{Q}}$ from Eq. (4.8), evaluated for the loop in a).

by

$$N_{\mathcal{H}}(\{\mathcal{L}_1, \mathcal{L}_2\}) = N_{\mathcal{H}}(\mathcal{L}_1) + N_{\mathcal{H}}(\mathcal{L}_2) + \frac{1}{8}\sum_{\boldsymbol{r}} \boldsymbol{A}_1(\boldsymbol{r}) \cdot \bar{\boldsymbol{B}}_2(\boldsymbol{r}) + \frac{1}{8}\sum_{\boldsymbol{r}} \boldsymbol{A}_2(\boldsymbol{r}) \cdot \bar{\boldsymbol{B}}_1(\boldsymbol{r}). \quad (4.34)$$

Since the two loops are non-overlapping by virtue of the hard core constraint, $\boldsymbol{A}_{1/2}(\boldsymbol{r})$ does not generate a finite field strength on all $\boldsymbol{r}$ where $\boldsymbol{B}_{2/1}(\boldsymbol{r}) \neq 0$ is finite. Hence, by application of a suitable gauge transformation Eq. (4.32), $\boldsymbol{A}_{1/2}(\boldsymbol{r}) = 0$ can be chosen to vanish on all such $\boldsymbol{r}$ and the cross-terms in the second line of Eq. (4.34) indeed vanish. Therefore, we only have to show that $N_{\mathcal{H}}(\mathcal{L}) = \mathcal{Q}(\mathcal{L})$ for dimer configurations containing a single loop $\mathcal{L}$ (all other dimers are then fixed along z-bonds) in their transition graph. This is done most easily by providing a specific instance of a vector potential $\boldsymbol{A}(\boldsymbol{r})$ that produces the loop $\mathcal{L}$ in the transition graph, and subsequently inserting this $\boldsymbol{A}(\boldsymbol{r})$ into Eq. (4.31).

To achieve this, let us first denote by $p = p(\boldsymbol{r}) = \{\boldsymbol{r}, \boldsymbol{r} + \boldsymbol{e}_x, \boldsymbol{r} + \boldsymbol{e}_x + \boldsymbol{e}_y, \boldsymbol{r} + \boldsymbol{e}_y\}$ the set that contains the four sites of an elementary plaquette on the 2D square lattice. Recall that a given loop $\mathcal{L} = \{\boldsymbol{r}_0, ..., \boldsymbol{r}_{|\mathcal{L}|-1}\}$ is given by an ordered set of sites and the direction of the ingoing loop segment at $\boldsymbol{r}_n$ is given by $\boldsymbol{\ell}_i(\boldsymbol{r}_n) = \boldsymbol{r}_n - \boldsymbol{r}_{n-1}$. Recall further, that

$v_{\mathcal{L}}$ denotes the interior of the 2D loop $\mathcal{L}$, see Fig. 4.2 and the discussion in Appendix B.4. Then, the following vector potential will lead to a configuration that contains the loop $\mathcal{L}$ in its transition graph:

- For all $\boldsymbol{r}, \boldsymbol{r}' \in \mathbb{Z}^2$ s.t. $p(\boldsymbol{r}) \cap v_{\mathcal{L}} = \emptyset$ and $p(\boldsymbol{r}') \cap v_{\mathcal{L}} \neq \emptyset$, choose

$$A_z(r_x, r_y, 0) - A_z(r'_x, r'_y, 0) = 1. \tag{4.35}$$

- For all $\boldsymbol{r}_n$ on the A-sublattice and $\alpha \in \{x, y\}$ chosen such that $\boldsymbol{e}_\alpha \cdot \boldsymbol{\ell}_i(\boldsymbol{r}_n) = 0$, choose

$$A_\alpha\Big(\boldsymbol{r}_n - \boldsymbol{\ell}_i(\boldsymbol{r}_n)\frac{1 + \boldsymbol{\ell}_i(\boldsymbol{r}_n) \cdot (\boldsymbol{e}_x + \boldsymbol{e}_y)}{2}\Big) = (\boldsymbol{e}_x + \boldsymbol{e}_y) \cdot [\boldsymbol{\ell}_i(\boldsymbol{r}_n) \times (\boldsymbol{e}_x + \boldsymbol{e}_y)]. \tag{4.36}$$

- Choose $A_\alpha(\boldsymbol{r}) = 0$ for all remaining plaquettes.

Using Eq. (4.28) and Eq. (4.30), it is straightforward to check that this choice of $\boldsymbol{A}(\boldsymbol{r})$ yields the correct dimer configuration that produces the loop $\mathcal{L}$. Furthermore, inserting Eq. (4.35) and Eq. (4.36) into the expression Eq. (4.31) for the Hopf Number $N_{\mathcal{H}}$, a lengthy but straightforward calculation shows that indeed $N_{\mathcal{H}} = \hat{\mathcal{Q}}$ is the same as the total chiral charge conservation law of Eq. (4.8). It is very instructive to convince oneself of the validity of $N_{\mathcal{H}} = \hat{\mathcal{Q}}$ through Fig. 4.14. In this Fig. 4.14b, we have entered the values of $\boldsymbol{A}(\boldsymbol{r})$ according to Eq. (4.35) and Eq. (4.36) for a specific example. The associated magnetic field values, dimer occupation numbers, and the Hopf number can then directly be read off.

As a results of these considerations, we conclude that the fractonic corner charges $\hat{\mathcal{C}}_{\boldsymbol{r}}$ carry a non-vanishing Hopf-charge. Similarly, the conserved chiral subcharges $\hat{Q}_\phi$ can be viewed as independently conserved Hopfion-subcharges, which provides an intriguing interpretation for the dynamics studied in Sec. 4.2 and Sec. 4.3. Since the Hopf charge exists also on the fully three-dimensional cubic lattice, it would be interesting to study which of our observed features, and under what circumstances, might carry over higher dimensions.

4.5 Conclusion & Outlook

In this chapter we have investigated the nonequilibrium properties of a bilayer dimer model using classically simulable automata circuits, adding to increasing recent interest in the dynamics of dimer models [1, 160, 366, 405–408]. We have found fracton-like dynamics of objects we termed 'corner charges' that are associated to a globally conserved chiral charge, which we have found to be equivalent to a topological soliton conservation law. The dynamics of the full quasi-2D system for finite flux densities is characterized by the formation of effective one-dimensional tubes that restrict the mobility of corner charges, a hallmark of fractonic behavior. This leads to an anomalously slow decay of local correlations, as charges can diffusive only along one instead of two independent

directions. Since the 1D tubes can only be destabilized by moving non-local winding loops through the system, they are stable up to a time that appears to diverge with system size, leading to non-ergodic behavior in the thermodynamic limit. In addition, we have identified the presence of statistically localized integrals of motion (SLIOMs) in a quasi-one-dimensional limit of the model. The hydrodynamic relaxation of these SLIOMs was found to be subdiffusively slow and can be described by the tracer diffusion of classical hard core particles. The applicability of this latter result extends beyond the specific model studied in this paper and describes the hydrodynamic behavior of SLIOMs more generally – provided they are not so strong as to localize the system as in Ref. [235]. Developing these ideas further and applying them to other quantum many-body systems will be in large part the content of Chapter 9.

Moreover, the results derived in this chapter should apply to bilayer versions of arbitrary dimer models on bipartite planar lattices, for which most of our constructions are expected to proceed in an analogous way. Which of our results and under what circumstances might also generalize to dimer models in the fully three-dimensional limit is less apparent. In particular, while the soliton conservation law utilized in this chapter exists in the 3D cubic dimer model as well, the equivalent of corner charges and the effect of finite flux densities is left as an open question.

Other than changing the lattice geometry, we can also vary the underlying static electric charge distribution of the lattice gauge theory that is dual to the dimer model [300]. Potential future work might conduct a systematic survey on the presence of soliton conservation laws depending on the underlying charge distribution. This could open a window for a more general glimpse into the thermalization dynamics of gauge theories via the study of late time transport properties.

Finally, while proposals to study lattice gauge theories like dimer models experimentally with Rydberg quantum simulators have already been put forward in [300] (although for the planar 2D case), it will be interesting to see whether bilayer dimer models can also potentially be obtained as realistic low energy theories in condensed matter systems such as (artificial) spin ice, or in the strong coupling limit of correlated fermion models [409]. Naturally, interest then also extends towards the equilibrium properties of such models [410, 411].

5

Local probes of topological edge states in two-dimensional quantum magnets

This chapter is based on the publication

> Johannes Feldmeier, Willian Natori, Michael Knap, Johannes Knolle, *"Local probes of topological edge states in two-dimensional quantum magnets"*, Phys. Rev. B 102, 134423 (2020)

Structure, text and figures have been adapted for the purposes of this thesis. The numerical data on the dynamical structure factor of the Kitaev honeycomb model has been obtained using code developed by Willian Natori and Johannes Knolle.

We have seen in the previous two chapters that constraints can induce very exotic nonequilibrium dynamics. In this chapter, we investigate potential ways in which an understanding of dynamics in constrained systems can aid with their detection in experiment, especially with an eye towards the long sought-after material realization of spin liquid states. These are characterized by their non-trivial topological properties, and it is those properties that we will target with our approach. The search for topological properties of insulating quantum magnets is an exciting, yet challenging task [261, 262]. While related electronic systems saw a swift verification of the bulk-boundary correspondence [412–415] because surface sensitive probes like angle resolved photoemission spectroscopy (ARPES) and scanning tunneling microscopy (STM) were readily available, similar smoking gun signatures have remained elusive for magnetic systems beyond one dimension [416, 417] due to the charge-neutral character of spin excitations. One route to address this obstacle leads to spin-sensitive local probes, which have recently been proposed as novel tools for identifying fascinating phases of matter such as quantum spin

liquids (QSLs) [258, 418–421].

Moreover, recent technological advances in the fabrication of van-der-Waals heterostructures draw particular attention to magnetic quantum systems in *two* dimensions [422, 423]. In this context, transport measurements of graphene on top of atomically thin insulating magnets have been employed to measure thermodynamic properties of the magnetic layer [424]. Here we propose similar heterostructures for tunneling-based surface-spectroscopy in order to probe magnetic excitations [425]. A contender to overcome the abovementioned challenges could thus be provided by spin-polarized scanning tunneling microscopy (SP-STM), which is sensitive to local spin excitations through inelastic tunneling processes [426–429]. This technique has been employed to characterize arrangements of interacting magnetic atoms, including the resolution of spin wave spectra [430, 431], and might provide access to localized boundary modes [432, 433]. The most direct application of our proposal may thus be the resolution of edge modes in topological magnon insulators (TMIs), indirect signatures of which have been observed in 2D magnets [434–439].

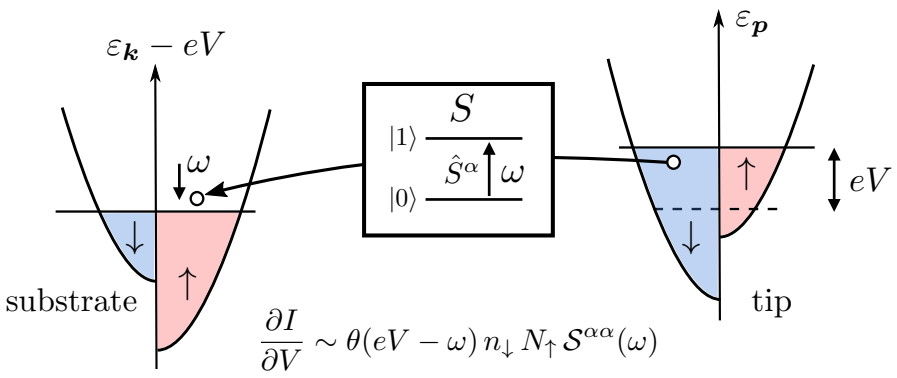

Figure 5.1: Spin-polarized scanning tunneling microscopy (SP-STM). We propose tunneling from a metallic and magnetic substrate to an STM tip via inelastic spin flips of an insulating magnetic layer (S) in between. A tunneling electron can excite a mode with energy ω in S provided the applied bias voltage exceeds this energy. The resulting conductance is proportional to the spin-dependent densities of states in tip, substrate, and the sample S, *c.f.* Eq. (5.8). Tuning the spin polarization in tip and substrate allows for selectively probing different types of spin excitations in the sample.

Particular strengths of SP-STM include atomic resolution as well as the ability to investigate anisotropies via selective polarization of tip and substrate, making it in principle well-suited for the study of highly anisotropic Kitaev spin liquids [241]. Conveniently, one of the prime material candidates [293, 334–336], the α-$\mathrm{RuCl_3}$ compound, can be exfoliated down to monolayer thickness [346] and first graphene heterostructures have been reported [347, 348]. Although this material displays an ordered zig-zag ground state [339, 340], there exists consistent evidence for the onset of a disordered state under the presence of a moderate magnetic field [337, 338, 341, 342]. Most strikingly, thermal Hall measurements on bulk samples show a fractional quantization of the thermal con-

ductivity [343] indicating the presence of chiral Majorana fermion edge states, a result whose origin is currently under debate [344, 345].

In the remainder of this chapter, after a brief summary of SP-STM, we first show that it allows for observing topological magnon edge states of TMIs. As our main result, we then determine qualitative features for potential SP-STM measurements of 2D magnets described by an extended Kitaev honeycomb model. By evaluation of the dynamical spin structure factor on open boundary conditions (OBCs) we find clear signatures associated with the existence of fractionalized gapless edge modes and emergent $\mathbb{Z}_2$ gauge fluxes.

5.1 Spin-polarized STM

5.1.1 Setup and model

We review some essential aspects of spin-polarized STM, largely based on the works of Refs. [428, 429, 440]. The setup is as follows: A metallic tip of the STM device (t) is located at a position $\boldsymbol{r} = (x, y)$ and at a vertical distance d above a metallic substrate (s). In between, a layer of an insulating spin system (S) is placed on top of the substrate, see Fig. 5.1. The Hamiltonian takes the form

$$\hat{H} = \hat{H}_t + \hat{H}_s + \hat{H}_S + \hat{H}_T, \tag{5.1}$$

where

$$\hat{H}_t = \sum_{\boldsymbol{p},\sigma} \varepsilon_{\boldsymbol{p},\sigma} \hat{a}^\dagger_{\boldsymbol{p},\sigma} \hat{a}_{\boldsymbol{p},\sigma} \tag{5.2}$$

and

$$\hat{H}_s = \sum_{\boldsymbol{k},\sigma} \varepsilon_{\boldsymbol{k},\sigma} \hat{b}^\dagger_{\boldsymbol{k},\sigma} \hat{b}_{\boldsymbol{k},\sigma} \tag{5.3}$$

describe the non-interacting electrons in tip and substrate, whose details are not crucial. $\hat{H}_S(\{\hat{\boldsymbol{S}}_i\})$ describes the interacting system of spins $\hat{\boldsymbol{S}}_i$ at positions $\boldsymbol{r}_i$. Finally, $\hat{H}_T$ models the tunneling of electrons between tip and substrate in the presence of an applied bias voltage V via

$$\hat{H}_T = \sum_{\boldsymbol{p},\boldsymbol{k},\sigma,\sigma'} \left[\hat{T}^{\sigma\sigma'}_{\boldsymbol{r}} \hat{a}^\dagger_{\boldsymbol{p},\sigma} \hat{b}_{\boldsymbol{k},\sigma'} e^{i\boldsymbol{k}\boldsymbol{r} + ieVt} + h.c. \right], \tag{5.4}$$

where $\hat{T}^{\sigma\sigma'}_{\boldsymbol{r}}$ depends on the spin system via an exchange coupling,

$$\hat{T}^{\sigma\sigma'}_{\boldsymbol{r}} = t_0 \, \delta_{\sigma\sigma'} + \sum_i t_1(\boldsymbol{r} - \boldsymbol{r}_i) \, \boldsymbol{\sigma}_{\sigma\sigma'} \cdot \hat{\boldsymbol{S}}_i. \tag{5.5}$$

Here, t_0 is the bare tunneling rate, while for the spin-dependent second term we follow Ref. [429] and assume the exponential form

$$t_1(\boldsymbol{r} - \boldsymbol{r}_i) = \Gamma_1 e^{-d/d_0} e^{-|\boldsymbol{r} - \boldsymbol{r}_i|/\lambda}, \tag{5.6}$$

with constants d_0, λ.

Within this setup, we focus on the tunneling conductance $\partial I/\partial V$ due to spin-dependent contributions. We provide a detailed derivation of $\partial I/\partial V$ in Sec. 5.1.2 below and briefly state the main result here. Defining the dynamical structure factor

$$\mathcal{S}_{ij}^{\alpha\alpha}(t) = \langle \hat{S}_i^{\alpha}(t)\hat{S}_j^{\alpha}(0)\rangle_S = \int d\omega\, e^{-i\omega t}\mathcal{S}_{ij}^{\alpha\alpha}(\omega), \tag{5.7}$$

Fermi's golden rule yields at zero-temperature [428, 429],

$$\frac{\partial I}{\partial V} = \frac{2e^2}{\hbar}\sum_{i,j,\alpha} t_1(\boldsymbol{r}-\boldsymbol{r}_i)t_1(\boldsymbol{r}-\boldsymbol{r}_j)\; c_{\alpha\beta}\int_0^{eV} d\omega\, \mathcal{S}_{ij}^{\alpha\beta}(\omega), \tag{5.8}$$

which contains a spin-weight function

$$c_{\alpha\beta} = \sum_{\sigma,\sigma'} n_\sigma(\varepsilon_F)N_{\sigma'}(\varepsilon_F)\sigma^{\alpha}_{\sigma'\sigma}\sigma^{\beta}_{\sigma\sigma'}. \tag{5.9}$$

Here, the σ^α are Pauli matrices and $n_\sigma(\varepsilon_F)/N_\sigma(\varepsilon_F)$ are the spin-dependent densities of states at the Fermi level for both tip/substrate. The intuition behind expression Eq. (5.8) is summarized in Fig. 5.1. Crucially, the prefactors $c_{\alpha\beta}$ depend on the *relative spin-polarization* of tip and substrate. This allows for a controlled selection of spin excitations that are to be probed [428, 429, 441]. We highlight three important settings considered in this work: *(1)* Non-polarized tip and substrate ($n_+ = n_-$ and $N_+ = N_-$): $c_{\alpha\beta} \sim \delta_{\alpha\beta}$ and independent of α. *(2)* Fully parallel-polarized tip and substrate ($n_- = N_- = 0$): $c_{\alpha\beta} \sim \delta_{\alpha,z}\delta_{\beta,z}$, where z was chosen as the common polarization axis. *(3)* Fully anti-polarized tip and substrate ($n_- = N_+ = 0$): $c_{\alpha\beta} \sim (1-\delta_{\alpha,z})(1-\delta_{\beta,z})$.

5.1.2 Derivation of conductance for scanning-tunneling-microscope

Before moving on to applying Eq. (5.8) to specific physical setups, here we provide some details on its derivation. The derivation presented in this section is essentially a mix of the derivations presented in Refs. [428, 429]. Let us describe the tripartite system laid out above in terms of the eigenstates $|\Psi\rangle := |n\rangle_S\,|\phi\rangle_t\,|\psi\rangle_s$ of its three unperturbed constituents with respective energies $E_\Psi = E_n^S + E_\phi^t + E_\psi^s$. The experimentally relevant tunneling current I between tip and substrate at inverse temperature β can then be obtained most directly by applying Fermi's golden rule,

$$\begin{aligned} I = \frac{2e}{\hbar}\sum_{\boldsymbol{p},\boldsymbol{k},\sigma,\sigma'}\sum_{\Psi,\tilde{\Psi}} e^{-\beta E_\psi}\Big\{ &\left|\langle\tilde{\Psi}|\,\hat{T}_{\boldsymbol{r}}^{\sigma\sigma'}\hat{a}_{\boldsymbol{p},\sigma}^\dagger\hat{b}_{\boldsymbol{k},\sigma'}\,|\Psi\rangle\right|^2\delta(E_{\tilde{\Psi}}-E_\Psi-eV) - \\ &- \left|\langle\tilde{\Psi}|\,(\hat{T}_{\boldsymbol{r}}^{\sigma\sigma'})^\dagger\hat{b}_{\boldsymbol{k},\sigma'}^\dagger\hat{a}_{\boldsymbol{p},\sigma}\,|\Psi\rangle\right|^2\delta(E_{\tilde{\Psi}}-E_\Psi+eV)\Big\}. \end{aligned} \tag{5.10}$$

Eq. (5.10) consists of two terms which we are going to treat seperately. The evaluation of the first matrix element can be decomposed into electron and spin sector via

$$e^{-\beta E_\Psi}\left|\langle\tilde{\Psi}|\,\hat{T}^{\sigma\sigma'}_{\boldsymbol{r}}\hat{a}^\dagger_{\boldsymbol{p},\sigma}\hat{b}_{\boldsymbol{k},\sigma'}\,|\Psi\rangle\right|^2 = e^{-\beta E^S_n}\left|\langle m|\hat{T}^{\sigma\sigma'}_{\boldsymbol{r}}|n\rangle\right|^2 e^{-\beta(E^t_\phi+E^s_\psi)}\left|\langle\tilde{\phi},\tilde{\psi}|\hat{a}^\dagger_{\boldsymbol{p},\sigma}\hat{b}_{\boldsymbol{k},\sigma'}|\phi,\psi\rangle\right|^2. \tag{5.11}$$

Furthermore, due to the non-interacting nature of the metallic tip and substrate, the on-shell condition becomes $\delta(E_{\tilde{\Psi}} - E_\Psi - eV) = \delta(E^S_m - E^S_n + \varepsilon_{\boldsymbol{p}} - \varepsilon_{\boldsymbol{k}} - eV)$. As this does not explicitly depend on $\tilde{\phi},\tilde{\psi},\phi,\psi$, we can carry out the corresponding summations in Eq. (5.10), i.e.

$$\begin{aligned}&\sum_{\phi,\psi}\sum_{\tilde{\phi},\tilde{\psi}} e^{-\beta(E^t_\phi+E^s_\psi)}\left|\langle\tilde{\phi},\tilde{\psi}|\hat{a}^\dagger_{\boldsymbol{p},\sigma}\hat{b}_{\boldsymbol{k},\sigma'}|\phi,\psi\rangle\right|^2 = \sum_{\phi,\psi} e^{-\beta(E^t_\phi+E^s_\psi)}\,\langle\phi,\psi|\hat{b}^\dagger_{\boldsymbol{k},\sigma'}\hat{b}_{\boldsymbol{k},\sigma'}\hat{a}_{\boldsymbol{p},\sigma}\hat{a}^\dagger_{\boldsymbol{p},\sigma}|\phi,\psi\rangle = \\ &= \langle\hat{b}^\dagger_{\boldsymbol{k},\sigma'}\hat{b}_{\boldsymbol{k},\sigma'}\rangle_\beta\,\langle\hat{a}_{\boldsymbol{p},\sigma}\hat{a}^\dagger_{\boldsymbol{p},\sigma}\rangle_\beta = f(\varepsilon_{\boldsymbol{k}})(1-f(\varepsilon_{\boldsymbol{p}})),\end{aligned} \tag{5.12}$$

where $f(\varepsilon)$ is the Fermi distribution function at a given inverse temperature. We then proceed by converting the momentum summations $\sum_{\boldsymbol{p},\sigma} \to \sum_\sigma \int d\varepsilon\ n_\sigma(\varepsilon)$, $\sum_{\boldsymbol{k},\sigma} \to \sum_\sigma \int d\varepsilon\ N_\sigma(\varepsilon)$ into integrals over the densities of states $n_\sigma(\varepsilon), N_\sigma(\varepsilon)$ of tip and substrate electrons. We further assume that only electrons near the Fermi level contribute to tunneling, thus setting the densities of states $n_\sigma(\varepsilon) \to n_\sigma(\varepsilon_F), N_\sigma(\varepsilon) \to N_\sigma(\varepsilon_F)$ constant. Inserting this and Eq. (5.12) into Eq. (5.10) we obtain for the first term:

$$\begin{aligned}&\sum_{\boldsymbol{p},\boldsymbol{k},\sigma,\sigma'}\sum_{\Psi,\tilde{\Psi}} e^{-\beta E_\psi}\left|\langle\tilde{\Psi}|\,\hat{T}^{\sigma\sigma'}_{\boldsymbol{r}}\hat{a}^\dagger_{\boldsymbol{p},\sigma}\hat{b}_{\boldsymbol{k},\sigma'}\,|\Psi\rangle\right|^2\,\delta(E_{\tilde{\Psi}} - E_\Psi - eV) = \\ &= \sum_{\sigma,\sigma'} n_\sigma(\varepsilon_F)N_{\sigma'}(\varepsilon_F)\sum_{n,m} e^{-\beta E^S_n}\left|\langle m|\hat{T}^{\sigma\sigma'}_{\boldsymbol{r}}|n\rangle\right|^2\times \\ &\qquad\qquad \times\int d\varepsilon\,d\varepsilon' f(\varepsilon')(1-f(\varepsilon))\,\delta(E^S_m - E^S_n + \varepsilon - \varepsilon' - eV) = \\ &= \sum_{\sigma,\sigma'} n_\sigma(\varepsilon_F)N_{\sigma'}(\varepsilon_F)\sum_{n,m} e^{-\beta E^S_n}\left|\langle m|\hat{T}^{\sigma\sigma'}_{\boldsymbol{r}}|n\rangle\right|^2\frac{eV-(E^S_m-E^S_n)}{1-e^{-\beta(eV-(E^S_m-E^S_n))}},\end{aligned} \tag{5.13}$$

where we carried out the integrals over $d\varepsilon, d\varepsilon'$ in the last step.

We now evaluate the remaining summations over the spin sector. Firstly, we find for the tunneling matrix element, concentrating exclusively on the contributions $\sim t_1^2$ due to spin fluctuations,

$$\left|\langle m|\hat{T}^{\sigma\sigma'}_{\boldsymbol{r}}|n\rangle\right|^2 = \sum_{\substack{i,j\\ \alpha,\beta}} t_1(\boldsymbol{r}-\boldsymbol{r}_i)\,t_1(\boldsymbol{r}-\boldsymbol{r}_j)\;\sigma^\alpha_{\sigma'\sigma}\sigma^\beta_{\sigma\sigma'}\,\langle n|\hat{S}^\alpha_i|m\rangle\,\langle m|\hat{S}^\beta_j|n\rangle\,. \tag{5.14}$$

We can then use the Lehmann representation of the Fourier transformed dynamical struc-

ture factor

$$\mathcal{S}_{ij}^{\alpha\beta}(\omega) = \int dt e^{i\omega t} \langle \hat{S}_i^{\alpha}(t) \hat{S}_j^{\beta}(0) \rangle = \sum_{n,m} e^{-\beta E_n^S} \langle n|\hat{S}_i^{\alpha}|m\rangle \langle m|\hat{S}_j^{\beta}|m\rangle \ \delta(\omega - (E_m^S - E_n^S)) \tag{5.15}$$

to realize that for an arbitrary function $F(\omega)$, the following relation holds:

$$\int d\omega \, \mathcal{S}_{ij}^{\alpha\beta}(\omega) \, F(\omega) = \sum_{n,m} e^{-\beta E_n^S} \langle n|\hat{S}_i^{\alpha}|m\rangle \langle m|\hat{S}_j^{\beta}|n\rangle \ F(E_m^S - E_n^S). \tag{5.16}$$

Using this relation upon inserting the matrix element Eq. (5.14) back into Eq. (5.13), we obtain for the first term of Eq. (5.10),

$$\begin{aligned}
&\sum_{\boldsymbol{p},\boldsymbol{k},\sigma,\sigma'} \sum_{\Psi,\tilde{\Psi}} e^{-\beta E_\psi} \left| \langle \tilde{\Psi}| \, \hat{T}_{\boldsymbol{r}}^{\sigma\sigma'} \hat{a}_{\boldsymbol{p},\sigma}^{\dagger} \hat{b}_{\boldsymbol{k},\sigma'} \, |\Psi\rangle \right|^2 \delta(E_{\tilde{\Psi}} - E_\Psi - eV) = \\
&= \sum_{i,j} \sum_{\alpha,\beta} t_1(\boldsymbol{r} - \boldsymbol{r}_i) t_1(\boldsymbol{r} - \boldsymbol{r}_j) \Big(\sum_{\sigma,\sigma'} n_\sigma(\varepsilon_F) N_{\sigma'}(\varepsilon_F) \sigma_{\sigma'\sigma}^{\alpha} \sigma_{\sigma\sigma'}^{\beta} \Big) \int d\omega \ \frac{eV - \omega}{1 - e^{-\beta(eV-\omega)}} \ \mathcal{S}_{ij}^{\alpha\beta}(\omega) \\
&\to \sum_{i,j} \sum_{\alpha} t_1(\boldsymbol{r} - \boldsymbol{r}_i) t_1(\boldsymbol{r} - \boldsymbol{r}_j) \, c_{\alpha\beta} \int d\omega \ \frac{eV - \omega}{1 - e^{-\beta(eV-\omega)}} \ \mathcal{S}_{ij}^{\alpha\alpha}(\omega),
\end{aligned} \tag{5.17}$$

where in the last step we identified the weight function $c_{\alpha\beta}$ of Eq. (5.9).

Repeating the same steps for the second term of the Fermi golden rule expression, we eventually arrive at the final expression for the current

$$I = \frac{2e}{\hbar} \sum_{i,j,\alpha} t_1(\boldsymbol{r} - \boldsymbol{r}_i) t_1(\boldsymbol{r} - \boldsymbol{r}_j) \, c_\alpha \int d\omega \, j_V(\omega) \, \mathcal{S}_{ij}^{\alpha\alpha}(\omega), \tag{5.18}$$

Eq. (5.18) contains the frequency weight function

$$j_V(\omega) = \frac{eV - \omega}{1 - e^{-\beta(eV-\omega)}} + \frac{eV + \omega}{1 - e^{\beta(eV+\omega)}}, \tag{5.19}$$

which reduces to $j_V(\omega) = (eV - \omega) \, \theta(eV - \omega)$ at zero temperature. Derivation of Eq. (5.18) with respect to V yields Eq. (5.8).

5.2 Topological magnon insulators

As a first example, we apply Eq. (5.8) to topological magnon edge states appearing in TMI-layers. For concreteness, we consider the well known example of a 2D Kagome fer-

romagnet featuring non-zero Dzyaloshinskii-Moriya (DM) interactions [442–444]:

$$\hat{H} = \sum_{\langle nm \rangle} -J\, \boldsymbol{S}_n \cdot \boldsymbol{S}_m + \boldsymbol{D}_{nm} \cdot (\boldsymbol{S}_n \times \boldsymbol{S}_m) - \boldsymbol{h} \cdot \sum_n \boldsymbol{S}_n, \tag{5.20}$$

where $\boldsymbol{D}_{nm}$ is the DM interaction on the bond nm, and $\boldsymbol{h}$ is an external magnetic field along $\hat{\boldsymbol{z}}||[111]$. Following Ref. [443], Eq. (5.20) can be brought into quadratic spin wave form by applying a standard Holstein-Primakoff approximation, leading to

$$\hat{H} = \sum_{\langle nm \rangle} b_n^\dagger H_{nm} b_m + \sum_n H_{nn} b_n^\dagger b_n + E_0. \tag{5.21}$$

Here, $H_{nm} = -S(J + iD)$ along all bonds oriented counter-clockwise within each elementary triangle and $H_{mn} = -S(J - iD)$ accordingly. The diagonal part is given by $H_{nn} = hS + JSM_n$, with M_n the number of nearest neighbors of site n, see Fig. 5.2 (a).

On a strip-geometry with periodic boundaries in the x-direction, see Fig. 5.2 (a), $\hat{H}$ can be block-diagonalized with respect to the k_x-momentum quantum number. We obtain

$$\hat{H} = \sum_{k_x} \sum_{l,l'} b_l^\dagger(k_x) \tilde{H}_{ll'}(k_x) b_{l'}(k_x) = \sum_{k_x} \sum_l \varepsilon_l(k_x)\, \tilde{b}_l^\dagger(k_x) \tilde{b}_l(k_x), \tag{5.22}$$

where $l \in \{0, ..., 6W\}$ ($W \in \mathbb{N}$) labels the sites within the unit cell as depicted in Fig. 5.2 (a), and the eigenmodes

$$\tilde{b}_l(k_x) = \sum_{l'} U_{l,l'}(k_x) b_{l'}(k_x) \tag{5.23}$$

can be evaluated numerically for finite W. The spectrum $\varepsilon_l(k_x)$ is shown in Fig. 5.2 (c) and displays edge modes within the bulk gaps between bands with non-zero Chern numbers [442].

In this geometry, we can express the spin operators through their one-dimensional Fourier transform, $S_n^\alpha(t) = \frac{1}{\sqrt{L_x}} \sum_{k_x} e^{ik_x x_n} S_{l_n}^\alpha(k_x, t)$, where x_n is the x-position of the Kagome-site n and l_n is its position within the unit cell. Similarly, the local dynamical structure factor can be expressed via a one-dimensional Fourier transform $\mathcal{S}_{nm}^{\alpha\beta}(\omega) = \sum_{k_x} e^{ik_x(x_n - x_m)} \mathcal{S}_{l_n l_m}^{\alpha\beta}(k_x, \omega)$. Insertion into the expression Eq. (5.8) for the conductance and using that $\sum_n \to \sum_{x_n, l_n}$ yields

$$\frac{\partial I}{\partial V} = \frac{2e^2}{\hbar} n(\varepsilon_F) N(\varepsilon_F) \times \sum_{l_n, l_m, k_x, \alpha} g_{l_n\, l_m}(k_x, \boldsymbol{r})\, c_{\alpha\beta} \int_0^{eV} d\omega\, \mathcal{S}_{l_n l_m}^{\alpha\beta}(k_x, \omega), \tag{5.24}$$

with

$$g_{l_n l_m}(k_x, \boldsymbol{r}) = \Big(\sum_{x_n} e^{ik_x x_n} t_1(\boldsymbol{r} - \boldsymbol{r}_n) \Big) \times \Big(\sum_{x_n} e^{-ik_x x_m} t_1(\boldsymbol{r} - \boldsymbol{r}_m) \Big). \tag{5.25}$$

The structure factor entering the differential conductance Eq. (5.24) can be determined

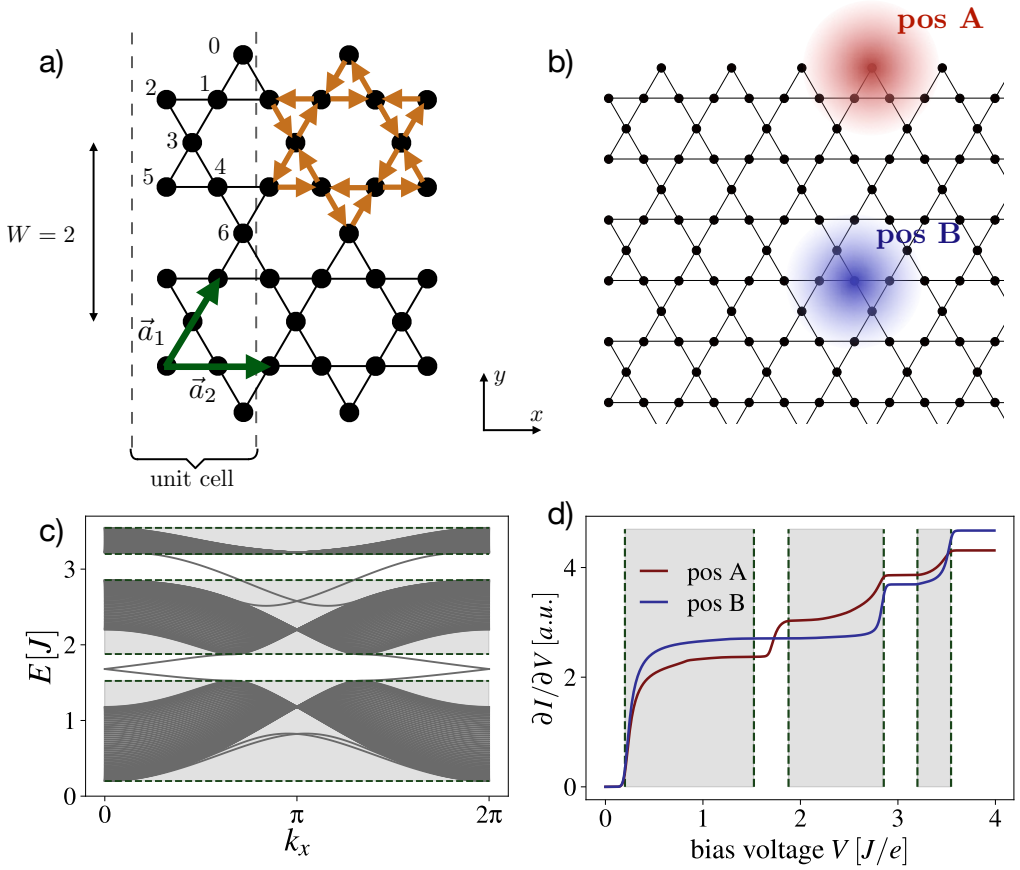

Figure 5.2: Topological Magnon Insulator. a) Geometry of the Kagome TMI setup. We consider open boundaries in y-direction, implying translational invariance only along the $\boldsymbol{a}_2$ lattice vector. The number of sites within a unit cell is $6W + 1$; the position of a site n is specified by (x_n, l_n), with x_n labelling the unit cell and $l_n \in \{0, ..., 6W\}$ labelling the site within a unit cell as depicted here. **b)** The STM tip is placed at the edge (pos A) or over the 2D bulk (pos B) of the Kagome layer, with color gradients indicating the range of the response. For numerical evaluations, a unit cell of $L_y = 181$ sites along the y-direction is used. Inset: lattice vectors (green) and directions of the DM interaction (orange). **c)** Energy spectrum for the magnon Hamiltonian with $J = 1.0$ and DM-term $D = 0.2$, containing edge states within the gaps of the three bulk bands. **d)** Conductance $\partial I/\partial V$ using Eq. (5.8). While the response at tip position B exhibits a flat conductance throughout all band gaps, at the edge (pos A) a finite response within the first gap is acquired, yielding a clear signature for the existence of topological edge magnons.

simply from its Lehmann representation at finite temperatures. Focusing on the $T = 0$ limit and on the spin-diagonal components of the structure factor, we obtain $\mathcal{S}^{zz}_{l_m l_n}(k_x, \omega) \sim \delta(\omega)$ and $\mathcal{S}^{yy}_{l_m l_n}(k_x, \omega) = \mathcal{S}^{xx}_{l_m l_n}(k_x, \omega)$ with

$$\mathcal{S}^{xx}_{l_m l_n}(k_x, \omega) = \sum_s U_{l_m, s}(k_x) U^*_{l_n, s}(k_x)\, \delta(\omega - \varepsilon_s(k_x)). \tag{5.26}$$

Eq. (5.26) makes the coupling of the structure factor to the local density of the eigenmodes manifest.

Furthermore, it is instructive to approximate the device function of Eq. (5.25) by turning

the sum into an integral and inserting the form of $t_1(\boldsymbol{r}-\boldsymbol{r}_n)$ from Eq. (5.6) to obtain

$$\sum_{x_n} e^{ik_x x_n} t_1(\boldsymbol{r}-\boldsymbol{r}_n) \approx \int dx_n\, e^{ik_x x_n} t_1(\boldsymbol{r}-\boldsymbol{r}_n) = \Gamma_1\, e^{-d/d_0} \int dx_n\, e^{ik_x x_n} e^{-|\boldsymbol{r}-\boldsymbol{r}_n|/\lambda} =$$
$$= 2\Gamma_1\, e^{-d/d_0} e^{ik_x x} \frac{|y-y_n|}{\sqrt{1+\lambda^2 k_x^2}} \times K_1\left(\frac{|y-y_n|}{\lambda}\sqrt{1+\lambda^2 k_x^2}\right), \tag{5.27}$$

where $K_1(\cdot)$ is a modified Bessel function of the second kind and all lengths are measured in units of the lattice spacing. $K_1(x)$ drops off exponentially for large arguments and diverges as $K_1(x) \sim 1/x$ for $x \to 0$, as would be relevant for e.g. the case $y = y_n$. We therefore see that the response acquired through the device function $g_{l_n l_m}(k_x, \boldsymbol{r})$ will only pick up sizeable contributions from momenta $k_x \lesssim 1/\lambda$. Importantly, the edge state in between the first and second energy band as displayed in Fig. 5.2 (c) of the main text is located directly at $k_x = 0$ and should therefore be able to contribute to the response as measured by the local conductance. The presence of a $k_x = 0$ edge state arises also for boundaries shaped differently than in Fig. 5.2 (a), see e.g. Ref [443]. We choose $\lambda = 1.0$ (units lattice spacing) in the following. Accordingly, $\partial I/\partial V$, evaluated for an *unpolarized* tip on the boundary of a system containing 181 sites along the y-direction, shows a finite response from topological magnon edge modes within the first band gap, see Fig. 5.2 (d).

5.3 **Kitaev spin liquid**

We proceed to characterize our main example, the extended Kitaev honeycomb model,

$$\hat{H} = \sum_{\langle ij\rangle_\alpha} J_\alpha\, \hat{\sigma}_i^\alpha \hat{\sigma}_j^\alpha + K \sum_{\langle ij\rangle_\alpha, \langle jk\rangle_\gamma} \hat{\sigma}_i^\alpha \hat{\sigma}_j^\beta \hat{\sigma}_k^\gamma, \tag{5.28}$$

where $\langle i,j\rangle_\alpha$ denotes nearest neighbors, with $\alpha \in \{x,y,z\}$ labelling the three inequivalent bond types, see Fig. 5.3 for a schematic picture of the setup. Following Ref. [241], the model can be solved by representing the spin operators $\hat{\sigma}_i^\alpha = i\hat{b}_i^\alpha \hat{c}_i$ in terms of four different Majorana species, resulting in

$$\hat{H} = i \sum_{\langle ij\rangle_\alpha} J_\alpha\, \hat{u}_{\langle ij\rangle_\alpha}\, \hat{c}_i \hat{c}_j + iK \sum_{\langle ij\rangle_\alpha, \langle jk\rangle_\gamma} \hat{u}_{\langle ij\rangle_\alpha} \hat{u}_{\langle jk\rangle_\gamma} \hat{c}_i \hat{c}_k. \tag{5.29}$$

Here, the $\hat{u}_{\langle ij\rangle_\alpha} = i\hat{b}_i^\alpha \hat{b}_j^\alpha$ are constants of motion with eigenvalues $u_{\langle ij\rangle_\alpha} = \pm 1$. This property renders the model of Eq. (5.29) exactly solvable. We further note that there exists a local $\mathbb{Z}_2$ gauge structure in the model since Eq. (5.29) is invariant under

$$\begin{aligned} \hat{c}_i &\to w_i\, \hat{c}_i \\ \hat{u}_{\langle ij\rangle_\alpha} &\to w_i\, \hat{u}_{\langle ij\rangle_\alpha}\, w_j, \end{aligned} \tag{5.30}$$

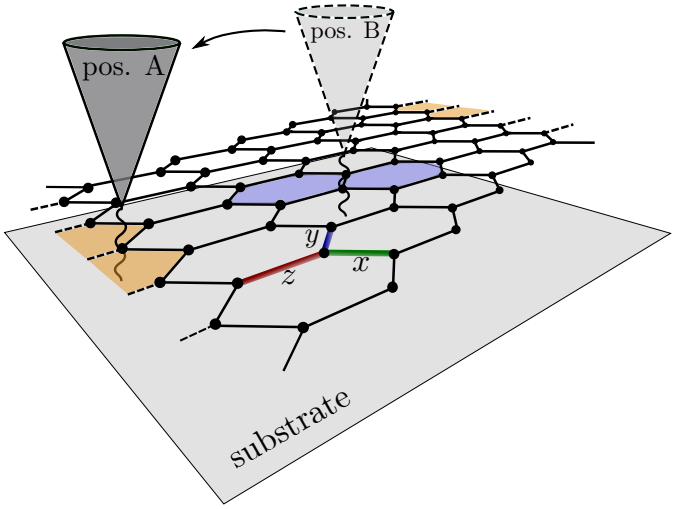

Figure 5.3: STM setup. Geometry of the STM setup and sketch of the Kitaev model Eq. (5.28). OBCs are introduced by setting the strength of the dashed bonds to $J_b \to 0$. Probing the local spin noise in the bulk requires the creation of a gapped flux-pair (blue). Moving to the boundary, these fluxes are gapless (orange), allowing for the detection of gapless Majorana edge modes.

for arbitrary $w_i \in \{\pm 1\}$[1]. It is then straightforward to verify that the plaquette Wilson loops

$$\hat{W}_p = \prod_{\langle ij\rangle \in p} \hat{u}_{\langle ij\rangle_\alpha} \tag{5.31}$$

are gauge invariant quantities under Eq. (5.30), where the product extends over the edges of an elementary hexagonal plaquette. The fluxes $\hat{W}_p \in \{\pm 1\}$, together with two additional non-local Wilson loops responsible for the topological ground state degeneracy on a torus thus label the gauge sector of the theory. Within a fixed sector of $u_{\langle ij\rangle_\alpha}$'s, Eq. (5.29) reduces to a Majorana hopping problem.

A convenient description of the model Eq. (5.29) is obtained by pairing the Majoranas into complex *matter* fermions

$$\hat{f}_{\boldsymbol{r}} = \frac{1}{2}(\hat{c}_{A\boldsymbol{r}} + i\,\hat{c}_{B\boldsymbol{r}}) \tag{5.32}$$

in each unit cell, and *gauge* fermions

$$\hat{\chi}_{\langle ij\rangle_\alpha} = \frac{1}{2}(\hat{b}^\alpha_i + i\,\hat{b}^\alpha_j) \tag{5.33}$$

on the bonds, $i \in A$, $j \in B$. Then, the

$$\hat{u}_{\langle ij\rangle_\alpha} = 2\hat{\chi}^\dagger_{\langle ij\rangle_\alpha}\hat{\chi}_{\langle ij\rangle_\alpha} - 1 \tag{5.34}$$

[1]We note that the $\mathbb{Z}_2$ structure becomes apparent due to the decomposition into real Majorana fermions. This is in contrast with a decomposition into complex auxilliary fermions with subsequent mean field approximation, for which one initially obtains a larger $SU(2)$ gauge structure, which may be broken down to $\mathbb{Z}_2$ upon further inspection [445].

can be expressed in terms of the gauge fermions, and the ground state is written as $|0\rangle = |M_0\rangle \otimes |F_0\rangle$, with $|M_0\rangle$ the ground state of the matter fermion problem defined by Eq. (5.29) within the flux-free gauge sector $|F_0\rangle$, for which $W_p = +1$ for all plaquettes. We can choose $u_{\langle ij\rangle_b} = +1$ to obtain this flux-free state.

To obtain OBCs, we choose a line of 'weak bonds' around the torus (z-bonds w.l.o.g.) whose strength $J_b \to 0$ vanishes. This results in a degeneracy throughout the many-body spectrum, as the insertion of flux pairs adjacent to bonds $\langle ij\rangle_b$ across the boundary comes without energy cost. A general ground state for OBCs can then be written as

$$|0\rangle = |M_0\rangle \otimes |F\rangle = |M_0\rangle \otimes |F_0\rangle_{bulk} \otimes |F\rangle_b \,, \tag{5.35}$$

where $|F_0\rangle_{bulk}$ is the flux-free sector of all bulk plaquettes and $|F\rangle_b$ is a general superposition of 2^{L-1} different boundary flux sectors for a boundary of length L. We will postpone a proof of this last result to Sec. 5.4 and proceed for now.

In order to determine the conductance through Eq. (5.8), we have to compute the dynamical structure factor $\mathcal{S}_{ij}^{\alpha\beta}(t) = \langle 0|\hat{\sigma}_i^\alpha(t)\hat{\sigma}_j^\beta(0)|0\rangle$ from a given ground state of Eq. (5.35). Following Refs. [446–448], the problem can be reduced to a Majorana quantum quench in the matter sector,

$$\mathcal{S}_{ij}^{\alpha\beta}(t) = \langle M_0|e^{it\hat{H}}\hat{c}_i e^{-it(\hat{H}+\hat{V}_{\langle il\rangle_\alpha})}\hat{c}_j|M_0\rangle \times \langle F|\,(\hat{\chi}_{\langle il\rangle_\alpha} + \hat{\chi}^\dagger_{\langle il\rangle_\alpha})(\hat{\chi}_{\langle jk\rangle_\beta} + \hat{\chi}^\dagger_{\langle jk\rangle_\beta})\,|F\rangle \,. \tag{5.36}$$

Here, we chose both i, j on sublattice A, and $\hat{V}_{\langle il\rangle_\alpha}$ is the modification of the Majorana model due to flux insertion $u_{\langle il\rangle_\alpha} \to -u_{\langle il\rangle_\alpha}$. For bonds $\langle jk\rangle_\beta$ adjacent to bulk plaquettes, the gauge sector of Eq. (5.36) reduces to $\mathcal{S}_{ij}^{\alpha\beta} \sim \delta_{\alpha\beta}\,\delta_{ij}$, i.e. the structure factor is ultra-local in the bulk due to the static nature of the gauge field [449]. In contrast, bonds $\langle jk\rangle_\beta = \langle jk\rangle_b$ across the boundary can acquire longer-range contributions $\mathcal{S}_{ij}^{\alpha\beta} \nsim \delta_{ij}$ due to the superposition $|F\rangle_b$ of boundary fluxes. Nevertheless, while Eq. (5.36) thus generally depends on the choice of $|F\rangle_b$, the on-site contributions $\mathcal{S}_{ii}^{\alpha\alpha}(t)$ are independent of the chosen state $|0\rangle$; we show this property in Sec. 5.4. Since these contributions dominate the STM response according to Eq. (5.8), any choice of $|0\rangle$ will lead to a qualitatively representative conductance $\partial I/\partial V$. We choose $|F\rangle_b = |F_0\rangle_b$ as flux-free in the following and numerically evaluate Eq. (5.36) using a Pfaffian approach [447]. In practice, we introduce a small but finite bond-strength $J_b \ll 1$ across the boundary, which provides additional physical insight on the emergence of a Majorana zero mode for $J_b = 0$.

Our main results are summarized in Fig. 5.4: In panel (a) we show the integrated density of states (DOS) for the matter fermions for $J = 1$, $K = 0.2$ in a background containing a flux pair adjacent to a weak bond $\langle ij\rangle_b$ across the boundary. For $J_b = 1$ we recover the result for periodic boundaries (PBCs) with an exponentially localized fermion bound state at the flux pair, with an energy $E = \Delta_F + E_1^F = 1.156J$ (grey dashed line), located in the

gap below the onset of a continuum band at $E = \Delta_F + E_2^F = 2.819J$. Here, $\Delta_F = 0.819J$ is the two-flux gap in the bulk and $E_{1/2}^F$ the first/second eigenstate of the matter model. As we decrease J_b, Fig. 5.4b shows how the bound state delocalizes along the boundary, eventually turning into a zero mode. This is reflected in the DOS by an emerging continuum of in-gap states (dashed blue lines in panel a), corresponding to a dispersive chiral Majorana edge mode, as well as a vanishing flux gap.

Crucially, these spectral properties of Majorana-flux bound states and the chiral Majorana edge modes are directly reflected in the local structure factor, displayed in Fig. 5.4 (c) and evaluated for $J_b = 0.01J$: $\mathcal{S}^{\alpha\alpha}_{i_B i_B}(\omega)$ at site i_B in the bulk (see Fig. 5.3) reflects the spectrum of PBCs via a sole, sharp contribution at the bound state energy and a broad continuum at higher frequencies. Note, similar signatures for the Majorana-flux bound state have been very recently predicted for planar tunneling spectroscopy [349]. In contrast, the component $\mathcal{S}^{zz}_{i_A i_A}(\omega)$ (blue) at a boundary site i_A contains no sharp contribution and instead exhibits a spectral response throughout the former excitation gap. This demonstrates that the structure factor couples directly to the gapless Majorana edge mode. The component $\mathcal{S}^{xx}_{i_A i_A}(\omega)$ involves the insertion of a gauge fermion at a bond adjacent to the system boundary, which results in the creation of a flux pair composed of one bulk and one boundary flux (one blue and one orange plaquette in Fig. 5.3). This induces a sharp onset of $\mathcal{S}^{xx}_{i_A i_A}(\omega)$ at a reduced flux gap $\Delta_F = 0.499J$, above which dispersive edge modes give a finite in-gap response.

The conductance derived from these results, see Fig. 5.4 (d), is evaluated via Eq. (5.8) for a small $\lambda = 0.1$ (units lattice constant), essentially focusing on the on-site response. For tip position B, the polarizations entering $c_{\alpha\beta}$ do not have qualitative effects due to symmetry of the bulk structure factor. The resulting conductance features a sharp step at the bound state energy. At the boundary (position A), the conductance varies drastically with changing $c_{\alpha\beta}$: An anti-polarized tip captures the features of $\mathcal{S}^{xx}_{i_A i_A}(\omega) = \mathcal{S}^{yy}_{i_A i_A}(\omega)$ through a sharp step for a bias voltage matching the reduced flux gap, followed by smaller steps due to edge states. These smaller steps merge into a continuum in the thermodynamic limit. Note, contrasting the response of the bulk and edge modes even enables the measurement of single flux and nearest-neighbor flux-pair energies. The latter has a value less than twice the single flux energy because of Majorana induced interactions. Finally, for a parallel-polarized setting, where $c_{\alpha\beta}$ exclusively picks up the $\mathcal{S}^{zz}_{i_A i_A}(\omega)$-component, the flux excitation has no effect, resulting in an approximately linear increase of $\partial I/\partial V$ throughout the bulk-gap, in particular also at zero bias, providing a clear signature of the chiral Majorana edge modes. We emphasize that the term 'Majorana edge mode' refers to fractionalized excitations that can be described effectively in the language of Majorana fermions, as is e.g. also the case in certain spin chains [450, 451].

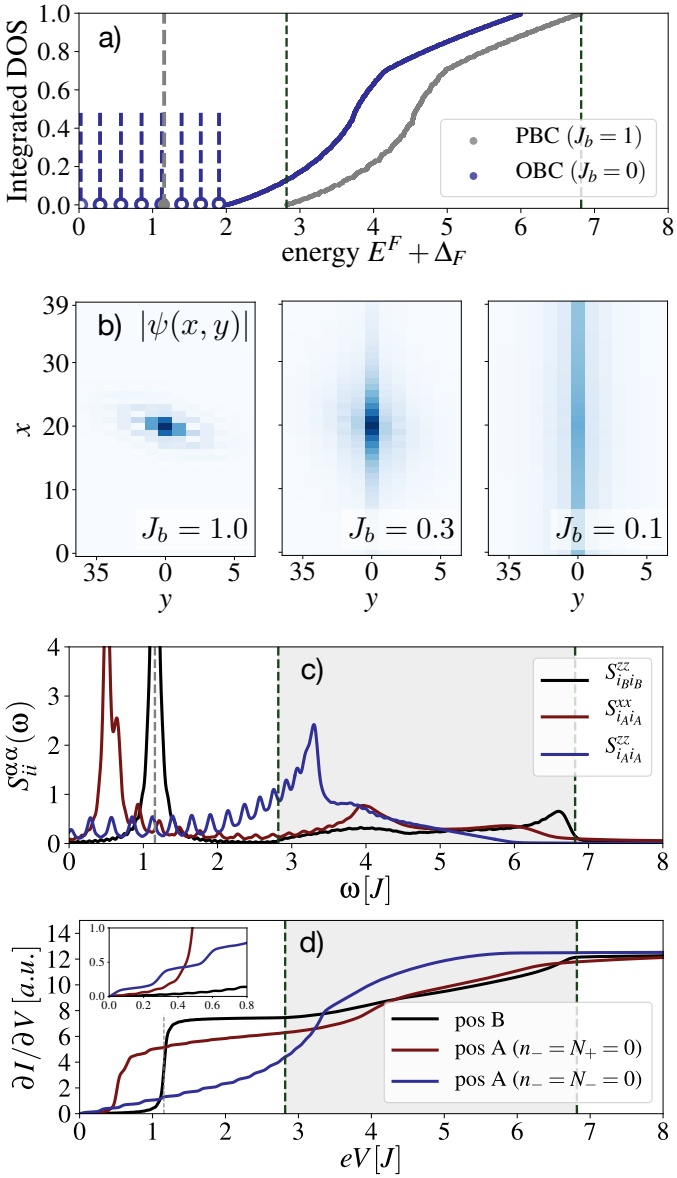

Figure 5.4: Kitaev spin liquid: Numerical results. a) Integrated DOS for the fermionic spectrum in the presence of a boundary flux-pair, both for PBCs ($J_b = 1$, gray) and OBCs ($J_b = 0$, blue). The gray-shaded area marks the gapped continuum band in the bulk, the dashed gray line the energy of the bound state. The blue circles with attached dashed lines show the energies of the in-gap edge modes at the given system size of 56×56 unit cells. For OBCs, the continuum band is shifted to lower energies due to the vanishing flux gap. **b)** The wave function $\psi(x, y)$ of the fermionic bound state on 40×40 unit cells delocalizes upon reducing the coupling J_b across the boundary (located at $y = 0$). **c)** Components of the *local* dynamical structure factor for 56×56 unit cells on OBCs; i_A and i_B mark lattice sites on the boundary and in the bulk, respectively, see Fig. 5.3. A finite frequency broadening was introduced for the sharp delta-response from the bound state. **d)** Conductance for the tip at positions A and B, and different polarizations of tip and substrate. In the bulk, the fermion bound state creates a sharp step within the gap. On the boundary, the step is replaced by a continuum due to the dispersive edge modes, starting from zero bias, see Inset.

5.4 The Kitaev honeycomb model with open boundaries

Before closing this chapter, we return to the subtleties that arise when combining the extended Kitaev Honeycomb model with open boundary conditions, particularly with

regards to its ground state degeneracy, which we have already hinted at in Sec 5.3. We discuss in detail how the boundary conditions impact the computation of the dynamical structure factor.

5.4.1 Physical Hilbert space

The decomposition of a spin-1/2 into four Majoranas introduced by Kitaev enlarges the Hilbert space. The projection back onto the physical Hilbert space is obtained by requiring that $\hat{D}_i = -i\hat{\sigma}_i^x\hat{\sigma}_i^y\hat{\sigma}_i^z = \hat{b}_i^x\hat{b}_i^y\hat{b}_i^z\hat{c}_i = 1$ for all sites. This condition can be enforced in terms of the bond and matter fermions via the projection operator

$$\hat{P} = \prod_i \frac{1+\hat{D}_i}{2} \sim \frac{1}{2}\left[1+(-1)^{N_f+N_\chi}\right], \tag{5.37}$$

where N_f/N_χ are the total number of matter/bond fermions. Eq. (5.37) demonstrates that only states with even total fermion number parity lie within the physical spin Hilbert space. As was shown in Refs. [452, 453], particular care needs to be taken within the gapless phase of the pure Kitaev model when projecting back to the physical Hilbert space.

5.4.2 Open boundaries

As outlined previously, open boundary conditions can be obtained by introducing a line of 'weak bonds' as shown in Fig. 5.5, where all terms in the Hamiltonian Eq. (5.28) of the main text involving such bonds are multiplied by a factor $J_b < 1$. The case of open boundaries is then retrieved for $J_b = 0$, which effectively cuts the system in half. For the practical evaluation of structure factors, we choose the value of the weak bonds very small, $J_b \ll 1$, but finite. This allows us to directly use the numerical method derived for periodic boundaries [447, 448]. In practice, we work on a cylindrical geometry, and neglect a non-local ground state degeneracy due to invariant Wilson loops winding around the cylinder, which does not affect our local probe results.

However, we emphasize that one has to be careful when taking the limit $J_b \to 0$. We discuss in the following how this limit impacts both the ground state structure as well as the dynamical spin correlations.

Ground state degeneracy: Gauge sector

As discussed above, the ground state of the translationally invariant system $J_b = 1$ is unique and lies in the sector of zero flux. This property remains true for any non-zero $J_b > 0$, for which the minimal flux gap is of order $\sim (J_b \cdot J)$, a property we have verified numerically on finite size systems. However, for $J_b = 0$ exactly, plaquette fluxes adjacent to the weak bonds can be inserted at the newly formed system boundary without energy cost. Formally, if we let $\langle ij\rangle_b$ denote one of the weak bonds as shown in Fig. 5.5, this

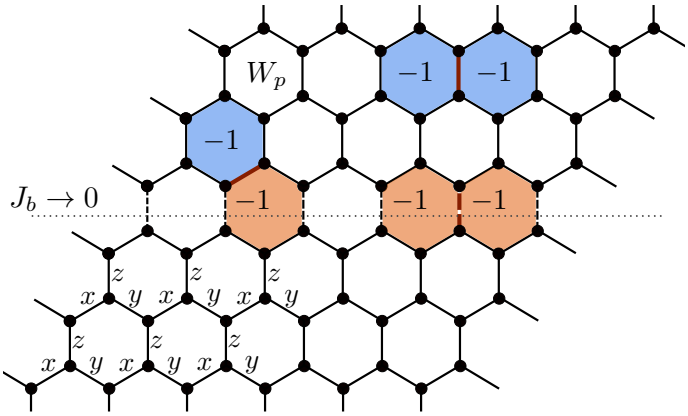

Figure 5.5: Kitaev model. The three types of bonds are labelled according to the anisotropic exchange interaction of the Hamiltonian Eq. (4) of the main text. The interactions along a line of z-bonds through the system are weakened by a factor $J_b < 1$, yielding open boundary conditions for $J_b = 0$. Inserting bond fermions (red bonds) flips the flux W_p of the two adjacent plaquettes. In the bulk, these flux excitations are gapped (blue plaquettes), while boundary plaquettes cost no energy and lead to degeneracies in the spectrum (orange plaquettes).

can be expressed via $[\hat{\chi}_{\langle ij\rangle_b}, \hat{H}] = 0$. We notice however that in order to obtain a valid transformation within the physical Hilbert space that respects the parity selection rule of Eq. (5.37), we need to create/annihilate an *even* number of boundary gauge fermions, starting from the original flux-free ground state. The set of transformations that relate different ground states is thus given by

$$u_{\langle ij\rangle_b} \to -u_{\langle ij\rangle_b}, \quad u_{\langle kl\rangle_b} \to -u_{\langle kl\rangle_b}, \tag{5.38}$$

for an arbitrary pair of boundary bonds $\langle ij\rangle_b$,$\langle kl\rangle_b$. From this we can infer the total ground state degeneracy D_f due to boundary fluxes for a system of linear length L along the open boundary to be

$$D = \binom{L}{0} + \binom{L}{2} + \binom{L}{4} + \ldots = 2^{L-1}. \tag{5.39}$$

We have observed this degeneracy due to boundary fluxes using exact diagonalization methods for the original spin Hamiltonian Eq. (5.28) on small system sizes. We notice further that this degeneracy applies to *all* eigenenergies throughout the entire many body spectrum.

We can now write down the form of a general state within this degenerate manifold. The gauge sector will then be flux-free in the bulk and consist of a general superposition of fluxes on the boundary, leading to Eq. (5.35) of the main text,

$$|0\rangle = |M_0\rangle \otimes |F_0\rangle_{bulk} \otimes |F\rangle_b \,, \tag{5.40}$$

with $|F\rangle_b$ a linear superposition of different boundary flux configurations.

Ground state degeneracy: Matter sector

As demonstrated in Kitaev's original work [241], the energy bands of the matter fermions carry non-trivial Chern number for non-zero K, which implies the existence of chiral edge states within the bulk gap and a zero energy edge mode on open boundary conditions. An example was given directly in the Appendix of [241]. We notice that on finite systems, the mode with zero energy might not be directly visible, as the exact momentum hosting it might not be part of the reciprocal lattice. However, in the thermodynamic limit we are guaranteed the existence of $|\tilde{M}_0\rangle = \hat{a}_0^\dagger |M_0\rangle$ with $E(\tilde{M}_0) = E(M_0)$.

Since $|\tilde{M}_0\rangle$ contains a matter fermion, we are now required to add an odd number of gauge fermions to obtain a physical state. In order to remain in a ground state, we add an odd number of *boundary* gauge fermions, for which there are in turn again

$$\tilde{D} = \binom{L}{1} + \binom{L}{3} + \binom{L}{5} + ... = 2^{L-1} \tag{5.41}$$

different possibilities. A general ground state within this matter sector is then given as

$$|\tilde{0}\rangle = |\tilde{M}_0\rangle \otimes |F_0\rangle_{bulk} \otimes |\tilde{F}\rangle\,, \tag{5.42}$$

with $|\tilde{F}\rangle$ a superposition of $\tilde{D}$ boundary flux sectors.

Taken together both matter and gauge sources of degeneracy, we obtain the total ground state degeneracy to be 2^L-fold.

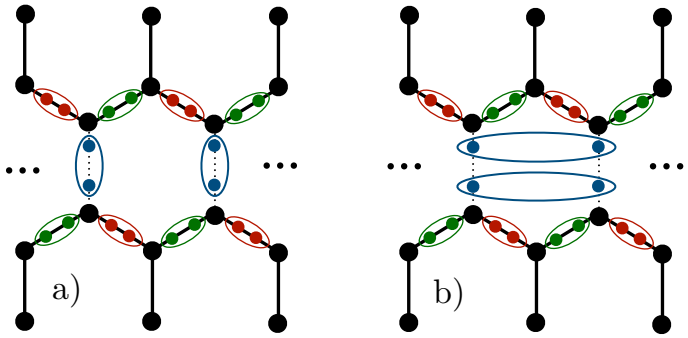

Figure 5.6: Majorana pairings: The Majorana fermions $\hat{b}_i^\alpha$ (colored according to α) are paired up to form the the gauge fermions $\hat{\chi}_{ij}$ living on bonds (i,j), whose occupation numbers commute with the Hamiltonian. If we introduce open boundaries by setting the exchange $J_b = 0$ on the line of vertical bonds shown here (dotted bonds), there arises an *ambiguity* in how to pair up the resulting 'dangling' Majoranas (shown in blue). **a)** The original pairing along the former bond is still valid, and produces the usual ultra-local expression for the spin structure factor. **b)** The Marojanas can now also be paired up in longer-range bonds (i,j), and the resulting fermion occupation numbers still commute with the Hamiltonian, allowing for longer-range contributions to the structure factor. The different pairings are related by a basis change within the degenerate ground state manifold.

Open boundaries: Structure factor

After this detailed discussion of the open boundary limit $J_b = 0$ in terms of ground state degeneracies, we wish to know how these results merge with our numerical approach of setting $J_b \ll 1$ but finite. In particular we would like to discuss how the dynamical structure factor differs between the unique ground state for $J_b > 0$ and a general ground state for $J_b = 0$ which is a superposition of 2^L different states from a degenerate manifold. Remarkably, while in general differences between the two cases do occur, the dominant on-site contribution relevant for the STM response will turn out to be independent of the chosen ground state, such that the limit $J_b \to 0$ is indeed continuous for the on-site spin correlations.

Let us take the system to be in one of the ground states $|0\rangle$ from Eq. (5.40) and consider two sites $i, j \in A$ which are *both* located on the boundary. We assume further, that the weak bonds that were removed in order to obtain open boundaries are z-bonds. We then compute the corresponding structure factor, using Eq. (5.36) of the main text and the fact that $[\hat{\chi}_{\langle il\rangle_b}, \hat{H}] = 0$ for boundary bonds,

$$\mathcal{S}^{zz}_{ij} = \langle M_0|e^{it\hat{H}}\hat{c}_i e^{-it\hat{H}}\hat{c}_j|M_0\rangle \times {}_b\Big\langle F\Big|(\hat{\chi}_{\langle il\rangle_b} + \hat{\chi}^\dagger_{\langle il\rangle_b})(\hat{\chi}_{\langle jk\rangle_b} + \hat{\chi}^\dagger_{\langle jk\rangle_b})\Big|F\Big\rangle_b. \tag{5.43}$$

Here, we have used that the bulk gauge sector remains unchanged, ${}_{bulk}\langle F_0|F_0\rangle_{bulk} = 1$. Because the boundary gauge sector $|F\rangle_b$ is now a general superposition, the expression Eq. (5.43) does *not* reduce to an on-site contribution $\sim \delta_{ij}$ like in the periodic case [446, 449].

An alternative way to see that there are indeed non-vanishing longer-range contributions beyond nearest neighbors to the structure factor for $J_b = 0$ comes from 'rewiring' the $\hat{b}^z_i$ - Majoranas on the boundary. As illustrated in Fig. 5.6, we can pair up the $\hat{b}^z_i$ in an arbitrary way to form new gauge fermions $\hat{\chi}_{(ij)_b}$, where $(ij)_b$ need not be lattice nearest neighbors. These new bond fermions still commute with the Hamiltonian and provide equally valid labellings of the model's gauge sector. Within this pairing, the new 'nearest neighbors' can clearly provide non-vanishing spin correlations in full analogy to the previous nearest neighbor contributions derived in Ref [446]. Thus, the rewiring of boundary Majoranas is equivalent to a basis change in the Fock space spanned by the occupation numbers $\hat{\chi}^\dagger_{\langle ij\rangle_b}\hat{\chi}_{\langle ij\rangle_b}$.

While the spin correlations for off-diagonal site pairs $i \neq j$ are thus clearly dependent on the chosen ground state out of the degenerate manifold, we see that for on-site terms $i = j$ the flux part in Eq. (5.43) simplifies due to $(\hat{\chi}_{\langle il\rangle_b} + \hat{\chi}^\dagger_{\langle il\rangle_b})(\hat{\chi}_{\langle ik\rangle_b} + \hat{\chi}^\dagger_{\langle ik\rangle_b}) = \mathbb{1}$. We can thus conclude that the on-site structure factor is independent of the chosen state and

$$\lim_{J_b\to 0}\left[\mathcal{S}^{\alpha\alpha}_{ii}(t)\big|_{J_b}\right] = \mathcal{S}^{\alpha\alpha}_{ii}(t)\big|_{J_b=0}. \tag{5.44}$$

The limit $J_b \to 0$ is therefore indeed continuous for this contribution and couples directly

to the on-site Majorana correlation function, providing an in principle even simpler expression than the quench problem that needs to be solved for bulk correlations. Furthermore, we do not expect Eq. (5.44) to change when including the degeneracy due to the zero energy matter mode $|\tilde{M}_0\rangle$: As the corresponding isolated mode is delocalized along the boundary, its effect on the local structure factor is expected to decrease as $\sim 1/L$ in system size. Furthermore, effects of finite temperature will smoothen out the response for $\omega \to 0$ in any case.

We have verified Eq. (5.44) independently on small finite size systems that can be treated with exact diagonalization and with matrix product state techniques [454]. The relation is convenient, as it allows us to draw direct conclusions about expected experimental signatures in open boundary conditions, while being able to formally work with the technical benefits of a periodic system.

5.5 Conclusions & outlook

In this chapter, we proposed tunable SP-STM measurements for probing site-local and spin-anisotropic characteristics of 2D quantum magnets. In particular, we obtained characteristic tunneling signatures of topological magnon edge modes for TMIs. As our main result, we established that fractionalized excitations described by visons and Majorana fermions in the Kitaev QSLs can be measured via SP-STM by contrasting bulk and boundary measurements. We emphasize that the idealized setup of perfectly (anti)parallel polarized tip and substrate is not crucial to our results: While it allowed us to isolate the contributions of different components of the local structure factor to the conductance, a more general situation with various contributions is still expected to show the main features of our results. In particular, by tuning the relative polarization to some realistic degree, the resulting accentuation/suppression of different features yields equivalent information about the system's underlying anisotropy.

Our analysis further demonstrates the direct coupling of the spin structure factor to the Majorana correlation function on the system boundary, leading to contributions beyond nearest neighbor separation due to a modified flux selection rule. In the future, it would be desirable to investigate whether such longer range correlations can be probed by spin noise spectroscopy measurements, possibly providing an even more direct probe of the chiral nature of the Majorana edge modes. Furthermore, the gapless nature of the edge response in the Kitaev model could open a route for a larger variety of spin-sensitive spectroscopy tools. In particular, nitrogen-vacancy (NV) magnetometry, typically operating on energy scales of up to $\sim 100\mathrm{GHz}$ [455], well below the typical values of exchange parameters of candidate materials in the THz-regime, might be used to further characterize 1D edge physics in several bulk Kitaev materials, i.e. α-$RuCl_3$ [293, 334–336]. In conclusion, we have established the potential of local SP-STM probes for confirming and qualitatively characterizing TMI and QSL physics. The observation of unambigous signa-

tures of topological magnon edge modes for the former, and magnetic Majorana fermions as well as gauge flux excitations for the latter, would provide a crucial step towards the long time goal of their controlled manipulation.

Part II

Emergent hydrodynamics in fractonic quantum matter with multipole conservation laws

6

Anomalous subdiffusion in dipole- and higher-moment-conserving quantum systems

This chapter is based on the publication

> Johannes Feldmeier, Pablo Sala, Giuseppe De Tomasi, Frank Pollmann, Michael Knap, *"Anomalous subdiffusion in dipole- and higher-moment-conserving quantum systems"*, Phys. Rev. Lett. 125, 245303 (2020)

Structure, text and figures have been adapted for the purposes of this thesis. Secs. 6.4,6.2 contain material not included in the publication. The numerical data for the small scale quantum model presented in Sec. 6.6 was obtained by Giuseppe De Tomasi.

In this chapter we move on to study the nonequilibrium dynamics of fracton systems, see the brief introduction in Sec. 2.3.2. To start, let us reiterate that very generally, thermal equilibrium of many-body systems is characterized by only a finite number of conserved quantities, such as energy, particle number or charge. A coarse grained nonequilibrium time evolution that irreversibly leads to such an equilibrium state is therefore expected to be dominated by transport of these quantities at late times, smoothing out inhomogeneities of the initial state [385]. This framework also extends to closed, interacting quantum systems, where the corresponding time scale of transport, separating 'early' and 'late' times, is usually marked by the onset of local thermalization. A phenomenological description of the ensuing dynamics can then be given in terms of a classical hydrodynamic description, with quantum properties merely entering the effective transport coefficients [58–60, 65, 66, 184, 189, 456, 457]. For conventional global $U(1)$ charge conservation laws, the universality class of the emerging hydrodynamics is generally expected

to be *diffusive*.

In fracton systems however, there exist intriguing conservation laws beyond such conventional global $U(1)$ charges, and we can wonder quite generally whether this might lead to novel hydrodynamics beyond diffusion at late times. A particularly interesting example is the combination of a global $U(1)$ charge together with the conservation of one or several of its higher multipole moments, such as the dipole- or quadrupole-moment. As we have outlined briefly in Sec. 2.3.2, such higher-moment conserving models have attracted much attention in the study of fracton systems [70, 269, 272, 274, 277, 279, 458, 459], and are realizable in synthetic quantum matter [197, 320, 321] or solid state systems [460, 461]. Indeed, the intertwined relation between the internal charge conservation law and its dipole moment has been shown to have significant impact on nonequilibrium properties [235, 236, 236–238, 462–464]. In the most severe cases, for short-ranged interactions and small local Hilbert space dimensions, dipole-conserving systems can fail to thermalize altogether due to a strong fragmentation of the many-body Hilbert space into exponentially many disconnected sectors [235–237].

In this chapter, we study the late time transport in *ergodic* models of dipole- and even higher multipole-moment-conserving one-dimensional lattice spin systems. We avoid the abovementioned strong Hilbert space fragmentation by including longer range interactions and sufficiently high spin representations. Building on the intuition of an effective classical description in the regime of incoherent transport, we employ a cellular automaton circuit approach to numerically study the long time dynamics (see e.g. [205, 387, 465] for related approaches). We will show how the presence of conserved multipoles leads to anomalously slow, subdiffusive transport of the underlying charge degree of freedom. We find that the associated subdiffusive universality classes are described by a cascade of dynamical exponents depending on the highest conserved moment. Furthermore, in order to explain these results we provide a detailed construction of a novel classical hydrodynamic theory for multipole-conserving many-body systems, in full agreement with our numerical results.

6.1 Higher-moment-conserving spin models

We start by introducing a set of spin models in one dimension that exhibit multipole-conserving dynamics. Even though numerically we will be concerned with generic circuit/automaton models in the absence of energy conservation for large parts of this chapter, the structure of multipole-conserving systems is most instructively illustrated using Hamiltonian models. We thus begin by constructing generic spin Hamiltonians conserving arbitrary moments of the charge (which corresponds to the z-basis magnetization here). The structure of these models serves as input for the definition of suitable automaton dynamics without energy conservation and also sets the stage for the investigation of *energy-conserving* quantum systems with multipole constraints in the subsequent chapter.

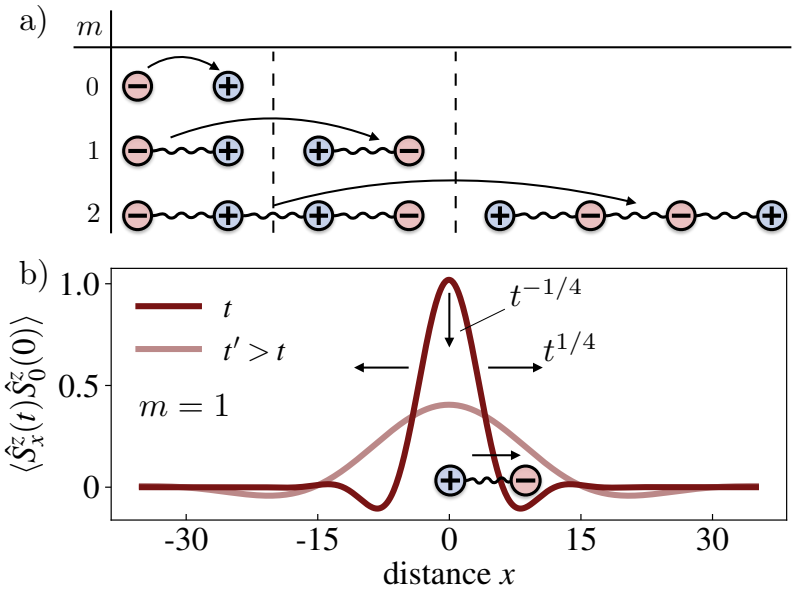

Figure 6.1: Higher Moment Conservation Laws. **a)** Recursive construction: A charge-conserving move ($m = 0$) creates a local dipole, which in turn is a charge-neutral dynamical object of a dipole-conserving model ($m = 1$). This process is iterated to conserve higher moments. **b)** The late time dynamics of charges exhibits subdiffusive decay, with algebraic exponents depending on the highest conserved charge moment (here: $m = 1$).

Once we understand the construction of such models, we find that the derivation of an effective hydrodynamic description ensues quite intuitively.

Our first goal is now to construct a spin Hamiltonian conserving both the total charge (i.e. the 0-th multipole moment)

$$Q^{(0)} = \sum_x \hat{S}^z_x, \tag{6.1}$$

as well as the dipole moment (the 1st multipole moment)

$$Q^{(1)} = \sum_x x\, \hat{S}^z_x \tag{6.2}$$

of the local magnetization. This definition of the dipole moment is not invariant under translations on the lattice and so we restrict our analysis to systems with open boundary conditions for simplicity in the following. We emphasize however that our results on the dynamics in the bulk of the system will be independent of the choice of boundary conditions. We implement the conservation of dipole moment recursively, starting from a simple Hamiltonian of the form

$$\hat{H} = \hat{H}^{(0)}_{r=2} + \hat{H}_z, \tag{6.3}$$

with

$$\hat{H}^{(0)}_{r=2} = \sum_x (\hat{S}^+_x \hat{S}^-_{x+1} + h.c.) \tag{6.4}$$

hosting local XY-type terms of range $r = 2$ that conserve the total charge $Q^{(0)}$. $\hat{H}_z$ contains arbitrary local terms diagonal in the $\hat{S}^z$-basis that render the model non-integrable. The $\hat{S}^{\pm}_x$, $\hat{S}^z_x$ are spin operators in a given spin representation S. Considering Eq. (6.4), an elementary term

$$h^{(0)}_2(x) \equiv \hat{S}^+_x \hat{S}^-_{x+1} \tag{6.5}$$

moves a charge between sites $x+1$ and x. Alternatively, we can intuitively interpret these elementary terms as creating a dipole against a homogeneous background, '$h^{(0)}_2(x) \sim \hat{d}^\dagger_x$' (we note however that the $\hat{d}^\dagger_x / \hat{d}_x$ are not creation / annihilation operators that fulfill canonical commutation relations). In this simple interpretation, a local term that conserves not only the charge but also the dipole moment $Q^{(1)}$ can then be obtained by simply multiplying the operator $h^{(0)}_2(x)$ with its hermitian conjugate at some shifted position, e.g.

$$h^{(1)}_3(x) = \left(h^{(0)}_2(x)\right)^\dagger h^{(0)}_2(x+1). \tag{6.6}$$

Building a model by summing over such local terms yields

$$\hat{H}^{(1)}_3 = \sum_x \hat{S}^-_x \left(\hat{S}^+_{x+1}\right)^2 \hat{S}^-_{x+2} + h.c., \tag{6.7}$$

a system that has been studied in the context of Hilbert space fragmentation [235, 236, 236–238, 463, 464].

Having constructed a model in Eq. (6.7) that conserves both $Q^{(0)}$ and $Q^{(1)}$, the above recursion can straightforwardly be iterated to obtain models conserving arbitrary moments of the charge,

$$Q^{(m)} = \sum_x x^m \hat{S}^z_x. \tag{6.8}$$

More formally, we consider an m^{th} moment conserving Hamiltonian of range r in the form

$$\hat{H}^{(m)}_r = \sum_x h^{(m)}_r(x) + h.c., \tag{6.9}$$

whose local terms can be expanded as

$$h^{(m)}_r(x) = \bigotimes_{i=0}^{r-1} \left(\hat{S}^{\mathrm{sgn}[\sigma_m(i)]}_{x+i}\right)^{|\sigma_m(i)|}, \text{with } \sigma_m(i) \in \mathbb{Z}, \tag{6.10}$$

where by definition $\sigma_m(0) \neq 0$, $\sigma_m(r-1) \neq 0$, and $\mathrm{sgn}[\cdot] \in \{+,-\}$ is the signum function. For the charge-conserving XY-terms, $\sigma_0(0) = -\sigma_0(1) = 1$. Again, arbitrary terms diagonal in $\hat{S}^z$ could be added to Eq. (6.10) without affecting the conservation laws. Analogous to the argument above, given $h^{(m-1)}_r(x)$, we can then construct a $(r+\ell)$-range term that

additionally conserves the m^{th} moment by imposing the recursion relation

$$\sigma_m(i) = -\sigma_{m-1}(i) + \sigma_{m-1}(i-\ell), \tag{6.11}$$

on the exponents of the spin ladder operators. Eq. (6.11) reflects the construction of $\hat{H}^{(m)}_{r+\ell}$ via shifting an elementary *m-pole* by ℓ sites. As illustrated in Fig. 6.1 (a), the elementary *m-pole* configurations have vanishing lower moments and a spatially independent m^{th} moment, similar to usual charges. However, their number is not conserved.

We notice that Eq. (6.11) can be rephrased as a discrete lattice derivative of spacing ℓ, $\sigma_m(i) = -\Delta_x\left[\sigma_{m-1}\right](i)$, which implies $\sigma_m(i) = (-\Delta_x)^m[\sigma_0](i)$. If the elementary XY-terms are interpreted as a finite difference with spacing $\ell = 1$, $(-\Delta_x)[f](0) = \sum_i \sigma_0(i)\, f(i)$ with some lattice function $f(i)$, the exponents $\sigma_m(i)$ effectively correspond to a lattice discretization of the $(m+1)^{st}$ derivative

$$(-\Delta_x)^{m+1}[f](0) = \sum_i \sigma_m(i)\, f(i). \tag{6.12}$$

Using the spin commutation relations and Eq. (6.12), we see that

$$[Q^{(n)}, h^{(m)}_r(x)] = \sum_i \sigma_m(i)\,(x+i)^n = (-\Delta_x)^{m+1}[x^n] = 0 \tag{6.13}$$

for $n \leq m$, i.e. all moments $Q^{(n\leq m)}$ are indeed conserved. The same holds for longer range Hamiltonians, using alternative discretization schemes of the involved derivatives. We note that this is a discretized version of the field theory construction in Ref. [279].

6.2 Emergent hydrodynamics

Given the models of Eqs. (6.9,6.10), we wish to understand the effective hydrodynamic theory that governs the time evolution of the course-grained charge density $\langle \hat{S}^z_x \rangle = \langle \hat{S}^z_x(t) \rangle$ at late times. Let us first emphasize the need for a hydrodynamic description beyond the simple diffusion equation

$$\frac{d}{dt}\langle \hat{S}^z_x \rangle - D\,\partial_x^2 \langle \hat{S}^z_x \rangle = 0, \tag{6.14}$$

which we expect to be applicable in systems conserving a conventional global charge but without further multipole conservation laws. If we consider a closed system with a domain wall initial state as depicted in Fig. 6.2, the diffusion equation Eq. (6.14) leads to a broadening of the charge (magnetization) density into an error-function. However, such a process clearly breaks the conservation of dipole moment, as there is a net current of charge from one half of the system into the other. Hence we conclude that Eq. (6.14) needs to be revised in the presence of dipole- or higher-moment conservation.

To understand how such a novel hydrodynamic description can emerge in the

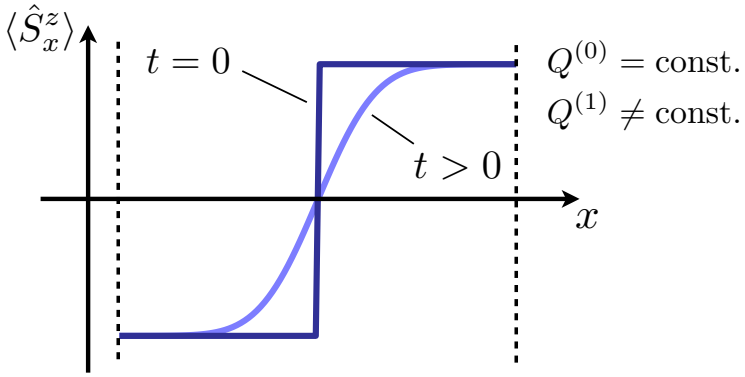

Figure 6.2: Domain wall melting. Starting from a domain wall initial state in a closed system, a simple diffusion equation gives rise to a broadening of the domain wall. This process breaks the conservation of dipole moment as there is a net current of charge from right to left half of the system. This demonstrates the need for a novel hydrodynamic description in the presence of dipole or higher multipole conservation laws.

multipole-conserving systems of Eqs. (6.9,6.10), we recall that the elementary terms of Eq. (6.10) can be viewed as moving elementary multipoles through the system. This allows us to define a local 'multipole current' $J_x^{(m)}$ via

$$J_x^{(m)} := -\frac{i}{\hbar}\big(h_r^{(m)}(x) - h.c.\big), \tag{6.15}$$

which reduces to the familiar charge current for the case $m = 0$ (in fact, this is a one-dimensional version of generalized currents appearing in fractonic systems [466]). The local multipole current $J_x^{(m)}$ characterizes the dynamics of the system and we wish to derive the change of the local charge density due to the presence of these local currents. To this end, we consider the Heisenberg evolution equation of the charge density $\hat{S}^z_x$. This yields

$$\frac{d}{dt}\hat{S}^z_x = \frac{i}{\hbar}[\hat{H}_r^{(m)}, \hat{S}^z_x] = (-\Delta_x)^{m+1} J_x^{(m)}, \tag{6.16}$$

where we used the relation Eq. (6.12). We emphasize that this form of the time evolution applies to arbitrary Hamiltonians conserving the m^{th} moment of the charge, with microscopic details only entering the precise form of $J_x^{(m)}$. Eq. (6.16) is a generalized version of the continuity equation, which reads $\frac{d}{dt}\hat{S}^z_x = (-\Delta_x)J_x^{(0)}$ in conventional charge-conserving systems. Here, Eq. (6.16) implies that the charge current in the system is given by the m-th derivative of an elementary multipole current [279]. Fig. 6.3 provides an intuitive illustration of Eq. (6.16) for the dipole-conserving case $m = 1$.

To arrive at a differential equation, we now go to a course-grained description where we consider the evolution of expectation values in the limit of long wavelengths, assuming large enough variation lengths in space:

$$\begin{aligned} \hat{S}^z_x(t) &\to \langle \hat{S}^z_x \rangle_t \\ \Delta_x &\to \partial_x. \end{aligned} \tag{6.17}$$

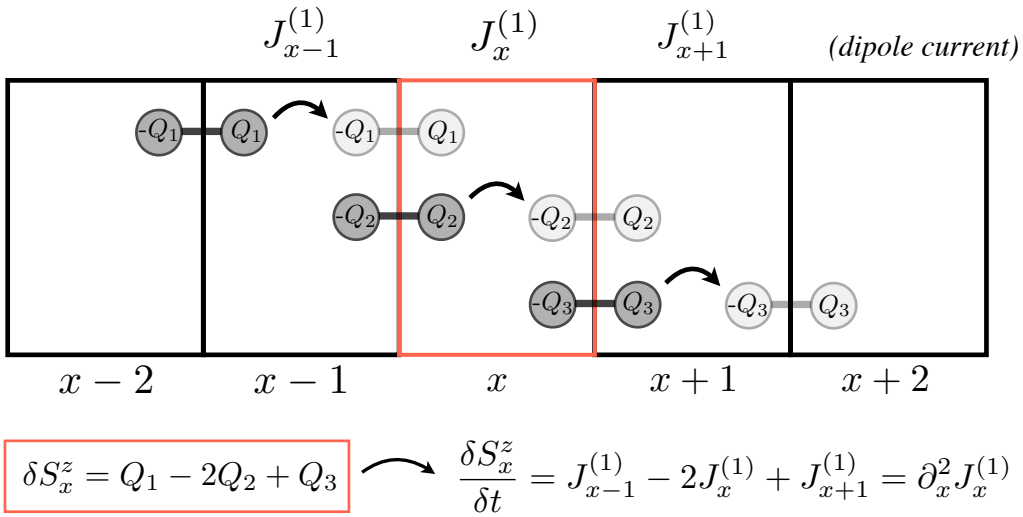

Figure 6.3: Dipolar continuity equation. We consider the dynamics of the local charge density resulting from the presence of local dipole currents $J^{(1)}_x$ in the system. This gives rise to a generalized continuity equation which takes the form of second derivative on a lattice, turning into a second spatial derivative in the limit of long wave lengths.

Insertion into Eq. (6.16) then leads to the continuity equation

$$\boxed{\frac{d}{dt}\langle \hat{S}^z_x \rangle_t = (-\partial_x)^{m+1} \langle J^{(m)}_x \rangle_t \,.} \tag{6.18}$$

Let us emphasize here for clarity that $\langle \hat{S}^z_x \rangle_t$ corresponds to a course-grained – *but nonequilibrium* – charge density as indicated by the subscript t in the expectation value. In particular, in this instance the brackets $\langle \cdot \rangle_t \neq \langle \cdot \rangle$ do not indicate an average over an equilibrium ensemble, for which $\frac{d}{dt}\langle \hat{S}^z_x \rangle = 0$ would clearly vanish. The relation between expectation values in- and out-of-equilibrium will be addressed in further detail in Sec. 6.5.

To obtain a closed equation for the coarse-grained charge density $\langle \hat{S}^z_x \rangle_t$, we require a hydrodynamic assumption which relates the multipole current to the derivatives of the charge density (see e.g. Ref. [467]). We therefore expand

$$\langle J^{(m)}_x \rangle_t = -D\,(\partial_x)^{\ell(m)} \langle \hat{S}^z_x \rangle_t \,, \tag{6.19}$$

and our task is to find the *lowest* possible (i.e. most scaling relevant) $\ell(m) \in \mathbb{N}$ such that $D \neq 0$ is consistent with the conservation of all moments $Q^{(n\leq m)}$ (In Sec. 6.5, we provide a scaling analysis that shows that non-linear terms in the expansion of $\langle J^{(m)}_x \rangle_t$ are irrelevant). We emphasize that here we have neglected the potential impact of energy conservation for simplicity. We return to the coupled hydrodynamics of charge *and* energy in the presence of multipole conservation laws in the next chapter of this thesis. For charge-conserving interacting quantum systems ($m = 0$), known to generically exhibit diffusive transport at late times [58–60, 65, 66, 184, 189, 456, 457], we should obtain Fick's

law

$$\langle J_x^{(0)} \rangle_t = -D\, \partial_x \langle \hat{S}_x^z \rangle_t \,, \tag{6.20}$$

i.e. $\ell(0) = 1$, resulting in the usual diffusion equation for $\langle \hat{S}_x^z \rangle_t$ upon insertion into Eq. (6.18). However, as seen in the domain wall example of Fig. 6.2, general solutions of the diffusion equation break higher-moment conservation.

How can we thus generalize Fick's law to higher conserved moments? We notice that in a closed system with open boundary conditions and in the absence of sinks or sources, the current

$$\langle J_x^{(m)} \rangle_{eq.} = \langle J_x^{(m)} \rangle_{t\to\infty} = 0 \tag{6.21}$$

is expected to vanish in equilibrium. Combining this condition with

$$\langle J_x^{(m)} \rangle_t = -D\, (\partial_x)^{\ell(m)} \langle \hat{S}_x^z \rangle_t \tag{6.22}$$

leads to the equilibrium charge distribution

$$\langle \hat{S}_x^z \rangle_{eq.} = a_0 + a_1\, x + ... + a_{\ell(m)-1}\, x^{\ell(m)-1} = \sum_{s=0}^{\ell(m)-1} a_s\, x^s. \tag{6.23}$$

Eq. (6.23) is a polynomial of degree $l(m) - 1$ and contains a number $\ell(m)$ of independent constants a_s which characterize the equilibrium state. On the other hand, since we assumed conservation of all moments $Q^{(n\leq m)}$, we know that that the equilibrium state of the charge density has to be characterized by $m + 1$ independent parameters. This immediately determines $\ell(m) = m + 1$, and the natural generalization of Fick's law is thus given by

$$\boxed{\langle J_x^{(m)} \rangle_t = -D\, (\partial_x)^{m+1} \langle \hat{S}_x^z \rangle_t \,.} \tag{6.24}$$

This coincides with the intuition of the finite difference construction of the multipole current $J_x^{(m)}$: the dynamics balances out inhomogeneities of the m^{th} derivative of the charge density.

Inserting the generalized Fick's law Eq. (6.24) relation back into the continuity equation Eq. (6.18) that determines the charge density dynamics, we finally arrive at the generalized hydrodynamic equation

$$\boxed{\frac{d}{dt} \langle \hat{S}_x^z \rangle_t = -D(-1)^{m+1} (\partial_x)^{2(m+1)} \langle \hat{S}_x^z \rangle_t \,,} \tag{6.25}$$

valid for generic thermalizing systems conserving all multipole moments up to and including m. We emphasize that our derivation not only predicts the hydrodynamic equation Eq. (6.25), but also the expected equilibrium distribution Eq. (6.23) in closed systems, where the corresponding constants $a_s = a_s(Q^{(n\leq m)})$ are uniquely fixed by the charge moments $Q^{(n\leq m)}$ of the initial state. In systems of size L they typically go as $|a_s| \sim \mathcal{O}(L^{-s})$,

but are manifest in e.g. observables involving macroscopic distances like $\langle \hat{S}^z_L \rangle - \langle \hat{S}^z_0 \rangle$.

We close the analysis of this section with the remark that usually, the hydrodynamic description of a system conserving $m+1$ quantities is given by a set of $m+1$ coupled equations for the associated densities and currents [385, 468, 469]. However the present systems are described by a *single* equation Eq. (6.25) for the charge density. This is due to the hierarchical structure of the conservation laws Eq. (6.8) that specify all $Q^{(m)}$ in terms of the fundamental charge density of the theory. In other words, the multipole conservation laws for $m \geq 1$ are not associated with an independent local density which would contribute a hydrodynamic mode. This is because, as we have commented on below Eq. (6.11), there is no conserved number of elementary local multipole objects.

6.3 Analytical solution and numerical verification

Eq. (6.25) is the central result of this chapter and it is worthwhile to consider its solutions in detail. Introducing the short hand $n(x,t) := \langle \hat{S}^z_x \rangle_t$ for the course-grained charge density, Eq. (6.25) takes the following form in momentum space,

$$\frac{d}{dt} n(q,t) = -\left[D q^{2(m+1)} t \right] n(q,t), \tag{6.26}$$

which is solved by $n(q,t) \sim \exp(-Dq^{2(m+1)}t)$. The normalized fundamental solution in real space is of the form

$$G^{(m)}(x,t) = \int \frac{dq}{2\pi} \exp(-Dq^{2(m+1)}t) \exp(-iqx) = \frac{1}{(Dt)^{1/2(m+1)}} F^{(m)}\left[\frac{x^{2(m+1)}}{t} \right], \tag{6.27}$$

where $F^{(m)}$ is a universal scaling function which can be written in terms of generalized hypergeometric functions [470]. We emphasize that Eq. (6.27) implies a dynamical exponent

$$z = 2(m+1) \tag{6.28}$$

that relates the scaling of space and time under scale transformations. The time evolution of a charge density profile starting from $G^{(m)}(x,0) = \delta(x)$ should then be described by Eq. (6.27). By standard linear response theory [385], the solution Eq. (6.27) should coincide with the (infinite temperature) dynamical correlation functions

$$C^{(m)}(x,t) = \langle \hat{S}^z_x(t) \hat{S}^z_0(0) \rangle \,, \tag{6.29}$$

where $\langle ... \rangle$ denotes an *equilibrium* average (notice the absence of the nonequilibrium subscript t) of $\hat{S}^z_x(t)\hat{S}^z_0(0)$ over all initial states in the Hilbert space. A more detailed analysis of the linear response arguments connecting Eq. (6.27) and Eq. (6.29) will be provided in Sec 6.4.

We now attempt to compute the correlations Eq. (6.29) numerically for a given model

in order to verify the qualitative prediction of subdiffusive hydrodynamics. In our numerical approach we do not attempt to solve the full time evolution of a dipole-conserving quantum Hamiltonian but instead focus on efficiently simulable automaton circuits [205, 386–388] that respect the same conservation laws of Eq. (6.8); see App. A.3 for an overview of this method. Since we anticipate the emergence of hydrodynamics at late times, the crucial properties of our models should reside solely in the structure of their conservation laws. Qualitatively, the hydrodynamic charge transport in the system at late times should then be independent of the precise nature of the microscopic evolution. Under the assumption that the conservation of energy is not crucial to understanding the dynamics of charge in the system, we expect to capture the correct hydrodynamics in these simple classically simulable circuits. We will return to verifying this assumption in the next chapter. Loosely speaking, the discrete automaton time evolution that we consider here consists of a sequential application of local updates mapping z-basis product states onto z-basis product states. The updates are designed to mimick the action of the Hamiltonian by updating between local strings of spins $\boldsymbol{s}(x) = (s_x, ..., s_{x+r-1})$, with $s_i \in \{-S, ..., S\}$, that are connected by the local terms of Eq. (6.10) and thus feature the same conserved charge moments. We provide the full details of our numerical approach in Sec. A.3.1. Furthermore, we emphasize here that throughout this thesis, different ways of implementing such effectively classical automata are utilized. The qualitative hydrodynamics that we are most interested in is not sensitive to the precise nature of this implementation. We have verified this robustness numerically, which indicates that our results are indeed representative of dynamical universality.

For concreteness, we study a dipole conserving model with $S = 1$ including interaction terms of Eq. (6.10) of ranges $r = 3$ and $r = 4$ [1], as well as a quadrupole conserving model with larger spin representation $S = 4$ including ranges $r = 4$ and $r = 5$, both on system sizes up to $L = 10^4$. While generally the hydrodynamic tails for given m are expected to be universal for sufficiently ergodic systems, in numerical practice, larger r and S will provide faster convergence to this long time behavior. As the dynamics is expected to become slower upon increasing m, i.e. the number of constraints, we choose a larger spin representation $S = 4$ in the quadrupole case to allow for a more accurate determination of algebraic exponents.

We show the results of the automaton evolution for the return probability $C^{(m)}(0, t)$ in Fig. 6.4 (b). In contrast to ordinary diffusive systems which possess the scaling $C^{(0)}(0, t) \sim t^{-1/2}$ [385], we numerically estimate the algebraic late time decay exponents to be $C^{(1)}(0, t) \sim t^{-0.248} \approx t^{-1/4}$ in the dipole-conserving model, and $C^{(2)}(0, t) \sim t^{-0.170} \approx t^{-1/6}$ for the conservation of quadrupole moment. These results are in very good agreement with the predictions of Eq. (6.25) and thus Eq. (6.27). Furthermore, Figure 6.4 (b,c) shows that indeed the full spatial profile of the scaling function Eq. (6.27) emerges at late times in the dynamical spin correlations, displaying full agreement with our numeri-

[1] This model was shown to thermalize for typical initial states in Ref. [235].

cal results for both $m = 1, 2$ upon fitting the only free parameter D. In particular, as demonstrated in Fig. 6.4 (c,d), $C^{(m)}(x,t)$ accurately follows the scaling collapse predicted by Eq. (6.27).

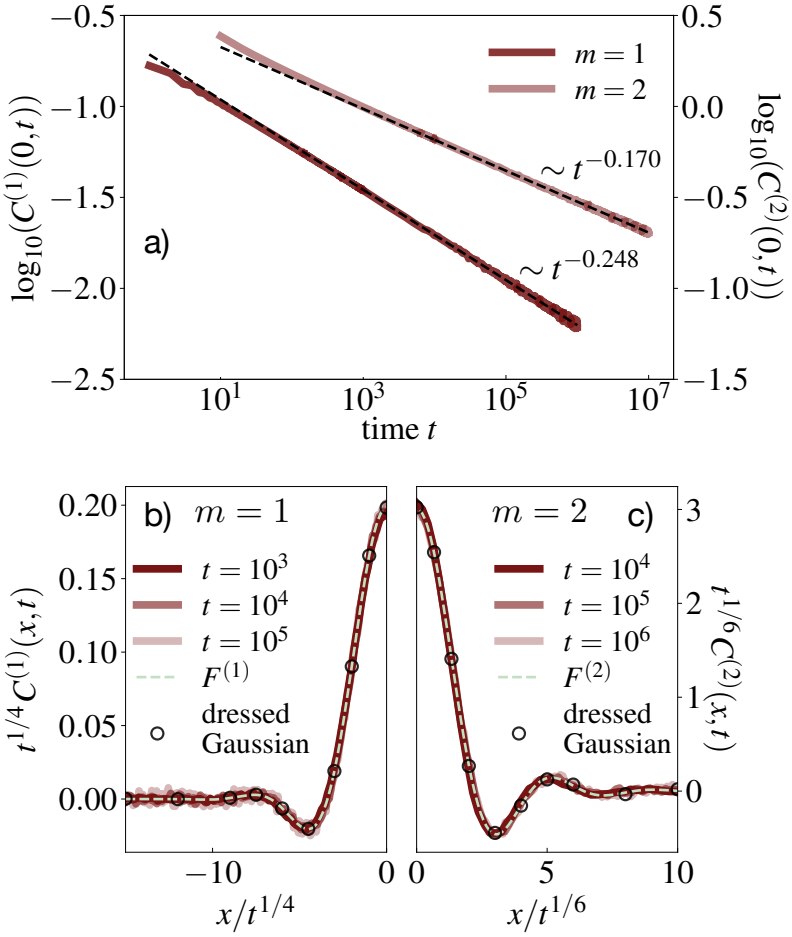

Figure 6.4: Hydrodynamics: Numerics. a) Return probability $C^{(m)}(0,t)$ for dipole- and quadrupole conservation. The long time behavior approaches an m-dependent algebraic decay $\sim t^{-1/2(m+1)}$. The numerical values of the exponents where extracted from fits over the latter three time decades (dashed lines). **b)+c)** Scaling collapse for $m = 1$ and $m = 2$ according to the long wave-length description Eq. (6.27). In addition to the numerical data, the fundamental solution of Eq. (6.27) (dashed line) and the corresponding Gaussian expansion (see main text) up to order $n = 4$ (circles) are shown. The system size is $L = 10^4$ and correlations were averaged over at least 10^3 random initial states in all panels.

We notice that for $m = 0$, Eq. (6.25) reduces to the usual diffusion equation and $C^{(0)}(x,t)$ is a Gaussian probability distribution describing the movement of an initially localized excitation through the system [385, 471]. In contrast, for $m \geq 1$, as shown in Fig. 6.4 and more generally clear from a vanishing second moment

$$\langle x^2 \rangle_{G^{(m)}} = \int dx\, x^2 G^{(m)}(x,t) = 0, \tag{6.30}$$

$C^{(m)}(x,t)$ *cannot* be interpreted as a probability distribution. Instead, the associated oscil-

lations in the profile of $C^{(m)}(x,t)$ form a characteristic signature of higher-moment conservation that can potentially also be observed in quench experiments of domain wall initial states, see Fig. 6.5 (b).

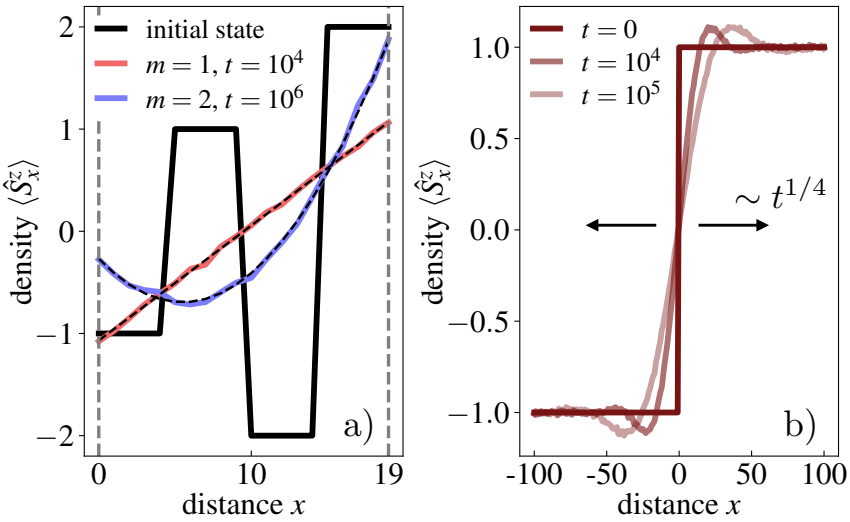

Figure 6.5: Implications of higher moment conservation. **a)** In a finite size system with open boundary conditions (gray dashed lines), the charge density relaxes to an equilibrium distribution that is a polynomial of order m (here: $S=3$). The black dashed lines are the analytical predictions from Eq. (6.23). **b)** The melting of a domain wall in a dipole conserving system for sufficiently large spin (here: $S=2$) appears as the cummulative distribution function of $C^{(1)}(x,t)$, with characteristic charge density oscillations.

In addition, we notice that the central peak of $C^{(m)}(x,t)$ in Fig. 6.4 (c,d) is well approximated by a Gaussian $g(x,t) = \exp\left(-x^2/\sigma^2(t)\right)/\sqrt{\pi\sigma^2(t)}$ with $\sigma(t) = (Dt)^{1/2(m+1)}$. The additional dressing density modulations can be understood heuristically if we interpret the Gaussian distribution $g(x,t)$ as describing the movement of an excitation through the system as part of m-poles. Conservation of $Q^{(m>0)}$ implies that a surrounding cloud of opposite charge has to be dragged along, see Fig. 6.1 (b). The effective length scale for this process is given by $\sigma(t)$. This intuition can be formalized by making an Ansatz

$$C^{(m)}(x,t) = c_0\, g(x,t) - c_2\big[g(x+\sigma(t)) + g(x-\sigma(t))\big] \approx g(x,t)[c_0 - 4c_2x^2/\sigma(t)^2]. \quad (6.31)$$

Thus, a positive charge moving to $x \pm \sigma(t)$ implies an increased likelihood of simultaneously finding a negative charge at x. Generalizing this physically motivated Ansatz, we can expand

$$C^{(m)}(x,t) = g(x,t) \sum_n c^{(m)}_{2n} \left(-\frac{x^2}{\sigma^2(t)}\right)^n. \quad (6.32)$$

Fig. 6.4 (c,d) shows excellent agreement already at low orders of the expansion, where each term provides an additional oscillation in the spatial profile of $C^{(m)}(x,t)$.

Finally, we emphasize that we cannot only verify the predictions of the hydrodynamic equation Eq. (6.25), but also the prediction Eq. (6.23) of the form of the equilibrium charge

distribution within our numerical approach. We do so in small systems by monitoring the charge distribution resulting from a fixed inital state at very late times. Fig. 6.5 (a) shows a chosen initial charge distribution in a system of size $L = 20$, as well as the late time distributions obtained from evolving the system using both dipole- and quadrupole-conserving automata. The resulting distributions are in very good agreement with the predicted polynomials of Eq. (6.23), validating our approach.

6.4 Fluctuating hydrodynamics

The previous sections have demonstrated that the hydrodynamic equation Eq. (6.25) accurately captures the dynamics in multipole-conserving many-body systems. However, there remain two questions that we briefly raised previously and that we now address in more detail: First, is Eq. (6.25) robust to adding additional multipole-conserving terms, i.e., does Eq. (6.25) represent the most relevant contribution to hydrodynamis in the long wave length scaling limit? And second, how is the relaxation of a nonequilibrium course-grained charge density $\langle \hat{S}^z_x \rangle_t$ as described by Eq. (6.25) connected to the dynamical correlation function Eq. (6.29) taken with respect to an equilibrium ensemble?

In this section we first tackle the latter question: Eq. (6.25) describes the dissipation of a nonequilibrium charge excitation while $\langle \hat{S}^z_x(t) \hat{S}^z_0(0) \rangle$ from Eq. (6.29) is related to fluctuations in equilibrium, and so we clearly require a *fluctuation-dissipation relation* connecting the two. This can be achieved following the approach of fluctuating hydrodynamics: We include microscopic noise in the hydrodynamic equation Eq. (6.25) with the goal of extending it to include fluctuations in equilibrium. The following derivations are analogous to the standard diffusive case [59, 472]. Let us return to the generalized continuity equation of Eq. (6.18),

$$\frac{d}{dt} \langle \hat{S}^z_x \rangle_t - (-\partial_x)^{m+1} \langle J^{(m)}_x \rangle_t = 0, \tag{6.33}$$

valid for systems conserving all multipole moments $Q^{(n \leq m)}$. We now extend the expansion $\langle J^{(m)}_x \rangle_t = -D \, (\partial_x)^{m+1} \langle \hat{S}^z_x \rangle_t$ discussed previously to include microscopic noise fluctuations $\xi(x,t)$ of the multipole current, i.e.

$$\langle J^{(m)}_x \rangle_t = -D \, (\partial_x)^{m+1} \langle \hat{S}^z_x \rangle_t + \xi(x,t). \tag{6.34}$$

We take the noise $\xi(x,t)$ to be uncorrelated,

$$\begin{aligned} \langle \xi(x,t) \, \xi(x',t') \rangle &= B^2 \, \delta(x-x') \, \delta(t-t') \\ \langle \xi(q,\omega) \xi(q',\omega') \rangle &= B^2 \, \delta(q+q') \, \delta(\omega+\omega'), \end{aligned} \tag{6.35}$$

where we have also provided the corresponding form of the correlations in Fourier space. As we will see, the strength B of the noise is tied to the correlation functions of the charge

density in equilibrium [59, 472] and is of microscopic origin. Using Eq. (6.34), the equation of fluctuating hydrodynamics for multipole-conserving systems becomes

$$\frac{d}{dt}\langle \hat{S}^z_x \rangle_t + D\,(-1)^{m+1}(\partial_x)^{2(m+1)}\langle \hat{S}^z_x \rangle_t = (-\partial_x)^{m+1}\xi(x,t). \tag{6.36}$$

For ease of notation, let us at this point introduce the short hand

$$n(x,t) := \langle \hat{S}^z_x \rangle_t \tag{6.37}$$

for the course-grained charge density, such that Eq. (6.36) reads

$$\frac{d}{dt}n(x,t) + D\,(-1)^{m+1}(\partial_x)^{2(m+1)}n(x,t) = (-\partial_x)^{m+1}\xi(x,t). \tag{6.38}$$

The solution of Eq. (6.38) is readily found by switching to momentum and frequency variables,

$$n(q,\omega) = \frac{(-iq)^{m+1}}{i\omega + Dq^{2(m+1)}}\,\xi(q,\omega). \tag{6.39}$$

With Eq. (6.39) at hand we can compute the correlations of the course-grained charge density $n(x,t) = \langle \hat{S}^z_x \rangle_t$ with respect to an equilibrium ensemble (at infinite temperature),

$$\begin{aligned}\langle n(x,t)n(0,0)\rangle &= \int \frac{dqdq'd\omega d\omega'}{(2\pi)^2}\, e^{i\omega t - iqx}\,\langle n(q,\omega)n(q',\omega')\rangle = \\ &= \int \frac{dqd\omega}{(2\pi)^2}\, e^{i\omega t - iqx}\frac{q^{2(m+1)}}{\omega^2 + D^2q^{4(m+1)}}B^2 = \\ &= \frac{B^2}{2D}\int \frac{dq}{2\pi}\, e^{-iqx}e^{-Dq^{2(m+1)}t} = \frac{B^2}{2D}\,G^{(m)}(x,t),\end{aligned} \tag{6.40}$$

where $G^{(m)}(x,t)$ is exactly the fundamental solution Eq. (6.27) to the hydrodynamic equation Eq. (6.25) in the absence of a fluctuating term. From the first to the second line we made use of Eq. (6.35) and we used the theory of residua to obtain the third line. We recall that $n(x,t) = \langle \hat{S}^z_x \rangle_t$ is the course-grained charge density, and so the left hand side of Eq. (6.40) corresponds to $\langle \hat{S}^z_x(t)\hat{S}^z_0(0)\rangle$ in our previous spin models. Therefore, we indeed find

$$C^{(m)}(x,t) = \langle \hat{S}^z_x(t)\hat{S}^z_0(0)\rangle = \frac{B^2}{2D}G^{(m)}(x,t), \tag{6.41}$$

which we have used in the numerical benchmarks of our hydrodynamic theory. Furthermore, in the static limit $t \to 0$ Eq. (6.40) gives rise to a fluctuation-dissipation relation (FDR)

$$\langle n(x)n(0)\rangle = \frac{B^2}{2D}\delta(x), \tag{6.42}$$

which relates the static correlations in equilibrium to the diffusion constant.

6.5 Scaling analysis

Within the framework of fluctuating hydrodynamics we can now answer the question initially posed in the previous section; whether our hydrodynamic equation Eq. (6.25) is robust to adding additional multipole-conserving terms? The key approximation in the derivation of Eq. (6.25) is the hydrodynamic assumption, stated in Eq. (6.34) within the fluctuating hydrodynamic description. Our goal is now to determine the relevance of additional terms in this expansion, provided that the required multipole conservation laws remain intact. Therefore, we set

$$\langle J_x^{(m)} \rangle_t = \langle J_x^{(m)} \rangle_t \left[(\partial_x)^j (\langle S_x^z \rangle_t)^i \right] = \sum_{j,i} \alpha_{i,j} \, (\partial_x)^j (\langle \hat{S}_x^z \rangle_t)^i + \xi(x,t), \tag{6.43}$$

with $i, j \in \mathbb{N}$ in a more general expansion of the coarse-grained multipole current. We present a general scaling analysis in the following, demonstrating that the term $j = 2(m+1)$, $i = 1$ is indeed the most relevant term consistent with conservation of all $Q^{(n \leq m)}$ in such an expansion. Again, the analysis closely follows the standard diffusive scenario laid out in Refs. [59, 472].

The starting point of our scaling approach are Eq. (6.36) and Eq. (6.35) and we consider a scale transformation $x \to x/\lambda$ with $\lambda > 1$. The scaling dimension of x under this rescaling, denoted by square brackets $[x]$, is thus given by $[x] = -1$. Upon demanding that Eqs. (6.36,6.35) be a fixed point under this rescaling, i.e. $[D] = 0$ and $[B] = 0$, the scaling dimensions of $t, \xi, \langle \hat{S}_x^z \rangle_t$ can be determined. First, we obtain

$$[t] = -2(m+1) \tag{6.44}$$

from the left hand side of Eq. (6.36), which reflects the dynamical exponent $z = 2(m+1)$ of the hydrodynamic theory Eq. (6.36). Second, integrating Eq. (6.35) over space and time leads to

$$\int dx dt \, \langle \xi(x,t) \xi(0,0) \rangle = B^2. \tag{6.45}$$

As the right hand side of this relation is scale invariant, $[B] = 0$, the scaling dimension of ξ (in one spatial dimension) must be

$$[\xi] = (-[t] - [x])/2 = m + 3/2. \tag{6.46}$$

Finally, inserting the scaling dimension of ξ into Eq. (6.36) implies that both left and right hand side of Eq. (6.36) must have dimension $2m + 5/2$, and therefore

$$[\langle \hat{S}_x^z \rangle_t] = 1/2. \tag{6.47}$$

Given these scaling dimensions, we can now assess whether additional terms included

in the expansion of $\langle J_x^{(m)} \rangle_t$ in Eq. (6.43) are relevant or not, provided they be consistent with multipole conservation laws. In particular, since both sides of Eq. (6.36) have a total scaling dimension $2m + 5/2$, we see that the term $\alpha_{i,j} \, (\partial_x)^j \, \langle S_x^z \rangle^i$ in Eq. (6.33) implies a scaling dimension

$$[\alpha_{i,j}] = m + 1 - j + \frac{1}{2}(1 - i) \tag{6.48}$$

of the corresponding coefficient $\alpha_{i,j}$. Therefore, all terms with $j > m + 1$, $i \geq 1$ as well as $j = m + 1$, $i > 1$ are irrelevant under the flow of the scaling.

How about potentially relevant/marginal terms, which have $j \leq m + 1$ and $1 \leq i \leq 2(m + 1 - j) + 1$? For $j = m + 1$ we are back to the term $(\partial_x)^{m+1} \langle \hat{S}_x^z \rangle_t$ which results in our hydrodynamic equation Eq. (6.25). All other relevant/marginal terms necessarily have $j < m + 1$, and thus *fewer* derivatives than the number of $m + 1$ independent constants necessary to characterize equilibrium. As a consequence, integrating the condition $\langle J_x^{(m)} \rangle_{eq.} = 0$ of a vanishing multipole current in equilibrium does not provide sufficiently many freely adjustable parameters for the equilibrium charge distribution. In other words, for terms with $j < m + 1$ it would always be possible to find initial states such that the conservation of some $Q^{(n \leq m)}$ is broken. All such term must thus be excluded in the expansion of Eq. (6.43). Overall, we indeed find that the expansion $\langle J_x^{(m)} \rangle \approx -D \, (\partial_x)^{m+1} \langle \hat{S}_x^z \rangle_t$ captures the unique, most scaling relevant term consistent with all multipole conservation laws.

6.6 Small scale quantum model with dipole conservation

As described in the previous section, we performed large scale numerical checks of the hydrodynamic theory Eq. (6.25) using effectively classical automaton-type dynamics. In this section we demonstrate that our results are also consistent with the full quantum time evolution of a dipole-conserving Hamiltonian. Although we are restricted to considering relatively small system sizes, our results are consistent with the subdiffusive dynamical exponent $z = 4$ predicted by our hydrodynamic theory. Larger scale simulations of Hamiltonian quantum dynamics will be addressed in the next chapter.

Here, for numerical feasability, we choose spin $S = 1/2$ and study the Hamiltonian given by

$$\hat{H} = \hat{H}_4^{(1)} + \hat{H}_5^{(1)}, \tag{6.49}$$

on open boundary conditions, where

$$\hat{H}_4^{(1)} = -\sum_{x=1}^{L-3} [S_x^+ S_{x+1}^- S_{x+2}^- S_{x+3}^+ + h.c.], \tag{6.50}$$

and

$$\hat{H}_5^{(1)} = -\sum_{x=1}^{L-4} [S_x^+ S_{x+1}^- S_{x+3}^- S_{x+4}^+ + h.c.]. \tag{6.51}$$

The parameter L corresponds to the length of the chain and it is readily verified that $\hat{H}$ conserves the total magnetization and dipole moment, i.e.,

$$[\hat{H}, \sum_x \hat{S}^z_x] = 0 \tag{6.52}$$

and

$$[\hat{H}, \sum_x x\hat{S}^z_x] = 0. \tag{6.53}$$

We focus on the largest sector of the Hilbert space connected by the Hamiltonian, which has $\sum_x \hat{S}^z_x = \sum_x x\hat{S}^z_x = 0$. We remark that the structure of the Hamiltonian $\hat{H}$ in Eq. (6.49) has been analyzed in detail in Refs. [235, 464], which demonstrated that $\hat{H}$ is ergodic and its Hilbert space is only weakly fragmented.

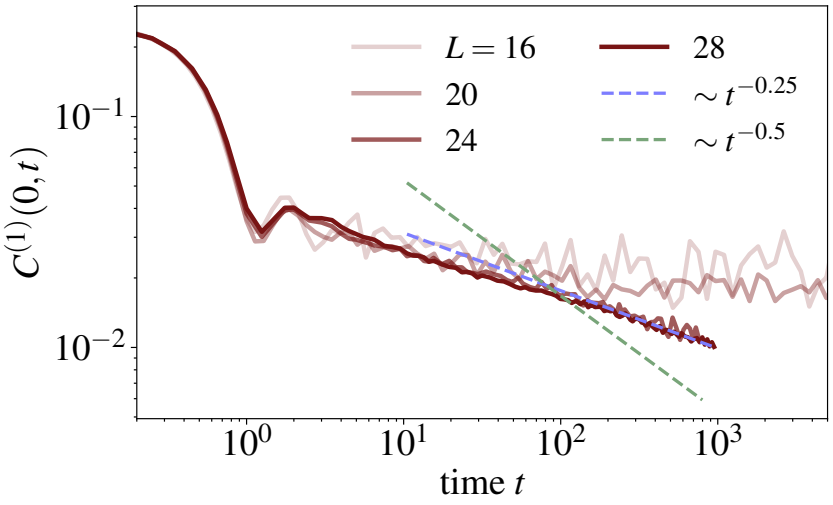

Figure 6.6: Return probability $C^{(1)}(t)$, defined in Eq. 6.54, for several system sizes $L \in \{16, 20, 24, 28\}$. $C^{(1)}(t)$ decays to zero algebraically $C^{(1)}(t) \sim t^{-\alpha}$, with α consistent with a subdiffusive relaxation $\alpha \approx 1/4$. The dashed-lines $\sim t^{-0.5}$ and $\sim t^{-0.25}$ serve as guides for the eye.

Here, we focus on the dynamics of the return probability of the spin correlation functions, which we define as

$$C^{(1)}(t) = \langle \delta\hat{S}^z_{L/2}(t)\delta\hat{S}^z_{L/2}(0)\rangle. \tag{6.54}$$

In Eq. (6.54), $\langle\cdot\rangle = \frac{1}{\mathcal{N}}\mathrm{Tr}[\cdot]$ is the normalized infinite-temperature trace, where $\mathcal{N}$ corresponds to the dimension of the connected Hilbert space sector that we restrict ourselfes to. Furthermore, we defined $\delta\hat{S}^z_{L/2}(t) = \hat{S}^z_{L/2}(t) - \langle\hat{S}^z_{L/2}(t)\rangle$, which removes a potential offset $\langle\hat{S}^z_{L/2}(t)$ due to finite size effects.

Figure 6.6 shows $C^{(1)}(t)$ for several system sizes $L \in \{16, 20, 24, 28\}$. For small system sizes $L \in \{16, 20\}$, $C^{(1)}(t)$ has been computed using exact diagonalization, and for $L \in \{24, 28\}$ using Chebyshev polynomials techniques for time evolution [473, 474]. As expected, already after a short time of order $O(1)$, $C^{(1)}(t) \sim t^{-\alpha}$ decays algebraically. The slow relaxation towards equilibrium is subdiffusive, $\alpha < 1/2$. In agreement with the

results obtained above, the observed decay appears to be consistent with the expected exponent $\alpha = 1/4$ for ergodic dipole-conserving Hamiltonians (blue dash-line in Fig. 6.6).

6.7 Unrestricted movement of multipoles

As a final undertaking in this chapter, we address how elementary multipoles move in generic systems with multipole conservation laws. In the simplest case $m = 0$, charges themselves correpond to the elementary mobile objects and they undergo diffusive dynamics. It is thus natural to ask whether in the case of m-pole conserving dynamics – where the charge is now subdiffusive – the unrestricted elementary m-pole objects perform diffusive motion as well. As we have argued above, there is no local multipole density beyond the charge density $\hat{S}^z_x$. However, we have provided a consistent definition of the local multipole current $J^{(m)}_x$ in our models through Eq. (6.15). We can thus check for a diffusive process by means of a Kubo formula: Let $\mathcal{J}^{(m)}(t) = \sum_x J^{(m)}_x(t)$ be the total multipole current in the system, then we can define a mean squared displacement $\left\langle \left(X^{(m)}\right)^2(t) \right\rangle$ via the current correlations

$$\left\langle \left(X^{(m)}\right)^2(t) \right\rangle := \frac{1}{L} \sum_{t'=0}^{t} \sum_{t''=0}^{t'} \langle \mathcal{J}^{(m)}(t'') \mathcal{J}^{(m)}(0) \rangle \,. \tag{6.55}$$

In the standard diffusive charge-conserving scenario this mean squared displacement scales linearly in time,

$$\left\langle \left(X^{(0)}\right)^2(t) \right\rangle \sim t. \tag{6.56}$$

We can thus speak of unrestricted, diffusive multipole motion if the scaling of Eq. (6.56) extends to higher multipole moments $m > 0$.

In order to verify that this is indeed the case we compute Eq. (6.55) within the automaton dynamics described in the previous section. In particular, the local updates of the automaton where chosen to mimic the action of the local Hamiltonian terms $h^{(m)}_r(x)$ and $\left(h^{(m)}_r(x)\right)^\dagger$, which move an elementary multipole either to the left or right, respectively. Therefore, each application of an update corresponding to $h^{(m)}_r(x)$ / $\left(h^{(m)}_r(x)\right)^\dagger$ yields a positive / negative contribution to $\mathcal{J}^{(m)}$, respectively. Fig. 6.7 shows that the mean squared displacement rapidly approaches a linear growth for both dipole- and quadrupole-conserving automata. Formally, this can be associated with a finite multipole-conductivity

6.8 Conclusions & outlook

In this chapter we have studied the long-time dynamics of higher-moment conserving models, obtaining a generalized hydrodynamic equation relevant for fractonic systems that leads to subdiffusive decay of charge correlations. We emphasize that for dipole-

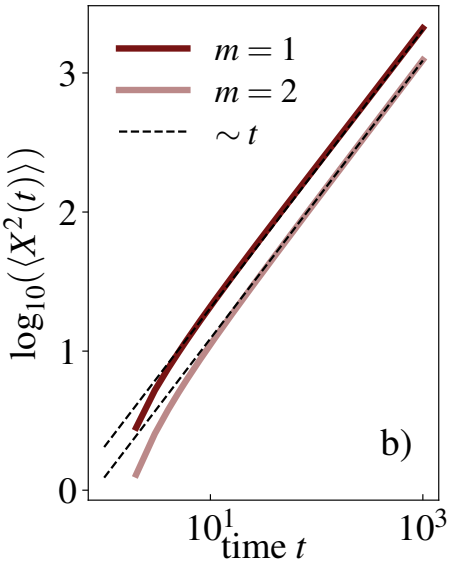

Figure 6.7: Multipole conductivity. The multipole mean squared displacement as defined in Eq. (6.43). The linear growth is indicative of a finite multipole conductivity.

conservation, our results are in agreement with the subdiffusive scaling experimentally observed in Ref. [197]. Therein, an initially prepared k-wave density mode of interacting fermions was found to decay as $\sim \exp(-k^4 t)$ in the presence of a strong, linearly tilted potential. As we outlined in Sec. 2.3.3, the linear potential couples directly to the center of mass $\sum_x x\,\hat{n}_x$ (see also [475]) and thus enforces an effective dipole-conservation on long length scales. The observed subdiffusive decay agrees with Eq. (6.25). We note further that the analysis of the present chapter suggests that an effective conservation of the quadrupole-moment may be obtained in a similar manner by application of a *harmonic* potential. We point out that independent works on the hydrodynamics of dipole-conserving fracton systems [206, 322, 389] appeared at the same time as our Ref. [2]. In particular, Ref. [389] derived the hydrodynamic equations, in agreement with our results, from an effective field theory approach [476–478]. Since then, a number of works have considered the hydrodynamics of systems with fracton mobility constraints [6, 103, 207, 479–483].

In addition to the subdiffusive decay of the return probability, we have identified oscillations in the spatial density profile both for delta and domain wall initial conditions. These oscillations are a characteristic property of the hydrodynamic universality class for multipole-moment-conserving fracton systems and should be detectable in quantum quench experiments. Furthermore, in the context of consed matter systems, the presence of higher-moment conservation would lead to a modified scaling of the full-width-half-maximum of the Lorentzian line shape as $\sim k^{2(m+1)}$ in Fourier space, which could be detectable in scattering experiments [484]. Finally, we emphasize again that we expect our results to be applicable to the long-time dynamics of closed quantum systems. We have obtained indications consistent with this expectation by studying a small system size quantum lattice model. However, a larger scale approach that also takes into ac-

count the conservation of energy – which we have not included in the hydrodynamic theory presented here, neither in our automaton circuit numerics – is desirable. In the following chapter, we will tackle these challenges.

7

Coupled hydrodynamics in dipole-conserving quantum systems

This chapter is based on the publication

> Ansgar Burchards, Johannes Feldmeier, Alexander Schuckert, Michael Knap, *"Coupled hydrodynamics in dipole-conserving quantum systems"*, Phys. Rev. B 105, 205127 (2022)

Structure, text and figures have been adapted for the purposes of this thesis. Secs. 7.2,7.3 contain material not included in the publication. The 2PI field theory approach and the associated numerical data presented as part of Sec. 7.3 have been devised and obtained by Ansgar Burchards.

Upon concluding the previous chapter, we posed the question of emergent hydrodynamics in closed quantum many-body systems that in addition to their fracton constraints also feature conservation of energy. Our previous numerical approach of random circuit time evolution was able to capture the novel hydrodynamic universality exhibited by multipole-conserving models and we formulated two key expectations: On the one hand, the universality class of subdiffusively slow charge dynamics persists upon including conservation of energy. And on the other hand, such hydrodynamics indeed emerges at late times from a unitary closed system quantum time evolution, of which we saw at least small scale numerical evidence. Both of these expectations require verification and we set out to achieve this goal in this chapter.

Specifically, in this chapter we investigate the nonequilibrium dynamics of a one-dimensional system of lattice bosons with charge-, dipole- and energy-conservation. We first derive a general set of equations within the framework of linear fluctuating hydro-

dynamics – similar to Chapter 6 – that take into account couplings between charge- and energy-excitations in the presence of dipole conservation; Sec. 7.1 and Sec. 7.2. As a result of this analysis we find that the dynamics of the model should exhibit a subdiffusive mode of mixed charge-energy excitations as well as a diffusive mode of pure energy excitations; a schematic example of the decay of general energy excitations – which have overlap with both modes – is illustrated in Fig. 7.1. We then go on to compare this effective hydrodynamic picture with the quantum time evolution of a specific bosonic lattice model, which is studied by means of nonequilibrium quantum field theory using a 2-particle-irreducible (2PI) effective action. Within this framework, we verify the applicability of our mode-coupled hydrodynamics in Sec. 7.3.3 and extract all components of a generalized diffusion matrix. An outlook and a discussion of how our results can be related to quantum simulation experiments are provided in Sec. 7.4. For details on the 2PI approach we refer to the publication of Ref. [6].

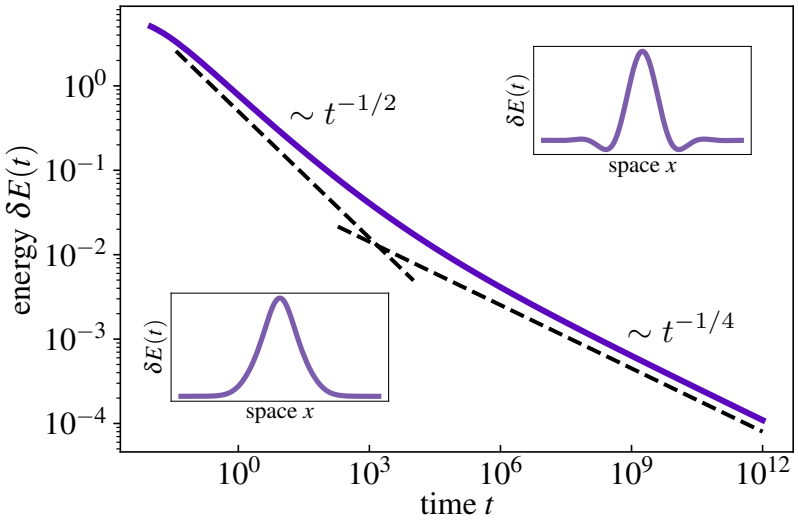

Figure 7.1: Coupled hydrodynamics in fractonic quantum matter. The decay of a generic local energy excitation in a dipole-conserving closed quantum system generally has overlap with *both* hydrodynamic modes present in the system: a diffusive mode with dynamical $z = 2$, visible at earlier times, as well as a subdiffusive mode with $z = 4$ which dominates the late time approach to equilibrium. The shown curve was obtained from the coupled hydrodynamic theory of Eq. (7.18). Insets: The full spatial profiles of the energy excitation at intermediate (lower left) and late (upper right) times.

7.1 Mode-coupled hydrodynamics

Building on the results of the previous chapter, we derive the fluctuating hydrodynamics of dipole- and energy-conserving systems within a mode-coupled Ansatz. As we restrict to dipole-conserving systems in this chapter, we adapt some of our notation accordingly.

We consider a one-dimensional quantum system whose time evolution is generated by a microscopic lattice Hamiltonian $\hat{H}$ that conserves a global U(1) charge $\hat{Q}$ as well as its associated dipole moment $\hat{P}$. Expressed in terms of microscopic charge and energy

densities $\hat{n}_x$ and $\hat{h}_x$, the conserved quantities read

$$\boxed{\hat{H} = \sum_x \hat{h}_x, \quad \hat{Q} = \sum_x \hat{n}_x, \quad \hat{P} = \sum_x x\, \hat{n}_x.} \tag{7.1}$$

Our goal is to formulate a long-wavelength description of transport for the set of conserved quantities (7.1) within linear fluctuating hydrodynamics. In this approach, hydrodynamic equations for the conserved macroscopic densities are combined with noise terms accounting for fluctuations that are generated by the underlying microscopic degrees of freedom.

Let us first consider the continuity equation of a single conserved quantity, such as energy

$$\partial_t e(x,t) = -\partial_x J^e(x,t), \tag{7.2}$$

where $e(x,t)$ and $J^e(x,t)$ are the coarse-grained energy and current densities. Taking the long-wavelength limit, a gradient expansion of the current can be performed. The first order term leads to Fick's law

$$J^e(x,t) = -D_e \partial_x e(x,t). \tag{7.3}$$

Including microscopic current fluctuations $\xi^e(x,t)$, we obtain the fluctuating hydrodynamic equation for a single diffusive mode,

$$\partial_t e(x,t) - D_e \partial_x^2 e(x,t) = B_e \partial_x \xi^e(x,t)\,, \tag{7.4}$$

where space and time are related by the dynamical exponent $z = 2$. We have absorbed the noise strength into the prefactor B_e, such that

$$\langle \xi^e(x,t) \xi^e(x',t') \rangle = \delta(x-x')\delta(t-t') \tag{7.5}$$

describes uncorrelated Gaussian white-noise of unit strength.

As we have seen in the previous chapter, the time evolution of the coarse-grained charge density $n(x,t)$ is drastically modified by dipole conservation. We recall that the fundamental dynamical objects in the system are *dipoles*, a fact we can incorporate by in-

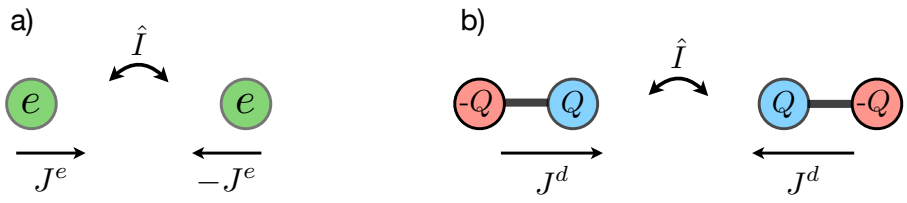

Figure 7.2: Symmetries of local current densities. a) The energy current is odd under inversion $\hat{I}$. **b)** Under inversion a positive dipole moving to the right is turned into a negative dipole moving to the left. As a result, the dipole current is even under inversion.

troducing a coarse-grained dipole current $J^d(x,t)$. We emphasize the change in notation $J^{(1)} \to J^d$ compared to the previous chapter. We have derived the fluctuating hydrodynamics of a single conserved charge combined with general multipole conservation laws previously. Nonetheless, we will find it very helpful in the following to briefly recount the most direct way of obtaining the correct equation specifically for dipole conservation. Importantly, as opposed to a more conventional charge current, $J^d(x,t)$ is *even* under spatial inversion $\hat{I}$, see Fig. 7.2, i.e.,

$$\hat{I}J^d(x,t)\hat{I} = J^d(-x,t). \tag{7.6}$$

Thus, the current transforms under inversion in the same way as the underlying charge density $n(x,t)$, and the corresponding continuity equation assumes the form [2, 389]

$$\partial_t n(x,t) = \partial_x^2 J^d(x,t). \tag{7.7}$$

In the absence of energy conservation, the generalized Fick's law

$$J^d(x,t) = -D_n \partial_x^2 n(x,t) \tag{7.8}$$

then preserves inversion invariance of the resulting hydrodynamic equation, see Eq. (6.38),

$$\partial_t n(x,t) + D_n \partial_x^4 n(x,t) = B_n \partial_x^2 \xi^d(x,t). \tag{7.9}$$

Here, we included dipole-current fluctuations $\xi^d(x,t)$ with

$$\langle \xi^d(x,t)\xi^d(x',t')\rangle = \delta(x-x')\delta(t-t'). \tag{7.10}$$

In systems exhibiting the full set of conserved quantities (7.1), we must find a description that combines Eq. (7.4) and Eq. (7.9) while taking into account possible couplings between the charge and energy densities. This amounts to including cross-terms in the derivative expansion of the currents J^d and J^e:

$$\begin{aligned} J^d &= -D_{nn}\partial_x^2 n - D_{ne}\partial_x^2 e \\ J^e &= -D_{en}\partial_x n - D_{ee}\partial_x e. \end{aligned} \tag{7.11}$$

Eq. (7.11) includes the most relevant (i.e. fewest derivatives) terms compatible with inversion symmetry of the resulting hydrodynamic equations. A potential coupling between the microscopic current fluctuations vanishes: $\xi^e\xi^d$ is odd under inversion according to our previous considerations, such that the expectation value

$$\langle \xi^e \xi^d \rangle = 0 \tag{7.12}$$

in an inversion invariant equilibrium ensemble. Combining Eq. (7.11) with the continuity

equations (7.2, 7.7) and switching to momentum space, our Ansatz becomes

$$\left[\partial_t + k^2 \underline{D}(k)\right] \begin{pmatrix} n \\ e \end{pmatrix} = ik\underline{B}(k) \begin{pmatrix} \xi^d \\ \xi^e \end{pmatrix}, \tag{7.13}$$

where we have defined the matrices

$$\underline{D}(k) = \begin{pmatrix} k^2 D_{nn} & k^2 D_{ne} \\ D_{en} & D_{ee} \end{pmatrix}, \quad \underline{B}(k) = \begin{pmatrix} ikB_n & 0 \\ 0 & B_e \end{pmatrix}. \tag{7.14}$$

As dipole conservation implies a diagonal matrix $\underline{B}(k)$ due to Eq. (7.12), only two of the diffusion constants entering $\underline{D}(k)$ will turn out to be independent. The details leading to this conclusion are presented in Sec. 7.2. In essence, this can be seen by considering the fluctuation-dissipation relation associated with Eq. (7.13):

$$\boxed{\underline{D}(k)\,\underline{C^s} + \underline{C^s}\,\underline{D}^T(k) = \underline{B}(k)\underline{B}^T(-k),} \tag{7.15}$$

where $\underline{C^s}$ is the matrix of static equilibrium correlations, see Eqs. (7.23,7.24) for the formal definition. The Onsager relations for kinetic coefficients require that $\underline{D}(k)\underline{C^s}$ is symmetric (see Sec. 7.2 below). Using Eq. (7.15) this is equivalent to

$$\boxed{C^s_{nn} D_{en} + C^s_{en} D_{ee} = 0,} \tag{7.16}$$

which further implies

$$C^s_{en} D_{nn} + C^s_{ee} D_{ne} = 0. \tag{7.17}$$

When the static equilibrium correlations are known, Eqs. (7.16, 7.17) can be used to determine two of the diffusion constants entering Eq. (7.14).

Solving the coupled hydrodynamic equations (7.13) in the long-wavelength limit predicts the existence of two independent modes, a diffusive energy-only mode as well as a subdiffusive energy-charge mode. In particular, inhomogeneities of the initial state decay according to

$$\boxed{\begin{pmatrix} n(k,t) \\ e(k,t) \end{pmatrix} = a\, e^{-D_{ee}k^2 t} \begin{pmatrix} 0 \\ 1 \end{pmatrix} + b\, e^{-\tilde{D}_{nn}k^4 t} \begin{pmatrix} 1 \\ -\frac{D_{en}}{D_{ee}} \end{pmatrix},} \tag{7.18}$$

where $\tilde{D}_{nn} = D_{nn} - \frac{D_{ne}D_{en}}{D_{ee}}$ is the renormalized subdiffusion constant governing the decay of the mixed energy-charge mode and the constants a, b are fixed by the initial state. In the next sections, we will discuss in detail the arguments leading to the fluctuation dissipation relation of Eq. (7.15) and the conditions of Eqs. (7.16,7.17). Following this discussion we study the dynamics of a specific, strongly interacting bosonic system using nonequilibrium quantum field theory. Within this approach we verify that Eq. (7.18) provides an accurate description of the quantum evolution emerging at late times. Furthermore,

comparing the microscopic dynamics to Eq. (7.18) we can extract the two constants D_{ee} and $\tilde{D}_{nn}$. Together with Eqs. (7.16, 7.17) this allows us to directly link all entries of the diffusion matrix (7.14) to model parameters of the microscopic Hamiltonian.

7.2 Solving the hydrodynamic equations

In the previous section we gave a brief overview of the most important aspects of the hydrodynamic equations in Eq. (7.13). This overview is sufficient to move on to the analysis of a specific quantum field theory with dipole-conserving dynamics in Sec. 7.3 below. Here, we give a detailed analysis of the solution of Eq. (7.13) and the derivation of the associated fluctuation dissipation relations.

7.2.1 General solution

Let us consider the mode-coupled hydrodyamic equation Eq. (7.13) in more detail. Introducing the vector notation

$$\boldsymbol{u}(x,t) = \begin{pmatrix} n(x,t) \\ e(x,t) \end{pmatrix}, \quad \boldsymbol{\xi}(x,t) = \begin{pmatrix} \xi^d(x,t) \\ \xi^e(x,t \end{pmatrix}, \tag{7.19}$$

Eq. (7.13) is written as

$$\big[\partial_t + k^2 \underline{D}(k)\big]\boldsymbol{u}(k,t) = ik\underline{B}(k)\boldsymbol{\xi}(k,t)., \tag{7.20}$$

which becomes in frequency space

$$\big[i\omega\mathbb{1} + k^2 \underline{D}(k)\big]\boldsymbol{u}(k,\omega) = ik\underline{B}(k)\boldsymbol{\xi}(k,\omega). \tag{7.21}$$

We have introduced the 2×2 identity matrix $\mathbb{1}$ in Eq. (7.21) to make its matrix structure explicit. The formal solution to Eq. (7.21) is thus given by

$$\boldsymbol{u}(k,\omega) = ik\big[i\omega\mathbb{1} + k^2 \underline{D}(k)\big]^{-1}\underline{B}(k)\,\boldsymbol{\xi}(k,\omega). \tag{7.22}$$

Using this result, we can obtain the matrix of dynamical correlations between the local densities. They are defined as

$$\begin{aligned} \underline{C}(x,t) &= \begin{pmatrix} C_{nn}(x,t) & C_{ne}(x,t) \\ C_{en}(x,t) & C_{ee}(x,t) \end{pmatrix} := \begin{pmatrix} \langle n(x,t)n(0,0)\rangle & \langle n(x,t)e(0,0)\rangle \\ \langle n(x,t)e(0,0)\rangle & \langle e(x,t)e(0,0)\rangle \end{pmatrix} = \\ &= \langle \boldsymbol{u}(x,t)\boldsymbol{u}^T(0,0)\rangle\,. \end{aligned} \tag{7.23}$$

The static equilibrium correlations are obtained from Eq. (7.23) via

$$\underline{C^s}(x) = \underline{C}(x,0). \tag{7.24}$$

In Fourier space, the dynamical correlations accordingly read

$$\underline{C}(k,\omega) = \int \frac{dxdt}{2\pi} e^{-ikx-i\omega t}\, \underline{C}(x,t) = \int dk' d\omega' \left\langle \boldsymbol{u}(k,\omega)\boldsymbol{u}^T(k',\omega')\right\rangle . \tag{7.25}$$

Using Eq. (7.22), the matrix $\underline{C}(k,\omega)$ can be evaluated as

$$\begin{aligned}\underline{C}(k,\omega) = &\int dk' d\omega' (-kk') \times \\ &\times \left\{ \left[i\omega \mathbb{1} + k^2 \underline{D}(k)\right]^{-1} \underline{B}(k) \left\langle \boldsymbol{\xi}(k,\omega)\boldsymbol{\xi}^T(k',\omega')\right\rangle \underline{B}^T(k') \left[i\omega' \mathbb{1} + (k')^2 \underline{D}^T(k')\right]^{-1} \right\}.\end{aligned} \tag{7.26}$$

Making use of the diagonal nature of the noise correlations,

$$\left\langle \boldsymbol{\xi}(k,\omega)\boldsymbol{\xi}^T(k',\omega')\right\rangle = \mathbb{1}\, \delta(k+k')\, \delta(\omega+\omega'), \tag{7.27}$$

Eq. (7.26) becomes

$$\underline{C}(k,\omega) = k^2 \left[i\omega \mathbb{1} + k^2 \underline{D}(k)\right]^{-1} \underline{B}(k) \underline{B}^T(-k) \left[-i\omega \mathbb{1} + (k)^2 \underline{D}^T(k)\right]^{-1}, \tag{7.28}$$

where we made use of the symmetry $\underline{D}(-k) = \underline{D}(k)$.

7.2.2 Leading order solution

We now diagonalize the diffusion matrix $\underline{D}(k)$,

$$\underline{D}(k) = \underline{V}(k) \underline{\Omega}(k) \underline{V}^{-1}(k), \tag{7.29}$$

where

$$\underline{\Omega}(k) = \begin{pmatrix} \omega_1(k) & 0 \\ 0 & \omega_2(k) \end{pmatrix} \tag{7.30}$$

is a diagonal matrix containing the dispersion of the two hydrodynamic modes. Explicitly, using Eq. (7.14), we obtain to leading order in k:

$$\begin{aligned} \omega_1(k) &= \left(D_{nn} - \frac{D_{ne}D_{en}}{D_{ee}}\right) k^2 + \mathcal{O}(k^4) \\ \omega_2(k) &= D_{ee} + \mathcal{O}(k^2) \\ \underline{V}(k) &= \begin{pmatrix} 1 & 0 \\ -\frac{D_{en}}{D_{ee}} & 1 \end{pmatrix} + \mathcal{O}(k^2). \end{aligned} \tag{7.31}$$

We obtain a subdiffusive mode $k^2\omega_1(k) \sim k^4$ of coupled charge-energy excitations, corresponding to the first column of $\underline{V}(k)$, as well as a diffusive mode $k^2\omega_2(k) \sim k^2$ of pure energy excitations, corresponding to the second column of $\underline{V}(k)$. The leading order solution of Eq. (7.31) is sufficient to determine the decay of inhomogeneities in the course-grained

charge and energy densities, resulting in Eq. (7.18). Interestingly however, the leading order will *not* be sufficient to derive the fluctuation-dissipation relations, for which the *exact* diagonalization of $\underline{D}(k)$ needs to be considered.

7.2.3 Conductivity and Onsager symmetry condition

We consider the conductivity matrix defined by the current correlations

$$\sigma_{ab}(k,\omega) = \frac{\beta}{2}\left\langle j^a(k,\omega) j^b(-k,-\omega)\right\rangle, \tag{7.32}$$

where $j^{a=n,e}$ are now the current densities of *charge* (whose current is obtained from the dipole current through a derivative) and energy. Due to the usual continuity equations, the conductivity matrix is related to the dynamical density correlations via

$$\sigma_{ab}(k,\omega) = \frac{\beta\omega^2}{2k^2} C_{ab}(k,\omega). \tag{7.33}$$

In particular, using the leading order results from Eq. (7.31) for the density correlations of Eq. (7.37), we can directly evaluate the zero-momentum conductivity in the static limit,

$$\lim_{\omega\to 0} \sigma(k=0,\omega) = \frac{\beta}{2}\begin{pmatrix} 0 & 0 \\ 0 & B_e^2 \end{pmatrix}. \tag{7.34}$$

As expected, only the diffusive energy mode sustains a finite conductivity. Furthermore, due to the reversability of the microscopic time evolution, the Onsager symmetry relations require that the conductivity matrix $\underline{\sigma}(k,\omega)$ be symmetric. Within an exact diagonalization of the diffusion matrix in Eq. (7.28) for the dynamical correlations, we obtain

$$\sigma_{ne}(k,\omega) - \sigma_{en}(k,\omega) \propto B_e^2 D_{ne} - B_n^2 D_{en}, \tag{7.35}$$

and must therefore set

$$B_e^2 D_{ne} = B_n^2 D_{en} \tag{7.36}$$

in order to obtain a symmetric conductivity matrix.

We remark that we can formally also define a 'dipole conductivity' via the correlations of the dipole current J^d, $\sigma_{dd} := \lim_{\omega\to 0}\lim_{k\to 0}\frac{\beta}{2}\left\langle J^d(k,\omega)J^d(-k,-\omega)\right\rangle$. Evaluating this expression yields a finite dipole conductivity $\sigma_{dd} = \frac{\beta}{2}B_n^2$, consistent with a diffusive motion of dipoles through the system as observed in the automaton dynamics of the previous chapter.

7.2.4 Static correlations

By inserting the diagonalization of $\underline{D}(k)$ from Eq. (7.29) into Eq. (7.28) we obtain

$$\begin{aligned}&\underline{C}(k,\omega) = \\ &= k^2\underline{V}(k)\big[i\omega\mathbb{1} + k^2\underline{\Omega}(k)\big]^{-1}\underline{V}^{-1}(k)\underline{B}(k)\underline{B}^T(-k)(\underline{V}^{-1})^T(k)\big[-i\omega\mathbb{1} + k^2\underline{\Omega}(k)\big]^{-1}\underline{V}^T(k).\end{aligned} \tag{7.37}$$

We now define

$$\begin{aligned}[p_1(\omega) &:= i\omega + \omega_1(k)]^{-1} \\ [p_2(\omega) &:= i\omega + \omega_2(k)]^{-1},\end{aligned} \tag{7.38}$$

as well as the symmetric matrix

$$\mathcal{M} := \underline{V}^{-1}(k)\underline{B}(k)\underline{B}^T(-k)(\underline{V}^{-1})^T(k). \tag{7.39}$$

We can then express Eq. (7.37) as

$$\underline{C}(k,\omega) = \underline{V}(k)\begin{pmatrix}\mathcal{M}_{11}\,p_1(\omega)p_1(-\omega) & \mathcal{M}_{12}\,p_1(\omega)p_2(-\omega)\\ \mathcal{M}_{21}\,p_2(\omega)p_1(-\omega) & \mathcal{M}_{22}\,p_2(\omega)p_2(-\omega)\end{pmatrix}\underline{V}^T(k). \tag{7.40}$$

Now, from Eq. (7.40) and using that

$$\int d\omega\, p_i(\omega)p_j(-\omega) = \frac{2}{\omega_i(k)+\omega_j(k)}, \tag{7.41}$$

the static equilibrium correlations become

$$\underline{C^s}(k) = \int d\omega\,\underline{C}(k,\omega) = \underline{V}(k)\begin{pmatrix}2\mathcal{M}_{11}\,[\omega_1(k)]^{-1} & \mathcal{M}_{12}\,[\omega_1(k)+\omega_2(k)]^{-1}\\ \mathcal{M}_{21}\,[\omega_1(k)+\omega_2(k)]^{-1} & 2\mathcal{M}_{22}\,[\omega_2(k)]^{-1}\end{pmatrix}\underline{V}^T(k). \tag{7.42}$$

Explicitly, the components of $\underline{C^s}(k)$ read

$$\begin{aligned}C^s_{nn}(k) &= \frac{B_e^2D_{ne}^2k^2 + B_n^2(D_{ee}^2 - D_{ne}D_{en}k^2 + D_{nn}D_{ee}k^2)}{(D_{nn}D_{ee}-D_{ne}D_{en})(D_{ee}+D_{nn}k^2)}\\ C^s_{ee}(k) &= \frac{B_n^2D_{en}^2 + B_e^2(-D_{ne}D_{en} + D_{nn}D_{ee} + D_{nn}^2k^2)}{(D_{nn}D_{ee}-D_{ne}D_{en})(D_{ee}+D_{nn}k^2)}\\ C^s_{en}(k) = C^s_{ne}(k) &= -\frac{B_n^2D_{en}D_{ee} + B_e^2D_{nn}D_{ne}k^2}{(D_{nn}D_{ee}-D_{ne}D_{en})(D_{ee}+D_{nn}k^2)}.\end{aligned} \tag{7.43}$$

Inspecting Eq. (7.43) we might be led to think that the static correlations have a non-trivial momentum-space dependence, which would lead to a spatial profile at time $t = 0$ that is not a sharply localized delta distribution. However, we see that the k-dependence in Eq. (7.43) is removed upon taking into account the Onsager symmetry relations of

Eq. (7.36), such that

$$\begin{aligned} C^s_{nn} &= \frac{B_n^2 D_{ee}}{D_{nn}D_{ee} - D_{ne}D_{en}} \\ C^s_{ee} &= \frac{B_e^2 D_{nn}}{D_{nn}D_{ee} - D_{ne}D_{en}} \\ C^s_{ne} &= C^s_{en} = \frac{B_n^2 D_{en}}{-D_{nn}D_{ee} + D_{ne}D_{en}} \end{aligned} \tag{7.44}$$

The static correlations are thus independent of k as required.

7.2.5 Fluctuation dissipation relation

In order to state the fluctuation dissipation relation for this systems of coupled hydrodynamic modes, we point out that we can interpret Eq. (7.20) as two coupled diffusive modes in which the charge mode has a scale-dependent diffusion constant. The natural candidate for the form of the fluctuation dissipation relations in our setup is then given by

$$\underline{D}(k)\,\underline{C^s} + \underline{C^s}\,\underline{D}^T(k) = \underline{B}(k)\underline{B}^T(-k), \tag{7.45}$$

which differs with respect to the more conventional case of two diffusive modes only through the additional k-dependence of $\underline{D}(k)$ and $\underline{B}(k)$. It can readily be verified that Eq. (7.45) indeed holds by inserting the static correlations $\underline{C^s}$ derived in Eq. (7.44). Eq. (7.45) thus represents the fluctuation dissipation relations in the system.

We remark that Eq. (7.45) also holds when inserting the (formally k-dependent) static correlations $\underline{C^s}(k)$ of Eq. (7.43), even before making use of the symmetry condition Eq. (7.36). This shows that the fluctuation dissipation relation and Onsager symmetry are a priori independent: The fluctuation dissipation relation follows from the hydrodynamic equations Eq. (7.20) alone, while Onsager symmetry is a more general consequence of microscopic time reversal symmetry. An equivalent form of the Onsager symmetry condition in our system demands that the matrix $\underline{D}(k)\underline{C^s}(k)$ of kinetic coefficients be symmetric. This leads to the equations

$$C^s_{nn}(k)D_{en} + C^s_{en}(k)D_{ee} = 0, \tag{7.46}$$

and

$$C^s_{en}(k)D_{nn} + C^s_{ee}(k)D_{ne} = 0. \tag{7.47}$$

By inserting the form Eq. (7.43) of the static correlations it can then be verified explicitly that the condition of Eq. (7.46) and that of Eq. (7.36) are in fact equivalent. Eqs. (7.46,7.47) determine two of the four constants entering the diffusion matrix $\underline{D}(k)$.

7.3 A bosonic quantum field theory

In the previous two sections we derived a coupled hydrodynamic theory for a subdiffusive charge mode in the presence of dipole-conservation as well as a diffusive energy mode. In this section we verify the accuracy of this hydrodynamic description in a bosonic quantum system with conserved dipole moment. The time evolution of the bosonic lattice model is evaluated using nonequilibrium quantum field theory on the Keldysh contour.

7.3.1 Model

We study a bosonic one-dimensional lattice Hamiltonian with dipole conservation,

$$\boxed{H = \underbrace{J\Big(\sum_i \hat{\phi}_{i-1}^\dagger \hat{\phi}_i^2 \hat{\phi}_{i+1}^\dagger + \text{h.c.}\Big)}_{H_{\text{pair}}} + \underbrace{U\sum_i \hat{n}_i(\hat{n}_i - 1)}_{H_U},} \tag{7.48}$$

where $\hat{\phi}_i^\dagger/\hat{\phi}_i$ denote bosonic creation/annihilation operators at site i and $\hat{n}_i = \hat{\phi}_i^\dagger\hat{\phi}_i$ are the corresponding occupation number operators. The first term describes a short-ranged and dipole-conserving hopping of bosons which can be interpreted as a kinetic term for particle-hole pairs. The second term constitutes a local repulsion between bosons. We note that the equilibrium phase diagram of this dipole-conserving Bose-Hubbard model has recently been discussed in Ref. [485]. We consider fillings above unity, where hydrodynamic behaviour is not expected to be inhibited by effects such as localization due to strong Hilbert space fragmentation [206, 235]. This regime is challenging to investigate by numerical methods such as exact diagonalization and matrix product states due to the unrestricted local Hilbert space dimension, the rapid build up of entanglement, as well as the large systems and late times that are in general required to reach the hydrodynamic regime. In the following we consider a nonequilibrium field theoretic approach that overcomes these limitations at the expense of approximating interaction effects.

7.3.2 Nonequilibrium field theory approach

We provide a brief, high level overview of the field theoretic approach employed in Ref. [6] to study the the time evolution of charge and energy in the model of Eq. (7.48). For details on the method and its implementation for the dipole-conserving system at hand we refer to Ref. [6].

We start from the microscopic action

$$S[\phi] = \int_{\mathcal{C}} dt \sum_i \overline{\phi}_i i\partial_t \phi_i - H(\overline{\phi}, \phi), \tag{7.49}$$

where the time integral runs along the Schwinger-Keldysh contour $\mathcal{C}$ and $H(\overline{\phi}, \phi)$ denotes

the normal-ordered Hamiltonian. The operators $\hat{\phi}_i$ ($\hat{\phi}_i^\dagger$) have been replaced by complex fields ϕ_i ($\bar{\phi}_i$). All quartic terms are removed by a Hubbard-Stratonovich transformation, which introduces a complex decoupling field χ for the correlated hopping term H_{pair} as well as a real decoupling field Δ for the onsite interaction term H_U. The action is expressed as

$$\begin{aligned} S[\phi,\chi,\Delta] = \int_{\mathcal{C}} dt \sum_i \Big\{ \overline{\phi}_i i\partial_t \phi_i + \sum_j \overline{\chi}_i V_{ij}^{-1} \chi_j + \frac{1}{2}\Delta_i U^{-1} \Delta_i \\ - \sqrt{2}\big(\overline{\chi}_i \overline{\phi}_i \phi_{i+1} + \overline{\phi}_{i+1}\phi_i\chi_i + \overline{\phi}_i\phi_i\Delta_i\big)\Big\}, \end{aligned} \tag{7.50}$$

with the matrix $V_{ij} = \frac{1}{2}(\delta_{i,j+1} + \delta_{i,j-1})$. In order to characterize the dynamics of charge and energy density we would like to compute the connected correlation functions

$$\begin{aligned} G_{ij}(t_1,t_2) =& \Big\langle T_{\mathcal{C}}\, \overline{\phi}_i(t_1)\phi_j(t_2)\Big\rangle, \quad D_{ij}(t_1,t_2) = \Big\langle T_{\mathcal{C}}\, \overline{\chi}_i(t_1)\chi_j(t_2)\Big\rangle \\ O_{ij}(t_1,t_2) =& \Big\langle T_{\mathcal{C}}\, \Delta_i(t_1)\Delta_j(t_2)\Big\rangle, \end{aligned} \tag{7.51}$$

where $T_{\mathcal{C}}$ denotes time ordering on the Keldysh contour. The nonequilibrium field theory approach is now based on deriving effective equations of motion for the correlations in Eq. (7.51). This is achieved via the 2PI effective action Γ^{2PI}, which generates such equations of motion through a stationarity condition [486]

$$\frac{\delta\Gamma^{\text{2PI}}[G,D,O]}{\delta K_{ij}(t_1,t_2)} = 0, \tag{7.52}$$

for $K = G, D, O$. Thus, the central object of this approach is the effective action Γ^{2PI}, which can be decomposed into 1-loop mean field contributions $\Gamma^{(\text{1loop})}$ and higher order contributions Γ_2 that are given by the sum over all vacuum 2PI diagrams [487, 488]. Approximating this by a subset of 2PI diagrams respects the underlying microscopic symmetries and global conservation laws [489], which in our case is crucial as we are interested in transport properties. For our model, Γ_2 is approximated in a $1/N$ expansion in the number of real field components ($N = 2$ here) to next-to-leading order, which constitutes a non-perturbative approximation including arbitrarily high orders in the interactions [457, 486, 488, 490–499]. Within this approximation the equations of motion are derived through Eq. (7.52). They are then solved numerically, see Ref. [6], with a complexity that generally scales quadratically in the simulated time and in the number of lattice sites.

7.3.3 Numerical analysis: Coupled hydrodynamics

Initial states

In order to verify the predictions made by the coupled hydrodynamic theory of Eq. (7.18), we want to study the dynamics of charge- and energy-inhomogeneities independently. Within the above 2PI field theory approach this can be achieved by constructing the initial states [6]

$$\rho = \bigotimes_i \exp\left\{-\beta_i(U\hat{n}_i(\hat{n}_i - 1) - \mu_i\hat{n}_i)\right\}. \tag{7.53}$$

Due to the uncorrelated nature of these states between different lattice sites, they have vanishing energy with respect to the correlated hopping term of the Hamiltonian. At the same time, β_i controls the local density fluctuations which carry energy under the density interaction term of the Hamiltonian. Therefore, adjusting the spatial profiles of inverse temperature β_i and chemical potential μ_i in the states Eq. (7.53) allows us to vary the energy and charge profiles of the initial state independently.

Charge subdiffusion

With the nonequilibrium quantum field theory and the possibility to implement the initial states Eq. (7.53) at hand, we can probe the dynamics of charge excitations. To this end, we start from an initial with an excess charge at site $i = 0$ on top of a homogeneous background with charge density n_B, leading to a profile $\langle n\rangle_i(t = 0) = n_B + \delta_{i,0}$. We then follow the profile $n_i(t)$ as a function of time, see Fig. 7.3. We find that already after relatively short time scales $t \gtrsim \mathcal{O}(1)$ (in units of the correlated hopping J) hydrodynamic behavior starts to emerge. Performing a scaling collapse of the charge profile, the dynamic exponent is indeed $z = 4$ as expected. In addition, the charge profile is clearly non-Gaussian and exhibits the oscillations characteristic of dipole-conserving hydrodynamics as derived in the previous chapter. In practice, the subdiffusive dynamical exponent $z = 4$ is very robust within the numerical quantum field theory simulations, both upon varying the background density n_B as well as the strength U of the onsite interactions.

If we set the bosonic density interaction $U > 0$, we expect that a local charge excitation also leads to a local excitation in the energy density. Upon varying U, we find that the charge dynamics merely experiences a renomralized diffusion constant; see Eq. (7.18). In contrast, for finite U the energy density couples to the charge density and is consequently dominated by the same subdiffusion at late times. This confirms our expectation that a subdiffusive mixed charge-energy-mode should exist. We then naturally expect that the strength of this mixing is proportional to U for small values of the onsite interaction, i.e. $D_{en}/D_{ee} \sim U$.

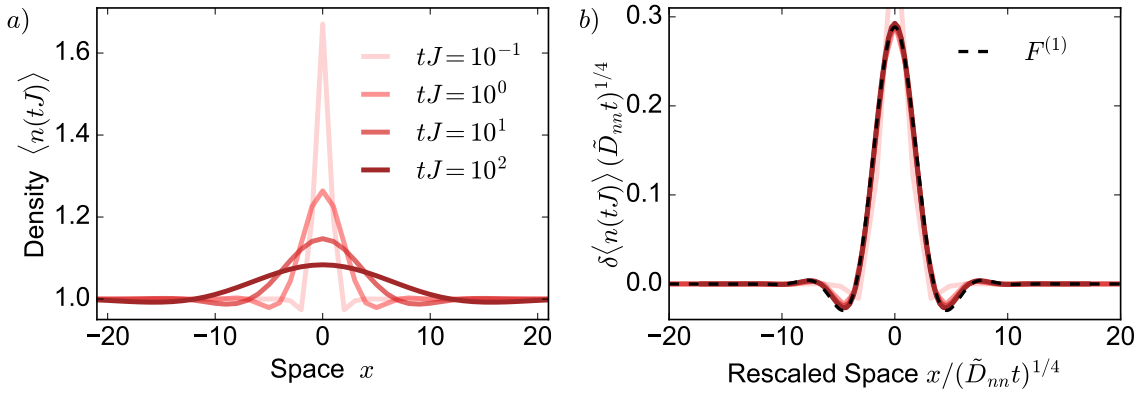

Figure 7.3: Charge dynamics. a) The time evolution of the charge profile at different times starting from an initial state with a localized excess charge on site $x = 0$. b) The rescaled charge profile collapses to the expected scaling function $F^{(1)}$ for dipole-conserving systems. The scaling collaps clearly shows a dynamical exponent $z = 4$.

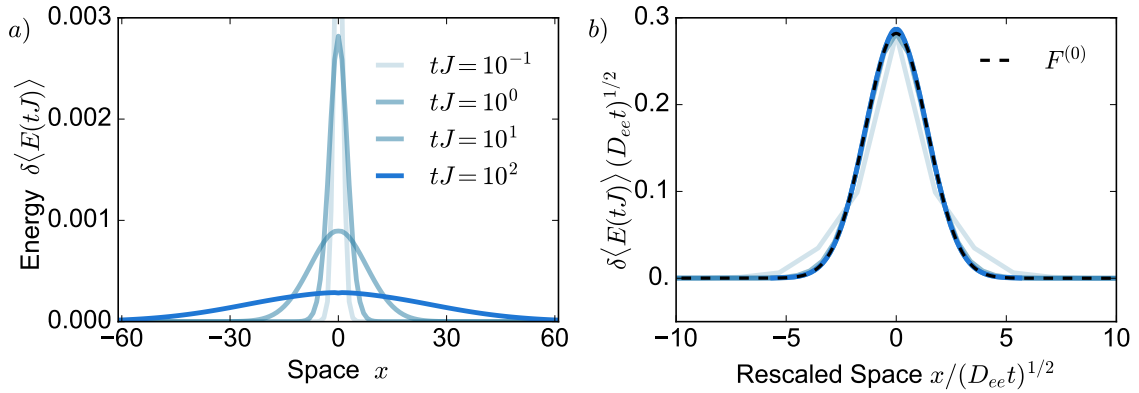

Figure 7.4: Energy dynamcis. a) The profile of the energy density at different times starting from an initial state with localized excess energy at $x = 0$ but with *homogeneous* charge density profile. b) A scaling collapse of the energy density profile reveals a Gaussian shape broadening according to a dynamical exponent $z = 2$.

Energy diffusion

In order to verify the predicted emergence of a second, diffusive pure energy mode, we now prepare initial states with *homogeneous* charge density n_B but a highly localized energy inhomogeneity at site $i = 0$. Intuitively, these are states where locally, particle number fluctuations are enhanced although the average occupation remains at n_B. The time evolution of the energy profile is depicted in Fig. 7.4. The height of the pure-energy excitation decays as $t^{-1/2}$ while the profile exhibits a scaling collapse to a Gaussian $F^{(0)}(x) = \frac{1}{\sqrt{2\pi}} e^{-x^2/2}$ as expected. These results qualitatively confirm the validity of the coupled hydrodynamic description of Eq. (7.18). Physically, the diffusive pure energy mode, which becomes the only energy mode for $U = 0$, is consistent with the diffusive motion of dipoles in the system: While there is no microscopic local dipole density in the system that directly reflects this process, diffusive dipole motion formally manifests itself in a formally finite dipole-conductivity as discussed in Sec. 7.2.3.

7.3.4 Numerical analysis: Elements of the diffusion matrix

As we have seen the microscopic model considered in this chapter allows us to directly connect the microscopics of the Hamiltonian with the macroscopic emergent hydrodynamics. We can therefore use our approach to extract the elements of the diffusion matrix $\underline{D}(k)$ of Eq. (7.14), and connect them with the microscopic parameters entering the lattice Hamiltonian Eq. (7.48). Before considering the numerical results of the 2PI field theory approach, we formulate some qualitative expectations for the scaling of the elements of $\underline{D}(k)$ with the parameters of our model.

Proper units

As our goal is to extract the elements of the diffusion matrix $\underline{D}(k)$ of Eq. (7.14) in the following, let us briefly discuss the proper units in which these elements should be given. Inspecting the decay of inhomogeneities in Eq. (7.18) and taking into account that the lattice spacing (as well as $\hbar$) was set to unity, it is clear that both $\tilde{D}_{nn}$ and D_{ee}, and thus also D_{nn}, can be measured in units of the correlated hopping energy scale J,

$$[D_{nn}] = [D_{ee}] = [J]. \tag{7.54}$$

The units of the remaining two constants D_{ne} and D_{en} can then be inferred from the Onsager symmetry conditions Eqs. (7.46,7.47),

$$\begin{aligned} [D_{en}] &= [C^s_{en}] + [D_{ee}] - [C^s_{nn}] = [J] + [J] - 0 = [J^2] \\ [D_{ne}] &= [C^s_{en}] + [D_{nn}] - [C^s_{ee}] = [J] + [J] - [J^2] = 0. \end{aligned} \tag{7.55}$$

Here, we have used that $[C^s_{en}] = [J]$, $[C^s_{ee}] = [J^2]$ and $[C^s_{nn}] = 0$ for the static correlations.

Scaling with correlated hopping J

Eqs. (7.54,7.55) provide us with the correct units of the diffusion matrix elements but are also indicative of the expected scaling of these elements with J. In particular, if we write the Hamiltonian Eq. (7.48) at some *fixed* ratio of U/J as

$$H = J \sum_i \Big\{ (\hat{\phi}^\dagger_{i-1} \hat{\phi}^2_i \hat{\phi}^\dagger_{i+1} + \hat{\phi}_{i-1} (\hat{\phi}^\dagger_i)^2 \hat{\phi}_{i+1} + \frac{U}{J} \hat{n}_i (\hat{n}_i - 1) \Big\}, \tag{7.56}$$

J becomes the only energy scale in the problem. Hence, on purely dimensional grounds we expect

$$D_{nn} \propto J, \quad D_{ee} \propto J, \quad D_{en} \propto J^2, \quad D_{ne} \propto J^0. \tag{7.57}$$

Eq. (7.57) can also be demonstrated explicitly: Let us consider a rescaling of J in Eq. (7.56) as $J \to cJ$ with some constant $c > 0$. This rescales the Hamiltonian $\hat{H} \to c\hat{H}$

and thus also the local energy density $e(x,t) \rightarrow e'(x,t) = c\,e(x,t)$. Starting from a given initial state, the rescaling of the Hamiltonian is equivalent to a rescaling of time, $\exp\{-i(c\hat{H})t\} = \exp\{-i\hat{H}(ct)\}$. The decay of inhomogeneities in the local charge density $n(x,t)$ and rescaled energy density $e'(x,t) = c\,e(x,t)$ is thus given simply by rescaling the time in Eq. (7.18) and multiplying the second line on its right hand side by the constant c:

$$\begin{pmatrix} n(k,t) \\ e'(k,t) \end{pmatrix} = a\, e^{-D_{ee}k^2 ct} \begin{pmatrix} 0 \\ c \end{pmatrix} + b\, e^{-\tilde{D}_{nn}k^4 ct} \begin{pmatrix} 1 \\ -\frac{D_{en}}{D_{ee}}c \end{pmatrix}. \tag{7.58}$$

At the same time, the dynamics of $n(x,t)$ and $e'(x,t)$ should be characterized by new effective diffusion constants D'_{nn}, $D'_{ne'}$, $D'_{e'n}$, $D'_{e'e'}$ and new initial conditions a', b',

$$\begin{pmatrix} n(k,t) \\ e'(k,t) \end{pmatrix} = a'\, e^{-D'_{e'e'}k^2 t} \begin{pmatrix} 0 \\ 1 \end{pmatrix} + b'\, e^{-\tilde{D}'_{nn}k^4 t} \begin{pmatrix} 1 \\ -\frac{D'_{e'n}}{D'_{e'e'}} \end{pmatrix}. \tag{7.59}$$

Direct comparison of Eq. (7.58) and Eq. (7.59) leads to the relations

$$\begin{aligned} a' = ca, \quad b' = b \\ \tilde{D}'_{nn} = c\tilde{D}_{nn}, \quad D'_{e'e'} = cD_{ee}, \quad \frac{D'_{e'n}}{D'_{e'e'}} = c\frac{D_{en}}{D_{ee}}. \end{aligned} \tag{7.60}$$

The latter two relations in the second line of Eq. (7.60) then imply

$$D'_{e'n} = c^2 D_{en}. \tag{7.61}$$

Together with the first relation in the second line of Eq. (7.60) this leads to

$$D'_{nn} = cD_{nn}, \quad D'_{ne'} = D_{ne}, \tag{7.62}$$

Together, Eqs. (7.60-7.62) reproduce our expectation Eq. (7.57).

Static correlations

The static infinite temperature correlations C^s_{ab} can be calculated analytically for the model of Eq. (7.48). They are given by

$$C^s_{nn} = \langle \hat{n}_i \hat{n}_i \rangle, \quad C^s_{ne} = C^s_{en} = \langle \hat{e}_i \hat{n}_i \rangle, \quad C^s_{ee} = \langle \hat{e}_i \hat{e}_i \rangle, \tag{7.63}$$

Here, the local energy density has been defined as

$$\hat{e}_i = h^U_i + \frac{1}{4}(\hat{h}^J_{i-1} + \hat{h}^J_{i-1}) + \frac{1}{2}\hat{h}^J_i, \tag{7.64}$$

with

$$h_i^U = U\hat{n}_i(\hat{n}_i - 1)$$
$$h_i^J = J\hat{\phi}_{i-1}^\dagger \hat{\phi}_i^2 \hat{\phi}_{i-1}^\dagger + h.c. \tag{7.65}$$

Notice that $\sum_i \hat{e}_i = \hat{H}$ as required. The density matrix at infinite temperature is given by $\rho = \frac{1}{Z} e^{-\beta\mu \sum_i \hat{n}_i}$, with $\beta\mu$ (for $\beta \to \infty$) such that $\langle \hat{n}_i \rangle = n_B$. From this density matrix we can compute the static correlations,

$$C_{nn}^s = n_B^2 + n_B$$
$$C_{en}^s = C_{ne}^s = U(4n_B^3 + 4n_B^2) \tag{7.66}$$
$$C_{ee}^s = 4U^2(5n_B^4 + 6n_B^3 + n_B^2) + 4J^2 n_B^2(n_B^2 + 2n_B + 1)$$

Extracting the diffusion matrix from numerical data

Finally, we consider the numerical results from our quantum field theory approach. From the time evolution and the decay of initially localized charge- and energy-excitations, we can fit the (sub)diffusion constants $\tilde{D}_{nn}$ and D_{ee} according to Eq. (7.18) upon Fourier transforming the k-space solutions back to real space.

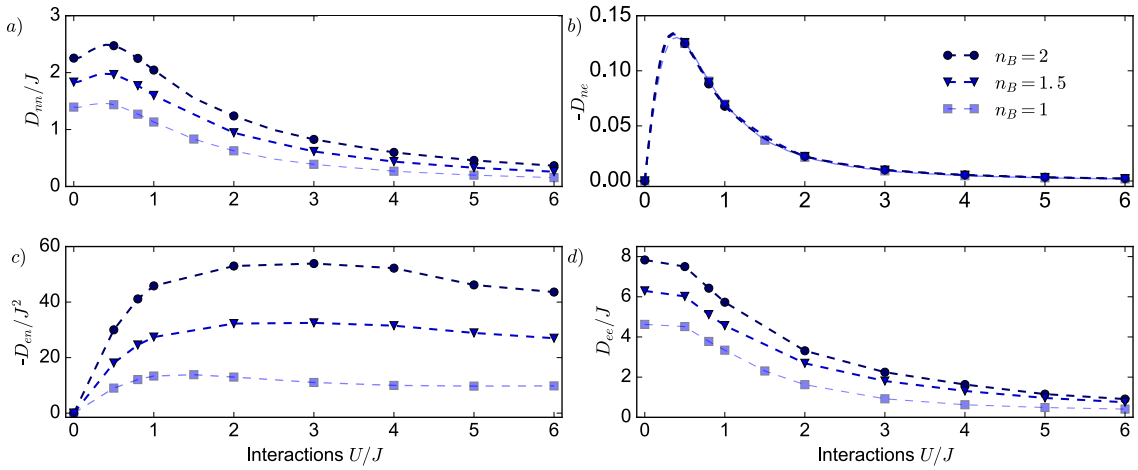

Figure 7.5: Diffusion matrix. The numerically determined values of the entries of the diffusion matrix Eq. (7.14) at infinite temperature, as functions of the local interaction strength U/J and for different average charge densities n_B. The different panels show **a)** D_{nn}, **b)** D_{ne}, **c)** D_{en}, and **d)** D_{ee}. a) Charge-charge diffusion constant D_{nn} governing the subdiffusive decay of charge excitations. The entry D_{ne} in **b)** was obtained using the Onsager relations. Dashed lines are obtained by applying Eq. (7.17) to a linear interpolation between the available numerical data points.

There are then several ways to extract the off-diagonal diffusion constant D_{en}. Here we choose to take an initial state with non-zero (but small) dipole moment and evolve to very late times, such that the steady state is reached. Similar to our arguments of Sec. 6.2 in the previous chapter, the steady state profile of both charge and energy density can be derived by setting the currents $J^d = J^e = 0$ to zero in equilibrium. Using this condition in

the hydrodynamic expansion of (7.11) results in linearly tilted charge *and* energy profiles in the long time limit, i.e.

$$\begin{aligned} n_{\text{eq}}(x) &= n_B + t_n x \\ \epsilon_{\text{eq}}(x) &= \epsilon_B + t_\epsilon x. \end{aligned} \tag{7.67}$$

The ratio of the two tilts t_n and t_e, if non-zero, is related to elements of the diffusion matrix as

$$\frac{D_{en}}{D_{\epsilon\epsilon}} = -\frac{t_\epsilon}{t_n}. \tag{7.68}$$

Due to the minus sign in this relation, we see that $D_{en} < 0$. Numerically, we can extract both the charge and energy density tilt and obtain the off-diagonal constant D_{en} through Eq. (7.68). We numerically find a parameter dependence of steady state tilt ratios as $D_{en}/D_{ee} = -t_\epsilon/t_n \approx -4Un_B$. This result coincides precisely with what is predicted by the Onsager symmetry Eq. (7.16) upon inserting the static equilibrium correlations at infinite temperature that we have calculated. We have thus demonstrated the emergence of the Onsager relations from our microscopic approach. Accordingly, within our hydrodynamic model we can then use Eq. (7.17) to determine also the diffusion constants D_{nn}, D_{ne} in terms of the numerically extracted value for $\tilde{D}_{nn}, D_{ee}, D_{en}$. We show all entries of the diffusion matrix as functions of interaction strength U and background charge density in Fig. 7.5.

Keeping the filling fixed, Fig. 7.5 shows that both diagonal entries of the diffusion matrix eventually become small as the interaction strength U becomes large. This agrees with our expectation that $U \to \infty$ corresponds to a Mott limit where the dynamics comes to a halt entirely. In addition, we see our expectation confirmed that the off-diagonal entries of the diffusion matrix vanish at $U = 0$. In this limit, charge and energy modes decouple.

In contrast, keeping the interaction strength fixed as we vary the charge density n_B of the system, excitations becomes more mobile and we find that within our numerics, both diagonal diffusion constants increase approximately linearly with n_B for $n_B \gtrsim 1$. We interpret this feature as a result of Bose-enhancement for increasing filling.

Finally, we remark that in principle, if the filling n_B is sufficiently small, effects of Hilbert space fragmentation in this dipole-conserving model should become relevant as the bosons can no longer find nearby particles to coordinate their movement with, leading to extremely slow relaxation or even localization [206, 235]. However, such features are beyond the field theory approach used here.

7.4 Conclusions & outlook

In this chapter we have studied the emergent, coupled hydrodynamics of charge and energy in a system of dipole-conserving lattice bosons at infinite temperature. We have confirmed the presence of a subdiffusive mode of mixed charge and energy excitations,

as well as a diffusive pure energy mode. The quantum field theoretic results were found to be well captured by an effective hydrodynamic model, which allowed us to extract the dependence of the generalized diffusion matrix on the parameters of the microscopic Hamiltonian.

We emphasize that our general hydrodynamic description is qualitatively independent of microscopic details. In particular, as noted in previous works on dipole-conserving hydrodynamics [2, 389] and in the previous chapter, the subdiffusion of charge with $z = 4$ is in agreement with an experimental study in a two-dimensional fermionic system in the presence of a tilted potential [197]. The associated Hamiltonian, described also in Sec. 2.3.3, is given by $\hat{H} = \hat{H}_{\mathrm{FH}} + F \sum_{\boldsymbol{r}} r_x \hat{n}_{\boldsymbol{r}}$, where $\hat{H}_{\mathrm{FH}}$ is the usual Fermi-Hubbard model. More generally and independent of whether we consider bosons or fermions and 1D or 2D, the center of mass (or dipole moment) in such a tilted setup is expected to be a conserved quantity up to times $\tau \sim \exp(F/t)$, i.e., exponentially long in the tilt strength, by the arguments of prethermalization [236, 320–322] (t is the usual single-particle hopping). Within this timescale the dynamics is governed by a dipole-conserving effective Hamiltonian, such as Eq. (7.48), with correlated hopping strength $J \sim U(t/F)^2$ in a basis obtained from the Schrieffer-Wolff transformation. Both the number of particles as well as their non-tilt energy are conserved densities in this basis. If the prethermal timescale τ is longer than the local thermalization time of the resulting effective dipole Hamiltonian, the coupled hydrodynamic theory of Eq. (7.13) will be applicable to these two modes. Our results should then be viewed as the system's 'prethermal hydrodynamics.' Whether the above condition is satisfied might be verified in quantum gas microscopes by measuring the fluctuations of the dipole moment. In addition, it is an interesting open question how the dynamics of the off-diagonal correlated hopping, and thus the energy, could be measured in cold atom quantum simulation experiments.

After the timescale of prethermalization the dipole moment is no longer strictly conserved; tilt energy and non-tilt energy of the effective Hamiltonian will then be converted into one another. Therefore, at the longest times the diffusive non-tilt energy ceases to be a well defined hydrodynamic mode as shown in Ref. [389]. Nevertheless, in this late-time regime the coarse-grained charge dynamics is still governed by an emergent hydrodynamic description equivalent to the hydrodynamics of dipole-moment conserving systems, leading to a subdiffusive mode with $z = 4$ [197, 389]. It is an interesting question for future work to determine whether this dynamical crossover has an impact on the value of the charge subdiffusion constant $\tilde{D}_{nn}$.

8

Critically slow operator spreading in constrained many-body systems

This chapter is based on the publication

> Johannes Feldmeier, Michael Knap, *"Critically slow operator spreading in constrained many-body systems"*, Phys. Rev. Lett. 127, 235301 (2021)

Structure, text and figures have been adapted for the purposes of this thesis.

The previous chapters have demonstrated that fractonic systems with dipole-conservation laws indeed feature exotic out-of-equilibrium dynamics, characterized by a novel universality class of hydrodynamic transport. However, in recent years it has been realized that hydrodynamic descriptions apply not only to emergent transport in generic interacting quantum many-body systems, but also to entanglement growth [61, 62, 225–227] and operator spreading [63–66, 189, 224]. The key characteristics of these processes at late times and long length scales are qualitatively independent of microscopic details [61, 63, 64]. As such, they can be captured in minimal models of random unitary circuits, which we have already seen to be simpler to handle – both analytically and numerically – than microscopic Hamiltonians. Once again, the central ingredient entering such models is the structure of their conservation laws which can qualitatively affect the aforementioned processes. For example, random unitary circuit studies have shown that the ballistically moving front of out-of-time-ordered correlations (OTOCs), which characterize the spatial spreading of operators, is augmented by algebraic tails caused by global $U(1)$ charge conservation [65, 66]. Given this impact of charge conservation on OTOCs and our results from previous chapters, it is natural to raise the interesting question whether the presence of a fractonic dipole conservation law may also affect the uni-

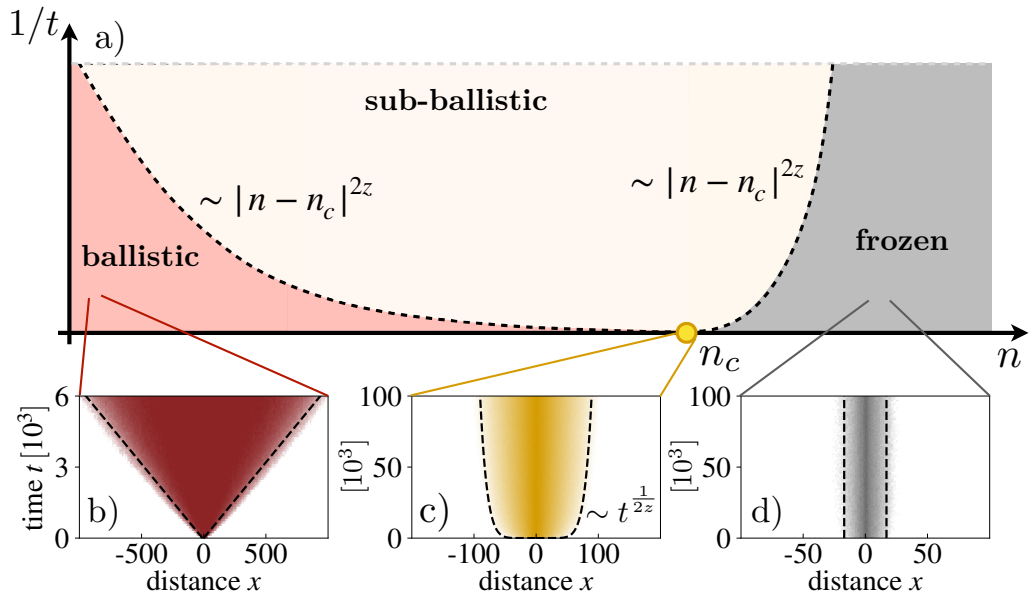

Figure 8.1: Dynamical phase diagram of operator spreading. Our dipole conserving system exhibits a localization transition at a critical density n_c. In the limit of long time scales, operators spread ballistically on the ergodic side $n < n_c$, and are frozen on the non-ergodic side $n > n_c$ of the transition. At the critical density, the operator front spreads sub-ballistically as $\sim t^{1/2z}$ with $z = 4$. The lower panels show the associated OTOC; Eq. (8.3). The sub-ballistic spread is visible also away from the critical density at finite times within a 'critical fan', bounded by a crossover time that diverges as $|n - n_c|^{-2z}$ upon approaching the transition.

versal aspects of operator dynamics.

In this chapter, we find such new behavior in the operator dynamics of a one-dimensional, dipole-conserving chain. As demonstrated in Ref. [206], such systems can be tuned from an ergodic phase with subdiffusive transport to a localized/strongly fragmented phase as a function of density. As the dynamics of operators is expected to exhibit universality, we can resort to the use of classically simulable automaton circuits [205, 386–388, 500] to determine the spread of the operator front in these different regimes. For more details on the numerical evaluation of OTOCs in such classically simulable circuits we refer to App. A.3. We find that while the OTOC front propagates ballistically at long times in the ergodic phase and freezes in the localized phase, the critical point between the two phases is characterized by a *sub-ballistic* spread, see Fig. 8.1. We provide a phenomenological model that explains these numerical results via the effects of long-lived and localized rare regions, leading to a description of the moving operator front in terms of a biased random walk with long waiting times.

8.1 Model and automaton circuit evolution

We focus on a one-dimensional chain of length L with 3-state onsite Hilbert space. The computational basis states are denoted by $|\boldsymbol{n}\rangle = |(n_{-L/2}, ..., n_{L/2-1})\rangle$, where $n_x \in \{0, 1, 2\}$ labels the local qutrit basis. Defining the occupation number operators $\hat{Z}_x$ via $\hat{Z}_x |\boldsymbol{n}\rangle =$

$n_x |\boldsymbol{n}\rangle$, we can construct a global $U(1)$ charge $\hat{Q} = \sum_x \hat{Z}_x$ as well as its associated dipole moment $\hat{P} = \sum_x x\, \hat{Z}_x$. In the following, we are interested in unitary time evolution operators $\hat{U}(t)$ that commute with both $\hat{Q}$ and $\hat{P}$ simultaneously. We decompose $\hat{U}(t) = \prod_i \hat{U}_i$ in terms of a layered circuit structure of local 4-site gates $\hat{U}_i$, see Fig. 8.2. The local gates $\hat{U}_i$ in turn are chosen randomly, subjected to the condition of preserving $\hat{Q}$ and $\hat{P}$. As selecting the $\hat{U}_i$'s from the full set of Haar random unitary gates proves challenging for large-scale numerical simulations, we again work with randomly chosen *automaton* gates [205, 386–388], see App. A.3 for further details, which satisfy the condition

$$\hat{U}_i |\boldsymbol{n}\rangle = e^{i\theta_{\boldsymbol{n}}} |\boldsymbol{n}'\rangle\,. \tag{8.1}$$

Thus, product states within the computational basis $|\boldsymbol{n}\rangle$ are, up to a phase $\theta_{\boldsymbol{n}}$, mapped to new product states within that basis. Such circuits can effectively be simulated as classical cellular automata and are valuable tools to capture universal dynamical properties at infinite temperature.

Let us reiterate that through the use of such random circuits subdiffusive transport can be established in the above model [2, 206, 207, 501], see Chapter 6, as observed in the (connected) charge correlations:

$$\overline{\langle \hat{Z}_x(t)\, \hat{Z}_0(0)\rangle}_{n=1} - 1 \sim t^{-1/z} F(x^z/t). \tag{8.2}$$

Here, $z = 4$ is the dynamical transport exponent, $F(\cdot)$ is a universal scaling function, $\overline{\cdots}$ is an explicit notation for the circuit average and $\langle\cdot\rangle_n$ denotes an ensemble average over initial states at a chemical potential $\mu(n)$ that fixes an average charge density n. Furthermore, Ref. [206] showed the existence of a *localization* transition at a critical density close to (and possibly exactly at) $n_c = 1.5$. Due to particle-hole symmetry there is another critical density $\tilde{n}_c = 0.5$. Here, we restrict our analysis to $1 \leq n \leq 2$ and work with $n_c = 1.5$ exactly in the analysis of our numerical results. For $n > n_c$ the charge correlations $\overline{\langle \hat{Z}_x(t)\, \hat{Z}_0(0)\rangle}_{n>n_c} - n^2 \to \text{const.} \neq 0$ no longer decay towards their equilibrium value.

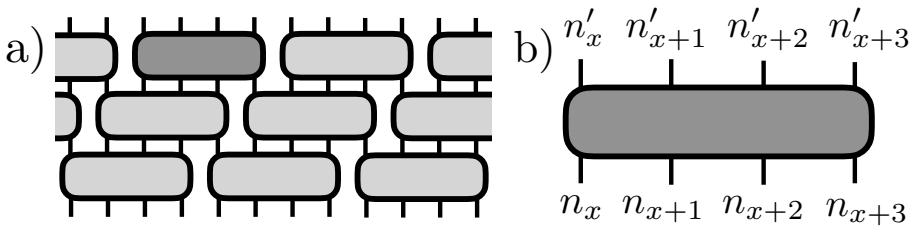

Figure 8.2: Time evolution. a) The time evolution is given by a layered circuit structure consisting of random unitary automaton gates of range four. **b)** The gates map local strings of occupation numbers to other such strings under the constraints of charge- and dipole-conservation.

8.2 Out-of-time-order correlators

We now proceed to study the spreading of operators. This can be done via out-of-time-ordered correlation functions (OTOCs). In particular, we consider the correlations

$$C_{ZX}^{(n)}(x,t) = \overline{\left\langle [\hat{Z}_x(t), \hat{X}_0(0)][\hat{Z}_x(t), \hat{X}_0(0)]^\dagger \right\rangle_n}, \tag{8.3}$$

where we have defined a shift operator $\hat{X}_0 = |2\rangle_0 \langle 0| + |0\rangle_0 \langle 1| + |1\rangle_0 \langle 2|$ that modifies the charge at site 0. We now make use the automaton evolution Eq. (8.1) introduced in the previous section to simplify the expression Eq. (8.3) of the OTOC to a form suitable for efficient numerical evaluation (see App A.3.2),

$$\begin{aligned} C_{ZX}^{(n)}(x,t) &= \sum_{\boldsymbol{n}} \frac{e^{-\mu \sum_x n_x}}{Z_n} \overline{\left[\langle \boldsymbol{n}|\hat{Z}_x(t)|\boldsymbol{n}\rangle - \langle \boldsymbol{n}|\, \hat{X}_0\, \hat{Z}_x(t)\, \hat{X}_0^\dagger\, |\boldsymbol{n}\rangle\right]^2} \\ &= \sum_{\boldsymbol{n}} \frac{e^{-\mu \sum_x n_x}}{Z_n} \overline{C_{ZX}(x,t;\boldsymbol{n})}. \end{aligned} \tag{8.4}$$

Here, we introduced a 'single-shot' OTOC $C_{ZX}(x,t;\boldsymbol{n})$ for a single initial state $|\boldsymbol{n}\rangle$ and a single circuit realization. This quantity is efficiently evaluated numerically and amounts to the local charge difference at site x between two initial states $|\boldsymbol{n}\rangle$, $\hat{X}_0^\dagger |\boldsymbol{n}\rangle$ that are evolved in parallel up to time t via the same circuit realization. The remaining sum over initial states $|\boldsymbol{n}\rangle$ in Eq. (8.4) can be sampled stochastically. We emphasize that the OTOC $C_{ZX}^{(n)}(x,t)$ for automaton time evolutions has been shown to reproduce the expected features of more general random unitary circuit structures [205, 386, 502, 503]. In the following, we consider the spread of the OTOC as a function of time by evaluating the expression of Eq. (8.4). We study how varying the average density n affects the dynamics of the OTOC. We first analyze the two limiting cases of densities n either deep in the ergodic or deep in the localized regime before discussing the fate of the OTOC at the critical point n_c.

8.3 OTOC in the ergodic regime

Let us first focus on the qualitative dynamics of the OTOC, Eq. (8.3), at long times deep in the ergodic phase. At half-filling $n = 1$, Fig. 8.1 (b) shows the common light-cone structure, with a ballistically propagating OTOC front. We can analyze the spatio-temporal form of the OTOCs in this regime in more detail. In particular, following the considerations of Refs. [65, 66], in the ergodic phase the OTOC $C_{ZX}^{(n)}(x,t)$ is expected to feature algebraic tails behind a ballistically propagating front. This is due to the overlap of the $\hat{Z}$ – operator with the conservation laws in the system, which implies the presence of a conserved operator weight in the Heisenberg time evolution that relaxes only hydrodynamically slow. With the subdiffusive transport properties of Eq. (8.2), the expected shape

of the arising tails is

$$1 - C_{ZX}^{(n)}(x,t) \sim (v_B t - x)^{-1/z} = (v_B t - x)^{-1/4}\,, \tag{8.5}$$

where v_B is the 'Butterfly' velocity, that is the speed of the propagating front. Eq. (8.5) describes an algebraic relaxation of the OTOC towards its stationary value (which has been normalized to unity here) and should be valid for $v_B t \gg x$, a long time after the front has passed the point at x. While we generally expect the tails Eq. (8.5) to emerge at very long times on the ergodic side of the localization transition, we note that the proximity to the localization transition at $n_c = 1.5$ can severely affect the dynamics on the numerically accessible timescales even at half-filling $n = 1$ (see e.g. Fig. 8.6 (a) below). Thus, within our accessible timescales, the chosen three-state local Hilbert space does not lie deep enough in the ergodic phase to verify Eq. (8.5).

Instead, here, we choose to go even further into the ergodic regime by increasing the local Hilbert space dimension to 5 (only within this paragraph) while remaining at half-filling ($n = 2$ here). Fig. 8.3 (a) displays the associated spatial shape of the corresponding ZX – OTOC for several instances at late times. We identify a clear tail behind the ballistic front, and the expected relation Eq. (8.5) provides a good fit to this tail. In addition, we verify in Fig. 8.3 (b) that the OTOC relaxes in time as $\sim t^{-1/4}$ behind the front as predicted by Eq. (8.5) as well. Furthermore, we notice that the ballistically moving front itself broadens diffusively according to

$$1 - C_{ZX}^{(n)}(x \approx v_B t, t) \approx \mathrm{erf}\Big(\frac{x - v_B t}{\sqrt{t}}\Big), \tag{8.6}$$

see the inset of Fig. 8.3 (a), where $\mathrm{erf}(\cdot)$ corresponds to the error function. This diffusive broadening is expected to be independent of the system's conserved quantitites and is in agreement with previous results for systems with either no conservation laws or charge conservation only [63–66].

8.4 OTOC in the localized regime

We now consider the automaton circuit evolution of our model with three-state local Hilbert space deep in the localized regime $n > n_c$. Here, find that the OTOC freezes in time, see Fig. 8.1 (d). Similarly to the ergodic regime, we can determine the spatial shape of this OTOC in the localized regime for $n > n_c$. In this regime, a finite density of 'eternally frozen' sites exists [206] whose charge value can never change during the circuit evolution, presenting a hard barrier to the spread of operators. As a consequence, the operator spreading is frozen. The localized phase can then be characterized by a correlation length $\xi \sim |n - n_c|^{-2}$ [206] that constitutes the relevant length scale in the problem. Hence,

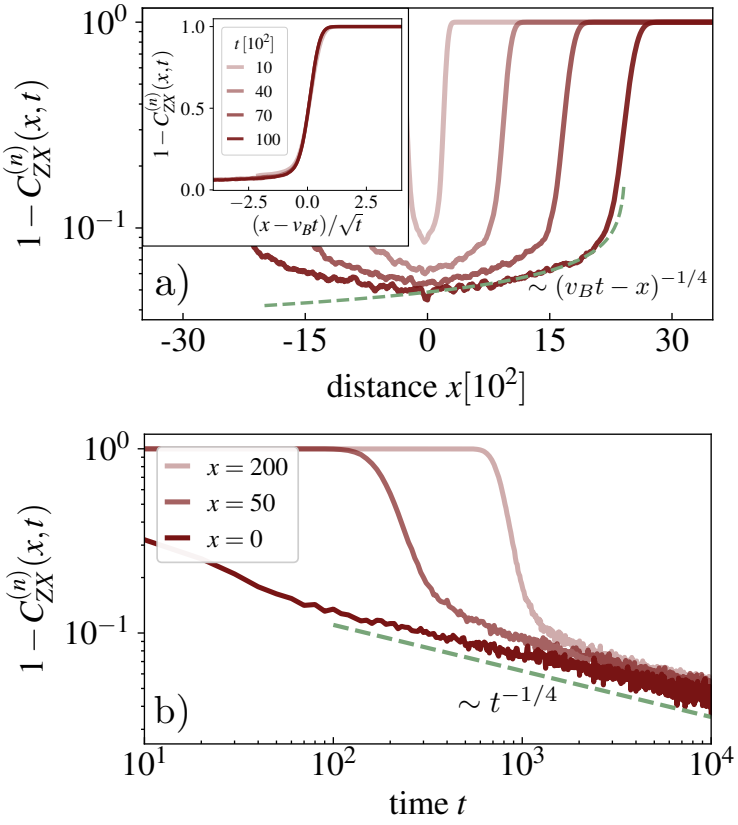

Figure 8.3: Algebraic tails from conservation laws. a) Spatial shape of the ZX – OTOC at several instances at late times; here for a dipole-conserving circuit with five-state local Hilbert space. The OTOC features an algebraic tail behind the ballistic front. **b)** In the region where the operator front has passed, the OTOC relaxes algebraically in time $\sim t^{-1/4}$.

we naturally expect the freezing of the OTOC to take place at the scale ξ, and further

$$C_{ZX}^{(n>n_c)}(x,t) \xrightarrow{t\to\infty} c\, e^{-x/\xi}, \tag{8.7}$$

with some constant c. We verify Eq. (8.7) in Fig. 8.4 (a), where we show $C_{ZX}^{(n>n_c)}(x,t)$ after convergence at long times and for different densities $n > n_c$. The exponential shape of Eq. (8.7) is clearly visible and one can also check the expected scaling $\xi \sim |n - n_c|^{-2}$, see Fig. 8.4 (b). The exponential form Eq. (8.7) should be a general feature of localized systems that are characterized by strong Hilbert space fragmentation, as has recently also been observed in [504].

8.5 OTOC in the critical regime

Finally, at the critical density $n = n_c = 1.5$, Fig. 8.1 (c) indicates a *sub-ballistic* spreading of the OTOC front. This point is an intriguing result: What is the mechanism behind the sub-ballistic spread? Can we understand the sub-ballistic exponent that describes the moving front? And how does this critical property affect the dynamics away from $n = n_c$?

To answer these questions, we consider the single-shot OTOCs $C_{ZX}(x,t;\boldsymbol{n})$ of Eq. (8.4),

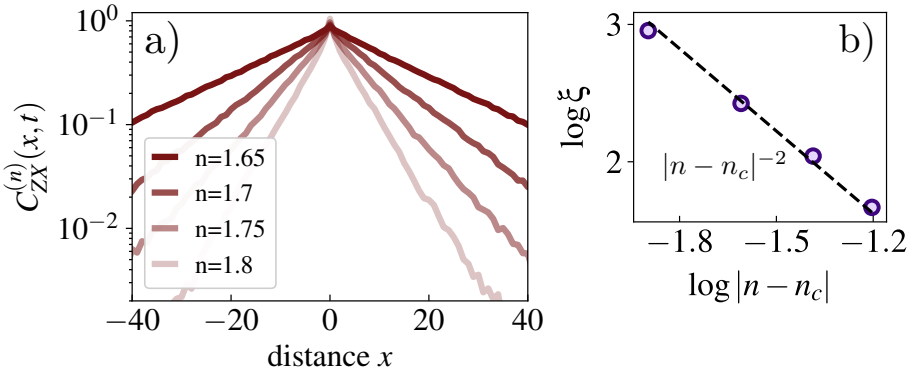

Figure 8.4: Exponential profile of OTOC in the localized regime. **a)** In the localized phase $n > n_c$, the OTOC assumes an exponential form. **b)** The decay is characterized by a correlation length ξ which diverges as $\sim |n - n_c|^{-2}$ towards the critical point.

see Fig. 8.5 (a) for a typical example at $n = 1$. Importantly, if we denote by $x_r(t)$ the rightmost site where $C_{ZX}(x, t; \boldsymbol{n}) \neq 0$ in Fig. 8.5 (a), we notice the presence of long waiting times τ that slow the propagation of the OTOC. Thus, in order to understand the long-time dynamics of the OTOC front in terms of the propagating boundary $\overline{\langle x_r(t)\rangle}$, we require to understand the origin and the probability distribution $p_n(\tau)$ of these waiting times. In the following, we develop a phenomenological model for the propagating boundary with waiting times, which we then verify numerically using automaton circuits.

8.5.1 Phenomenological model

Let us consider a toy example that illustrates the presence of waiting times in the spreading of the OTOC: Take a small patch of seven fully filled sites, described by a state $|m\rangle = |2\,2\,2\,2\,2\,2\,2\rangle$. Upon inserting e.g. the operator $\hat{X}_0$ at the central site, we obtain the state $\hat{X}_0\,|m\rangle = |2\,2\,2\,1\,2\,2\,2\rangle$. There are now *no* dipole-conserving, 4-site gates acting within the patch that can change this charge distribution. This observation crucially depends on dipole-conservation: For charge-conservation only, one could always randomly shift the site with reduced charge, leading, for generic systems, to a diffusively spreading OTOC within this patch [66]. Here, instead, the OTOC is 'trapped' inside the localized region, implying a waiting time τ that lasts until the localized region is breached from the *outside*.

We can develop this argument more systematically as depicted in Fig. 8.5 (b): We assume a localized region of length ℓ in which the average charge density exceeds the critical value, i.e. $\sum_{x=x_0}^{x_0+\ell-1}(n_x - n_c) > 0$, embedded in a system with average density below the critical value. We then expect that an operator inserted into this region implies an OTOC that is effectively 'stuck' until the localized region has melted from the outside. The latter is a transport process that is governed by the subdiffusive exponent $z = 4$ of Eq. (8.2), and we therefore predict the mean waiting time associated to a localized region of length ℓ to be $\tau = \tau(\ell) \sim \ell^z = \ell^4$. For the purpose of this argument, we assume that the prefactor

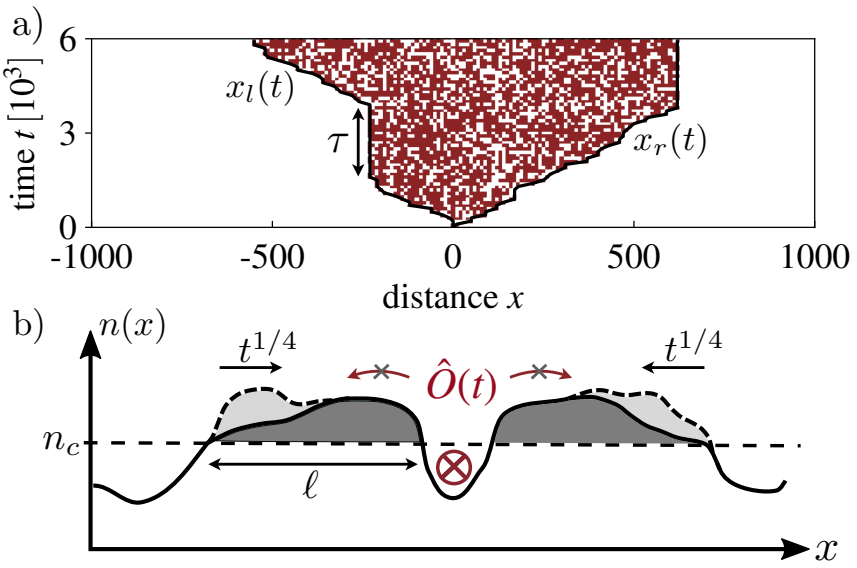

Figure 8.5: Origin of waiting times for operator spreading. a) The single-shot OTOC, shown for a randomly chosen initial state at half-filling $n = 1.0$, experiences waiting times that slow its spread. **b)** A generic state chosen at an average density $n < n_c$ locally features regions of size ℓ whose density exceeds the critical value n_c. An operator inserted into such a localized region cannot escape from within – a property inherent to the fractonic constraint of dipole-conservation. Instead, the operator is subject to a waiting time $\tau \sim \ell^z = \ell^4$ set by the time required for transport to melt the frozen region from the outside.

in this relation stays finite for all background densities at and below n_c. Now, given $\tau(\ell)$, we are required to determine the density-dependent distribution $p_n(\ell)$ which yields the probability of a localized region having length ℓ. This can be achieved using an argument based on random walk theory: Consider a small localized region of length ℓ' with

$$N(\ell') := \sum_{x=x_0}^{x_0+\ell'-1} (n_x - n_c) > 0. \tag{8.8}$$

If we increase this region by one site to the right, we obtain $N(\ell'+1) = N(\ell') + n - n_c + \delta$, where n is the average density of the system and δ is a random variable with mean zero. Therefore, $N(\ell')$ performs a biased random walk and we obtain a closed, localized region of length ℓ' when $N(\ell') = 0$ crosses zero. We are thus interested in the probability distribution of the lengths ℓ of first passage of zero, which assumes the asymptotic form [505]

$$p_n(\ell) \sim \ell^{-3/2} \exp(-\ell/\ell_c). \tag{8.9}$$

Herein, $\ell_c \sim |n - n_c|^{-2}$ close to the transition, i.e. the system 'sees' the non-critical value of the density only above a length scale where typical density fluctuations $\delta n \sim 1/\sqrt{\ell}$ of a region of length ℓ are comparable to $|n - n_c|$. Equipped with the distribution $p_n(\ell)$ of localized regions and the waiting time $\tau(\ell)$ associated to such regions, we can make a qualitative estimate for the probability distribution $p_n(\tau)$ of waiting times by setting

$p_n(\tau)\, d\tau = p_n(\ell(\tau))\, d\ell$, which yields

$$\boxed{p_n(\tau) \sim \tau^{-(1+1/2z)} \exp\{-(\tau/\tau_c)^{1/z}\},} \tag{8.10}$$

where

$$\boxed{\tau_c \sim |n - n_c|^{-2z}, \qquad z = 4.} \tag{8.11}$$

Eq. (8.10) and Eq. (8.11), valid for $n \leq n_c$, are the central predictions of this work. From the tail of this waiting time distribution [506], which enters the biased walk performed by the OTOC boundary $x_r(t)$, and from the localization of the system for $n > n_c$ [206] , we can predict the long-time dynamics of the OTOC front

$$\overline{\langle x_r(t)\rangle} \sim t^{\alpha} \qquad \text{with} \qquad \begin{cases} \alpha = 1, \ n < n_c \\ \alpha = \frac{1}{2z}, \ n = n_c \\ \alpha = 0, \ n > n_c \end{cases} . \tag{8.12}$$

In particular, Eq. (8.12) agrees with the limiting cases studied in Fig. 8.1 (b-d), where a sub-ballistic spread with exponent $1/2z$ separates a ballistic and a frozen long-time regime.

8.5.2 Numerical analysis & discussion

We can verify the predictions made in Eqs. (8.10-8.12) in more detail by numerically evaluating the OTOC front $\overline{\langle x_r(t)\rangle}$ and the waiting time distribution $p_n(\tau)$, which is accessible through the single-shot OTOCs $C_{ZX}(x, t; \boldsymbol{n})$. Fig. 8.6 (a) shows the propagation of the front $\overline{\langle x_r(t)\rangle}$ for different densities n. For densities $n < n_c$ below the critical point, $\overline{\langle x_r(t)\rangle}$ first enters a sub-ballistic regime but starts to bend upwards at late times. Close to half-filling, the simulated times are sufficient to observe the bend continue until ballistic propagation is reached, Eq. (8.12). The time at which the upwards bend sets in grows larger upon approaching the critical point. This is due to the algebraic contribution to the waiting time distribution that impacts the dynamics prior to the timescale on which the stretched exponential in Eq. (8.10) becomes fully relevant. At the critical density $n = n_c$, no such bend is visible on the accessible timescales and our numerical findings follow the $\sim t^{1/2z} = t^{1/8}$ spread predicted in Eq. (8.12). We further note that Eq. (4) additionally predicts a $t^{1/2z}$–scaling of the *broadening* of the OTOC front, which we have also verified numerically. In the localized phase $n > n_c$, Fig. 8.6 (a) demonstrates that $\overline{\langle x_r(t)\rangle} < \text{const.}$ remains bounded and the OTOC freezes at long times.

We show the numerically sampled distributions $p_n(\tau)$ in Fig. 8.6 (b) and indeed find a decay $\sim \tau^{-(1+1/2z)} = \tau^{-9/8}$ at the critical point. For $n < n_c$, the distribution $p_n(\tau)$ follows the critical line for some time and eventually crosses over into a faster-than-algebraic decay. We check that this faster decay corresponds to the stretched exponential of Eq. (8.10) by plotting the quantity $g_n(\tau) := p_n(\tau)/p_{n_c}(\tau)$, which we expect to go as $\exp\{-(\tau/\tau_c)^{1/4}\}$

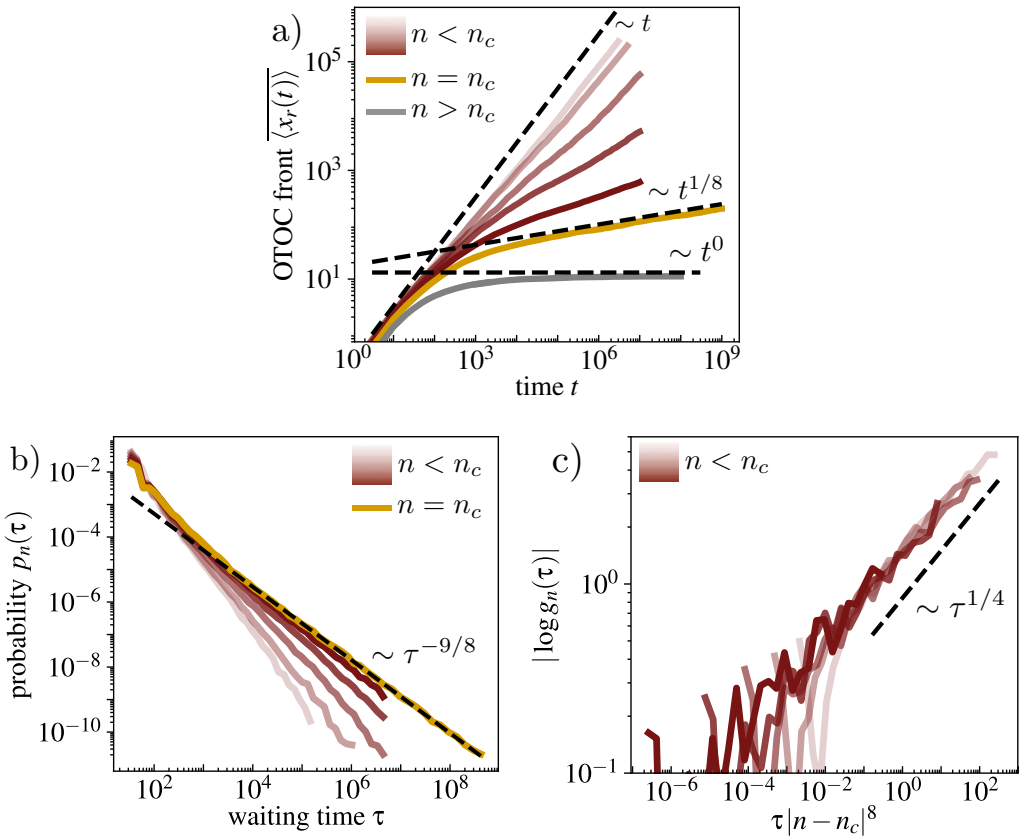

Figure 8.6: OTOC front and waiting time distributions. a) Average $\overline{\langle x_r(t)\rangle}$ of the position of the OTOC front as defined in Fig. 8.5 (b). For $n < n_c$, an upward bending towards an expected ballistic growth can be observed on the simulated timescales for densities deep in the ergodic phase. At the critical density $n_c = 1.5$, the dynamics of the front shows the sub-ballistic power law $\overline{\langle x_r(t)\rangle} \sim t^{1/8}$, and the spread remains bounded $\langle x_r(t)\rangle < \text{const.}$ in the localized phase. The densities shown are $n = 1.0 - 1.5$ in steps of 0.1 (light to dark red), as well as $n = 1.7$. **b)** Probability distributions $p_n(\tau)$ of waiting times in the automaton circuit dynamics evaluated at densities below and at n_c (same values as in **a)**). The distribution $p_{n_c}(\tau)$ at the critical point follows an algebraic decay $\sim \tau^{-9/8}$. For values $n < n_c$ in the ergodic phase, $p_n(\tau)$ bends downwards to a faster-than-algebraic decay. **c)** This faster decay is of the form of a streched exponential, as confirmed by inspecting $g_n(\tau) = p_n(\tau)/p_{n_c}(\tau) \sim \exp\{-(\tau/\tau_c)^{1/4}\}$. Plotting this quantity as a function of $\tau|n - n_c|^8$ leads to a scaling collapse at late times, consistent with $\tau_c \sim |n - n_c|^{-2z} = |n - n_c|^{-8}$. The densities shown are $n = 1.2 - 1.4$ in steps of 0.05.

for long times; Fig. 8.6 (c). Plotting $g_n(\tau)$ as a function of $\tau|n - n_c|^8$ leads to a scaling collapse at late times, in agreement with Eq. (8.11).

Having collected numerical evidence in favor of the phenomenologically derived distributions $p_n(\tau)$, we summarize our results via a dynamical phase diagram that captures the spread of the OTOC front in Fig. 8.1 (a): In the long time limit, the spread is described by Eq. (8.12). For finite times and below the critical density, we predict the OTOC to cross over from a sub-ballistic to a ballistic spread on a time scale given by the crossover time τ_c of the distribution $p_n(\tau)$ in Eq. (8.11). We expect a similar crossover time scale to arise on the frozen side of the transition, as the longest but finite waiting times are of order $\xi^z \sim |n - n_c|^{2z}$, with ξ the correlation length in the frozen phase [206]. We emphasize that

due to the approximation of neglecting potentially parameter-dependent prefactors in the relation $\tau \sim \ell^z$, which we assumed in our phenomenological argument, the spreading of the OTOC at the critical point can in principle experience corrections. However, on our numerically accessible timescales, the Eqs. (8.10-8.12) appear fully consistent.

8.6 Conclusions & outlook

In this chapter, we have analyzed the dynamics of operators in a dipole-conserving chain through the spreading of out-of-time-order correlators (OTOCs). The exotic fracton-like mobility constraints lead to an intricate phase diagram of operator dynamics, Fig. 8.1 (a), that features a critical point where the OTOC front spreads *sub-ballistically*. From the scaling properties of this critical point we derived a 'critical fan', within which operators spread sub-ballistically at finite times even away from the critical density. The slow operator spread $\sim t^{1/8}$ also bounds the growth of entanglement as well as charge transport, which is obstructed by the same localized regions. Our results suggest for the associated critical transport exponent $z_{\mathrm{tr}} \geq 8$, consistent with the numerical findings of Ref. [206]. The exact transport properties at the critical point are an interesting open question.

While we numerically studied specific automaton circuits, the two main ingredients of our phenomenological description, an ergodic dynamical phase with $z = 4$ and a localized dynamical phase, can be found more generally for systems with dipole-conservation [2, 197, 235, 236]. Scaling properties at the critical point should not be affected by specific model parameters. We therefore expect the same critical operator dynamics to apply universally to dipole-conserving chains. Furthermore, while we focused on the $C^{(n)}_{ZX}$-OTOC, the sub-ballistic spread is expected to be robust to an arbitrary choice of local operators in Eq. (8.3). Specifically, in App. A.3.3 we demonstrate that for automaton circuits, the front of the XX-OTOC is bounded up to a factor of two by the front of the ZX-OTOC.

We conjecture that our results also generalize to systems conserving all multipoles up to the m-th moment, where the above findings should be amended simply by substituting the subdiffusive transport exponents $z \to 2(m+1)$, derived in Chapter 6, Refs. [2, 389]. Our results pave the way for finding new universality classes of operator growth, which might bear relevance to fractonic models in higher dimensions [4] and other constrained systems.

9 Emergent tracer dynamics in constrained quantum systems

This chapter is based on the publication

> Johannes Feldmeier, William Witczak-Krempa, Michael Knap, *"Emergent tracer dynamics in constrained quantum systems"*, Phys. Rev. B 106, 094303 (2022)

Structure, text and figures have been adapted for the purposes of this thesis.

Throughout this thesis we have established how the presence of constraints can lead to exotic thermalization dynamics in quantum many-body systems. In particular, the presence of dynamical constraints can lead to the emergence of novel subdiffusive hydrodynamic universality classes [2, 4–6, 103, 104, 197, 205–207, 322, 389, 479–481, 507].

In this chapter, we study the emergence of another classical process in the dynamics of interacting quantum many-body systems: the tracer motion of tagged particles. While at first sight the notion of a tagged particle appears to be at odds with the indistinguishability of quantum particles in many-body systems, here we show how the effects of kinetic constraints can nonetheless lead to the emergence of such tracer motion. For this purpose we focus on the dynamics of one-dimensional systems with a conserved pattern of effective spins or charges throughout much of this work, see Fig. 9.1 for an illustration. This setup is similar to certain nearest-neighbor simple exclusion processes in classical two-component systems, where tracer motion describes the local component imbalance [508]. Similar constraints have recently also been discussed in the context of fractonic quantum systems in terms of "Statistically Localized Integrals of Motion" (SLIOMs) [237], which can be interpreted as an effective conserved pattern. We also point to Chapter 4, where we

have already seen how such a conserved pattern can lead to exotic dynamical properties, albeit in a model with very complex underlying microscopic structure. In this chapter we make the concepts alluded to in Chapter 4 concrete, formulating them in a rigorous manner, extending them and applying them to realistic microscopic systems that can be implemented in current quantum simulation platforms.

More generally, in this chapter we investigate the dynamics of local spin correlations in one-dimensional systems featuring a conserved number of spinful particles. The setup is similar to the tJ – model, which consists of spinful fermions with the condition of no double occupancies. In our case, the usual Heisenberg spin exchange is substituted by constrained spin interactions: We require that some or even all multipole moments of the spin pattern formed by the particles are conserved. For much of this work we focus on random unitary circuits that satisfy these constraints. We will therefore call the systems studied in this work 'tJ – like'. We find that the anomalously slow tracer diffusion of hard core particles in one dimension plays a vital role in describing their dynamical spin correlations.

The mapping between spin correlations and tracer dynamics becomes exact for systems with an exactly conserved spin pattern, where the tracer motion gives rise to a subdiffusive dynamical exponent $z = 4$. Such systems are similar in structure to the tJ_z – model, where spin interactions diagonal in the z-basis preserve the spin pattern. We thus call such systems 'tJ_z – like'. This framework yields a unifying picture to understand the dynamics of constrained lattice models studied in recent works that can be mapped—either directly or effectively—to a tJ_z – like structure [4, 104, 237, 509, 510]. We use this picture to derive the full long-time profile of the dynamical spin correlations in a random unitary tJ_z – circuit model and a random XNOR circuit [104].

Although our main focus is on the dynamics of generic systems, we demonstrate that the tracer picture is applicable also to certain integrable quantum systems. These feature an effective conserved spin pattern but their dynamics *per se* is insensitive to this pattern. As examples we consider the integrable $J_z \to 0$ limit of the tJ_z – model and the folded XXZ chain [511–514]. Through the tracer picture we are able to reproduce their spin diffusion constants at infinite temperature and predict the full profile of their spin correlations at late time, in agreement with our numerical simulations.

We then consider models in which only a finite number of moments of the spin pattern are conserved. The resulting spin correlations are given by a convolution of the tracer motion and the internal dynamics of the pattern. As a consequence, we find that the tracer-motion universality is robust to breaking the pattern conservation if all moments up to at least the quadrupole moment of the pattern are conserved. In addition, for dipole-conserving spin interactions we uncover a competition between two hydrodynamic processes that both have dynamical exponent $z = 4$ but that exhibit different scaling functions. The long-time profile of the spin correlations is then described by a non-universal mixture of these two scaling functions. We argue that this intriguing situa-

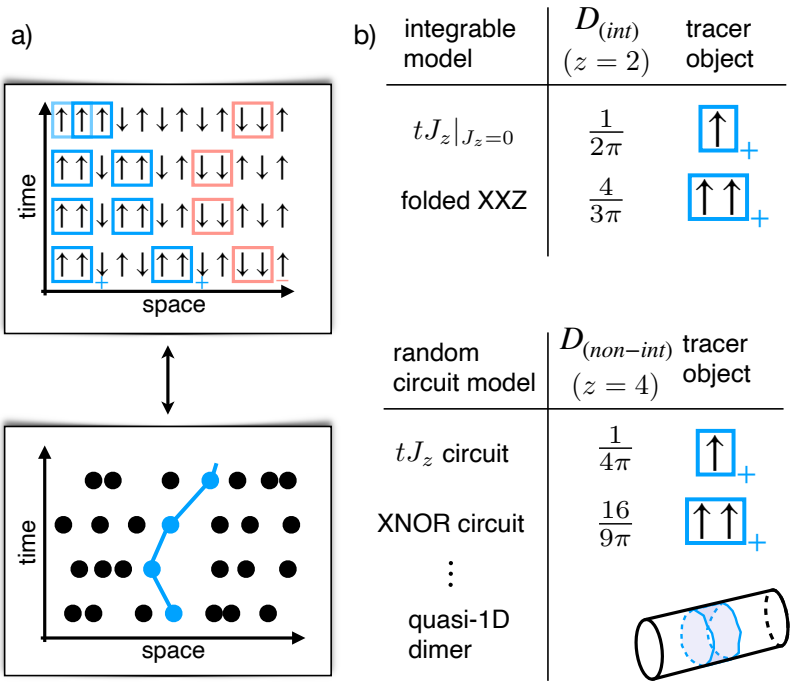

Figure 9.1: Tracer diffusion in constrained quantum systems. a) We consider one-dimensional systems with a pattern of effective excitations (blue and red squares) which is conserved during the time evolution. Infinite temperature dynamical correlation functions in such an ensemble map directly on the tracer probability distribution of hard core random walkers. The fundamental objects of tracer diffusion are the effective excitations of the conserved pattern. **b)** Solving the tracer problem provides us with quantitatively accurate descriptions of transport in a number of generic random unitary circuit models as well as integrable quantum systems. The effective conserved patterns can assume a complex structure as in the quasi one-dimensional dimer model studied in Ref. [4].

tion is reminiscent to phase coexistence at a first order transition between a Gaussian and a non-Gaussian hydrodynamic phase.

The remainder of this chapter is structured as follows: In Sec. 9.1 we introduce the tJ – like models studied in this work and derive a general expression for their spin correlations at late times. We apply these results to specific random unitary circuit examples in Sec. 9.2, treating in detail the random XNOR model [104]. We consider two integrable models in Sec. 9.3 and discuss cases where only a finite number of multipole moments of the pattern are conserved in Sec. 9.4.

9.1 Models and spin correlations

We introduce a novel class of tJ – like many-body systems of spinful particles in one dimension with constrained spin interaction terms. The constraints are such that either the entire spin pattern or a finite number of multipole moments of the pattern are conserved. We derive a general expression for the infinite temperature dynamical spin correlations at late times in such systems.

9.1.1 Constrained tJ – like systems

We are interested in conservation laws inherent to models of the form

$$\begin{aligned} \hat{H}_m &= -t \sum_{x=-L/2}^{L/2-1} \sum_{\sigma} (\hat{\tilde{c}}^{\dagger}_{x+1,\sigma} \hat{\tilde{c}}_{x,\sigma} + h.c.) + \hat{H}_{S,m} \\ [\hat{H}_{S,m}, &\sum_x x^n \hat{S}^z_x] = 0 \quad \forall\, n \leq m. \end{aligned} \tag{9.1}$$

Eq. (9.1) describes a constant number of spinful fermions with nearest-neighbor hopping on a one-dimenional lattice, with the usual tJ – constraint of no double occupancies (indicated by the tilde over the fermion operators; the fermionic nature of the particles is not essential here). A spin pattern is then formed by the fermions in a squeezed space where all empty sites are removed. The spin interaction $\hat{H}_{S,m}$ between the fermions is generalized to not only conserve the total magnetization but potentially higher moments of this spin pattern (all up to the mth moment) as well. Examples for $\hat{H}_{S,m}$ include

$$\begin{aligned} \hat{H}_{S,0} &= J \sum_x \hat{\boldsymbol{S}}_x \cdot \hat{\boldsymbol{S}}_{x+1} + ... \\ \hat{H}_{S,1} &= J \sum_x (\hat{S}^+_x \hat{S}^-_{x+1} \hat{S}^-_{x+2} \hat{S}^+_{x+3} + h.c.) + ... \\ &... \\ \hat{H}_{S,\infty} &= J \sum_x \hat{S}^z_x \hat{S}^z_{x+1} + ..., \end{aligned} \tag{9.2}$$

where '...' refers to diagonal terms in the $z-$basis or to longer-range off-diagonal terms that fulfill the conservation law of Eq. (9.1). We note that $\hat{H}_0 = \hat{H}_{tJ}$ is a conventional tJ – model while $\hat{H}_\infty = \hat{H}_{tJ_z}$ is a tJ_z – model in which the entire spin pattern is a constant of motion. Lattice spin models such as Eq. (9.2) provide a novel way of interpolating between these two limiting cases; one can construct such models recursively [2].

The Hamiltonians of Eqs. (9.1,9.2) serve as our starting motivation and we can qualitatively determine their universal late-time dynamics at high energies by considering *generic* many-body systems with the same Hilbert space structure and conserved quantities. To introduce a model-independent notation we expand any state $|\psi\rangle$ with a fixed number N_f of particles as $|\psi\rangle = \sum_{\boldsymbol{x},\boldsymbol{\sigma}} \psi(\boldsymbol{x},\boldsymbol{\sigma}) \, |\boldsymbol{x},\boldsymbol{\sigma}\rangle$ in terms of the basis states

$$|\boldsymbol{x},\boldsymbol{\sigma}\rangle\,, \quad x_1 < ... < x_{N_f}, \;\; \sigma_i \in \{\pm 1\}. \tag{9.3}$$

Here, $\boldsymbol{x}$ labels the positions of the particles on the chain from left to right and $\boldsymbol{\sigma}$ their respective spins in the $z-$basis. The time evolution represented by the unitary $\hat{U}_m(t)$

should then fulfill

$$\boxed{[\hat{U}_m(t), \sum_{j=1}^{N_f} j^n \hat{\sigma}_j] = 0 \quad \forall n \leq m,} \tag{9.4}$$

and can be Hamiltonian, such as in Eq. (9.1), or generic, such as in random unitary quantum circuits or classical stochastic lattice gases; either case is expected to exhibit the same universal dynamical behavior. We emphasize that the conservation of moments in Eq. (9.4) applies to the squeezed-space variables of the pattern, which are related to the original spins non-locally. In particular, the moments $\sum_x x^n \hat{S}^z_x$ in the original spin space are *not* conserved due to the hopping part of Eq. (9.1). We will make use of the non-local property Eq. (9.4) throughout our work and show that various constrained models studied recently are part of this effective description.

9.1.2 Generic structure of dynamical spin correlations

We derive a general expression for the dynamical spin correlations in a system described by Eqs. (9.3,9.4) under the assumption of chaotic, thermalizing dynamics at infinite temperature. Integrable dynamics will be considered in Sec. 9.3. We will assume open boundary conditions in a system of length L containing a fixed number of N_f particles, i.e. density $\rho = N_f/L$. The spin operator $\hat{S}^z_r$ at site r can then be expressed in terms of the pattern spin operators $\hat{\sigma}_j$ via

$$\hat{S}^z_r = \sum_{j=1}^{N_f} \delta_{\hat{x}_j, r}\, \hat{\sigma}_j. \tag{9.5}$$

The time evolution $\hat{U}_m(t)$ applied to a basis state $|\boldsymbol{x}, \boldsymbol{\sigma}\rangle$ is given by

$$\hat{U}_m(t)\, |\boldsymbol{x}, \boldsymbol{\sigma}\rangle = \sum_{\boldsymbol{x}', \boldsymbol{\sigma}'} a(\boldsymbol{x}'\boldsymbol{\sigma}'|\boldsymbol{x}\boldsymbol{\sigma}; t)\, |\boldsymbol{x}', \boldsymbol{\sigma}'\rangle\,, \tag{9.6}$$

with the matrix elements $a(\boldsymbol{x}'\boldsymbol{\sigma}'|\boldsymbol{x}\boldsymbol{\sigma}; t)$ normalized to $\sum_{\boldsymbol{x}', \boldsymbol{\sigma}'} |a(\boldsymbol{x}'\boldsymbol{\sigma}'|\boldsymbol{x}\boldsymbol{\sigma}; t)|^2 = 1$. Using Eqs. (9.5,9.6), the dynamical spin correlations read

$$\begin{aligned} C(r,t) &:= \langle \hat{S}^z_r(t) \hat{S}^z_0(0) \rangle = \\ &= \frac{1}{\mathcal{N}} \sum_{\substack{\boldsymbol{x}, \boldsymbol{\sigma}, i \\ \boldsymbol{x}', \boldsymbol{\sigma}', j}} \sigma'_j \sigma_i\, \delta_{x'_j, r} \delta_{x_i, 0}\, |a(\boldsymbol{x}'\boldsymbol{\sigma}'|\boldsymbol{x}\boldsymbol{\sigma}; t)|^2, \end{aligned} \tag{9.7}$$

where the normalization $\mathcal{N} = \mathcal{N}_n \mathcal{N}_s$ is given by the number of different particle position $\mathcal{N}_n = \binom{L}{N_f}$ on the lattice and the number of different spin patterns $\mathcal{N}_s = 2^{N_f}$. The expectation value $\langle \cdot \rangle$ is taken with respect to an 'infinite temperature' ensemble over all basis states. Under $\hat{U}_m(t)$, both the number of particles as well as the total magnetization of the spin pattern are conserved and we expect both of their local densities to contribute a hydrodynamic mode at long length scales and late times. In general, the precise transport

coefficients of the particle mode and the spin pattern mode are determined by a mode-coupled Ansatz and the details of the microscopic time evolution. Nonetheless, we expect that *qualitatively*, we can describe the hydrodynamic behavior of the two modes independently at late times in thermalizing systems. We therefore make the approximation to set

$$|a(\boldsymbol{x}'\boldsymbol{\sigma}'|\boldsymbol{x}\boldsymbol{\sigma};t)|^2 \simeq p_n(\boldsymbol{x}'|\boldsymbol{x};t)\, p_s(\boldsymbol{\sigma}'|\boldsymbol{\sigma};t) \tag{9.8}$$

in Eq. (9.7), where we introduced the particle and spin path distributions $p_n(\boldsymbol{x}'|\boldsymbol{x};t)$ and $p_s(\boldsymbol{\sigma}'|\boldsymbol{\sigma};t)$; they fulfill $\sum_{\boldsymbol{x}'} p_n(\boldsymbol{x}'|\boldsymbol{x};t) = 1 = \sum_{\boldsymbol{\sigma}'} p_s(\boldsymbol{\sigma}'|\boldsymbol{\sigma};t)$. The spin correlations of Eq. (9.7) are thus determined by the following two expressions which describe spin pattern dynamics and particle dynamics, respectively:

$$\begin{aligned} F(j-i,t) &:= \frac{1}{\mathcal{N}_s}\sum_{\boldsymbol{\sigma},\boldsymbol{\sigma}'} \sigma'_j\sigma_i\, p_s(\boldsymbol{\sigma}'|\boldsymbol{\sigma};t) \\ K(j-i,r;t) &:= \frac{1}{\mathcal{N}_n}\sum_{\boldsymbol{x},\boldsymbol{x}'} \delta_{x'_j,r}\delta_{x_i,0}\, p_n(\boldsymbol{x}'|\boldsymbol{x};t) = \\ &= P(j,r|i,0;t)\, P(i,0). \end{aligned} \tag{9.9}$$

In the last step we introduced the probability $P(i,0)$ to find the ith particle (counted from the left) at site $x=0$, as well as the probability $P(j,r|i,0;t)$ to find the jth particle at site $x=r$ at time t given that particle i was located at site $x=0$ at time 0. We can rewrite the latter probability as

$$P(j,r|i,0;t) = \sum_{\ell} P(j,r|i,\ell;0)\, P(i,\ell|i,0;t). \tag{9.10}$$

We notice that $P(j,r|i,\ell;0)$ in Eq. (9.10) is simply the probability to find particle j at r given that particle i is at ℓ at the same time. It has the exact expression ($\theta(\cdot)$ is the Heaviside theta function)

$$\begin{aligned} P(j,r|i,\ell;0) =\ & \delta_{i-j,0}\,\delta_{r-\ell,0} + \\ & + \theta(j-i-1)\theta(r-\ell-1)\frac{\binom{r-\ell-1}{j-i-1}\binom{L-r+\ell-1}{N-j+i-1}}{\binom{L}{N}} + \\ & + \theta(i-j-1)\theta(\ell-r-1)\frac{\binom{\ell-r-1}{i-j-1}\binom{L-\ell+r-1}{N-i+j-1}}{\binom{L}{N}} \\ \overset{|i-j|\gg 1}{\approx}\ & \frac{1}{\sqrt{\pi\left(\frac{1}{\rho^2}-\frac{1}{\rho}\right)|j-i|}}\exp\left\{-\frac{\left[r-\ell-\frac{j-i}{\rho}\right]^2}{\left(\frac{1}{\rho^2}-\frac{1}{\rho}\right)|j-i|}\right\}, \end{aligned} \tag{9.11}$$

where in the last line we made an approximation for large $|i-j| \gg 1$, leading to a Gaussian centered around $r-\ell-\frac{j-i}{\rho} = 0$ with width proportional to $\sqrt{|i-j|}$.[1] For the second

[1] The last line of Eq. (9.11) actually follows in a grand canonical setting with average density ρ of particles. Nonetheless, the location of the center and the scaling of the width remain valid for fixed particle number.

expression on the right hand side of Eq. (9.10) we define

$$P(i,\ell|i,0;t) =: G_{tr}(\ell,t), \tag{9.12}$$

since $P(i,\ell|i,0;t)$ traces the motion of particle i, which we assume to be in the bulk of the spin pattern. $G_{tr}(\ell,t)$ thus corresponds to the time dependent tracer probability distribution of a bulk particle. Using Eqs. (9.11,9.12) in Eqs. (9.9,9.10) we obtain

$$\begin{aligned} K(j-i,r;t) &= P(i,0)\int d\ell\, P(j,r|i,\ell;0)\, G_{tr}(\ell,t) \simeq \\ &\simeq P(i,0)\, G_{tr}\Big(r-\frac{j-i}{\rho},t\Big). \end{aligned} \tag{9.13}$$

The last line follows since $G_{tr}(\ell,t)$ is in general a probability distribution whose width increases in time while the width of $P(j,r|i,\ell;0)$ is a constant of order $\sqrt{|j-i|}$. Therefore, at late times $G_{tr}(\ell,t)$ is much broader and we can substitute the approximation $P(j,r|i,\ell;0) \simeq \delta(r-\ell-\frac{j-i}{\rho})$ into Eq. (9.13). Finally, inserting Eq. (9.13) and Eq. (9.9) into Eq. (9.7) we find

$$\boxed{C(r,t) = \int dj\, F(j,t)\, G_{tr}(r-j/\rho,t) = [\tilde{F} \star G_{tr}](r,t),} \tag{9.14}$$

with $\tilde{F}(j,t) = \rho\, F(\rho j,t)$. The dynamical spin correlations $C(r,t)$ at late times are thus given quite generally as a convolution between the internal dynamics of the spin pattern and the tracer distribution of a distinguishable particle on the lattice. Since $G_{tr}(\ell,t)$ follows the trajectory of the ith particle (with some i in the bulk) counted from the left, the relevant tracer problem is one of hard core interacting particles that can never swap relative positions. We note that in reciprocal space Eq. (9.14) represents two independent decay processes of long wavelength k-modes.

9.2 Random unitary circuits with conserved pattern

We use the result of Eq. (9.14) to study a number of tJ_z – like models with a spin pattern that is a constant of motion. We remark that the results of this section should apply very generally to models featuring recently introduced "Statistically Localized Integrals of Motion" (SLIOMs) [237], which can be interpreted as a conserved pattern.

If the entire pattern is constant, the spin dynamics becomes trivial, $F(j,t) = \delta(j)$ for all times in Eq. (9.14) and thus

$$C(r,t) \simeq G_{tr}(r,t) \tag{9.15}$$

maps directly to a tracer problem. Due to the trivial pattern dynamics, our initial approximation Eq. (9.8) simply becomes $|a(\boldsymbol{x}'\boldsymbol{\sigma}|\boldsymbol{x}\boldsymbol{\sigma};t)|^2 \simeq p_n(\boldsymbol{x}'|\boldsymbol{x};t)$, i.e., the matrix elements of the time evolution can be considered approximately independent of the underlying spin

pattern when inserted into Eq. (9.7). In fact, with a conserved pattern the correlations of Eq. (9.7) can be recast as

$$C(r,t) = G_{\rm tr}(r,t) + R(r,t), \tag{9.16}$$

where $R(r,t)$ is the difference between the *exact* correlations and the tracer distribution. It reads explicitly

$$R(r,t) = \frac{1}{\mathcal{N}} \sum_{\substack{\boldsymbol{x},\boldsymbol{x}',\boldsymbol{\sigma} \\ i\neq j}} \sigma_j \sigma_i \, \delta_{x'_j,r} \, \delta_{x_i,0} |a(\boldsymbol{x}'\boldsymbol{\sigma}|\boldsymbol{x}\boldsymbol{\sigma};t)|^2, \tag{9.17}$$

and captures contributions to $C(r,t)$ due to spins $j \neq i$ moving to site r at time t, given that spin i started at site $x = 0$ initially. Due to the summation over the spin values σ_j, $R(r,t)$ acquires both a positive and negative contribution from σ_j and $-\sigma_j$, respectively. We then expect generically that contributions to $R(r,t)$ from spins j with $|j-i| \gg 1$ vanish approximately due to cancellation of positive and negative contributions, justifying Eq. (9.15). In this section, we will consider generic systems where $R(r,t) = 0$ exactly upon averaging over the random time evolution, and in Sec. 9.3 integrable quantum systems in which $R(r,t) = 0$ exactly since the time evolution is indeed independent of the underlying pattern, hence in both cases $|a(\boldsymbol{x}'\boldsymbol{\sigma}|\boldsymbol{x}\boldsymbol{\sigma};t)|^2 = p_n(\boldsymbol{x}'|\boldsymbol{x};t)$. In either case, since $C(r,t) = G_{\rm tr}(r,t)$ exactly, we will be able to use existing results from the theory of tracer dynamics to obtain full long-time spin correlation profiles.

Here, we first consider systems subject to a random time evolution, such as a classical stochastic lattice gas or random unitary quantum circuits. Averaging over the random evolution (denoted by $\overline{\cdots}$) we are interested in the associated averaged correlations $\overline{C(r,t)}$. For certain models that we consider, $\overline{R(r,t)} = 0$ (see below) and thus the mapping to tracer dynamics is exact upon averaging over the random evolution, $\overline{C(r,t)} = G_{\rm tr}(r,t)$. The resulting tracer problem we have to solve is one of particles hopping randomly on a one-dimensional lattice subject to a hard core exclusion principle. The hard core property is a direct consequence of the pattern conservation. Of particular interest to us is the nearest neighbor simple exclusion process in one dimension, for which the long time tracer distribution function is known to be [396–398, 515]:

$$G_{\rm tr}(\ell,t) \to G_{\rm tr}^{(nI)}(\ell,t) := \frac{1}{(16Dt\pi^2)^{1/4}} \exp\Big\{-\frac{\ell^2}{4\sqrt{Dt}}\Big\}, \tag{9.18}$$

where the superscript (nI) indicates that we are considering generic, *non-integrable* systems. $G_{\rm tr}^{(nI)}(\ell,t)$ takes the form of a Gaussian that broadens subdiffusively slowly,

$$\langle \Delta\ell(t)^2 \rangle = 2\sqrt{Dt}. \tag{9.19}$$

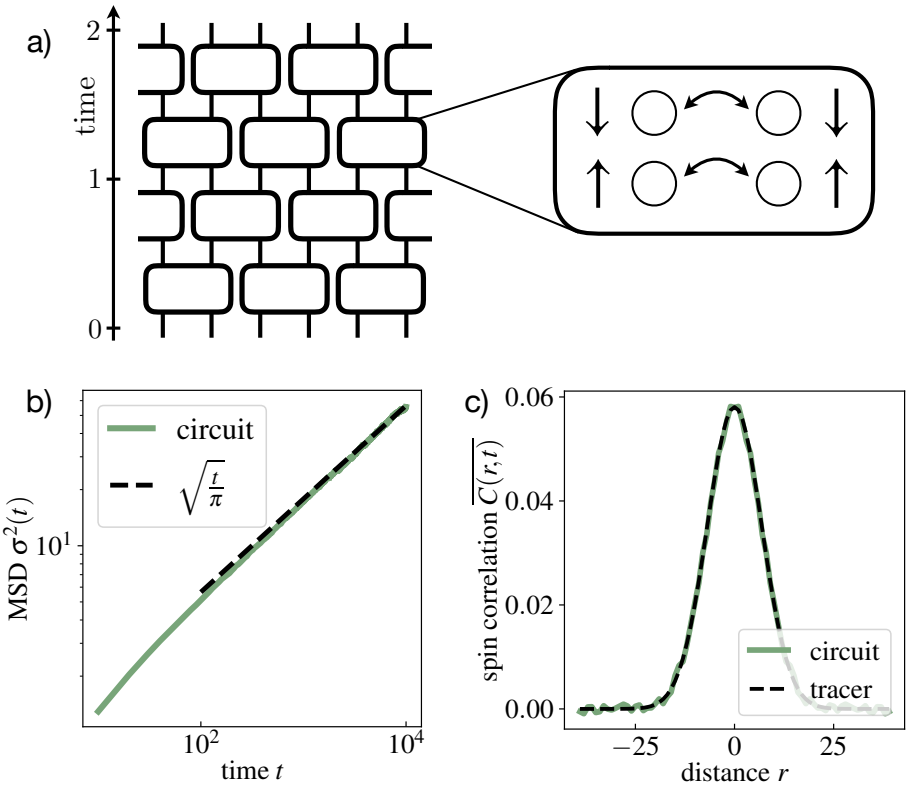

Figure 9.2: Random tJ_z – circuit. (a) In the random tJ_z – circuit we consider a three-state local Hilbert space and two-site local random unitary gates. The local gates connect states with spins hopping between neighboring lattice sites. **(b)** The mean squared displacement (MSD) associated to the spin correlations $C(r,t)$ agrees with the tracer prediction of Eq. (9.25) for particle density $\rho = 2/3$ and single particle hopping rate $\Gamma = 1$. **(c)** The form of the correlations $C(r,t)$ at time $t = 7000$ of the circuit evolution. It assumes a Gaussian shape as expected from the tracer distribution. We obtain these numerical results by sampling the discrete stochastic Markov process of Eq. (9.23). The data was averaged over 1000 randomly chosen product initial states of the Markov process in a system of length $L = 5000$.

The generalized diffusion constant D is determined via the density ρ of particles on the chain and the bare hopping rate Γ per time step of an inividual particle,

$$D = \frac{\Gamma}{\pi}\left(\rho^{-1} - 1\right)^2. \tag{9.20}$$

We consider two examples in detail in the following, the random tJ_z – model and the random XNOR model, for which Eqs. (9.18,9.20) will provide us with the exact long time spin correlations after identifying conserved spin patterns in the appropriate variables.

9.2.1 Random circuit tJ_z – model

Circuit model

Our first example is a direct implementation of a random version of the tJ_z – model. We consider a chain with local Hilbert space spanned by the states $|q\rangle = |-1\rangle, |0\rangle, |1\rangle$. Each

basis state can be written as $|\boldsymbol{q}\rangle = |\boldsymbol{x}, \boldsymbol{\sigma}\rangle$ and we demand that the pattern $\boldsymbol{\sigma}$ of ± 1-spins be a constant of motion. We then consider a random unitary time evolution given by

$$\hat{U}(t) = \prod_{\ell=1}^{tL} \hat{U}_\ell, \tag{9.21}$$

where individual two-site gates $\hat{U}_\ell$ are arranged spatially as shown in Fig. 9.2. Each of the $\hat{U}_\ell$ is given by

$$\hat{U}_\ell = \sum_s \hat{P}_{\ell,s} \hat{U}_{\ell,s} \hat{P}_{\ell,s}, \tag{9.22}$$

where s labels the symmetry sectors of the two-site *local* Hilbert space that are connected under the constraint of keeping $\boldsymbol{\sigma}$ constant. Specifically, there are five sectors that contain only a single local configuration, $\{|-1,-1\rangle\}$, $\{|-1,1\rangle\}$, $\{|1,-1\rangle\}$, $\{|1,1\rangle\}$, and $\{|0,0\rangle\}$, as well as two sectors that contain two states each, $\{|0,1\rangle, |1,0\rangle\}$, $\{|0,-1\rangle, |-1,0\rangle\}$. $\hat{P}_s$ is a projector onto these connected sectors. The unitary operators $\hat{U}_{\ell,s}$ acting within each sector are then chosen randomly from the Haar measure.

Mapping to classical Markov process

Averaging the time evolution over the random gates, the associated circuit-averaged probabilities required to compute the spin correlations $\overline{C(r,t)}$ are given by a classical discrete Markov process [65, 66, 68, 104]. Specifically, we follow Ref. [104] in introducing the notation $|\boldsymbol{x}, \boldsymbol{\sigma}) := |\boldsymbol{x}, \boldsymbol{\sigma}\rangle \langle \boldsymbol{x}, \boldsymbol{\sigma}|$ for the projector onto the state $|\boldsymbol{x}, \boldsymbol{\sigma}\rangle$, as well as an associated inner product $(\hat{A}|\hat{B}) := \mathrm{Tr}\left[\hat{A}\hat{B}^\dagger\right]$ for operators. The matrix elements for the time evolution are then given by [104]

$$\boxed{\overline{|a(\boldsymbol{x}'\boldsymbol{\sigma}|\boldsymbol{x}\boldsymbol{\sigma};t)|^2} = (\boldsymbol{x}', \boldsymbol{\sigma}|\hat{\mathcal{T}}^t|\boldsymbol{x}, \boldsymbol{\sigma}),} \tag{9.23}$$

with a transfer matrix $\hat{\mathcal{T}}$ given by

$$\begin{aligned} \hat{\mathcal{T}} &= \bigotimes_{\ell=1}^{L} \hat{\mathcal{T}}_\ell \\ \hat{\mathcal{T}}_\ell &= \sum_s \frac{1}{d_s} \sum_{s_1, s_2 \in s} |s_1)(s_2|, \end{aligned} \tag{9.24}$$

where d_s is the size of the local two-site symmetry sector s. A brief review of the derivation of Eqs. (9.23,9.24) is provided in App. A.2.

We see that Eqs. (9.23,9.24) describe the averaged probabilities $\overline{|a(\boldsymbol{x}'\boldsymbol{\sigma}|\boldsymbol{x}\boldsymbol{\sigma};t)|^2}$ in terms of a stochastic lattice gas: For each applied gate a particle hops with probability $1/2$ to an empty neighboring site and stays at its position if the neighboring site is occupied by another particle. In particular, $\overline{|a(\boldsymbol{x}'\boldsymbol{\sigma}|\boldsymbol{x}\boldsymbol{\sigma};t)|^2} = \overline{|a(\boldsymbol{x}'|\boldsymbol{x};t)|^2}$ is *independent* of the spin pat-

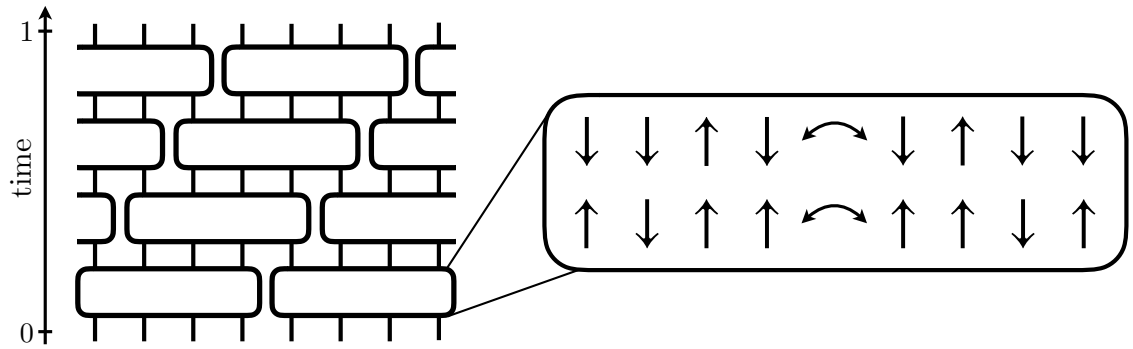

Figure 9.3: Random XNOR circuit. In the random XNOR circuit we consider a two-state local Hilbert space and four-site local random unitary gates. The allowed moves under these gates connect local configurations by exchanging nearest neighbor states, conditioned on the two surrounding sites being in the same state.

tern $\boldsymbol{\sigma}$. Thus, the contribution $\overline{R(x,t)}$ of equation Eq. (9.17) vanishes due to cancellation of positive and negative spin contributions. The long-time mean squared displacement of the tracer process is in turn exactly described by the simple nearest-neighbor exclusion process through Eqs. (9.18-9.20). In our case, the density of particles is given by $\rho = 2/3$ at infinite temperature. Furthermore, for a single time step consisting of two layers as shown in Fig. 9.2 (a) there are two attempted moves at rate $1/2$ per particle, such that we can effectively set $\Gamma = 1$. This yields $D = 1/4\pi$ for the random circuit tJ_z – model, see also Fig. 9.1. The theory of tracer diffusion of hard core particles in one dimension thus predicts a mean squared displacement

$$\sigma^2(t) := \sum_r r^2 \, \overline{C(r,t)} = \sqrt{t/\pi} \tag{9.25}$$

at long times t with a Gaussian shape of the averaged correlations $\overline{C(r,t)}$. The mean squared displacement thus grows subdiffusively $\sim \sqrt{t}$ as opposed to conventional diffusive growth $\sim t$. We confirm this prediction by numerically sampling the stochastic Markov process Eq. (9.23) which yields the spin correlations in Fig. 9.2 (b+c).

9.2.2 Random circuit XNOR model

We consider a second example of generic unitary quantum dynamics where we can use the tracer formulae Eqs. (9.18-9.20) to derive the long-time behavior of local spin correlations, the random XNOR circuit [104]. The model is an effective spin $S = 1/2$ system with Hilbert space spanned by the local states $|\uparrow\rangle, |\downarrow\rangle$. The local unitaries $\hat{U}_\ell$ that generate the time evolution are *four-site* gates that conserve both the total magnetization $\hat{M} = \sum_x \hat{S}^z_x$ as well as the number of Ising domain walls $\hat{D} = \sum_x (\hat{S}^z_{x+1} - \hat{S}^z_x)^2$. Therefore, $\hat{U}_\ell$ can exchange the central two spins only if the outer two spins have the same value, see Fig. 9.3. Writing $\hat{U}_\ell = \sum_s \hat{P}_s \hat{U}_s \hat{P}_s$ as in Eq. (9.22), the only symmetry sectors s that contain more than a single state are $\{|\uparrow,\uparrow,\downarrow,\uparrow\rangle, |\uparrow,\downarrow,\uparrow,\uparrow\rangle\}$ and $\{|\downarrow,\uparrow,\downarrow,\downarrow\rangle, |\downarrow,\downarrow,\uparrow,\downarrow\rangle\}$. We refer to this

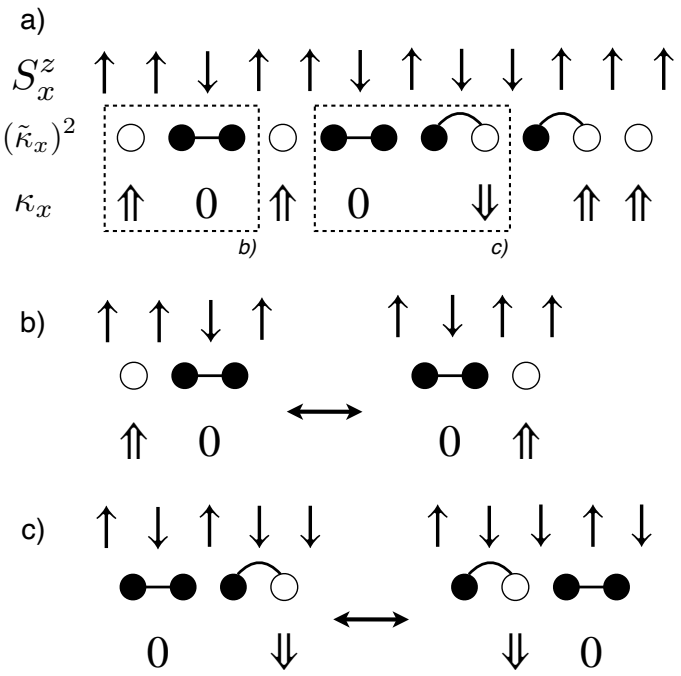

Figure 9.4: Conserved charge pattern in the random XNOR circuit. a) Mapping between original spin-$1/2$ degrees of freedom and an effective conserved superspin pattern. Going from left to right, two neighboring aligned spins are mapped to a corresponding superspin $\Uparrow$ or $\Downarrow$, while two neighboring domain walls map to a vacant site 0. The pattern of non-zero superspins is conserved under random XNOR dynamics. In the domain wall picture (empty and filled circles), the mobile vacancies correspond to domain wall pairs (●—●). Furthermore, in the domain wall picture the objects that form a conserved pattern are given by single bonds of aligned spins (○) as well as single domain walls paired up with a neighboring aligned bond (◠○). This domain wall conserved pattern is obtained by removing all mobile domain wall pairs (●—●) see also Fig. 9.5. **b)+c)** Elementary XNOR moves within the above mapping. In superspin language, vacancies 0 and superspins $\Uparrow$ / $\Downarrow$ exchange positions. In domain wall language, a mobile domain wall pair exchanges positions with one of the objects contributing to the domain wall pattern (i.e. ○ or ◠○).

system as the random XNOR model following Ref. [104], which established that spin correlations in this model show subdiffusive transport with $z = 4$. While the dynamical exponent is in agreement with the tracer picture, the tJ_z – like existence of a conserved pattern is not immediately apparent in the random XNOR model. We first describe the mapping to such a conserved pattern using the original spin variables $S^z_x \in \{\uparrow, \downarrow\}$, see also Refs. [509, 516]. We then construct an equivalent mapping using domain wall variables $\hat{S}^z_{x+1} - \hat{S}^z_x$, see also Refs. [510, 513, 517]. Combining both pictures, we will be able to explain the full form of the spin correlations $\overline{C(r,t)}$ at long times.

Conserved pattern: spin picture

Let us consider a state $|\boldsymbol{s}\rangle$ with $s_x \in \{\uparrow, \downarrow\}$ in a system of length L. We map this state (bijectively up to boundary terms) to a state $|\boldsymbol{\tau}\rangle$ of effective 'superspin' degrees of freedom $\tau_i \in \{\Uparrow, 0, \Downarrow\}$ on a chain of length $\tilde{L}(\boldsymbol{s})$ which explicitly depends on the state $|\boldsymbol{s}\rangle$ in the original spin-$1/2$ picture, see also Refs. [509, 516]. We start at the left end $x = -L/2$ of the

original chain and consider the bond between the first two spins $s_{-L/2}, s_{-L/2+1}$. There are two possibilities:

1. If $s_{-L/2} = s_{-L/2+1}$, we add $\tau = \Uparrow$ and $\tau = \Downarrow$ to the superspin configuration, for $s_{-L/2} = \uparrow$ and $s_{-L/2} = \downarrow$, respectively.

2. If $s_{-L/2} \neq s_{-L/2+1}$, consider the next bond between $s_{-L/2+1}, s_{-L/2+2}$: If $s_{-L/2+1} = s_{-L/2+2}$, we again accordingly add $\tau = \Uparrow$ or $\tau = \Downarrow$ to the superspin configuration for $s_{-L/2+1} = \uparrow$ and $s_{-L/2+1} = \downarrow$, respectively. On the other hand, if also $s_{-L/2+1} \neq s_{-L/2+2}$, we add the superspin $\tau = 0$.

The above steps determine the first element (from the left) of the superspin configuration. The next superspin is determined by moving to the next bond between two spins and repeating the above steps. This process is reiterated until all bonds in the original picture have been accounted for, yielding $|\boldsymbol{\tau}\rangle = |\boldsymbol{\tau}(\boldsymbol{s})\rangle$. An example of this mapping is illustrated in Fig. 9.4 (a).

With the superspin description $|\boldsymbol{\tau}\rangle$ we are back to a tJ – like Hilbert space structure. Under the random XNOR dynamics described above (see also Fig. 9.4) the number and the pattern of non-zero superspins are indeed conserved: On the one hand, every bond of aligned spins contributes a non-zero superspin and the total number of aligned nearest neighbor spins is constant due to domain wall conservation. On the other hand, two opposite superspins located next to each other, e.g. $|... \Uparrow\Downarrow ...\rangle$, translate into a local configuration of four spins, $|... \uparrow\uparrow\downarrow\downarrow ...\rangle$, on which the XNOR gates of Fig. 9.3 can only act trivially. Hence, $\Uparrow$ and $\Downarrow$ can never exchange relative positions. If we write $|\boldsymbol{\tau}\rangle = |\boldsymbol{x}, \boldsymbol{\sigma}\rangle$ as before, the pattern $\boldsymbol{\sigma}$ is conserved. Through this mapping we are led back to the random circuit tJ_z – constraints considered in the previous section, accounting for the dynamical exponent $z = 4$.

In addition, we also analyze in the following how the conserved superspin pattern translates *quantitatively* into the correlations of the original spin variables. To this end, we define the quantities

$$\hat{\kappa}_x := \frac{1}{2}(\hat{S}^z_x + \hat{S}^z_{x+1}) \tag{9.26}$$

within the spin-1/2 picture, which detect whether the bond between the spins at $x, x+1$ contributes a non-zero superspin to $|\boldsymbol{\tau}\rangle$. The dynamic correlation function $\overline{\langle \hat{\kappa}_{2r}(t)\hat{\kappa}_0(0)\rangle}$ then probes how a non-zero superspin excitation initially located between sites $0, 1$ spreads to the bond between $2r, 2r+1$. Crucially, according to the random XNOR gates depicted in Fig. 9.4, the non-zero superspins $\Uparrow, \Downarrow$ *only move by steps of length two* with respect to the original lattice. At the same time they move only by a distance r within the compressed superspin pattern $\boldsymbol{\tau}$. Since the superspin description reduces to the random tJ_z – model analyzed above we can write

$$\overline{\langle \hat{\kappa}_{2r}(t)\hat{\kappa}_0(0)\rangle} = \frac{1}{2} G^{(nI)}_{\mathrm{tr}}(r, t). \tag{9.27}$$

Here, the prefactor $1/2$ corresponds to the probability of finding a non-zero superspin between sites $0, 1$. The hopping rate of superspins entering Eq. (9.27) through Eq. (9.20) can again effectively be set to $\Gamma = 1$ for the circuit geometry of Fig. 9.3. On the other hand, care needs to be taken to determine the density ρ of non-zero superspins, as the infinite temperature average in the original spin variables s_x *does not* transfer directly to an infinite temperature average in the superspin picture. We will derive this density below in the domain wall picture, see Eq. (9.39); for now we quote only the obtained result $\rho = 3/4$ entering Eq. (9.27).

Inserting the definition Eq. (9.26) of $\hat{\kappa}_x$ back into Eq. (9.27) we obtain

$$\frac{1}{2}G^{(nI)}_{\mathrm{tr}}(r,t) = \frac{1}{4}\Big(\overline{\langle \hat{S}^z_{2r-1}(t)\hat{S}^z_0(0)\rangle} + 2\overline{\langle \hat{S}^z_{2r}(t)\hat{S}^z_0(0)\rangle} + \overline{\langle \hat{S}^z_{2r+1}(t)\hat{S}^z_0(0)\rangle}\Big), \tag{9.28}$$

where we made use of translational invariance in the bulk. We could have performed an equivalent calculation for the correlation $\overline{\langle \hat{\kappa}_{2r+1}(t)\hat{\kappa}_0(0)\rangle}$ and thus

$$\frac{1}{2}G^{(nI)}_{\mathrm{tr}}(r,t) = \frac{1}{4}\Big(\overline{\langle \hat{S}^z_{2r}(t)\hat{S}^z_0(0)\rangle} + 2\overline{\langle \hat{S}^z_{2r+1}(t)\hat{S}^z_0(0)\rangle} + \overline{\langle \hat{S}^z_{2r+2}(t)\hat{S}^z_0(0)\rangle}\Big), \tag{9.29}$$

which will be relevant for resolving the A/B-sublattice structure further below. From Eq. (9.28) we then obtain the mean squared displacement at long times,

$$\begin{aligned}
\sigma^2(t) &= \sum_r r^2 \overline{\langle \hat{S}^z_r(t)\hat{S}^z_0(0)\rangle} \\
&\xrightarrow{t\gg 1} \frac{1}{2}\sum_r (2r)^2 \Big\{\overline{\langle \hat{S}^z_{2r-1}(t)\hat{S}^z_0(0)\rangle} + 2\overline{\langle \hat{S}^z_{2r}(t)\hat{S}^z_0(0)\rangle} + \overline{\langle \hat{S}^z_{2r+1}(t)\hat{S}^z_0(0)\rangle}\Big\} = \\
&= \sum_r (2r)^2 G^{(nI)}_{\mathrm{tr}}(r,t) = \sum_r r^2 G^{(nI)}_{\mathrm{tr}}(r,16t) = \frac{8}{3\sqrt{\pi}}\sqrt{t},
\end{aligned} \tag{9.30}$$

where we used Eqs. (9.19,9.20) with $\rho = 3/4$ and $\Gamma = 1$. We can absorb the factor of 16 in $G^{(nI)}_{\mathrm{tr}}(r,16t)$ into the effective (sub)diffusion constant to obtain $D = 16/9\pi$, see also Fig. 9.1. Again the dynamics is subdiffusive with $z = 4$.

To verify this prediction we simulate the circuit of Fig. 9.3 numerically, again using the mapping to a classical Markov process. The derivation of the associated transfer matrix $\hat{\mathcal{T}}$ proceeds in full analogy to the tJ_z – case. Fig. 9.6 (b) demonstrates the validity of Eq. (9.30). In addition, Eq. (9.28) predicts a Gaussian enveloping shape of the charge correlations, which we numerically verify in Fig. 9.6 (a). Intriguingly however, Eq. (9.28) in principle allows for additional sublattice structure. We indeed find sizeable staggered oscillations on top of the Gaussian in Fig. 9.6 (a). These oscillations do not decay at large times and thus hint at additional structure in the model. In order to explain and quantitatively describe these short-distance oscillations, we will switch to a domain wall picture in the following.

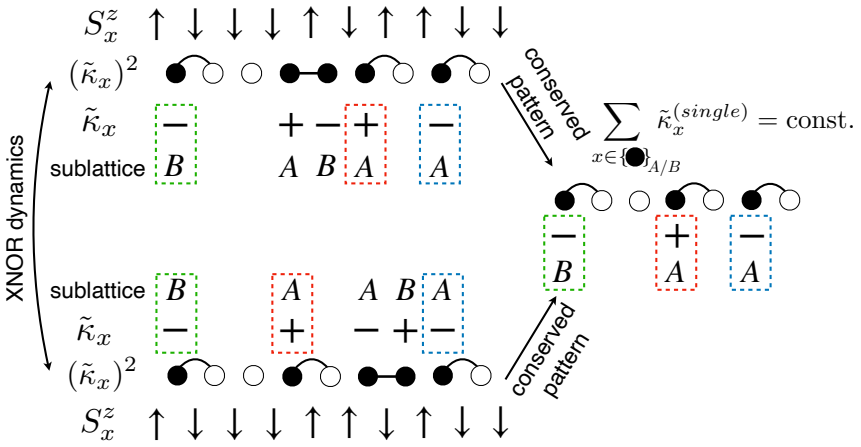

Figure 9.5: Sublattice symmetry. In the domain wall picture, we obtain a conserved pattern by removing all mobile domain wall pairs (illustrated as ●—●). The resulting pattern is formed by single aligned bonds (○) and pairs of a single domain wall with an aligned bond to its right (◠). The pattern is subject to an exclusion constraint of nearest neighbor domain walls, i.e. every filled circle necessarily has at least two empty circle neighbors (one to the left and one to the right). The sublattice charge of all charged domain walls $\hat{\tilde{\kappa}}$ that are not part of a mobile pair is then conserved. This is due to the mobile pairs having a spatial extension of length two, such that single domain walls exchanging their position with such pairs only move by steps of length two at a time, hence preserving their sublattice. They also preserve their charge value since the domain wall charges are perfectly anticorrelated globally.

Conserved pattern: domain wall picture

An alternative description of the Hilbert space structure can be given in terms of the domain wall charge variables

$$\hat{\tilde{\kappa}}_x := \frac{1}{2}(\hat{S}^z_{x+1} - \hat{S}^z_x), \tag{9.31}$$

which ascribes a sign depending on whether the local configuration is $|...\downarrow\uparrow...\rangle$ or $|...\uparrow\downarrow...\rangle$. After fixing the leftmost spin, a complete description of a spin configuration is also given in terms of the locations of its domain walls, $(\tilde{\kappa}_x)^2$, regardless of their sign. We can construct a domain wall version of the conserved charge pattern, see also Refs. [510, 513, 517]: Starting from the left of the system, neighboring domain walls are paired up into mobile pairs ●—● , see Fig. 9.4 (a). The remaining single domain walls are paired up with their corresponding right neighbor bond that connects two aligned spins, ◠ . Defined in this way, the dynamics in the system is generated by mobile domain wall pairs (●—●) moving through the system, exchanging positions with single bonds of aligned spins (○) and with the pairs of domain walls and aligned bonds (◠). The elementary dynamical processes are depicted in Fig. 9.4 (b+c). By removing all mobile domain wall pairs, see e.g. Fig. 9.5, we obtain a conserved pattern in the domain wall description formed by single aligned bonds ○ and the pairs ◠ of domain wall and aligned bond. The conserved pattern thus exhibits a blockade of nearest neighbor domain walls. The number of conserved patterns with such a blockade grows as a Fibonacci sequence in system size. This Fibonacci number then also corresponds to the number of disconnected subsectors in the Hilbert space [509, 510].

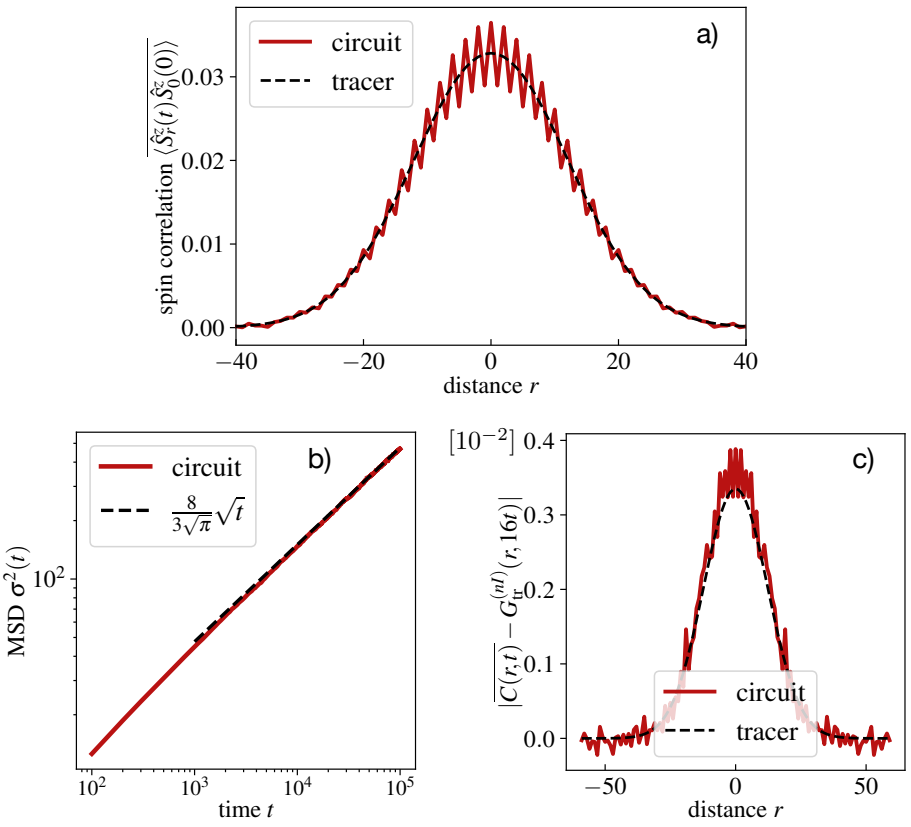

Figure 9.6: Random XNOR model: Numerical results. **a)** Spatial shape of the spin correlation function at time $t = 10^4$ of the random circuit shown in Fig. 9.3. The black dashed line corresponds to the Gaussian of the tracer probability distribution predicted by Eq. (9.44). **b)** The mean squared displacement $\sigma^2(t)$ of the spin correlations agrees with the late time prediction of Eq. (9.30). **c)** The absolute value $\left|C(r,t) - G^{(nI)}_{\rm tr}(x,16t)\right|$ of the oscillations on top of the Gaussian shape as seen in a). The black dashed line corresponds to the prediction of Eq. (9.44). The results demonstrate the quantitative accuracy of the tracer description. The data was averaged over 12800 random initial states of the associated stochastic Markov process in a system of length $L = 5000$. An additional average over $\pm r$ was taken in a) and c), yielding symmetric profiles.

Due to the two-site spatial extension of the domain wall pairs, the total A/B sublattice charge of all domain walls $\hat{\tilde{\kappa}}_x$ that are not part of a mobile pair is a conserved quantity, see Fig. 9.5. Formally, we can express

$$\hat{\tilde{\kappa}}_x = \hat{\tilde{\kappa}}_x^{(single)} + \hat{\tilde{\kappa}}_x^{(pair)}, \tag{9.32}$$

where $\hat{\tilde{\kappa}}_x^{(single)}$ is the domain wall charge operator for *single* domain walls while $\hat{\tilde{\kappa}}_x^{(pair)}$ is the operator for domain walls that are part of mobile *pairs*. The two sublattice charges

$$\hat{\mathcal{Q}}_{A/B} = \sum_{x\in A/B} \hat{\tilde{\kappa}}_x^{(single)} = \text{const.} \tag{9.33}$$

are conserved quantities. The operator $\hat{\tilde{\kappa}}_x$ thus separates into a part that has overlap with the sublattice conservation laws of Eq. (9.33) and a part not associated to any such

conservation law ($\sum_{x\in A/B} \hat{\tilde{\kappa}}_x^{(pair)} \neq \text{const.}$). The domain wall charge correlation function on the even sublattice at late times will thus be dominated by the transport associated to the conserved quantity $\hat{\mathcal{Q}}_A$, i.e.

$$\overline{\langle \hat{\tilde{\kappa}}_{2r}(t)\hat{\tilde{\kappa}}_0(0)\rangle} \overset{t\gg 1}{=} \overline{\langle \hat{\tilde{\kappa}}_{2r}^{(single)}(t)\hat{\tilde{\kappa}}_0^{(single)}(0)\rangle}. \tag{9.34}$$

Corrections to Eq. (9.34) are expected to decay quickly (generically exponentially fast) in time. Since the single domain wall charges are part of a conserved pattern as described above their dynamical correlations are again given by the tracer distribution,

$$\overline{\langle \hat{\tilde{\kappa}}_{2r}(t)\hat{\tilde{\kappa}}_0(0)\rangle} \overset{t\gg 1}{=} C_0\, G_{\text{tr}}^{(nI)}(r,t), \tag{9.35}$$

with constant prefactor C_0 to be determined. The density ρ and the hopping rate Γ entering Eq. (9.35) are the same as in the spin picture above.

To compute C_0 we equate Eqs. (9.34,9.35) and take the sum over r,

$$C_0 = \sum_r \langle \hat{\tilde{\kappa}}_{2r}^{(single)} \hat{\tilde{\kappa}}_0^{(single)} \rangle\,, \tag{9.36}$$

resulting in a simple *static* (notice the absence of the circuit average) correlation function at infinite temperature. We can express Eq. (9.36) as

$$C_0 = \left\langle \left(\hat{\tilde{\kappa}}_0^{(single)}\right)^2 \right\rangle \sum_r \left\langle \hat{\tilde{\kappa}}_{2r}^{(single)} \right\rangle', \tag{9.37}$$

where $\langle\cdot\rangle'$ denotes a modified infinite temperature average with a single positive domain wall *fixed* to sit at site 0. The factor $\left\langle \left(\hat{\tilde{\kappa}}_0^{(single)}\right)^2 \right\rangle$ is determined within the mapping to a conserved pattern from Fig. 9.4: $\left\langle \left(\hat{\tilde{\kappa}}_0^{(single)}\right)^2 \right\rangle = \#(\overset{\frown}{\bullet\circ})/L$ corresponds to the density of single domain walls paired up with a neighboring aligned spin bond. Using that the overall density of domain walls is $1/2$ and that by symmetry $\#(\overset{\frown}{\bullet\circ})/L = \#(\bullet\!\!-\!\!\bullet)/L$, we obtain

$$\begin{aligned} \frac{L}{2} &= 2\cdot \#(\bullet\!\!-\!\!\bullet) + \#(\overset{\frown}{\bullet\circ}) = 3\cdot \#(\overset{\frown}{\bullet\circ}) \\ &\to \left\langle \left(\hat{\tilde{\kappa}}_0^{(single)}\right)^2 \right\rangle = \#(\overset{\frown}{\bullet\circ})/L = 1/6. \end{aligned} \tag{9.38}$$

With this result we can also compute the density ρ of hard core particles (corresponding to the density of non-zero superspins of the previous section) that we used in Eq. (9.30):

$$\rho = 1 - \frac{\#(\bullet\!\!-\!\!\bullet)}{\#(\bullet\!\!-\!\!\bullet) + \#(\circ)} = 1 - \frac{L/6}{L/6 + L/2} = 3/4. \tag{9.39}$$

The remaining correlation function $\left\langle \hat{\tilde{\kappa}}_{2r}^{(single)} \right\rangle'$ in Eq. (9.37) refers only to single domain walls and can thus be computed within the ensemble of possible conserved domain wall

patterns, see Fig. 9.5. Making use of this property we derive the exact value of this correlation function in Sec. 9.3.3 and quote here our final result

$$\boxed{C_0 = \frac{1}{12}(\varphi - 1)} \tag{9.40}$$

for the constant C_0, where $\varphi = (1+\sqrt{5})/2$ is the golden ratio. Then, inserting the definition Eq. (9.31) in Eq. (9.35) yields

$$C_0\, G_{\rm tr}^{(nI)}(r,t) = \frac{1}{4}\Big(2\overline{\langle \hat{S}^z_{2r}(t)\hat{S}^z_0(0)\rangle} - \overline{\langle \hat{S}^z_{2r-1}(t)\hat{S}^z_0(0)\rangle} - \overline{\langle \hat{S}^z_{2r+1}(t)\hat{S}^z_0(0)\rangle}\Big). \tag{9.41}$$

Performing the equivalent derivation for the correlations $\overline{\langle \hat{\tilde{\kappa}}_{2r+1}(t)\hat{\tilde{\kappa}}_0(0)\rangle}$ gives us the additional relation

$$-C_0\, G_{\rm tr}^{(nI)}(r,t) = \frac{1}{4}\Big(2\overline{\langle \hat{S}^z_{2r+1}(t)\hat{S}^z_0(0)\rangle} - \overline{\langle \hat{S}^z_{2r}(t)\hat{S}^z_0(0)\rangle} - \overline{\langle \hat{S}^z_{2r+2}(t)\hat{S}^z_0(0)\rangle}\Big). \tag{9.42}$$

Adding Eqs. (9.28,9.41) as well as Eqs. (9.29,9.42) finally yields the long time correlations

$$\begin{aligned} \overline{\langle \hat{S}^z_{2r}(t)\hat{S}^z_0(0)\rangle} &= \frac{1}{2}(1+2C_0)\, G_{\rm tr}^{(nI)}(r,t) \\ \overline{\langle \hat{S}^z_{2r+1}(t)\hat{S}^z_0(0)\rangle} &= \frac{1}{2}(1-2C_0)\, G_{\rm tr}^{(nI)}(r,t), \end{aligned} \tag{9.43}$$

which we can rewrite as

$$\boxed{\overline{C(r,t)} = \overline{\langle \hat{S}^z_r(t)\hat{S}^z_0(0)\rangle} = [1 + 2C_0(-1)^r]\, G_{\rm tr}^{(nI)}(r,16t).} \tag{9.44}$$

Eq. (9.44) explains the staggered oscillations observed numerically in Fig. 9.6 (a). To check that our quantitative description (i.e. the constant C_0 of Eq. (9.40)) is accurate, we show in Fig. 9.6 (c) that the quantity $\left|\overline{C(r,t)} - G_{\rm tr}^{(nI)}(x,16t)\right|$ agrees well with the prediction of Eq. (9.44) (additional corrections cannot be excluded, however). We emphasize that the staggering of the correlations decribed by Eq. (9.44) persists up to infinite time.

9.2.3 **Random circuit dimer model**

Let us recap only briefly a third example of tJ_z – like dynamics in the dimer model on a bilayer square lattice geometry that we have encountered in Chapter 4, Ref. [4]. The system has a short direction along which periodic boundaries are chosen, making the geometry quasi one-dimensional, and the time evolution is generated by local plaquette flips of parallel dimers,

$$\hat{H} = -J \sum_p \left(|\square\rangle\langle\square| + h.c. \right). \tag{9.45}$$

The model is equivalent to a model of closed directed loops and site-local charges on a square lattice cylinder with short circumference. The existence of a conserved charge pattern and its role in inducing a dynamical exponent $z = 4$ due to the emergence of a hard core tracer problem has been discussed already in Chapter 4. We reiterate that intuitively, the site-local charges in the model are dimers that go in between the two layers, positive or negative depending on which sublattice they occupy. When a charge is enclosed by a loop, it cannot escape the loop under the dynamics of Eq. (9.45). In the presence of a finite density of loops that wind across the circumference of the cylinder (with the same chirality), a conserved pattern is formed by the summing up charges always in between two such loops, see Fig. 9.1 and Chapter 4 for the details. The tracer prediction of $z = 4$ and the Gaussian shape of the dynamical charge correlations have been verified numerically in Chapter 4. Only the precise values of effective (sub)diffusion constants are unknown since the mapping to a conserved pattern is an effective one.

9.3 Integrable quantum systems with conserved pattern

The presence of a conserved charge pattern can also be of use in *integrable* tJ_z – like quantum systems and, in certain cases, provides an alternative route to determine the long time profile and diffusion constant of their spin correlations at infinite temperature. The associated tracer motion relevant for the correlations $C(r,t)$ from Eq. (9.14) is one with *ballistically* instead of diffusively moving particles. As single particles move ballistically, the many-body tracer distribution will be diffusive. A similar situation was considered in Refs. [465, 518], where the spin diffusion constant of an interacting deterministic classical cellular automaton with invariant spin pattern and pattern-independent dynamics was computed exactly. According to Eq. (9.14), this spin diffusion is directly associated with a Gaussian tracer distribution with the same diffusion constant,

$$G_{tr}(\ell,t) \to G_{tr}^{(I)}(\ell,t) = \frac{1}{\sqrt{4\pi D t}} \exp\Big\{-\frac{\ell^2}{4Dt}\Big\}. \tag{9.46}$$

The superscript (I) indicates an integrable process which implies a broadening of G_{tr} as $\sim \sqrt{t}$ (instead of $\sim t^{1/4}$ which we have obtained for generic systems in Sec. 9.2). Using the result of Ref. [465], the diffusion constant D of Eq. (9.46) is determined by the density ρ of particles along the chain as well as their effective velocity v_{eff},

$$\begin{aligned} \langle \Delta x^2 \rangle &= 2Dt \\ D &= \frac{v_{\text{eff}}}{2}(\rho^{-1} - 1). \end{aligned} \tag{9.47}$$

In the discrete time cellular automaton considered in Ref. [465], all particles have a fixed velocity of $v_{\text{eff}} = 2$.

9.3.1 Integrable tJ_z – model

The above connection can be put to direct use in the integrable $J_z \to 0$ limit of the tJ_z – model [519],

$$\hat{H}_t = -\frac{1}{2}\sum_{x,\sigma}(\hat{\tilde{c}}^\dagger_{x+1,\sigma}\hat{\tilde{c}}_{x,\sigma} + h.c.), \tag{9.48}$$

which features only the hopping of spinful fermions with forbidden double occupancy. The matrix elements $a(\boldsymbol{x}'\boldsymbol{\sigma}|\boldsymbol{x}\boldsymbol{\sigma},t) = a(\boldsymbol{x}'|\boldsymbol{x},t)$ of the time evolution obtained from Eq. (9.48) do not depend on the pattern $\boldsymbol{\sigma}$, so $R(r,t) = 0$ in Eq. (9.17), and the mapping to a tracer problem is exact at all times. At infinite temperature, the density of particles is $\rho = 2/3$ and we can determine the effective velocity v_{eff} by noting that $\hat{H}_t$ can be mapped to a problem of spinless free fermions [519],

$$\hat{H}_t = -\sum_k \cos(k)\hat{f}^\dagger_k\hat{f}_k. \tag{9.49}$$

We give an intuitive argument for why this is possible: Since the dynamics is oblivious to the conserved spin pattern, for a given inital basis state we can simply *i)* 'write down' the invariant spin pattern for bookkeeping purposes, *ii)* remove the fermions' spins, *iii)* perform the time evolution with a Hamiltonian of spinless fermion hopping (of same hopping strength), and then *iv)* reintroduce the pattern afterwards. Steps *i)* and *iv)* in this mapping are of course highly non-local.

At infinite temperature we then expect all momentum modes of Eq. (9.49) to be occupied with equal probability. While Ref. [465] derived Eq. (9.47) for an automaton in which every particle has the same absolute velocity, here we need to consider a distribution of different momentum modes. We expect that the mean displacement of the equivalent tracer process depends only on the average of the absolute velocity and thus predict the effective velocity for Eq. (9.47) to be given by the average absolute group velocity of Eq. (9.49):

$$v_{\text{eff}} = \frac{1}{2\pi}\int_{-\pi}^{\pi} dk\, |\partial_k \cos(k)| = \frac{2}{\pi}. \tag{9.50}$$

This leads to the infinite temperature spin diffusion constant

$$D_t = \frac{1}{2\pi} \tag{9.51}$$

for the quantum model $\hat{H}_t$ of Eq. (9.48). Eq. (9.47) also yields the diffusion constant at infinite temperature but with fixed density $\rho \neq 2/3$ or chemical potential μ such that $\beta\mu = \text{const.}$ as $\beta \to 0$.

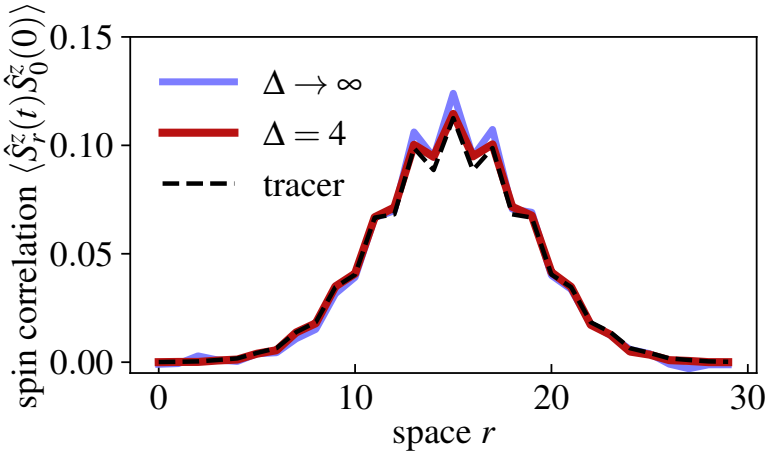

Figure 9.7: Folded XXZ chain. Profile of the dynamical spin correlation function for the folded XXZ chain of Eq. (9.53) (blue curve, $\Delta \to \infty$) at time $t = 18$ in a system of length $L = 30$. The black dashed line shows the prediction of Eq. (9.55), there are no fit parameters. The red line shows the profile obtained for the XXZ chain Eq. (9.52) at anisotropy $\Delta = 4$, illustrating good agreement with Eq. (9.55) at intermediate times, even for moderate values of anisotropy.

9.3.2 Folded XXZ spin chain

As a second example we consider an integrable version of the random XNOR model, the folded XXZ chain. It is obtained from the integrable XXZ model

$$\hat{H}_{\mathrm{XXZ}} = -\sum_i \frac{1}{2}(\hat{S}^+_i \hat{S}^-_{i+1} + \hat{S}^-_i \hat{S}^+_{i+1}) + \Delta \hat{S}^z_i \hat{S}^z_{i+1} \tag{9.52}$$

in the limit of large anisotropy $\Delta \to \infty$, which using a Schrieffer-Wolff transformation yields

$$\hat{H}_{\mathrm{fXXZ}} = -\sum_i (\frac{1}{4} + \hat{S}^z_{i-1}\hat{S}^z_{i+2})(\hat{S}^+_i \hat{S}^-_{i+1} + \hat{S}^-_i \hat{S}^+_{i+1}). \tag{9.53}$$

$\hat{H}_{\mathrm{fXXZ}}$ remains integrable and many of its thermodynamic and dynamic properties have been analyzed in recent works [511–514]. We note that $\hat{H}_{\mathrm{fXXZ}}$ consists of four-site spin- and domain wall-conserving terms and thus features the same effective conserved pattern of superspins as the random XNOR model above. In particular, it can be demonstrated that in the superspin picture, the folded XXZ chain becomes equivalent to the integrable limit of the tJ_z – model from Eq. (9.48), $\hat{H}_{\mathrm{fXXZ}} \to \hat{H}_t$ [516]. As a consequence, the spin diffusion constant D_{fXXZ} of the folded XXZ chain can be obtained from the diffusion constant D of superspins determined by the Hamiltonian $\hat{H}_t$ of Eq. (9.48). In order to relate the two, we recall that the infinite temperature average in the original spin picture implies a density $\rho = 3/4$ of superspins in the associated integrable tJ_z – model. Furthermore, in the original lattice superspins always move by two sites. The variance

$\langle \Delta x^2 \rangle = 2D_{\mathrm{fXXZ}} t$ of the original spin correlation profile is thus determined by

$$\begin{aligned} \frac{2D_{\mathrm{fXXZ}}\, t}{4} &= \frac{\langle \Delta x^2 \rangle}{4} = 2Dt \\ \rightarrow D_{\mathrm{fXXZ}} &= \frac{4}{3\pi}, \end{aligned} \tag{9.54}$$

where we have used that $D = 1/3\pi$ for $\rho = 3/4$ and $v_{\mathrm{eff}} = 2/\pi$ in Eq. (9.47). The value of D_{fXXZ} in Eq. (9.54) is in agreement with previous analytical results [456, 520], obtained using generalized hydrodynamics [182, 183], as well as numerical results for the XXZ chain [521, 522]. In addition, following the analysis of the sublattice domain wall charge in the XNOR model, see Fig. 9.5, we predict the full long time profile of the dynamical spin correlations for the folded XXZ chain to be

$$\boxed{C(r,t) = [1 + 2C_0(-1)^r]\, G^{(I)}_{tr}(r,t).} \tag{9.55}$$

Here, $G^{(I)}_{tr}(r,t)$ is from Eq. (9.46) with $D = D_{\mathrm{fXXZ}}$. In particular, the long time profile features characteristic staggered oscillations of strength $2C_0$ with C_0 from Eq. (9.40).

These oscillations also lead to a distinct contribution to the spin conductivity $\sigma(k,\omega) = \frac{\beta}{2} \langle j(k,\omega) j(-k,-\omega) \rangle$, with spin current $j(k,\omega)$. Using the continuity equation $\partial_t S^z_x(t) + \partial_x j(x,t) = 0$, we relate $\sigma(k,\omega) = \frac{\beta\omega^2}{2k^2} C(k,\omega)$ and obtain

$$\sigma(k = \pi, \omega \to 0) = \frac{C_0 \beta}{2} D_{\mathrm{fXXZ}}. \tag{9.56}$$

The finite momentum conductivity of the folded XXZ chain thus exhibits a finite contribution at $k = \pi$.

We verify Eq. (9.55) numerically for the folded XXZ chain of Eq. (9.53) in systems of finite size and at intermediate time scale in Fig. 9.7. We consider a chain of size $L = 30$ spins by making use of the conserved pattern and employing sparse matrix evolution. The infinite temperature average for the spin correlations was approximated by averaging over 10^5 randomly chosen product initial states for the time evolution. We find good agreement with Eq. (9.55) already at a time $t = 18$ in Fig. 9.7. Furthermore, we note that the anisotropic XXZ chain of Eq. (9.52) has recently been implemented in quantum simulation experiments [200]. In a simple perturbative argument, the Hamiltonian $\hat{H}_{\mathrm{fXXZ}}$ should provide a good estimate for the time evolution of $\hat{H}_{\mathrm{XXZ}}$ up to times $t \sim \Delta^2$ in the anisotropy. Signatures of Eq. (9.55) should thus be visible at intermediate times already at moderate anisotropy strength. We demonstrate this numerically in Fig. 9.7 by time-evolving an infinite temperature density matrix perturbed by a spin excitation in the center of the chain. We use matrix product state methods with a bond dimension $\chi = 1200$ for the time evolution with the anisotropic XXZ Hamiltonian of Eq. (9.52) [454]. We find good agreement with the folded limit and the expression in Eq. (9.55) already for $\Delta = 4$ at a time $t = 18$ in Fig. 9.7.

We conclude this section with the following remark: As discussed previously, the folded XXZ Hamiltonian $\hat{H}_{\mathrm{fXXZ}}$ maps to the integrable limit $\hat{H}_t$ of the tJ_z – model in the superspin picture. Similarly, one can apply the reverse of this mapping to the tJ_z – like deterministic cellular automaton studied in Refs. [465, 518], which is effectively a local automaton for the superspins. Under the reverse mapping we then obtain an automaton for spin-$1/2$ variables that is able to mimic the long-time dynamics of the folded XXZ chain. A different cellular automaton mimicking the folded XXZ dynamics, which exhibits different left- and right-mover velocities, has recently been studied in Ref. [523]. In our prescription outlined above the automaton obtained from Ref. [465] by inverting the mapping from superspins to spin-$1/2$ is non-local in the spin-$1/2$ variables and features symmetric left- and right-movers of equal speed instead.

9.3.3 **Strength of staggered oscillations**

In this section we derive the exact analytical expression Eq. (9.40) for the constant C_0 defined in Eq. (9.35). This constant determines the strength of the staggered oscillations on top of the Gaussian enveloping shape for the dynamical spin correlation profile in both the random XNOR circuit and the folded XXZ model, *cf.* Eqs. (9.44,9.55). We recall that according to Eq. (9.37), C_0 can be written in the domain wall picture as

$$C_0 = \left\langle \left(\hat{\tilde{\kappa}}_0^{(single)} \right)^2 \right\rangle \sum_r \left\langle \hat{\tilde{\kappa}}_{2r}^{(single)} \right\rangle', \tag{9.57}$$

where the expectation value $\langle \cdot \rangle'$ is taken with respect to an ensemble where a domain wall with positive charge $\tilde{\kappa}_0^{(single)} = 1$ is fixed to sit at bond 0. We have already evaluated $\left\langle \left(\hat{\tilde{\kappa}}_0^{(single)} \right)^2 \right\rangle = 1/6$ in the main text and so we focus on the correlation function

$$\left\langle \hat{\mathcal{Q}}_A \right\rangle' := \sum_r \left\langle \hat{\tilde{\kappa}}_{2r}^{(single)} \right\rangle'. \tag{9.58}$$

$\left\langle \hat{\mathcal{Q}}_A \right\rangle'$ counts the A-sublattice charge of single domain walls provided a positive domain wall is located at the origin. The sublattice charge Eq. (9.58) refers only to *single* domain walls and is conserved in the time evolution. In particular, $\left\langle \hat{\mathcal{Q}}_A \right\rangle'$ can be calculated entirely within the ensemble of all possible conserved domain wall patterns, see Fig. 9.5, where mobile domain wall pairs have already been removed. This is our approach in the following.

We first recall that the ensemble of possible conserved patterns in the domain wall picture is subject to an exclusion principle of nearest-neighbor domain walls, see Fig. 9.5. That is, a bond with a domain wall must have two aligned bonds as its neighbors. For simplicity and without loss of generality we can always assume the leftmost domain wall in the system to have positive charge, fixing a $\mathbb{Z}_2$ degree of freedom for the staggering.

The exclusion property then gives rise to a Fibonacci sequence for the number $N_p(\ell)$ of possible conserved pattern configurations for a number ℓ of bonds:

$$N_p(\ell) = N_p(\ell-1) + N_p(\ell-2). \tag{9.59}$$

Given that a (positive) domain wall is fixed to sit at the origin, let us move to the right of the origin and derive the probability $p(r)$ to encounter the *next* domain wall exactly at a distance r. We find $p(1) = 0$ due to the exclusion principle and

$$p(r \geq 2) = \frac{N_p(\ell - r)}{N_p(\ell)} \xrightarrow{\ell\to\infty} \varphi^{-r}, \tag{9.60}$$

with the golden ratio $\varphi = \frac{1+\sqrt{5}}{2}$. As required, $\sum_{r=1}^{\infty} p(r) = 1/(\varphi^2 - \varphi) = 1$. Let us then further derive the probability $p(A|A)$ that as we go to right from a domain wall located on the A sublattice, the next domain wall we encounter is again located on the A sublattice,

$$p(A|A) = \sum_{n=1}^{\infty} p(2n) = \varphi^{-2} \sum_{n=0}^{\infty} \varphi^{-2n} = \frac{1}{\varphi^2 - 1} = \frac{1}{\varphi}, \tag{9.61}$$

where we used the defining equation of the golden ratio in the last equality. From this result, we also obtain the probability $p(B|A) = 1 - p(A|A)$ to find the next domain wall we encounter on the B sublattice, given that the previous one is located on the A sublattice. Similarly, we have $p(B|B) = p(A|A)$ and $p(A|B) = p(B|A)$.

We now take into account that the charges of the domain walls have to be perfectly anticorrelated, i.e., if there is a positive domain wall at the origin, the next domain wall we encounter to the right must have negative charge. Therefore, moving to the right from the positive domain wall at the origin, we can determine the charge of the next domain wall that we find at an A sublattice bond by counting the number of B sublattice domain walls in between. The probability $p(A, n_B = 0, A)$ to find no other domain wall between two consecutive A domain walls is $p(A, n_B = 0, A) = p(A|A)$. The probability to find a number $n_B \geq 1$ of B sublattice domain walls between two consecutive A domain walls is given by

$$\begin{aligned} p(A, n_B \geq 1, A) &= p(A|B)\big[p(B|B)\big)\big]^{n_B - 1} p(B|A) = \\ &= \big[1 - p(A|A)\big]^2 \big[p(A|A)\big]^{n_B - 1}. \end{aligned} \tag{9.62}$$

If the number of B sublattice domain walls between two consecutive A domain walls is even, the two A domain walls have opposite charge. If the number of B sublattice domain walls between two consecutive A domain walls is odd, they have equal charge. Therefore, the probability to find two consecutive A sublattice domain walls with opposite charge is

given by

$$\begin{aligned} P_- &= \sum_{n=0}^{\infty} p(A, n_B = 2n, A) \\ &= p(A|A) + \big[1 - p(A|A)\big]^2 p(A|A) \sum_{n=0}^{\infty} \big[p(A|A)\big]^{2n} \\ &= p(A|A) + \big[1 - p(A|A)\big]^2 \frac{p(A|A)}{1 - \big[p(A|A)\big]^2} = \frac{2}{\varphi^2}, \end{aligned} \tag{9.63}$$

where in the last equality we inserted Eq. (9.61). Accordingly, the probability to find two consecutive A sublattice domain walls with equal charge is given by

$$P_+ = 1 - P_- = 1 - \frac{2}{\varphi^2}. \tag{9.64}$$

We note that $P_- \approx 0.764 > 0.5$, i.e. two consecutive A domain wall charges are anticorrelated. This is a 'remainder' of the perfect anticorrelation between two consecutive domain walls irrespective of the sublattice.

Let us finally take a randomly chosen conserved domain wall pattern configuration with a positive domain wall fixed at the origin and consider the r-th A sublattice domain wall to the right from the origin. The charge of the r-th A domain wall is then determined by a sequence of exactly r pairs of two consecutive A domain walls. The probability to find $r' \leq r$ anticorrelated consecutive A domain wall pairs in this sequence is $\binom{r}{r'}(P_-)^{r'}(P_+)^{r-r'}$, where the binomial coefficient accounts for the reordering of the anticorrelated pairs in the sequence. Since the domain wall at the origin is positive, a sequence containing r' anticorrelated consecutive domain wall pairs implies a charge of $(-1)^{r'}$ for the r-th A domain wall. Perfoming a sum over the possible number $0 \leq r' \leq r$ of anticorrelated pairs in the sequence and summing over the charge contributions from all A sublattice domain walls we obtain

$$\begin{aligned} \left\langle \hat{\mathcal{Q}}_A \right\rangle' &= 1 + 2 \sum_{r=1}^{\infty} \sum_{r'=0}^{r} \binom{r}{r'} (-1)^{r'} (P_-)^{r'} (P_+)^{r-r'} = \\ &= 1 + 2 \sum_{r=1}^{\infty} (P_+ - P_-)^r = \frac{P_+}{P_-} = \frac{\varphi^2}{2} - 1. \end{aligned} \tag{9.65}$$

In the first line of the above equation, the first term of unity is due to the positive contribution of the positive charge fixed at the origin, while the factor of two is due to symmetric contributions from right and left of the origin. According to Eq. (9.58), Eq. (9.65) yields the correlation function $\sum_r \left\langle \hat{\tilde{\kappa}}_{2r}^{(single)} \right\rangle'$. Inserting into Eq. (9.57) finally we obtain

$$\boxed{C_0 = \frac{1}{6}\Big(\frac{\varphi^2}{2} - 1\Big) = \frac{1}{12}(\varphi - 1),} \tag{9.66}$$

completing our proof.

9.4 Broken pattern conservation

In this section, we return to random unitary circuit models but relax the condition of an exactly conserved spin pattern. In particular, we consider constrained 'tJ_m – like' models in which only a certain number m of moments of the spin pattern remains constant, see Eqs. (9.1,9.3). Remarkably, breaking the pattern conservation does not immediately imply conventional diffusion but the resulting dynamics sensitively depends on the number of conserved moments. To see this, we note that the pattern-internal spin dynamics in the presence of m conserved multipole moments is governed by the following hydrodynamic equation for the coarse-grained spin density $\langle \hat{\sigma}_x(t) \rangle$ [2, 389],

$$\partial_t \langle \hat{\sigma}_x \rangle + (-1)^m D_s \, \partial_x^{2m+2} \langle \hat{\sigma}_x \rangle = 0. \tag{9.67}$$

Eq. (9.67) describes (sub)diffusive dynamics with dynamical exponent $z = 2m + 2$ and its fundamental solution, which corresponds to the spin part of Eq. (9.9) via linear response, reads in momentum space:

$$F(k,t) = \frac{1}{\sqrt{2\pi}} \exp(-D_s \, k^{2m+2} t), \tag{9.68}$$

normalized such that $\int dx \, F(x,t) = 1$. Using Eq. (9.68) in Eq. (9.14) we obtain the spin correlations in momentum space,

$$C(k,t) = G_{tr}(k,t) \, F(k,t) = \frac{1}{2\pi} \exp\Big\{ -D_s \, k^{2m+2} t - \sqrt{Dt} \, k^2 \Big\}, \tag{9.69}$$

which we will analyze for different values of m in the following. While $m = 0$ leads to conventional diffusion, $m \geq 2$ preserves the tracer mapping at long times. The case $m = 1$ turns out to be special, with a competition between two processes that have the same dynamical exponent but different scaling functions.

9.4.1 $m = 0$: Diffusion

For $m = 0$, under rescaling space and time in Eq. (9.69) according to $k \to k/\lambda$, $t \to \lambda^z t = \lambda^2 t$, we obtain

$$C(k,t) \sim \exp\Big\{ -D_s k^2 t - \sqrt{Dt} \, k^2/\lambda \Big\} \xrightarrow{\lambda \to \infty} \exp\Big\{ -D_s k^2 t \Big\}. \tag{9.70}$$

This implies that the dynamical exponent is $z = 2$. Therefore, if only the total spin of the pattern is conserved the correlations $C(k,t)$ are described by conventional diffusion as expected. We verify this result numerically in tJ – like random unitary circuits with

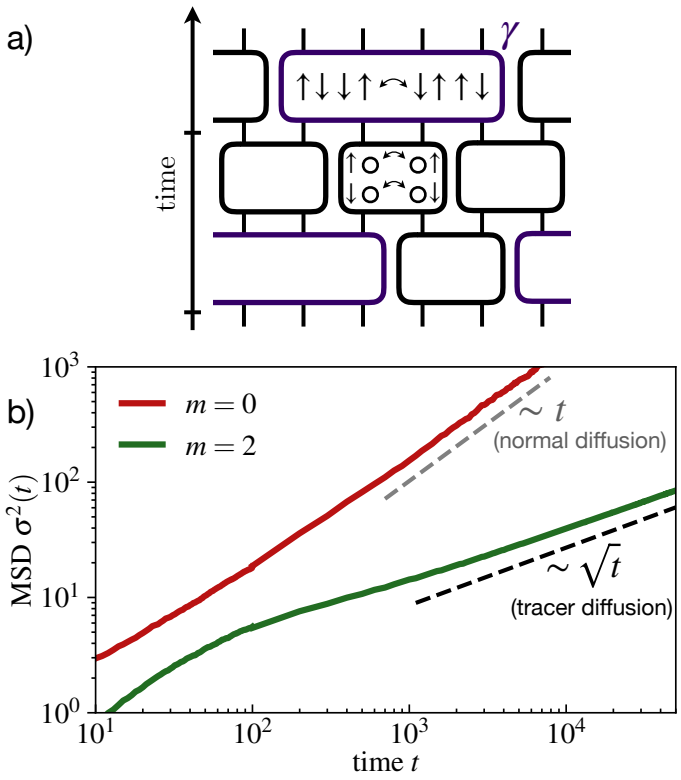

Figure 9.8: Moment-conserving random circuit evolution. a) We consider tJ_m – like random circuits with spin terms that conserve a given number m of multipole moments (in the depicted example the dipole moment $m = 1$) of the spin pattern. The spin terms are applied with some probability γ, the particle hopping terms with probability $1 - \gamma$. **b)** The dynamics of random circuits with multipole moment conserving spin pattern depends on the number m of conserved moments. If only the total spin of the pattern is conserved ($m = 0$), the mean-squared displacement $\sigma^2(t) \sim t$ follows conventional diffusion. If all moments up to the quadrupole moment ($m = 2$) or higher are conserved, $\sigma^2(t) \sim \sqrt{t}$ remains dominated by anomalously slow hard core tracer motion.

charge-conserving two-spin gates, see Fig. 9.8 (a). The mean squared displacement $\sigma^2(t)$ of the resulting real space correlations $\overline{C(r,t)}$ indeed scales diffusively $\sigma^2(t) \sim t$ at long times as shown in Fig. 9.8 (b).

9.4.2 $m \geq 2$: Tracer diffusion

On the other hand, rescaling $k \to k/\lambda$, $t \to \lambda^z t = \lambda^4 t$ for $m \geq 2$ in Eq. (9.69) yields

$$C(k,t) \sim \exp\Big\{-D_s k^{2m+2} t/\lambda^{2m-2} - \sqrt{Dt}\, k^2\Big\} \xrightarrow{\lambda\to\infty} \exp\Big\{-\sqrt{Dt}\, k^2\Big\}, \tag{9.71}$$

and the dynamical exponent is $z = 4$. Thus, if all moments of the spin pattern up to at least the quadrupole moment are conserved the long-time correlations remain dominated by the anomalously slow tracer motion of Eq. (9.18). Again, we verify this numerically by computing the mean-squared displacement $\sigma^2(t) = \sum_r r^2\, \overline{C(r,t)}$ of a random time evolution with $m-$pole conserving spin interactions, see Fig. 9.8 (b). In practice, we have to make sure to avoid localization of the spin pattern dynamics due to a strong fragmentation

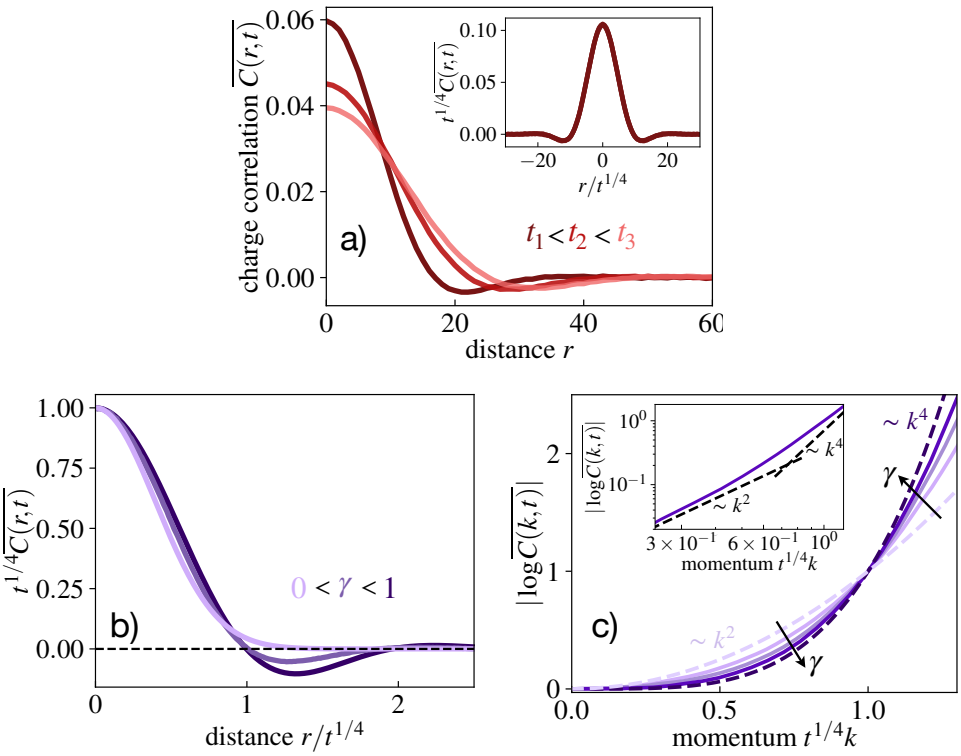

Figure 9.9: Hydrodynamic phase mixing. a) The profile of the spin correlations at different times for a probability $\gamma \neq 0$ of random circuit updates that conserve the dipole-moment of the spin pattern. *Inset*: A scaling collapse of the profiles determines the dynamical exponent $z = 4$. **b)** The scaling function associated to some $0 \leq \gamma \leq 1$ is neither the Gaussian, that is associated to hard core tracer diffusion, nor the fundamental solution of the dipole-conserving hydrodynamic equation Eq. (9.67). It is instead given by a convolution of the two. Here, the scaling functions are normalized such that their value at $r = 0$ is equal to one. **c)** Logarithm of the Fourier transform $C(k,t)$ of the real space correlations $C(r,t)$. The momentum axis has been rescaled independently for different γ, defined in such a way that all curves coincide at $t^{1/4}k = 1$, $|\log \overline{C(k,t)}| = 1$. This allows us to directly compare the relative strengths of the $(kt^{1/4})^2$– and $(kt^{1/4})^4$– contributions to $|\log \overline{C(k,t)}|$ for different γ. We see that increasing the probability γ of dipole-conserving spin updates leads to an increasing weight of the $(t^{1/4}k)^4$-term in Eq. (9.74). Inset: On a double logarithmic scale the crossover from $(kt^{1/4})^2$– to $(kt^{1/4})^4$– behavior becomes visible.

of the Hilbert space into disconnected subsectors, which can occur for all $m \geq 1$ [235–237]. This is achieved by choosing spin-gates of sufficient range, which ensures ergodicity of the spin dynamics. As expected, the system is described by $z = 4$ subdiffusive tracer dynamics in the case of quadrupole conservation $m = 2$, i.e. $\sigma^2(t) \sim \sqrt{t}$, see Fig. 9.8 (b).

9.4.3 $m = 1$: Hydrodynamic phase coexistence

For the special case of $m = 1$, both terms in the exponent of $C(k,t)$ are equally relevant under the rescaling $k \to k/\lambda$, $t \to \lambda^4 t$,

$$C(k,t) \xrightarrow{\lambda \to \infty} \exp\left\{-D_s k^4 t - \sqrt{Dt}\, k^2\right\}. \tag{9.72}$$

The correlation function $C(k,t)$ is thus subject to a competition between two inequivalent dynamical processes that both have $z = 4$ but that have different forms of their respective scaling function. Notably, although $C(k,t) = C(kt^{1/4})$ is a function of $kt^{1/4}$, it can not be written in terms of some universal scaling function $\mathcal{K}(\cdot)$ that is independent of microscopic details. Instead,

$$C(k,t) = \mathcal{K}\Big(k(Dt)^{1/4}, D_s/\sqrt{D}\Big), \tag{9.73}$$

i.e. the form of $C(kt^{1/4})$ depends non-trivially on the ratio $D_s/\sqrt{D}$ which determines the mixture of the two universal processes. Specifically, we can express

$$\boxed{\log C(k,t) = -(D_s + \sqrt{D})\Big[\mu\,(kt^{1/4})^4 + (1-\mu)\,(kt^{1/4})^2\Big],} \tag{9.74}$$

where $\mu = \mu(D_s/\sqrt{D}) = \frac{D_s}{\sqrt{D}}(1 + \frac{D_s}{\sqrt{D}})^{-1}$ and $0 \leq \mu \leq 1$. The specific mixture, and thus the long time and length scale profile of the spin correlations, is sensitive to microscopic details of the time evolution, reminiscent of UV-IR-mixing [482, 483, 524–528]. This results in a continuously varying hydrodynamic universality class controlled by the microscopic mixing parameter μ. Here, we identify a hydrodynamic universality class with both the dynamical exponent and the scaling function.

We confirm these theoretical considerations numerically in Fig. 9.9, where we consider a random unitary time evolution with dipole-conserving dynamics within the spin pattern, see Fig. 9.8 (a). To ensure ergodicity, we use dipole-conserving spin updates ranging over eight sites. For any given probability γ at which non-trivial spin pattern rearrangements occur the dynamical exponent is $z = 4$, as demonstrated by the scaling collapse of $\overline{C(r,t)}$ evaluated at different times in Fig. 9.9 (a). However, varying this probability γ effectively controls the ratio $D_s/\sqrt{D}$ and leads to different scaling functions as shown in Fig. 9.9 (b). In particular, the limiting distributions are a Gaussian for $\gamma = 0$ and the dipole-conserving hydrodynamic scaling function of Eq. (9.68) (for $m = 1$) as $\gamma \to 1$. In addition, we numerically compute the Fourier transform $C(k,t)$ of the correlation profile to verify the prediction of Eq. (9.74). Fig. 9.9 (c) shows that increasing the rate γ of the spin dynamics leads to an increasing contribution of the $(kt^{1/4})^4$−term to $\log C(k,t)$.

The arbitrary mixing of two distinct dynamical scaling functions as in Eq. (9.74) can be viewed as phase coexistence of two hydrodynamic phases, in analogy with more conventional phase coexistence occuring at first order equilibrium transitions. To make this analogy more tangible, let us imagine a situation in which the dynamics of the spin pattern is given by

$$F_\alpha(k,t) = \frac{1}{\sqrt{2\pi}}\,\exp(-D_s\,|k|^\alpha t), \tag{9.75}$$

now with some general exponent $0 < \alpha < \infty$ whose value is governed by some underlying model (e.g. through the power-law decay of a long-ranged spin term in the

constrained tJ – like models). Using that $C_\alpha(k,t) = F_\alpha(k,t)G_{tr}(k,t)$, we obtain the dynamical exponent z as a function of α:

$$z(\alpha) = \begin{cases} \alpha, \text{ for } \alpha < 4 \\ 4, \text{ for } \alpha \geq 4 \end{cases} . \tag{9.76}$$

In particular, $\alpha > 4$ corresponds to Gaussian tracer motion while $\alpha < 4$ is associated with non-Gaussian scaling functions. In addition, for $\alpha \neq 4$ we can always write the real space correlations $C_\alpha(r,t)$ as

$$C_\alpha(r,t) = (Dt)^{-1/4}\mathcal{F}_\alpha\big(r(Dt)^{-1/4}\big), \tag{9.77}$$

with a normalized universal scaling function $\int dx\, \mathcal{F}_\alpha(x) = 1$. If we thus consider $\alpha = 4$ to separate a Gaussian and a non-Gaussian dynamical phase, we can accordingly define an order parameter that quantifies the non-Gaussianity of the scaling function for a given α via

$$\begin{aligned} h(\alpha) &:= \min_{\lambda>0} \int dx \left(\lambda\, \mathcal{F}_\alpha(\lambda x) - \frac{1}{\sqrt{\pi}} \exp(-x^2)\right)^2 = \\ &= \begin{cases} \frac{1}{2\pi} \min\limits_{\lambda>0} \int dk \left(e^{-(|k|/\lambda)^\alpha} - e^{-k^2/4}\right)^2, & \alpha < 4 \\ 0, & \alpha > 4 \end{cases} . \end{aligned} \tag{9.78}$$

We have evaluated $h(\alpha)$ numerically in Fig. 9.10, where we see a clear discontinuity at $\alpha = 4$. The central property $\Delta h(\alpha = 4) > 0$ can also be demonstrated analytically. In particular, the variance of the $\alpha \to 4^-$ scaling function vanishes, as opposed to a Gaussian [2]. This jump in the order parameter suggests that we can indeed interpret the point $\alpha = 4$ as a first order dynamical transition, with Eq. (9.74) describing the Gaussian/non-Gaussian phase mixture.

9.5 Conclusions & outlook

In this chapter, we investigated the emergent hydrodynamics of general tJ – like many-body systems in one dimension with constrained spin interactions. We found that for chaotic, thermalizing systems the dynamical spin correlation function at infinite temperature is given by a convolution of the dynamics of the underlying spin pattern and the tracer motion of hard core particles. In tJ_z – like systems all multipole moments of the spin pattern are constants of motion and spin correlations are given by tracer dynamics alone. This allowed us to demonstrate the emergence of subdiffusion with dynamical exponent $z = 4$ in several random circuit lattice models that feature a (effective) constant spin pattern. Using results from the theory of tracer motion we provided expressions for the full long-time profile of dynamical spin correlations in these models. It will be interesting to see in the future whether additional one-dimensional systems fall under this dynamical

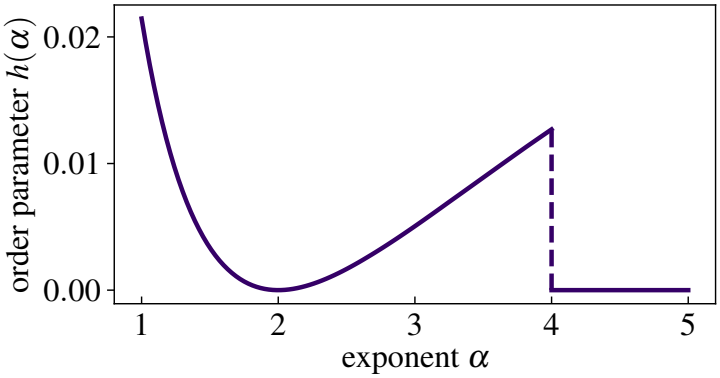

Figure 9.10: Hydrodynamic order parameter. The order parameter $h(\alpha)$ of Eq. (9.78) quantifies the deviation of the charge correlation profile from a Gaussian. α labels the exponent of the spin pattern's internal dynamics, see Eq. (9.75). There is a clear discontinuity at $\alpha = 4$, where long-time dynamical correlations switch between Gaussian tracer motion and a non-Gaussian dipole-conserving profile. As a consequence, $\alpha = 4$ can be interpreted as a first order dynamical transition, which allows for phase coexistence of distinct hydrodynamic universality classes.

universality class. We also remark that although we mostly focused on situations with a conserved $\sigma_i = \pm 1$ spin pattern, our results generalize to patterns of higher effective spin $\sigma_i = -|S|, ..., |S|$. In such an instance, all odd power spin density correlations of the form

$$\left\langle \left(\hat{S}^z_x(t)\right)^{2n+1} \left(\hat{S}^z_0(0)\right)^{2n+1} \right\rangle , \tag{9.79}$$

with integer n, reduce to the same tracer process up to a global prefactor. We emphasize that our results apply to infinite temperature correlations. Whether extensions to finite temperatures are possible depends sensitively on whether the average charge of the pattern vanishes also at finite temperatures for a given model.

We further established a connection to integrable tJ_z – like quantum systems which feature conserved spin patterns and a time evolution that is independent of the pattern. By mapping to a tracer problem of ballistically moving particles, we were able to reproduce the spin diffusion constant of the folded XXZ chain and provided its full long-time correlation profile. The characteristic staggered oscillations of the resulting correlation profile can be verified in quantum simulation experiments on XXZ chains already at moderate anisotropy. We further point out a connection to the anomalous full counting statistics of current correlations that were recently reported for the XXZ chain, the XNOR circuit, and for a deterministic classical automaton with conserved pattern, Refs. [529, 530]. Ref. [529] provides a picture in which such correlations can be understood as the effective tracer motion of a single domain wall. Our unifying picture on the intrinsic structure of these models shows that their anomalous counting statistics has the same underlying mechanism. We therefore expect that such anomalous statistics appear in all pattern-conserving systems.

Moreover, it is interesting to study non-integrable Hamiltonian quantum systems with

conserved patterns, e.g. via the tJ_z – model at finite J_z or via adding diagonal interactions to the folded XXZ model. For example, a stochastic spin chain closely related to the folded XXZ model is the so-called Ising-Kawasaki model [531, 532], taken in a particular limit: the Hamiltonian H_{fXXZ} is supplemented by nearest-neighbor (NN) and next-nearest-neighbor (NNN) Ising terms. The name derives from the fact that the quantum Hamiltonian is obtained from the Markov operator of a classical Ising chain undergoing Kawasaki magnetization-conserving dynamics. The NNN Ising coupling does not commute with H_{fXXZ}, leading to integrability breaking in many sectors [510] while preserving the pattern conservation described above. Such systems should fall under the same universality class as the generic random circuits considered in this work and we expect them to exhibit $z = 4$ subdiffusive hard core tracer dynamics. A version of the folded XXZ model in which integrability is broken by noise was recently studied in Ref. [533], concluding $z = 4$ as well.

In addition, we investigated the dynamics of generic systems in which only a finite number of multipole moments of the spin pattern remains conserved. We found that the characteristics of tracer dynamics survive if at least the multipole moments up to and including the quadrupole moment are constant. Intriguingly, if only the moments up to the dipole are conserved there emerges a special scenario in which spin correlations are subject to a competition between two hydrodynamic processes with dynamic exponent $z = 4$ but different scaling functions. The resulting shape of the long-time correlations are then susceptible to microscopic details of the time evolution and we find the situation to be reminiscent of the coexistence of different hydrodynamic phases at a first order transition. How such a scenario may qualitatively arise in systems other than the ones considered here is an interesting open question for future research.

10
Summary and outlook

To conclude, let us take stock and summarize the main findings of this thesis, put into the context laid out in the introductory Chapters 1,2. We started out posing general questions about the interplay between the out-of-equilibrium quantum dynamics of many-body systems and the presence of dynamical constraints. This program was motivated by advances in quantum simulations experiments, whose unprecedented degree of control over interacting quantum systems allows for evermore direct access to their exotic nonequilibrium properties. Our guiding questions concerned the possibilities of absence of thermalization and presence of slow relaxation in constrained systems. These questions were formulated in a very open-ended way and so our trajectory in this thesis has led us to many answers, scrambled over a diverse set of exciting many-body problems: From ergodicity-breaking and glassy relaxation dynamics to novel hydrodynamic universality classes and emergent tracer problems. From quantum dimers on various geometries over spin liquids to exotic fracton models.

In the Part I of the thesis we studied nonequilibrium dynamics in many-body systems with local gauge constraints. Such constraints are fundamental in physics and their implementation in quantum simulators is at the forefront of many experimental efforts. We demonstrated in Chapter 3 that the quantum dimer model on a square lattice features an intriguing low energy phase dominated by dispersionless, immobile excitations. Due to the restricted mobility of these excitations, the system can reach thermal equilibrium only after extremely long times, for which we provided a lower bound. On the system sizes accessible to numerics, thermalization was even found to be absent altogether. Although the numerical tools to evaluate the question of thermalization in this system are limited to small lattices, it is nonetheless interesting to ask what the actual thermalization time in the quantum dimer model turns out to be. While we provided a lower bound for this time,

we indeed expect it to be even larger in practice since other causes of slow relaxation such as prethermalization might play a role as well. Furthermore, Refs. [406, 407] suggested the presence of a localized phase in a disordered dimer model, based on numerical results. Although it is difficult to infer properties of the thermodynamic limit from results on small lattices and although 'avalanche' arguments suggest instability of many-body-localization in dimensions $d > 1$ [138, 534], it would be interesting to explore whether there could be ways to escape these arguments in constrained systems such as the dimer model. This could be an exciting question to study in the future. Another exciting direction is the investigation of quantum many-body scars, which have been demonstrated to exist in quantum dimer models [535, 536].

In Chapter 4 we uncovered the rich structure of a dimer model on a bilayer geometry, deriving its many conservation laws analytically. We investigated the dynamics of this system under a random unitary time evolution and found a number of exotic features that resemble the physics of fractons. Most notable, for initial states featuring extensive non-local winding numbers, the thermalization process separates into several stages: The system first relaxes along a quasi one-dimensional tube and only then appears to show non-trivial dynamics along the second direction perpendicular to the tube. The timescale at which relaxation in this perpendicular direction sets in was found numerically to diverge algebraically in system size, providing a possible novel form of ergodicity-breaking – within a connected sector of the Hilbert space – due to non-local winding numbers. It would be interesting to see whether similar conservation laws and dynamical phenomena occur in other non-planar dimer models or link models with $U(1)$ gauge structure more generally. In this context, we have seen that a global Hopf-charge in the bilayer dimer model assumes a somewhat complex form in terms of the original dimer operators. It could thus be an interesting undertaking to develop an algorithm that 'learns' such conservation laws from snapshots of the time evolution, which could then be applied to other dimer models[1].

In Chapter 5 we investigated how local probes – spin-polarized scanning tunneling microscopy (STM) in particular – might aid in the detection of topological edge modes of magnetic insulators. Our main example concerned the Kitaev honeycomb model, an exactly solvable $\mathbb{Z}_2$ spin liquid. We calculated the local dynamical structure factor of the Kitaev model on open boundary conditions, which is the relevant quantity entering the tunneling conductance. We determined qualitative signatures of the presence of edge modes and how the underlying anisotropy of the Kitaev model might be revealed by tuning the spin-polarization of the STM setup. It will be interesting to see in the future whether such a setup can be implemented in experiment and whether alternative local 'qubit' probes – for example nitrogen vacancy centers – can investigate the dynamics of gapless chiral edge states [537].

In Part II of the thesis we turned our attention to fracton systems in which several mul-

[1]The author thanks Annabelle Bohrdt for insightful discussions and first steps in this direction.

tipole moments of a global $U(1)$ charge are conserved. While models with such a combination of symmetries can show a strong fragmentation of the Hilbert space [235–238], here we focused on a generic setting in one dimension where the system does thermalize. In Chapter 6 we found that this thermalization proceeds in an anomalously slow, subdiffusive manner using random circuit time evolution and we derived an associated model of linear fluctuating hydrodynamics. These considerations generalize to higher dimensions as well [389]. The subdiffusive relaxation of spin/charge excitations is in agreement with cold atom experiments in the presence of a strong tilted potential [197]. We then proceeded in Chapter 7 to discuss in detail a coupled hydrodynamic theory of charge-, dipole- and energy-conservation as is relevant to Hamiltonian dynamics. We found a subdiffusive mode of mixed charge and energy excitations as well as a diffusive pure energy mode. This general model was then demonstrated to be in agreement with a nonequilibrium quantum field theory study of a Bose-Hubbard model with dipole-conservation. We emphasize that our investigations considered the dynamics of multipole-conserving models at high energies, and the associated hydrodynamic universality classes of course also apply to classical systems with the same conservation laws. It would also be highly interesting to study the properties of multipole-conserving quantum systems at low energies and how they could be realized in experiment.

In Chapter 8 we investigated how the presence of dipole-conservation can also constrain the spreading of quantum information. By evaluating out-of-time-ordered correlations (OTOCs) in classically simulable automaton circuits we demonstrated the presence of a sub-ballistic light cone of operator spreading at a critical point separating an ergodic and a localized, strongly fragmented phase. We constructed a phenomenological model for the scaling behavior of the OTOC near the critical point, which we found to be in agreement with our numerical results. The sub-ballistic light cone was demonstrated to impact operator dynamics within a 'critical fan' even away from the phase transition point on very long time scales. A particularly interesting feature of our investigation was the use of 'single-shot OTOCs' within our numerical approach, providing access to the long waiting times in the spread of the operator front. Analysis of such single-shot OTOCs yields more information than that of the average OTOC on its own, and it is an interesting research direction for the future to determine how this can be made use of beyond our results of Chapter 8.

In Chapter 9 we investigated the dynamics of one-dimensional chains of spinful particles with conventional hopping but constrained spin interactions. We derived a general expression for the late-time dynamical spin correlations, which assume the form of a convolution of a hard core tracer distribution function of a tagged particle and the internal hydrodynamics of the spin pattern. If the spin pattern is conserved, subdiffusive tracer motion dominates the late-time dynamical correlations in generic systems. We use this connection to derive exact expressions for transport coefficients in a couple of random circuit models. We further find that our results apply to certain integrable

quantum systems, providing a simple way to reproduce their diffusion constants. Finally, we studied a novel way of interpolating between a conserved spin pattern and diffusive hydrodynamics within the pattern by allowing only for dipole-conserving spin interactions. We found that such a setup gives rise to intriguing novel hydrodynamic behavior in which details of the microscopic evolution explicitly enter the long-time scaling form of the profile of dynamical spin correlations. It would be very interesting to see whether a similar situation can arise in different setups than the one studied in Chapter 9. It is further interesting to note that tracer dynamics could provide a novel tool to study localization in disordered one-dimensional many-body systems. In particular, the availability of snapshots in quantum gas microscopes could provide direct experimental access to the tracer motion studied in Chapter 9.

To summarize, we encountered a rich phenomenology of nonequilibrium dynamics in constrained systems. We found that there can indeed be novel ways of avoiding thermalization and that slow relaxation occurs in many different settings. In particular, in line with general expectations, the emergence of hydrodynamic transport constitutes an example of universality out of equilibrium and we uncovered the presence of novel universality classes in constrained systems. We also found what appears to be a new kind of critical behavior in the dynamics of operators. Much of the investigations in this thesis focused on the relaxation of local observables. In the future, it could be interesting to study the physics of constrained models from a perspective of quantum information. For instance, it would be exciting to investigate in more detail the interplay between constraints and the dynamics of entanglement. Recently, immense interest arose in combining unitary time evolution with local projective measurements [538–542]. Adding measurements as a new element to the dynamics of many-body systems with constraints could be a highly interesting line of investigation in the future. Quite generally, there are exciting new questions waiting to be tackled at the interface of quantum information and many-body physics with constraints.

A
Overview of methods

A.1 Exact diagonalization and sparse matrix evolution

In principle, the most direct way to solve for the dynamics of a quantum system is to compute all eigenstates and eigenvectors of its Hamiltonian exactly. Since the size of the Hilbert space $|\mathcal{H}| = 2^L$ grows exponentially with the system size (here for qubits) and the time complexity for diagonalization of a matrix $t = \mathcal{O}(|\mathcal{H}|^3)$ scales with the third power in the size of the matrix (in practice), this approach quickly becomes unfeasible once the system size exceeds about $L \approx 16$ spin-$1/2$'s [384]. Usually however, the Hamiltonian will correspond to a sparse matrix. In this case, if one is interested in the dynamics starting from some initial state $|\psi\rangle$, fast matrix-vector multiplication can be used to perform time evolution on somewhat larger system sizes $L \approx 26$, based on a Trotter decomposition $e^{-i\hat{H}t}|\psi\rangle \approx \left(e^{-i\hat{H}\delta t}\right)^{t/\delta t}|\psi\rangle$.

In addition, it is often possible to exploit the presence of symmetries in the problem in order to reach larger system sizes. Symmetries lead to a block-diagonal structure of the Hamiltonian and one can then focus on a specific symmetry sector, which is smaller and therefore more efficient to work with than the full Hilbert space. In practice, one can often make use of lattice symmetries or the presence of a conserved total particle number. It is also worth noting that many of the problems studied in this thesis feature *local* constraints. Due to the local nature of the constraints, the resulting connected subspaces may not have tensor product structure, i.e. we cannot view them as being composed of many independent local Hilbert spaces[1]. This implies that the Hilbert space dimension of connected subsectors in constrained systems may grow asymptotically with a different exponent than the original spin-$1/2$ Hilbert space. The prime example for this is the

[1] A non-tensor-product structure of the Hilbert space can have interesting consequences for the entanglement properties of random quantum states [543]

nearest-neighbor blockaded chain in which two neighboring qubits cannot both be in the $|1\rangle$-state. This constraint is directly relevant for Rydberg atom systems [51] and we also touch upon it in Chapter 9. The Hilbert space in this model grows as a Fibonacci sequence $|\mathcal{H}| \simeq \frac{1}{\sqrt{5}}\varphi^L$ asymptotically for large L, where $\varphi = \frac{1+\sqrt{5}}{2}$ is the golden ratio. We notice that this is not the case for typical subsectors of global symmetries. For example, the largest connected sector in a qubit model with conserved global magnetization is just the central binomial coefficient $\binom{L}{L/2} \sim \sqrt{\frac{2}{\pi L}}2^L$, whose dominant exponential growth is still 2^L. Similarly, a reduced Hilbert space size due to local constraints occurs in the dimer models whose dynamics we consider within exact diagonalization and sparse matrix time evolution in Chapter 3. In particular, the number of dimer coverings on a square lattice with open boundary conditions is known to grow asymptotically as $|\mathcal{H}| \sim e^{GL^2/\pi} \approx 1.34^{L^2}$, where G is Catalan's constant [370]. Due to this feature we can reach a square lattice of size 8×8 using sparse matrix time evolution in Chapter 3.

Importantly, the local constraints that lead to this reduced Hilbert space dimension can also help us in practice to construct a basis set of constrained subspaces. This means that we do not need to iterate through all 2^{2L^2-2L} possibilities of having a dimer/having no dimer on each of the $2L^2 - 2L$ links of a square lattice with open boundaries in order to decide for each possibility whether it is a valid dimer configuration. For an 8×8 lattice this would in fact be practically impossible. Instead, we start from the full set of valid dimer configurations for a small lattice. We then expand the system size by adding a new lattice site with a dimer attached to it. For all configurations already within our set we then find the possible orientations of this new dimer such that all local constraints are fulfilled. The procedure is then iterated until the desired system size is reached. Instead of building the system 'qubit-by-qubit', we thus construct it 'one local Gauss law at a time'.

Such a local construction scheme to generate the basis states of a constrained subspace no longer works in general for global constraints such as the conservation of the total dipole moment. In particular, due to Hilbert space fragmentation [235–237], dipole-conserving systems have more disjoint subspaces than is indicated by the global charge and dipole conservation laws. For such cases one must to use a different scheme to obtain the basis of a connected subspace, for example by constructing the Krylov subspaces of given seed states through repeated applications of the Hamiltonian. In practice, finding the basis of a connected subsector can be a numerically costly task, sometimes even more so than the actual time evolution once the desired subsector basis has been obtained.

Exact diagonalization and sparse matrix evolution are ultimately limited to small systems and therefore have clear shortcomings. However, in lack of more efficient and controlled numerical tools such as for ground states, they are nonetheless vital in making progress towards understanding quantum dynamics out of equilibrium, especially in the context of thermalization and its absence.

A.2 **Haar random unitary circuits**

The use of random circuit unitary time evolution as a proxy for generic non-integrable quantum dynamics has led to many exciting insights over recent years. In particular, it was demonstrated that universal processes such as operator dynamics [63–66, 189, 224], growth of Rényi entanglement entropies [61, 62, 225–227] as well as transport [65, 66, 68] can be captured within such simplified models, both with and without $U(1)$ charge conservation. Unitary circuits can also be used to construct time-periodic Floquet dynamics by periodically repeating layers of random unitary gates. Such a procedure allows for calculations of the spectral form factor (SFF), which contains information about the level statistics of the Floquet unitary and thus serves as a diagnostic for the emergence of quantum chaos [67, 68, 87, 103, 104], *cf.* Sec. 2.1.2. From a technical perspective, one makes use of averages over the Haar ensemble of unitary matrices. In many cases this simplifies the quantities of interest, sometimes even allowing for analytical results and often easing the complexity of their numerical evaluation. In this appendix, we provide a brief review of the properties of random unitary circuits that are most relevant to this thesis. Specifically, based on work of Refs. [65, 66, 68, 104], we review below how dynamical charge/spin correlation functions in systems with conserved quantities can be evaluated as stochastic discrete Markov processes.

To start, consider a unitary time evolution $\hat{U}(t)$ that is composed of local unitary gates in a one-dimensional system of qudits; we have in mind the 'brickwork' circuit structure that appears repeatedly throughout the thesis. We can therefore write

$$\hat{U}(t) = \prod_{\ell=1}^{ctL} \hat{U}_\ell, \tag{A.1}$$

where the $\hat{U}_\ell$ are local gates, L is the system size and c is some $\mathcal{O}(1)$ constant that depends on the precise definition of a single time step; we use, $c = 1$ in the standard brickwork layout. We will choose the local $\hat{U}_\ell$ as random unitaries all independently of each other (this is therefore not a periodic Floquet time evolution). Let us now assume that the system has symmetries that are diagonal in the computational z-basis[2], inducing a block-diagonal structure in the local gates. Formally, if $\hat{P}_{\ell,s}$ is the projector on the *local* symmetry sector s at the sites where the gate $\hat{U}_\ell$ acts (and simply the identity on all other sites), we have $[\hat{U}_\ell, \hat{P}_{\ell,s}] = 0$. For example, the local symmetry sector s could correspond to the total charge on the sites that the gate $\hat{U}_\ell$ acts on. $\hat{U}_\ell$ can thus be written in an explicitly block-diagonal form

$$\hat{U}_\ell = \sum_s \hat{P}_{\ell,s} \hat{U}_{\ell,s} \hat{P}_{\ell,s}. \tag{A.2}$$

The $\hat{U}_{\ell,s}$ acting within a symmetry sector in Eq. (A.2) are then chosen randomly from the

[2]This is the case for all models we consider in this thesis

space of unitary matrices of size $d_s \times d_s$ with respect to the Haar measure, where d_s is the dimension of symmetry sector s.

Within this setup, let us consider two states $|\boldsymbol{z}\rangle$, $|\boldsymbol{z}'\rangle$ in the computational z-basis. In order to characterize transport properties in the z-basis, we are interested in the amplitudes

$$a(\boldsymbol{z}'|\boldsymbol{z};t) := \langle \boldsymbol{z}'|\hat{U}(t)|\boldsymbol{z}\rangle\,, \tag{A.3}$$

and our goal is to compute the associated probability

$$\overline{|a(\boldsymbol{z}'|\boldsymbol{z};t)|^2}, \tag{A.4}$$

where $\overline{\cdots}$ denotes an average over the random unitary gates $\hat{U}_{\ell,s}$ from Eq. (A.2). We can recast Eq. (A.4) in a 'path integral' form, such that

$$\overline{|a(\boldsymbol{z}'|\boldsymbol{z};t)|^2} = \overline{\Big|\sum_{\{\boldsymbol{z}_\ell\}}\prod_{\ell=1}^{tL}\langle \boldsymbol{z}_\ell|\hat{U}_\ell|\boldsymbol{z}_{\ell-1}\rangle\Big|^2}, \tag{A.5}$$

with $\boldsymbol{z}_0 = \boldsymbol{z}$ and $\boldsymbol{z}_{tL} = \boldsymbol{z}'$ fixed. The matrix elements $\langle \boldsymbol{z}_\ell|\hat{U}_\ell|\boldsymbol{z}_{\ell-1}\rangle$ appearing in Eq. (A.5) are each either zero or just a single complex entry of one of the random matrices $\hat{U}_{\ell,s}$. We can then use the property of averages over moments of random unitary matrices,

$$\overline{(U_{\ell,s})^*_{ij}(U_{\ell,s})_{mn}} = \frac{1}{d_s}\delta_{im}\delta_{jn}. \tag{A.6}$$

Using Eq. (A.6) we conclude that if $\boldsymbol{z}_\ell \neq \boldsymbol{z}'_\ell$ or $\boldsymbol{z}_{\ell-1} \neq \boldsymbol{z}'_{\ell-1}$, then

$$\overline{[\langle \boldsymbol{z}_\ell|\hat{U}_\ell|\boldsymbol{z}_{\ell-1}\rangle]^*\,\langle \boldsymbol{z}'_\ell|\hat{U}_\ell|\boldsymbol{z}'_{\ell-1}\rangle} = 0. \tag{A.7}$$

Therefore, only the diagonal parts of the path integral history in Eq. (A.5) survive upon expanding the amplitude squared,

$$\overline{|a(\boldsymbol{z}'|\boldsymbol{z};t)|^2} = \sum_{\{\boldsymbol{z}_\ell\}}\prod_{\ell=1}^{tL}\overline{\Big|\langle \boldsymbol{z}_\ell|\hat{U}_\ell|\boldsymbol{z}_{\ell-1}\rangle\Big|^2} \tag{A.8}$$

At this point, let us introduce the notation of Ref. [104], $|\boldsymbol{z}) := |\boldsymbol{z}\rangle\langle\boldsymbol{z}|$ for the projector on the state $|z\rangle$ as well as the inner product $(\hat{A}|\hat{B}) := \mathrm{Tr}[\hat{A}\hat{B}^\dagger]$ for operators. We can then recast the above diagonal terms as

$$\overline{\Big|\langle \boldsymbol{z}_\ell|\hat{U}_\ell|\boldsymbol{z}_{\ell-1}\rangle\Big|^2} = \mathrm{Tr}\Big[|\boldsymbol{z}_\ell\rangle\langle\boldsymbol{z}_\ell|\,\overline{\hat{U}_\ell\,|\boldsymbol{z}_{\ell-1}\rangle\langle\boldsymbol{z}_{\ell-1}|\,\hat{U}_\ell^\dagger}\Big] =: (\boldsymbol{z}_\ell|\hat{\mathcal{T}}_\ell|\boldsymbol{z}_{\ell-1}), \tag{A.9}$$

where the transfer matrix $\hat{\mathcal{T}}_\ell$ is determined by evaluating the left hand side of Eq. (A.9).

Doing so using Eq. (A.6) once more, this results in

$$\hat{\mathcal{T}}_\ell = \sum_s \frac{1}{d_s} \sum_{s_1,s_2 \in s} |s_1)(s_2|, \tag{A.10}$$

where crucially, the sums over s_1, s_2 are over *local* z-basis configurations that belong to the local symmetry sector s. In particular, $\hat{\mathcal{T}}_\ell$ acts as the identity outside the sites that $\hat{U}_\ell$ acts on. Inserting Eq. (A.10) back into Eq. (A.8), we obtain

$$\overline{|a(\boldsymbol{z}'|\boldsymbol{z};t)|^2} = (\boldsymbol{z}'| \prod_{\ell=1}^{tL} \hat{\mathcal{T}}_\ell |\boldsymbol{z}). \tag{A.11}$$

Notice that there is no circuit average on the right hand side of Eq. (A.11), and so the transfer matrices repeat after one brickwork layer, such that one can define

$$\hat{\mathcal{T}} := \prod_{\ell=1}^{L} \hat{\mathcal{T}}_\ell, \tag{A.12}$$

and therefore

$$\overline{|a(\boldsymbol{z}'|\boldsymbol{z};t)|^2} = (\boldsymbol{z}'|\hat{\mathcal{T}}^t|\boldsymbol{z}). \tag{A.13}$$

We used this result in Chapter 9. Inspecting the form Eq. (A.10) of the local transfer matrices, we see that the probabilty to go from state $|\boldsymbol{z}\rangle$ to $|\boldsymbol{z}'\rangle$ within time t in the circuit is (upon circuit averaging) given by a classical stochastic Markov process in which z-basis product states are updated locally by rearranging the configuration randomly, with the constraint that the symmetry sectors are preserved. Such a discrete Markov process can be sampled efficiently. With a way to numerically sample the Markov process of Eq. (A.4), we can determine the dynamical z-basis charge correlations in a straightforward manner via

$$\langle \hat{Z}_x(t)\hat{Z}_0(0)\rangle = \frac{1}{\mathcal{N}} \sum_{\boldsymbol{z},\boldsymbol{z}'} z_0 z'_x |a(\boldsymbol{z}'|\boldsymbol{z},t)|^2, \tag{A.14}$$

where $\mathcal{N}$ is a normalization factor. Numerically, $\mathcal{N}$ corresponds to the number of initial $|\boldsymbol{z}\rangle$-states that were sampled.

A.3 Quantum automaton circuits

Apart from the Haar random unitary circuits described above, throughout this thesis we often use so-called *automaton circuits* [205, 386–388]. Automaton-circuits are unitary quantum circuits in which there exists a special basis, by convention the computational z-basis, that is left invariant under applications of automaton gates. Formally, for a z-basis state $|\boldsymbol{z}\rangle$ and an automaton gate $\hat{U}$, we have

$$\hat{U}\,|\boldsymbol{z}\rangle = e^{i\theta_{\boldsymbol{z}}}\,|\boldsymbol{z}'\rangle\,. \tag{A.15}$$

Thus, automaton gates act as *permutations* within the computational z-basis up to a phase factor. Clearly, if we have an initial state $|\psi\rangle = |\boldsymbol{z}\rangle$ that is a z-basis product state, the time-evolved state $|\psi(t)\rangle = e^{i\theta(t)}\,|\boldsymbol{z}(t)\rangle$ will remain a z-basis state up to a global phase. The dynamics within the z-basis is therefore comparable to a cellular automaton, hence the nomenclature. We emphasize that for product initial states that are not in the computational z-basis, gates of the form Eq. (A.15) do generate entanglement.

Automaton circuits have recently become popular tools to study the thermalization process of quantum many-body systems [2, 205–207, 229, 388, 502]. As is the case with Haar random unitary circuits, the central idea is to use automaton circuits as a proxy for generic Hamiltonian dynamics. Due to their simple automaton form in the z-basis, many quantities of interest can be studied in a numerically efficient way in these circuits. For example, transport properties such as dynamical charge/spin correlation functions can be obtained in a straightforward manner by sampling over z-basis initial states for the effectively classical automaton time evolution. This yields similar expressions to the ones derived in the previous Sec. A.2, see Eq. (A.14). However, if we restrict ourselves to automaton circuits we can essentially skip the derivation that was necessary for Haar random unitaries, as the automaton condition Eq. (A.15) immediately implies that z-basis correlation functions can be sampled in a classical way. Automaton circuits and Haar random unitary circuits thus yield equivalent results for transport properties in the z-basis. Automaton circuits have been employed to study transport in a number of lattice systems, see Refs. [2, 205–207], as well as Chapters 4,6,8 of this thesis.

A comment is in order: In Chapter 9 we use the discrete Markov process that results from Haar random unitary gates to compute dynamical correlation functions while Chapters 4,6,8 use an automaton approach. This has mostly 'historic' reasons (apart from Chapter 8, see discussion about OTOCs below), and we have verified that both approaches provide equivalent results (i.e., the same hydrodynamic universality classes), as expected for the universal processes studied in these Chapters. One can in fact use random automaton circuits for which dynamical correlations in the z-basis also quantitatively agree with the Haar random unitary case. Again, mostly for historic reasons we employ slightly different implementations of the unitary automaton time evolution. We emphasize again that our results do not depend on such details of the microscopic implementation. Below, in Sec. A.3.1, we describe the details of the automaton evolution that was used for the multipole-moment-conserving spin chains. Qualitatively however, as far as transport properties are concerned, we can think of the evolution in the same way as for the discrete Markov process of Sec. A.2.

We point out that automaton circuits are very useful also beyond studies of transport. In particular, automaton circuits allow for an efficient numerical computation of out-of-time-ordered correlations (OTOCs), see Ref. [205], which are important quantities in the context of quantum information dynamics. For automaton circuits the computation of OTOCs is significantly simpler than for Haar random unitaries. In addition, it has

been demonstrated that automaton circuits – despite being less generic than Haar random unitaries – reproduce the qualitative features of operator dynamics that are expected in a generic time evolution [205, 386, 502, 503]. This is also demonstrated in Chapter 8. We show below in Secs. A.3.2,A.3.3 how OTOCs can be evaluated in automaton circuits. These results are essential to the investigations of Chapter 8.

Finally, we mention that automaton circuits have also been used to study the dynamics of entanglement for non-z-basis product initial states. Ref. [229] chose a setup in which the local gates – in addition to fulfilling the automaton condition Eq. (A.15) – where also *Clifford* gates, i.e. preserving the generalized group of Pauli matrices. Clifford circuits allow for a classically efficient way to compute Rényi entanglement entropies in large scale systems [539, 544]. Ref. [229] studied circuits with a $U(1)$ charge conservation law and found diffusive growth of Rényi entanglement entropies $S_n(t) \sim \sqrt{t}$, Eq. (2.17), for $n > 1$, verifying results obtained in Haar random unitary circuits [62, 228]. We comment here that the combination of $U(1)$ charge conservation and the defining relation of Clifford gates to leave the Pauli group invariant is sufficient for the automaton condition Eq. (A.15) to hold. In other words, all charge-conserving Clifford gates are also automaton gates. In total there remain only 64 two-qubit Clifford gates with charge conservation[3]. Remarkably however, this set of gates is able to capture the generic features of entanglement growth. A larger set of automaton gates in the absence of conservation laws has recently been employed in a study of unitary dynamics with interspersed projective measurements. As in Haar random unitary circuits, a measurement-induced transition between a phase with low, area-law entanglement and a phase with high, volume-law entanglement has been found upon tuning the frequency at which measurements are peformed [500].

A.3.1 Automaton circuit used in Chapter 6

Let us provide the details on the stochastic automaton scheme that we studied numerically in Chapter 6 of this thesis. The automaton evolution can be expressed in terms of a classically simulable circuit where the updates are represented as unitary operators $\hat{U}_r^{(m)}(x)$ of range r, acting on local strings of z-basis configurations $|\boldsymbol{s}(x)\rangle = |s_x, ..., s_{x+r-1}\rangle$ and conserving all $Q^{(n\leq m)}$. These operators connect two states $|\boldsymbol{s}(x)\rangle$ and

$$|\boldsymbol{s}'(x)\rangle = \hat{U}_r^{(m)}(x)\,|\boldsymbol{s}(x)\rangle\,, \tag{A.16}$$

defined such that [205]

$$\hat{U}_r^{(m)}(x)\,|\boldsymbol{s}'(x)\rangle = |\boldsymbol{s}(x)\rangle\,. \tag{A.17}$$

Therefore, $\hat{U}_r^{(m)}(x)$ acts as a usual σ^x Pauli matrix in the subspace spanned by $|\boldsymbol{s}(x)\rangle$ and $|\boldsymbol{s}'(x)\rangle$. For states that are locally frozen due to the boundaris of the chosen spin represen-

[3]The author thanks Zack Weinstein for many fruitful discussions on the topic of Clifford circuits.

tation, $\hat{U}_r^{(m)}(x)$ acts as the identity. For a selected $h_r^{(m)}(x)$ of Eq. (6.10), there are potentially *two* possible updates for a given $|\boldsymbol{s}(x)\rangle$, namely

$$|\boldsymbol{s}'(x)\rangle = h_r^{(m)}(x)\,|\boldsymbol{s}(x)\rangle \tag{A.18}$$

and

$$|\boldsymbol{s}''(x)\rangle = \left(h_r^{(m)}(x)\right)^\dagger |\boldsymbol{s}(x)\rangle\,. \tag{A.19}$$

Therefore, we require *two* independent unitary gates $\hat{U}_{r,A}^{(m)}(x)$ and $\hat{U}_{r,B}^{(m)}(x)$ describing all possible updates associated to a local term of $\hat{H}_r^{(m)}$. These update operators are the building blocks of the automaton evolution. The definition of a single time step in terms of these gates for the case $m = 1$, taking into account only $\hat{H}_3^{(1)}$, is illustrated in Fig. A.1.

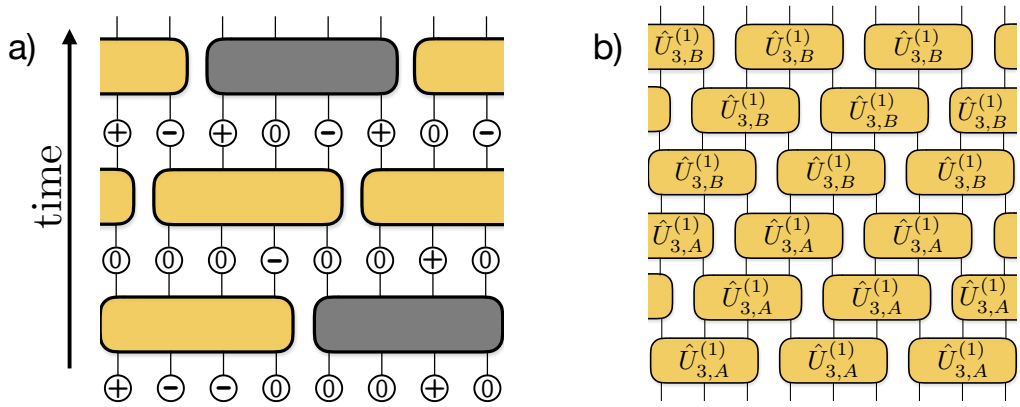

Figure A.1: Automaton circuit evolution. a) Illustration of a single run in an automaton circuit for $m = 1$ using dipole-conserving updates of range four between product states (spin representation $S = 1$). With some finite probability, updates are either applied (yellow gates) not (grey gates), yielding effectively stochastic updates. **b)** Detailed definition of a single time step of the automaton circuit evolution as described in the text, here for dipole-conserving updates of range three.

We can further provide a more explicit construction of the two local unitaries $\hat{U}_{r,A/B}^{(m)}(x)$ in the following way: let us define the elementary unitary operators $\hat{U}_{\boldsymbol{s},\boldsymbol{s}'}$, which act as

$$\hat{U}_{\boldsymbol{s},\boldsymbol{s}'}\,|\boldsymbol{s}(x)\rangle = |\boldsymbol{s}'(x)\rangle \tag{A.20}$$

and

$$\hat{U}_{\boldsymbol{s},\boldsymbol{s}'}\,|\boldsymbol{s}'(x)\rangle = |\boldsymbol{s}(x)\rangle\,, \tag{A.21}$$

and as the identity on all states outside the two-state subspace spanned by $\{|\boldsymbol{s}(x)\rangle\,, |\boldsymbol{s}'(x)\rangle\}$. We can define such an elementary unitary for every pair $(\boldsymbol{s}(x), \boldsymbol{s}'(x))$ of local spin configurations that are connected by the Hamiltonian $\hat{H}_r^{(m)}$. Because in general, as described above, a given $|\boldsymbol{s}\rangle$ can be connected to two other configurations by $\hat{H}_r^{(m)}$, we can seperate the set of all possible pairs $(\boldsymbol{s}(x), \boldsymbol{s}'(x))$ into two subsets A and B, such that a given $\boldsymbol{s}(x)$ appears only at most *once* as part of a pair $(\boldsymbol{s}(x), \boldsymbol{s}'(x))$ in A, and analogously in B. We can then define the abovementioned $\hat{U}_{r,A/B}^{(m)}(x)$ in terms of the elementary

unitaries acting only on pairs within one of the two sets A and B via

$$\hat{U}_{r,A}^{(m)} = \prod_{(\boldsymbol{s},\boldsymbol{s}')\in A} \hat{U}_{\boldsymbol{s},\boldsymbol{s}'} \tag{A.22}$$

and analogously for $\hat{U}_{r,B}^{(m)}$. Due to the construction of the sets A and B, the unitaries in the product of Eq. (A.22) all commute.

The relation of the circuit dynamics to the Hamiltonian $\hat{H}_r^{(m)}$ can then be expanded even further by endowing each application of an update between $|\boldsymbol{s}(x)\rangle$ and $|\boldsymbol{s}'(x)\rangle$ with an acceptance probability $p \sim \left|\langle \boldsymbol{s}'(x)| \left(h_r^{(m)}(x) + h.c.\right) |\boldsymbol{s}(x)\rangle\right|^2$ proportional to the associated Fermi-golden-rule rate. According to this probability, the update gate is either applied or substituted by an identity operator. This turns our circuit into a *stochastic* automaton.

A.3.2 The ZX – OTOC

Here we demonstrate how the numerical evaluation of out-of-time-order correlations can be performed efficiently in automaton circuits, see also Ref [205]. In particular, our goal is to show that the simple expression of Eq. (8.4) of Chapter 8 for the form of the ZX – OTOC can be derived from the automaton condition. For concreteness, let us restrict to the same setup as in Chapter 8, i.e. a three-state onsite Hilbert space $|0\rangle$, $|1\rangle$, $|2\rangle$ and expectation values $\langle ...\rangle_n$ evaluated at a chemical potential corresponding to an average density $0 \leq n \leq 2$. Recall that we consider the correlations

$$C_{ZX}^{(n)}(x,t) = \overline{\left\langle [\hat{Z}_x(t), \hat{X}_0(0)][\hat{Z}_x(t), \hat{X}_0(0)]^\dagger \right\rangle}_n, \tag{A.23}$$

with the shift operator $\hat{X}_0 = |2\rangle_0 \langle 0| + |0\rangle_0 \langle 1| + |1\rangle_0 \langle 2|$ acting at site 0. We first expand the commutators in Eq. (A.23) to obtain

$$\begin{aligned} C_{ZX}^{(n)}(x,t) =& \overline{\left\langle \hat{Z}_x(t)\hat{X}_0(0)\hat{X}_0^\dagger(0)\hat{Z}_x(t)\right\rangle}_n + \overline{\left\langle \hat{X}_0(0)\hat{Z}_x(t)\hat{Z}_x(t)\hat{X}_0^\dagger(0)\right\rangle}_n \\ &- \overline{\left\langle \hat{Z}_x(t)\hat{X}_0(0)\hat{Z}_x(t)\hat{X}_0^\dagger(0)\right\rangle}_n - \overline{\left\langle \hat{X}_0(0)\hat{Z}_x(t)\hat{X}_0^\dagger(0)\hat{Z}_x(t)\right\rangle}_n . \end{aligned} \tag{A.24}$$

The first two terms on the right hand side of Eq. (A.24) are time-ordered contributions while the latter two are out-of-time-ordered. Using that $\hat{X}_0\hat{X}_0^\dagger = 1$, the first term of Eq. (A.24) evaluates to

$$\begin{aligned} &\overline{\left\langle \hat{Z}_x(t)\hat{X}_0(0)\hat{X}_0^\dagger(0)\hat{Z}_x(t)\right\rangle}_n = \sum_n \frac{e^{-\mu(n)\sum_x n_x}}{Z_n} \overline{\langle n|\, \hat{Z}_x(t)\hat{Z}_x(t)\, |n\rangle} = \\ &\sum_{n,m} \frac{e^{-\mu(n)\sum_x n_x}}{Z_n} \overline{\langle n|\, \hat{Z}_x(t)\, |m\rangle \langle m|\, \hat{Z}_x(t)\, |n\rangle} = \sum_n \frac{e^{-\mu(n)\sum_x n_x}}{Z_n} \overline{\left(\langle n|\, \hat{Z}_x(t)\, |n\rangle\right)^2}, \end{aligned} \tag{A.25}$$

where in the last equality we have explicitly made use of the automaton condition Eq. (8.1), which fixes $|m\rangle = |n\rangle$ in the sum over m. Analogously, we obtain for the second term in Eq. (A.24)

$$\overline{\left\langle \hat{X}_0(0)\hat{Z}_x(t)\hat{Z}_x(t)\hat{X}_0^\dagger(0)\right\rangle_n} = \sum_n \frac{e^{-\mu(n)\sum_x n_x}}{Z_n}\overline{\left(\langle n|\,\hat{X}_0\hat{Z}_x(t)\hat{X}_0^\dagger\,|n\rangle\right)^2}, \tag{A.26}$$

and for the third term

$$\overline{\left\langle \hat{Z}_x(t)\hat{X}_0(0)\hat{Z}_x(t)\hat{X}_0^\dagger(0)\right\rangle_n} = \sum_n \frac{e^{-\mu(n)\sum_x n_x}}{Z_n}\overline{\langle n|\,\hat{Z}_x(t)\,|n\rangle\,\langle n|\,\hat{X}_0\hat{Z}_x(t)\hat{X}_0^\dagger\,|n\rangle}. \tag{A.27}$$

The fourth term of Eq. (A.24) is equal to Eq. (A.27) after using cyclicity of the trace as well as $[\hat{Z}_x(t), \sum_x n_x] = 0$. Collecting all terms and inserting them into Eq. (A.24), the OTOC takes the convenient form

$$C_{ZX}^{(n)}(x,t) = \sum_{\boldsymbol{n}} \frac{e^{-\mu\sum_x n_x}}{Z_n}\overline{\left[\langle \boldsymbol{n}|\hat{Z}_x(t)|\boldsymbol{n}\rangle - \langle \boldsymbol{n}|\,\hat{X}_0\,\hat{Z}_x(t)\,\hat{X}_0^\dagger\,|\boldsymbol{n}\rangle\right]^2}, \tag{A.28}$$

which corresponds to Eq. (8.4) of the main text.

A.3.3 The XX – OTOC

In Chapter 8 we focused exclusively on the dynamics of the ZX – OTOC. Here, we argue that our results are indeed more general and should generalize to other OTOCs as well. In particular, we show that for automaton circuits, the spreading of the front $\overline{\langle x_{XX}(t)\rangle}$ of the OTOC $C_{XX}^{(n)}(x,t)$ can quite generally be bounded by $\overline{\langle x_{XX}(t)\rangle} \lesssim 2\overline{\langle x_r(t)\rangle}$, with $\overline{\langle x_r(t)\rangle}$ the front of the ZX – OTOC $C_{ZX}^{(n)}(x,t)$.

To show this, we first write down the expression for the XX – OTOC,

$$C_{XX}^{(n)}(x,t) = \sum_{\boldsymbol{n}} \frac{2e^{-\mu\sum_x n_x}}{Z_n}\left(1 - \overline{\mathrm{Re}\,\langle \boldsymbol{n}|\hat{X}_x(t)\hat{X}_0\hat{X}_x^\dagger(t)\hat{X}_0^\dagger|\boldsymbol{n}\rangle}\right), \tag{A.29}$$

and consider its out-of-time-ordered part. We notice that for a given $|\boldsymbol{n}\rangle$ there is always a region $r(t) \subset \mathbb{Z}$ of size $|r(t)|$ around the origin $x = 0$ such that both

$$\begin{aligned} \hat{U}(t)\,|\boldsymbol{n}\rangle &= |\boldsymbol{n}(t)\rangle_{r(t)} \otimes |\boldsymbol{n}(t)\rangle_{\bar{r}(t)} \\ \hat{U}(t)\hat{X}_0^\dagger\,|\boldsymbol{n}\rangle &= |\boldsymbol{n}'(t)\rangle_{r(t)} \otimes |\boldsymbol{n}(t)\rangle_{\bar{r}(t)} \end{aligned} \tag{A.30}$$

hold true, where $\bar{r}(t) = \mathbb{Z}\backslash r(t)$ is the complement of $r(t)$ and $|\boldsymbol{n}(t)\rangle_{r(t)}$ denotes the restriction of a state $|\boldsymbol{n}(t)\rangle$ to the region $r(t)$. According to Eq. (A.30) the two states only differ inside the region $r(t)$. Furthermore, we are guaranteed the existence of an $x_{XX}(t) > 0$

such that for all $x \geq x_{XX}(t)$ and all $t' \in [0,t]$ we can write

$$\begin{aligned}\hat{U}^\dagger(t')\hat{X}_x^\dagger\hat{U}(t)\,|\boldsymbol{n}\rangle &= |\boldsymbol{n}(t-t')\rangle_{r(t-t')} \otimes |\boldsymbol{m}(t,t')\rangle_{s_x(t,t')} \otimes |\boldsymbol{n}(t-t')\rangle_{\bar{r}(t-t')\setminus s_x(t,t')} \\ \hat{U}^\dagger(t')\hat{X}_x^\dagger\hat{U}(t)\hat{X}_0^\dagger\,|\boldsymbol{n}\rangle &= |\boldsymbol{n}'(t-t')\rangle_{r(t-t')} \otimes |\boldsymbol{m}(t,t')\rangle_{s_x(t,t')} \otimes |\boldsymbol{n}(t-t')\rangle_{\bar{r}(t-t')\setminus s_x(t,t')}\,,\end{aligned} \tag{A.31}$$

where $s_x(t,t') \subset \mathbb{Z}$ is some region of size $|s_x(t,t')|$ around x, see Fig. A.2 for an illustration. It can be verified that for all x for which Eq. (A.31) holds,

$$1 - \mathrm{Re}\,\langle \boldsymbol{n}|\hat{X}_x^\dagger(t)\hat{X}_0^\dagger\hat{X}_x(t)\hat{X}_0|\boldsymbol{n}\rangle = 0 \tag{A.32}$$

in Eq. (A.29). Thus, $x_{XX}(t)$ constitutes the boundary of the single-shot OTOC that is associated to $C_{XX}^{(n)}(x,t)$. We emphasize that Eq. (A.31) will hold for some t' in general only if it also holds for all $t'' < t'$, i.e. if the two regions $r(t-t'')$ and $s_x(t,t'')$ do not overlap for any $t'' < t'$. This is why we are generally required to demand that Eq. (A.31) hold for all $t' \in [0,t]$ and not only for $t' = t$.

The above requirement that the two regions do not overlap implies that the boundary $x_{XX}(t)$ should fulfill

$$x_{XX}(t) \approx \frac{1}{2}\left(|r(t-t')| + |s_{x_{XX}(t)}(t,t')|\right) \tag{A.33}$$

for all $t' \in [0,t]$ and therefore

$$x_{XX}(t) \approx \frac{1}{2}\max_{t'}\left[|r(t-t')| + |s_{x_{XX}(t)}(t,t')|\right]. \tag{A.34}$$

In order to obtain $\overline{\langle x_{XX}(t)\rangle}$, we now make the following approximations: 1) The regions $r(t-t')$ and $s_{x_{XX}(t)}(t,t')$ are expected to evolve approximately independently and thus

$$\overline{\langle x_{XX}(t)\rangle} \approx \frac{1}{2}\max_{t'}\left[\overline{\langle|r(t-t')|\rangle} + \overline{\langle|s_{x_{XX}(t)}(t,t')|\rangle}\right]. \tag{A.35}$$

2) After averaging, the region $s_{x_{XX}(t)}(t,t')$ should grow only as a function of t', independently of t and $x_{XX}(t)$ (see Fig. A.2). In particular, it should grow at the same rate as the region r. We therefore set $\overline{\langle|s_{x_{XX}(t)}(t,t')|\rangle} = \overline{\langle|r(t')|\rangle}$. Using these two approximations as well as the growth $\overline{\langle|r(t)|\rangle} = 2\overline{\langle x_r(t)\rangle} = 2v_B t^\alpha$ of the region r which is given by the boundary of the ZX – OTOC, we obtain

$$\begin{aligned}\overline{\langle x_{XX}(t)\rangle} &\approx \max_{t'\in[0,t]}\left[\overline{\langle x_r(t-t')\rangle} + \overline{\langle x_r(t')\rangle}\right] = \\ &= \max_{t'\in[0,t]}\left[v_B(t-t')^\alpha + v_B(t')^\alpha\right] = 2^{1-\alpha}\,v_B t^\alpha = \\ &= 2^{1-\alpha}\overline{\langle x_r(t)\rangle} \leq 2\overline{\langle x_r(t)\rangle}.\end{aligned} \tag{A.36}$$

The above argument is expected to hold whenever the ZX – OTOC is described by an algebraic growth $\overline{\langle x_r(t)\rangle} = v_B t^\alpha$ with $\alpha \leq 1$. In particular, we see that the XX – OTOC spreads with the same algebraic exponent, which concludes our argument.

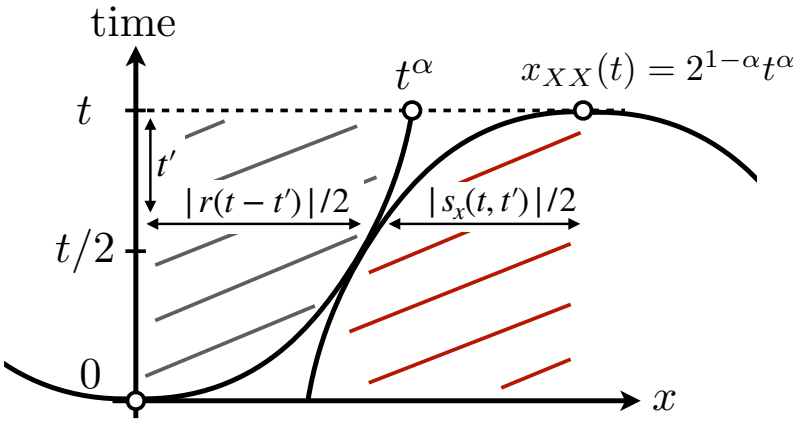

Figure A.2: Bounding the XX – OTOC. The forward and backward time evolution, up to t and t' respectively, define two regions $r(t-t')$ and $s_x(t,t')$ around the positions 0 and x where $\hat{X}$-operators have been inserted in Eq. (A.29). The front of the OTOC has not yet reached position x when the two regions have no overlap.

A.4 Matrix product states

A numerical technique underpinning many breakthrough advances in the study of quantum many-body systems over the last decade are tensor networks and – more specifically – matrix product states (MPS). The MPS Ansatz provides access to controlled results on large scale systems that are often beyond the reach of other methods. In this thesis we use matrix product states only on a couple of occasions – using the TeNPy library [454] – to verify some of our analytical conclusions about dynamics in the Kitaev honeycomb model on open boundaries in Chapter 5, as well as in Chapter 9 to compute the dynamical spin correlation function of the XXZ spin chain at finite anisotropy strength. As the method appears sparingly in this thesis, we refer to some of the many excellent reviews in the literature for details [18, 19, 454, 545].

In order to briefly sketch some key aspects of the MPS Ansatz [19], we note that any quantum state $|\psi\rangle = \sum_{i_1,\ldots,i_N} \psi_{i_1,\ldots,i_N} |i_1,\ldots,i_N\rangle$ ($i_n \in \{0,1\}$ for qubits) can be represented as

$$\psi_{i_1,\ldots,i_N} = A^{[i_1]}_{\alpha_1\alpha_2} A^{[i_2]}_{\alpha_3\alpha_4} \ldots A^{[i_N]}_{\alpha_{2N-1}\alpha_{2N}}, \tag{A.37}$$

where the convention of summation over repeated indices is adopted. Here, the $A^{[i_n]}_{\alpha_{2n-1}\alpha_{2n}}$ are matrices of 'bond dimensions' $\chi_{n-1} \times \chi_n$. In principle, in order to capture a general quantum state, the maximum bond dimension appearing in the expression Eq. (A.37) has to be exponentially large in the system size N. This is because the amount of entanglement that can be captured within the Ansatz Eq. (A.37) scales logarithmically with the bond

dimension and a general quantum state exhibits volume law entanglement. However, ground states of gapped local Hamiltonians in one dimension satisfy an area law [546] and can be captured using a finite amount of entanglement and thus a finite maximum bond dimension χ. Given the MPS Ansatz Eq. (A.37) and a Hamiltonian, the ground state can be found efficiently using the density matrix renormalization group (DMRG) [16–19].

Most important in the context of this thesis, there also exist methods to perform time evolution with MPS states, such as the time-evolving block decimation (TEBD) [547], the time-dependent variational principle (TDVP) [548, 549], or performing Heisenberg time evolution by evolving a MPS representation of operators instead of states [186]. In general, the entanglement of an MPS and thus the required bond dimension will increase during the evolution, such that the reachable times are limited. In practice one truncates the bond dimension at some maximum value [19]; however, such truncations usually lead to the violation of conservation laws, such that transport properties may be challenging to extract. Recent works attempt to resolve this issue and find conserving truncation schemes which are able to give reliable numerical values for the transport coefficients [186–188, 191, 192].

A.5 **Monte Carlo simulations**

In Chapter 4 we showed results from a Monte Carlo simulation of the classical dimer model on a bilayer geometry with an energy function $E = \hat{H}_V$ that counts the number of flippable plaquettes in the system. In this appendix we provide the details on the loop-update Monte Carlo algorithm that was used to obtain these results. We also point to Refs. [378–382], where the algorithm is described in detail, of which we give a brief review in this section.

For simplicity, let us illustrate the algorithm on a planar square lattice dimer configuration, see Fig. A.3. The generalization to the bilayer geometry is straightforward. We start by randomly selecting one of the sites in the system, which we label as $\boldsymbol{r}_0$. There is a dimer emanating from $\boldsymbol{r}_0$ and connecting it to a neighboring site $\boldsymbol{r}_1$. From the perspective of $\boldsymbol{r}_1$, the dimer emanates in one of the four directions $+x, +y, -x, -y$, which we label as $\ell = 1, 2, 3, 4$ respectively, see Fig. A.3. Next, we remove the dimer from its current orientation ℓ and insert it into a new orientation k into which it emanates from $\boldsymbol{r}_1$. The new orientation k is selected with a probability $P_{\ell k}$ ($\sum_k P_{\ell k} = 1$) which satisfies detailed balance locally and can be obtained from a subroutine described below. Once a new orientation k has been selected, we follow the dimer along this orientation to a new site labelled by $\boldsymbol{r}_2$. The site $\boldsymbol{r}_2$ in turn is also connected through another dimer to a site $\boldsymbol{r}_3$, and we move to $\boldsymbol{r}_3$, remove the dimer emanating from it, and reinsert it in a new orientation as in the previous step. This process is then reiterated until we reach the starting site $\boldsymbol{r}_0$ and the loop closes. The loop update is accepted with probability $\min\{1, \exp[-\beta \Delta E]\}$, where β is the inverse temperature and $\Delta E = V(N_{\text{final}} - N_{\text{initial}})$ is given by the difference in

the number of parallel dimer plaquettes between final configuration and initial configuration, ensuring detailed balance. Fig. A.3 shows that this algorithm works by effectively breaking up a dimer into two monomers and moving one of the monomers through the lattice until they reunite to form a dimer.

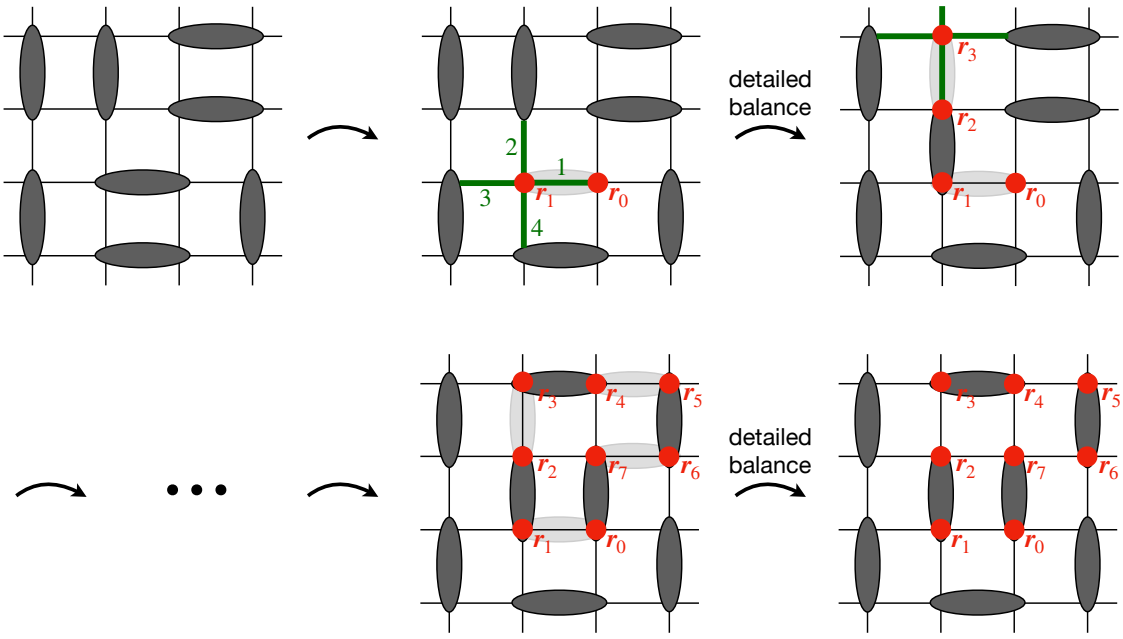

Figure A.3: Monte Carlo loop updates (see text for detailed description). The algorithm proceeds by randomly selecting a site $\boldsymbol{r}_0$ which is connected to $\boldsymbol{r}_1$ by a dimer. This dimer is removed and reinserted in a new orientation around $\boldsymbol{r}_1$ that is selected probabilistically, based on a local detailed balance rule. This elementary step is iterated until the loop closes. The new configuration is accepted or rejected with a probability given by detailed balance.

Let us now describe how the probabilities $P_{\ell k}$ to shift a dimer that originally emanates into direction ℓ to a new direction k are selected. In principle, detailed balance has been ensured upon accepting/rejecting the update once the loop closes as describe in the previous paragraph. However, by adjusting the probabilities $P_{\ell k}$ that decide *locally* which direction the loop takes next, the performance of the algorithm is significantly enhanced. One first introduces the dimer fugacities

$$\omega_{\ell=1,\ldots,4} = \exp[-\beta V N_\ell], \tag{A.38}$$

where N_ℓ is the number of flippable plaquettes that the dimer in orientation ℓ is part of. Notice that N_ℓ depends on the local surrounding configuration. Demanding that detailed balance be fulfilled locally can be expressed as

$$P_{\ell k}\, \omega_\ell = P_{k\ell}\, \omega_k. \tag{A.39}$$

Using this relation and the fact that $\sum_k P_{\ell k} = 1$, one can define the weights

$$a_{\ell k} := P_{\ell k}\, \omega_\ell, \tag{A.40}$$

which satisfy

$$\begin{aligned} \sum_k a_{\ell k} &= \omega_\ell \\ a_{\ell k} &= a_{k \ell}. \end{aligned} \tag{A.41}$$

The first line of Eq. (A.41) provides us with a set of 4 linear equations for the $a_{\ell k}$, of which 10 are independent after using the detailed balance condition in the second line of Eq. (A.41). For the bilayer geometry, where there are $\ell = 1, ..., 5$ possible orientations, we obtain 5 equations for 15 independent weights $a_{\ell k}$. These equations are underdetermined and so one can optimize the weights $a_{\ell k}$ further by minimizing the number of 'bounces', in which the loop retraces the path that it came from. This can be done by demanding

$$\sum_\ell a_{\ell \ell} \stackrel{!}{=} \min. \tag{A.42}$$

The minimization procedure Eq. (A.42) under the condition of Eq. (A.41) constitutes a linear programming task. In our numerical implementation we used the open source lp_solve package to perform it [550]. In practice, for a fixed inverse temperature β, we can determine the weights $a_{\ell k}$ and thus the probabilities $P_{\ell k}$ in advance and tabulate them for all possible values of N_ℓ that determine the fugacities via Eq. (A.38).

B

Additional calculations for the bilayer dimer model

B.1 Proof of Eq. (4.7)

We first restate Eq. (4.7) from Chapter 4 of the main text in a more formal version in order to set up the proof.

Claim: Let us consider an arbitrary directed loop $\mathcal{L} = \{\boldsymbol{r}_0, \boldsymbol{r}_1, ..., \boldsymbol{r}_{N-1}\}$ on the square lattice that fulfills the following two conditions:

(i) $\mathcal{L}$ is *closed:* $|\boldsymbol{r}_{n+1} - \boldsymbol{r}_n| = 1$ for all $n \in \{0, ..., N-1\}$, with $\boldsymbol{r}_N \equiv \boldsymbol{r}_0$.

(ii) $\mathcal{L}$ is *non-intersecting:* $\boldsymbol{r}_n = \boldsymbol{r}_m \iff n = m$.

Furthermore, let us denote by $v_{\mathcal{L}} \subset \mathbb{Z}^2$ the set of lattice points that form the interior of the loop $\mathcal{L}$ as shown in Fig. 4.2 (a) (see also a more formal definition of $v_{\mathcal{L}}$ in the discussion around Eq. (B.23) of Appendix B.4).

Given these definitions, the following identity holds:

$$\Delta N_{AB}(v_{\mathcal{L}}) = \frac{1}{4} \sum_{n=0}^{N-1} (-1)^{x_n + y_n} \Big(\boldsymbol{\ell}_o(\boldsymbol{r}_n) \wedge \boldsymbol{\ell}_i(\boldsymbol{r}_n) \Big), \tag{B.1}$$

where $\Delta N_{AB}(v_{\mathcal{L}})$ is the difference between the number of A/B sublattice sites contained within the set $v_{\mathcal{L}}$, and $\boldsymbol{\ell}_o(\boldsymbol{r}_n) = \boldsymbol{r}_{n+1} - \boldsymbol{r}_n$, $\boldsymbol{\ell}_i(\boldsymbol{r}_n) = \boldsymbol{r}_n - \boldsymbol{r}_{n-1}$. Note that $\boldsymbol{\ell}_{i/o} \in \{\pm \boldsymbol{e}_x, \pm \boldsymbol{e}_y\}$, and $\boldsymbol{r}_{-1} = \boldsymbol{r}_0$ by definition. The symbol '$\wedge$' denotes the wedge-product, which yields a

scalar for the two-dimensional vectors considered here: $\boldsymbol{a} \wedge \boldsymbol{b} = a_x b_y - a_y b_x$.

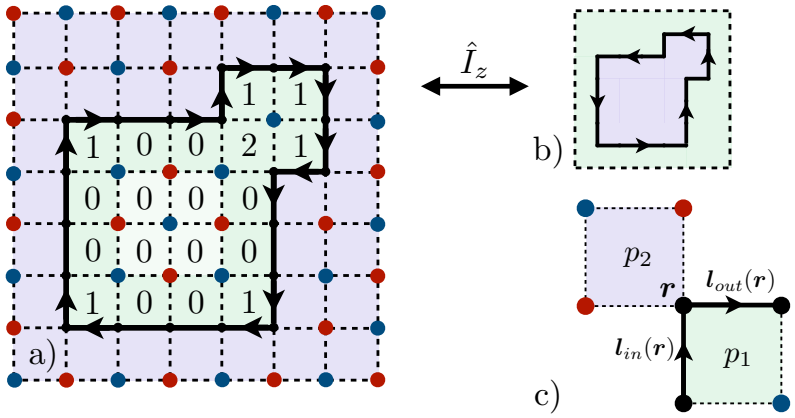

Figure B.1: Proof of Eq. (4.7). a) A closed, directed loop $\mathcal{L}$ (black) encloses a region $V_\mathcal{L}$ (green shaded). The difference in the number of A (blue) and B (red) sublattice sites contained within $V_\mathcal{L}$ can be traced back to the corners of $\mathcal{L}$. **b)** Changing the direction of $\mathcal{L}$ exchanges interior and exterior of $\mathcal{L}$. **c)** For every corner, there exist two plaquettes p_1 and p_2 that potentially obtain a non-trivial difference of A and B sublattice sites. Which of these plaquettes is contained within the area $V_\mathcal{L}$ enclosed by $\mathcal{L}$ is determined by the chirality of $\mathcal{L}$.

Proof: Let us first denote by

$$p(\boldsymbol{r}) = \{\boldsymbol{r}, \boldsymbol{r} + \boldsymbol{e}_x, \boldsymbol{r} + \boldsymbol{e}_x + \boldsymbol{e}_y, \boldsymbol{r} + \boldsymbol{e}_y\} \tag{B.2}$$

the four sites contained within an elementary plaquette p of the square lattice. Since

$$\bigcup_{p \subseteq (v_\mathcal{L} \cup \mathcal{L})} p \backslash \mathcal{L} = v_\mathcal{L}, \tag{B.3}$$

we can rewrite the left hand side of Eq. (B.1) as

$$\Delta N_{AB}(v_\mathcal{L}) = \frac{1}{4} \sum_{p \subseteq (v_\mathcal{L} \cup \mathcal{L})} \Delta N_{AB}\big(p \backslash \mathcal{L}\big), \tag{B.4}$$

with the sum running over all plaquettes contained within $v_\mathcal{L} \cup \mathcal{L}$. The factor $1/4$ compensates for the overcounting that results from each site being adjacent to four different plaquettes, see Fig. B.1 (a).

We see that for those plaquettes in $v_\mathcal{L} \cup \mathcal{L}$ that are not touched by $\mathcal{L}$, i.e. $p \backslash \mathcal{L} = p$, we have $\Delta N_{AB}(p) = 2 - 2 = 0$ immediately, see Fig. B.1 (a). Thus, it is sufficient to focus on plaquettes with a non-vanishing intersection $p \cap \mathcal{L} \neq \emptyset$. Crucially, we then recognize that a non-vanishing $\Delta N_{AB}\big(p \backslash \mathcal{L}\big) \neq 0$ can only be realized if there is at least one connected section of $\mathcal{L}$ passing through an *odd* number of sites in p, see Fig. B.1 (c). We can then

expand

$$\Delta N_{AB}(p\backslash\mathcal{L}) = \sum_{\boldsymbol{r}\in p\backslash\mathcal{L}} (-1)^{r_x+r_y} = -\sum_{\boldsymbol{r}\in p\cap\mathcal{L}} (-1)^{r_x+r_y} = -\sum_{n=0}^{N-1} (-1)^{x_n+y_n} \big|\{\boldsymbol{r}_n\} \cap p\big| =$$
$$= \sum_{n=0}^{N-1} (-1)^{x_n+y_n} \big|\{\boldsymbol{r}_n\} \cap p\big| \Big[\big|\{\boldsymbol{r}_{n+1}\}\cap p\big|\big|\{\boldsymbol{r}_{n-1}\}\cap p\big| - \\ - \big(1-\big|\{\boldsymbol{r}_{n+1}\}\cap p\big|\big)\big(1-\big|\{\boldsymbol{r}_{n-1}\}\cap p\big|\big)\Big], \tag{B.5}$$

where $|...|$ denotes the number of elements contained within a given set, and $\big|\{\boldsymbol{r}\}\cap p\big| \in \{0,1\}$ determines whether $\boldsymbol{r}$ is contained in p or not. The first term in the square brackets of Eq. (B.5) corresponds to a section $\{\boldsymbol{r}_{n-1}, \boldsymbol{r}_n, \boldsymbol{r}_{n+1}\} \subset \mathcal{L}$ running through three sites of the plaquette p, while in the second term only the site $\boldsymbol{r}_n$, and *not* the sites $\boldsymbol{r}_{n-1}, \boldsymbol{r}_{n+1}$, is part of p. These contributions correspond to p_1 and p_2 in Fig. B.1 (c), respectively. Including the sum $\sum_{p\subseteq(v_\mathcal{L}\cup\mathcal{L})}$ from Eq. (B.4) we obtain

$$\Delta N_{AB}(v_\mathcal{L}) = \frac{1}{4}\sum_{n=0}^{N-1} (-1)^{x_n+y_n} \sum_{p\subseteq(v_\mathcal{L}\cup\mathcal{L})} \big|\{\boldsymbol{r}_n\}\cap p\big| \Big[\big|\{\boldsymbol{r}_{n+1}\}\cap p\big|\big|\{\boldsymbol{r}_{n-1}\}\cap p\big| - \\ - \big(1-\big|\{\boldsymbol{r}_{n+1}\}\cap p\big|\big)\big(1-\big|\{\boldsymbol{r}_{n-1}\}\cap p\big|\big)\Big]. \tag{B.6}$$

Two evaluate the sum over p in Eq. (B.6), we look at the two terms in the square brackets seperately. For the first term, we have

$$\sum_{p\subseteq V_\mathcal{L}} \big|\{\boldsymbol{r}_n\}\cap p\big|\,\big|\{\boldsymbol{r}_{n+1}\}\cap p\big|\big|\{\boldsymbol{r}_{n-1}\}\cap p\big| = \delta\big(\boldsymbol{\ell}_o(\boldsymbol{r}_n)\wedge\boldsymbol{\ell}_i(\boldsymbol{r}_n) - 1\big). \tag{B.7}$$

This relation can be understood in the following way: since all three $\boldsymbol{r}_{n-1}, \boldsymbol{r}_n, \boldsymbol{r}_{n+1}$ are supposed to be part of one plaquette p, the loop $\mathcal{L}$ needs to have a corner at $\boldsymbol{r}_n$, see Fig. B.1 (c). Thus, $\boldsymbol{\ell}_o(\boldsymbol{r}_n)\wedge\boldsymbol{\ell}_i(\boldsymbol{r}_n) \neq 0$ needs to be finite. Furthermore, if there indeed is a corner of $\mathcal{L}$ at $\boldsymbol{r}_n$, there exists exactly one plaquette $p\subset\mathbb{Z}^2$ such that $\{\boldsymbol{r}_{n-1}, \boldsymbol{r}_n, \boldsymbol{r}_{n+1}\} \in p$. However, this plaquette will only be contained in $v_\mathcal{L}\cup\mathcal{L}$, and thus in the sum over p in Eq. (B.7), if $\boldsymbol{\ell}_o(\boldsymbol{r}_n)\wedge\boldsymbol{\ell}_i(\boldsymbol{r}_n) = 1$, giving rise to the delta function. Note that changing the direction of $\mathcal{L}$ (via the inversion operator $\hat{I}_z$) nominally exchanges in- and outside of $\mathcal{L}$, see Fig. B.1 (b).

Analogously, we obtain for the second term of Eq. (B.6)

$$\sum_{p\subseteq V_\mathcal{L}} \big|\{\boldsymbol{r}_n\}\cap p\big|\,\big(1-\big|\{\boldsymbol{r}_{n+1}\}\cap p\big|\big)\big(1-\big|\{\boldsymbol{r}_{n-1}\}\cap p\big|\big) = \delta\big(\boldsymbol{\ell}_o(\boldsymbol{r}_n)\wedge\boldsymbol{\ell}_i(\boldsymbol{r}_n) + 1\big). \tag{B.8}$$

Inserting both Eq. (B.7) and Eq. (B.8) into Eq. (B.6), and using that

$$\delta\big(\boldsymbol{\ell}_o(\boldsymbol{r}_n) \wedge \boldsymbol{\ell}_i(\boldsymbol{r}_n) - 1\big) - \delta\big(\boldsymbol{\ell}_o(\boldsymbol{r}_n) \wedge \boldsymbol{\ell}_i(\boldsymbol{r}_n) + 1\big) = \boldsymbol{\ell}_o(\boldsymbol{r}_n) \wedge \boldsymbol{\ell}_i(\boldsymbol{r}_n) \tag{B.9}$$

due to $\boldsymbol{\ell}_o(\boldsymbol{r}_n) \wedge \boldsymbol{\ell}_i(\boldsymbol{r}_n) \in \{-1, 0, 1\}$, results in Eq. (B.1) and thus completes our proof.

B.2 Proof of Eq. (4.8)

As stated in the main text, independent of the chosen boundary conditions, the following quantity is invariant under the dynamics of $\hat{H}_J$:

$$\hat{\mathcal{Q}} = \sum_{\boldsymbol{r}} (-1)^{r_y + r_y} \big(\hat{\boldsymbol{\ell}}_o(\boldsymbol{r}) \wedge \hat{\boldsymbol{\ell}}_i(\boldsymbol{r})\big), \tag{B.10}$$

where

$$\begin{aligned} \hat{\boldsymbol{\ell}}_o(\boldsymbol{r}) &= \sum_{\alpha \in \{\pm x, \pm y\}} \boldsymbol{e}_\alpha \, \hat{n}^{(l)}_{\boldsymbol{r},\alpha} \\ \hat{\boldsymbol{\ell}}_i(\boldsymbol{r}) &= \sum_{\alpha \in \{\pm x, \pm y\}} \boldsymbol{e}_\alpha \, \hat{n}^{(l)}_{\boldsymbol{r}-\boldsymbol{e}_\alpha,\alpha}. \end{aligned} \tag{B.11}$$

From the form $\hat{H}_J = \hat{H}_J^{(h)} + \hat{H}_J^{(l)}$ given in Eq. (4.4) and Eq. (4.5), we notice that any local term in $\hat{H}_J^{(h)}$ creates or annihilates a trivial loop of length two that contains no corners. It is therfore directly verified that $[\hat{H}_J^{(h)}, \hat{\mathcal{Q}}] = 0$.

To show that the remaining $\hat{H}_J^{(l)}$ also commutes with $\hat{\mathcal{Q}}$, let us consider a local plaquette move $\hat{h}_p^{(l)}$ from $\hat{H}_J^{(l)}$ and show that $[\hat{h}_p^{(l)}, \hat{\mathcal{Q}}] = 0$. Here, $p = \{\boldsymbol{r}_{p,1}, \boldsymbol{r}_{p,2}, \boldsymbol{r}_{p,3}, \boldsymbol{r}_{p,4}\}$ labels the four sites of a given plaquette p in counter-clockwise order (starting at the bottom left site) as defined in Eq. (B.2). According to Eq. (4.4), the local term $\hat{h}_p^{(l)}$ is given either by

$\hat{h}_p^{(l)} = |$ $\rangle \langle$ $| + h.c.,$ (B.12)

or

$\hat{h}_p^{(l)} = |$ $\rangle \langle$ $| + h.c.,$ (B.13)

and the following arguments proceed analogously for either choice. Using

$$[\hat{h}_p^{(l)}, \hat{\boldsymbol{\ell}}_o(\boldsymbol{r}) \wedge \hat{\boldsymbol{\ell}}_i(\boldsymbol{r})] = [\hat{h}_p^{(l)}, \hat{\boldsymbol{\ell}}_o(\boldsymbol{r})] \wedge \hat{\boldsymbol{\ell}}_i(\boldsymbol{r}) + \hat{\boldsymbol{\ell}}_o(\boldsymbol{r}) \wedge [\hat{h}_p^{(l)}, \hat{\boldsymbol{\ell}}_i(\boldsymbol{r})], \tag{B.14}$$

we can compute

$$
\begin{aligned}
&[\hat{h}_p^{(l)}, \hat{\mathcal{Q}}] = \sum_{\boldsymbol{r}\in p} (-1)^{r_x+r_y} [\hat{h}_p^{(l)}, \hat{\boldsymbol{\ell}}_o(\boldsymbol{r}) \wedge \hat{\boldsymbol{\ell}}_i(\boldsymbol{r})] = \\
&= \Big(\hat{\boldsymbol{\ell}}_o(\boldsymbol{r}_{p,1}) \wedge [\hat{h}_p^{(l)}, \hat{\boldsymbol{\ell}}_i(\boldsymbol{r}_{p,1})] + \hat{\boldsymbol{\ell}}_o(\boldsymbol{r}_{p,3}) \wedge [\hat{h}_p^{(l)}, \hat{\boldsymbol{\ell}}_i(\boldsymbol{r}_{p,3})] - \\
&\qquad - [\hat{h}_p^{(l)}, \hat{\boldsymbol{\ell}}_o(\boldsymbol{r}_{p,2})] \wedge \hat{\boldsymbol{\ell}}_i(\boldsymbol{r}_{p,2}) - [\hat{h}_p^{(l)}, \hat{\boldsymbol{\ell}}_o(\boldsymbol{r}_{p,4})] \wedge \hat{\boldsymbol{\ell}}_i(\boldsymbol{r}_{p,4}) \Big) + \\
&\quad + \Big([\hat{h}_p^{(l)}, \hat{\boldsymbol{\ell}}_o(\boldsymbol{r}_{p,1})] \wedge \hat{\boldsymbol{\ell}}_i(\boldsymbol{r}_{p,1}) + [\hat{h}_p^{(l)}, \hat{\boldsymbol{\ell}}_o(\boldsymbol{r}_{p,3})] \wedge \hat{\boldsymbol{\ell}}_i(\boldsymbol{r}_{p,3}) - \\
&\qquad - \hat{\boldsymbol{\ell}}_o(\boldsymbol{r}_{p,2}) \wedge [\hat{h}_p^{(l)}, \hat{\boldsymbol{\ell}}_i(\boldsymbol{r}_{p,2})] - \hat{\boldsymbol{\ell}}_o(\boldsymbol{r}_{p,4}) \wedge [\hat{h}_p^{(l)}, \hat{\boldsymbol{\ell}}_i(\boldsymbol{r}_{p,4})] \Big),
\end{aligned}
\tag{B.15}
$$

where we have grouped the arising terms into two contributions marked by round brackets, which we are going to consider separately.

For the term in the first round bracket of Eq. (B.15), the hard-core constraint implies, through direct evaluation,

$$
\begin{aligned}
&[\hat{h}_p^{(l)}, \hat{\boldsymbol{\ell}}_i(\boldsymbol{r}_{p,1})] = \\
&= \hat{h}_p^{(l)} \, (\boldsymbol{e}_y - \boldsymbol{e}_x) \times \delta(\hat{\boldsymbol{\ell}}_i(\boldsymbol{r}_{p,1}) + \boldsymbol{e}_x) \, \delta(\hat{\boldsymbol{\ell}}_o(\boldsymbol{r}_{p,2}) + \boldsymbol{e}_x) \, \delta(\hat{\boldsymbol{\ell}}_i(\boldsymbol{r}_{p,3}) - \boldsymbol{e}_x) \, \delta(\hat{\boldsymbol{\ell}}_o(\boldsymbol{r}_{p,4}) - \boldsymbol{e}_x) + \\
&+ \hat{h}_p^{(l)} \, (\boldsymbol{e}_x - \boldsymbol{e}_y) \times \delta(\hat{\boldsymbol{\ell}}_i(\boldsymbol{r}_{p,1}) + \boldsymbol{e}_y) \, \delta(\hat{\boldsymbol{\ell}}_o(\boldsymbol{r}_{p,2}) - \boldsymbol{e}_y) \, \delta(\hat{\boldsymbol{\ell}}_i(\boldsymbol{r}_{p,3}) - \boldsymbol{e}_y) \, \delta(\hat{\boldsymbol{\ell}}_o(\boldsymbol{r}_{p,4}) + \boldsymbol{e}_y)
\end{aligned}
$$

$$
[\hat{h}_p^{(l)}, \hat{\boldsymbol{\ell}}_i(\boldsymbol{r}_{p,3})] = \ldots = -[\hat{h}_p^{(l)}, \hat{\boldsymbol{\ell}}_i(\boldsymbol{r}_{p,1})]
$$

$$
\begin{aligned}
&[\hat{h}_p^{(l)}, \hat{\boldsymbol{\ell}}_o(\boldsymbol{r}_{p,2})] = \\
&= \hat{h}_p^{(l)} \, (-\boldsymbol{e}_x - \boldsymbol{e}_y) \times \delta(\hat{\boldsymbol{\ell}}_i(\boldsymbol{r}_{p,1}) + \boldsymbol{e}_x) \, \delta(\hat{\boldsymbol{\ell}}_o(\boldsymbol{r}_{p,2}) + \boldsymbol{e}_x) \, \delta(\hat{\boldsymbol{\ell}}_i(\boldsymbol{r}_{p,3}) - \boldsymbol{e}_x) \, \delta(\hat{\boldsymbol{\ell}}_o(\boldsymbol{r}_{p,4}) - \boldsymbol{e}_x) + \\
&+ \hat{h}_p^{(l)} \, (\boldsymbol{e}_x + \boldsymbol{e}_y) \times \delta(\hat{\boldsymbol{\ell}}_i(\boldsymbol{r}_{p,1}) + \boldsymbol{e}_y) \, \delta(\hat{\boldsymbol{\ell}}_o(\boldsymbol{r}_{p,2}) - \boldsymbol{e}_y) \, \delta(\hat{\boldsymbol{\ell}}_i(\boldsymbol{r}_{p,3}) - \boldsymbol{e}_y) \, \delta(\hat{\boldsymbol{\ell}}_o(\boldsymbol{r}_{p,4}) + \boldsymbol{e}_y)
\end{aligned}
$$

$$
[\hat{h}_p^{(l)}, \hat{\boldsymbol{\ell}}_o(\boldsymbol{r}_{p,4})] = \ldots = -[\hat{h}_p^{(l)}, \hat{\boldsymbol{\ell}}_o(\boldsymbol{r}_{p,2})],
\tag{B.16}
$$

see Fig. 4.1 (c) from the main text for an intuition about the terms appearing in Eq. (B.16). Inserting Eq. (B.16) into the first term of Eq. (B.15) yields

$$
\begin{aligned}
&\Big(\hat{\boldsymbol{\ell}}_o(\boldsymbol{r}_{p,1}) \wedge [\hat{h}_p^{(l)}, \hat{\boldsymbol{\ell}}_i(\boldsymbol{r}_{p,1})] + \hat{\boldsymbol{\ell}}_o(\boldsymbol{r}_{p,3}) \wedge [\hat{h}_p^{(l)}, \hat{\boldsymbol{\ell}}_i(\boldsymbol{r}_{p,3})] - \\
&\qquad - [\hat{h}_p^{(l)}, \hat{\boldsymbol{\ell}}_o(\boldsymbol{r}_{p,2})] \wedge \hat{\boldsymbol{\ell}}_i(\boldsymbol{r}_{p,2}) - [\hat{h}_p^{(l)}, \hat{\boldsymbol{\ell}}_o(\boldsymbol{r}_{p,4})] \wedge \hat{\boldsymbol{\ell}}_i(\boldsymbol{r}_{p,4}) \Big) = \\
&= \hat{h}_p^{(l)} \Big(\big(\hat{\boldsymbol{\ell}}_o(\boldsymbol{r}_{p,1}) - \hat{\boldsymbol{\ell}}_o(\boldsymbol{r}_{p,3}) \big) \wedge (\boldsymbol{e}_y - \boldsymbol{e}_x) + \big(\hat{\boldsymbol{\ell}}_i(\boldsymbol{r}_{p,4}) - \hat{\boldsymbol{\ell}}_i(\boldsymbol{r}_{p,2}) \big) \wedge (\boldsymbol{e}_x + \boldsymbol{e}_y) \Big) \times \\
&\qquad \times \Big[\delta(\hat{\boldsymbol{\ell}}_i(\boldsymbol{r}_{p,1}) + \boldsymbol{e}_x) \, \delta(\hat{\boldsymbol{\ell}}_o(\boldsymbol{r}_{p,2}) + \boldsymbol{e}_x) \, \delta(\hat{\boldsymbol{\ell}}_i(\boldsymbol{r}_{p,3}) - \boldsymbol{e}_x) \, \delta(\hat{\boldsymbol{\ell}}_o(\boldsymbol{r}_{p,4}) - \boldsymbol{e}_x) - \\
&\qquad - \delta(\hat{\boldsymbol{\ell}}_i(\boldsymbol{r}_{p,1}) + \boldsymbol{e}_y) \, \delta(\hat{\boldsymbol{\ell}}_o(\boldsymbol{r}_{p,2}) - \boldsymbol{e}_y) \, \delta(\hat{\boldsymbol{\ell}}_i(\boldsymbol{r}_{p,3}) - \boldsymbol{e}_y) \, \delta(\hat{\boldsymbol{\ell}}_o(\boldsymbol{r}_{p,4}) + \boldsymbol{e}_y) \Big].
\end{aligned}
\tag{B.17}
$$

While arranging the terms in Eq. (B.17) we have used the fact that

$$[\hat{h}_p^{(l)}, \hat{\boldsymbol{\ell}}_{i/o}(\boldsymbol{r})] \neq 0 \Rightarrow [\hat{h}_p^{(l)}, \hat{\boldsymbol{\ell}}_{o/i}(\boldsymbol{r})] = 0. \tag{B.18}$$

Let us now focus on the round bracket of the right hand side of Eq. (B.17): There are in total 34 different possible (i.e. compatible with the hard core constraint) combinations of eigenvalues of the four operators $\hat{\boldsymbol{\ell}}_o(\boldsymbol{r}_{p,1}), \hat{\boldsymbol{\ell}}_o(\boldsymbol{r}_{p,3}), \hat{\boldsymbol{\ell}}_i(\boldsymbol{r}_{p,2}), \hat{\boldsymbol{\ell}}_i(\boldsymbol{r}_{p,4})$ appearing in Eq. (B.17):

- 16 possibilities from $\hat{\boldsymbol{\ell}}_o(\boldsymbol{r}_{p,1}) \in \{-\boldsymbol{e}_x, -\boldsymbol{e}_y\}$, $\hat{\boldsymbol{\ell}}_o(\boldsymbol{r}_{p,3}) \in \{\boldsymbol{e}_x, \boldsymbol{e}_y\}$, $\hat{\boldsymbol{\ell}}_i(\boldsymbol{r}_{p,2}) \in \{-\boldsymbol{e}_x, \boldsymbol{e}_y\}$, $\hat{\boldsymbol{\ell}}_i(\boldsymbol{r}_{p,4}) \in \{\boldsymbol{e}_x, -\boldsymbol{e}_y\}$ independently.
- 4 possibilities from $\hat{\boldsymbol{\ell}}_o(\boldsymbol{r}_{p,1}) = \boldsymbol{e}_x$, $\hat{\boldsymbol{\ell}}_i(\boldsymbol{r}_{p,2}) = \boldsymbol{e}_x$, $\hat{\boldsymbol{\ell}}_o(\boldsymbol{r}_{p,3}) \in \{\boldsymbol{e}_x, \boldsymbol{e}_y\}$, $\hat{\boldsymbol{\ell}}_i(\boldsymbol{r}_{p,4}) \in \{\boldsymbol{e}_x, -\boldsymbol{e}_y\}$.
- 4 possibilities from $\hat{\boldsymbol{\ell}}_o(\boldsymbol{r}_{p,1}) = \boldsymbol{e}_y$, $\hat{\boldsymbol{\ell}}_i(\boldsymbol{r}_{p,4}) = \boldsymbol{e}_y$, $\hat{\boldsymbol{\ell}}_o(\boldsymbol{r}_{p,3}) \in \{\boldsymbol{e}_x, \boldsymbol{e}_y\}$, $\hat{\boldsymbol{\ell}}_i(\boldsymbol{r}_{p,2}) \in \{-\boldsymbol{e}_x, \boldsymbol{e}_y\}$.
- 4 possibilities from $\hat{\boldsymbol{\ell}}_o(\boldsymbol{r}_{p,3}) = -\boldsymbol{e}_x$, $\hat{\boldsymbol{\ell}}_i(\boldsymbol{r}_{p,4}) = -\boldsymbol{e}_x$, $\hat{\boldsymbol{\ell}}_o(\boldsymbol{r}_{p,1}) \in \{-\boldsymbol{e}_x, -\boldsymbol{e}_y\}$, $\hat{\boldsymbol{\ell}}_i(\boldsymbol{r}_{p,2}) \in \{-\boldsymbol{e}_x, \boldsymbol{e}_y\}$.
- 4 possibilities from $\hat{\boldsymbol{\ell}}_o(\boldsymbol{r}_{p,3}) = -\boldsymbol{e}_y$, $\hat{\boldsymbol{\ell}}_i(\boldsymbol{r}_{p,2}) = -\boldsymbol{e}_y$, $\hat{\boldsymbol{\ell}}_o(\boldsymbol{r}_{p,1}) \in \{-\boldsymbol{e}_x, -\boldsymbol{e}_y\}$, $\hat{\boldsymbol{\ell}}_i(\boldsymbol{r}_{p,4}) \in \{\boldsymbol{e}_x, -\boldsymbol{e}_y\}$.
- 1 possibility from $\hat{\boldsymbol{\ell}}_o(\boldsymbol{r}_{p,1}) = \boldsymbol{e}_x$, $\hat{\boldsymbol{\ell}}_i(\boldsymbol{r}_{p,2}) = \boldsymbol{e}_x$, $\hat{\boldsymbol{\ell}}_o(\boldsymbol{r}_{p,3}) = -\boldsymbol{e}_x$, $\hat{\boldsymbol{\ell}}_i(\boldsymbol{r}_{p,4}) = -\boldsymbol{e}_x$.
- 1 possibility from $\hat{\boldsymbol{\ell}}_o(\boldsymbol{r}_{p,1}) = \boldsymbol{e}_y$, $\hat{\boldsymbol{\ell}}_i(\boldsymbol{r}_{p,4}) = \boldsymbol{e}_y$, $\hat{\boldsymbol{\ell}}_o(\boldsymbol{r}_{p,3}) = -\boldsymbol{e}_y$, $\hat{\boldsymbol{\ell}}_i(\boldsymbol{r}_{p,2}) = -\boldsymbol{e}_y$.

It is then a straightforward task to go through all 34 listed possibilities and check that in each case, the round bracket on the right hand side of Eq. (B.17), and thus the left hand side of Eq. (B.17) itself, vanishes.

We can then repeat this derivation analogously for the second round bracket on the right hand side of Eq. (B.15), which consequently also vanishes, such that overall, we indeed find $[\hat{h}_p, \hat{\mathcal{Q}}] = 0$, proving Eq. (B.10).

B.3 Conservation of chiral subcharges

In this Appendix we formally show the invariance of the chiral subcharges $\hat{Q}_\phi$ under the Hamiltonian $\hat{H}_J = \hat{H}_J^{(l)} + \hat{H}_J^{(h)}$ given in Eq. (4.4) and Eq. (4.5), as argued for in Sec. 4.1.

Taking care of $\hat{H}_J^{(l)}$ first, we verify through direct inspection of the possible loop moves in Eq. (4.4) that $[\hat{H}_J^{(l)}, \hat{q}_{\boldsymbol{r}}(\phi)] = 0$ for all $\boldsymbol{r}$ and ϕ, with $\hat{q}_{\boldsymbol{r}}(\phi)$ from Eq. (4.11). This immediately implies $[\hat{H}_J^{(l)}, \hat{Q}_\phi] = 0$ for all ϕ.

Moving on to $\hat{H}_J^{(h)}$ from Eq. (4.5) next, we use that $[\hat{l}^\dagger_{\boldsymbol{r},\alpha}\, \hat{l}^\dagger_{\boldsymbol{r}+\boldsymbol{e}_\alpha,-\alpha}, \hat{\phi}_{\boldsymbol{r}'}] = 0$ and thus also $[\hat{l}^\dagger_{\boldsymbol{r},\alpha}\, \hat{l}^\dagger_{\boldsymbol{r}+\boldsymbol{e}_\alpha,-\alpha},\, \hat{q}_{\boldsymbol{r}'}(\phi)] = 0$ for all $\boldsymbol{r}, \boldsymbol{r}'$. We can then compute the commutator

$$[\hat{H}_J^{(h)}, \hat{Q}_\phi] = \sum_{\boldsymbol{r},\alpha} (-1)^{r_x+r_y} \left\{ \hat{l}^\dagger_{\boldsymbol{r},\alpha}\, \hat{l}^\dagger_{\boldsymbol{r}+\boldsymbol{e}_\alpha,-\alpha}\, \hat{h}_{\boldsymbol{r}}\, \hat{h}_{\boldsymbol{r}+\boldsymbol{e}_\alpha} \left[\delta\left(\hat{\phi}_{\boldsymbol{r}+\boldsymbol{e}_\alpha} - \phi\right) - \delta\left(\hat{\phi}_{\boldsymbol{r}} - \phi\right) \right] \right\} + \\ + \sum_{\boldsymbol{r},\alpha} (-1)^{r_x+r_y} \left\{ \hat{l}_{\boldsymbol{r},\alpha}\, \hat{l}_{\boldsymbol{r}+\boldsymbol{e}_\alpha,-\alpha}\, \hat{h}^\dagger_{\boldsymbol{r}}\, \hat{h}^\dagger_{\boldsymbol{r}+\boldsymbol{e}_\alpha} \left[\delta\left(\hat{\phi}_{\boldsymbol{r}} - \phi\right) - \delta\left(\hat{\phi}_{\boldsymbol{r}+\boldsymbol{e}_\alpha} - \phi\right) \right] \right\}. \tag{B.19}$$

To demonstrate that Eq. (**??**) indeed vanishes, we have to show that

$$\hat{h}_{\boldsymbol{r}}\, \hat{h}_{\boldsymbol{r}+\boldsymbol{e}_\alpha}\, \hat{\phi}_{\boldsymbol{r}} = \hat{h}_{\boldsymbol{r}}\, \hat{h}_{\boldsymbol{r}+\boldsymbol{e}_\alpha}\, \hat{\phi}_{\boldsymbol{r}+\boldsymbol{e}_\alpha} \tag{B.20}$$

for both $\alpha = x, y$, which directly yields zero upon insertion into Eq. (**??**). Setting $\alpha = x$, we see from the definition of $\hat{\phi}_{\boldsymbol{r}}$ in Eq. (4.10) that

$$\hat{h}_{\boldsymbol{r}}\, \hat{h}_{\boldsymbol{r}+\boldsymbol{e}_x}\, \hat{\phi}_{\boldsymbol{r}} - \hat{h}_{\boldsymbol{r}}\, \hat{h}_{\boldsymbol{r}+\boldsymbol{e}_x}\, \hat{\phi}_{\boldsymbol{r}+\boldsymbol{e}_x} = \hat{h}_{\boldsymbol{r}}\, \hat{h}_{\boldsymbol{r}+\boldsymbol{e}_x} (\hat{n}^{(l)}_{\boldsymbol{r},y} - \hat{n}^{(l)}_{\boldsymbol{r}+\hat{e}_y,-y}) = 0. \tag{B.21}$$

The last equality in Eq. (B.21) is due to the hard core constraint: if there is a charge at site $\boldsymbol{r}$, then there cannot be a loop segment running through $\boldsymbol{r}$. This proves Eq. (B.20) for $\alpha = x$. For $\alpha = y$, Eq. (B.20) can be verified in the following way: Assume $\hat{n}^{(h)}_{\boldsymbol{r}+\hat{e}_y} = 1$, i.e. an interlayer charge occupies the site at $\boldsymbol{r}+\boldsymbol{e}_y$ (otherwise, Eq. (B.20) yields zero immediately). Consider a loop segment that gives a contribution $+1$ to $\hat{\phi}_{\boldsymbol{r}}$. This segment enters the horizontal string to the left of $\boldsymbol{r} + \boldsymbol{e}_y$ from below and has two options: 1) It leaves the string going upwards, therefore also giving a contribution $+1$ to $\hat{\phi}_{\boldsymbol{r}+\boldsymbol{e}_y}$. 2) It leaves the string going downwards, thus giving no contribution to $\hat{\phi}_{\boldsymbol{r}+\boldsymbol{e}_y}$, but yielding an additional contribution -1 to $\hat{\phi}_{\boldsymbol{r}}$, and therefore net contribution zero. In both cases, $\hat{\phi}_{\boldsymbol{r}} = \hat{\phi}_{\boldsymbol{r}+\boldsymbol{e}_y}$. The same argument holds for loop segments running in the opposite direction. Note that this argument relies on $\hat{n}^{(h)}_{\boldsymbol{r}+\boldsymbol{e}_y} = 1$, otherwise a loop might enter the horizontal string without leaving it, by running directly through site $\boldsymbol{r} + \boldsymbol{e}_y$. This proves Eq. (B.20) for $\alpha = y$.

Intuitively, the proof can be summarized as follows: Loop-dynamics can deform the shape, position, and number of loops in the system, but never change the net charge contained inside the interior of the loops. The dynamics of charges occurs as creation and annihilation of oppositely charged interlayer dimers on neighboring lattice sites, which thus are both enclosed by the same net chirality.

B.4 **Proof of Eq. (4.13)**

In order to prove Eq. (4.13) of the main text, we first introduce a formal definition of the 'interior' $v_{\mathcal{L}}$ of a closed loop $\mathcal{L}$ on open boundaries, as illustrated in Fig. 4.2. To do so, let

us first define a string operator

$$\hat{\phi}^{(\mathcal{L})}_{\boldsymbol{r}} = \sum_{\substack{r'_x=0 \\ (r'_x,r_y)\in\mathcal{L}}}^{r_x-1} \Big[\hat{n}^{(l)}_{(r'_x,r_y),y} - \hat{n}^{(l)}_{(r'_x,r_y+1),-y}\Big], \tag{B.22}$$

which is similar to Eq. (4.10), but sums only over sites contained in the set $\mathcal{L} = \{\boldsymbol{r}_0, ..., \boldsymbol{r}_{|\mathcal{L}|-1}\}$. We can then define $\tilde{v}_\mathcal{L} = \{\boldsymbol{r} \notin \mathcal{L} : \ |\phi^{(\mathcal{L})}_{\boldsymbol{r}}| = 1\}$, which gives us a set of sites enclosed by $\mathcal{L}$ (but excluding $\mathcal{L}$ itself) on open boundary conditions, see Fig. 4.2. Notice however that due to the chirality of $\mathcal{L}$, its interior should become the complement of $\tilde{v}_\mathcal{L}$ upon reversing the chirality (again excluding $\mathcal{L}$ itself). On a $V = [0, L_x] \times [0, L_y]$ lattice, the interior of $\mathcal{L}$ is thus given by

$$v_\mathcal{L} = \frac{1}{2}\Big(1 + \phi^{(\mathcal{L})}_{\boldsymbol{r}\in\tilde{v}_\mathcal{L}}\Big)\, \tilde{v}_\mathcal{L} \cup \frac{1}{2}\Big(1 - \phi^{(\mathcal{L})}_{\boldsymbol{r}\in\tilde{v}_\mathcal{L}}\Big)\, V\backslash(\tilde{v}_\mathcal{L} \cup \mathcal{L}). \tag{B.23}$$

Note that $\phi^{(\mathcal{L})}_{\boldsymbol{r}\in\tilde{v}_\mathcal{L}} \in \{-1, +1\}$ is independent of the chosen $\boldsymbol{r} \in \tilde{v}_\mathcal{L}$.

With these definitions, we can start from the right hand side of Eq. (4.13) and rewrite

$$\sum_\phi \phi\, \hat{Q}_\phi = \sum_{\boldsymbol{r}} (-1)^{r_x+r_y} \sum_\phi \phi\, \hat{q}_{\boldsymbol{r}}(\phi) = \sum_{\boldsymbol{r}} (-1)^{r_x+r_y} \sum_\mathcal{L} \phi^{(\mathcal{L})}_{\boldsymbol{r}'\in\tilde{v}_\mathcal{L}} \ \big|\{\boldsymbol{r}\} \cap \tilde{v}_\mathcal{L}\big|\ \hat{n}^{(h)}_{\boldsymbol{r}}, \tag{B.24}$$

where $\big|\{\boldsymbol{r}\} \cap \tilde{v}_\mathcal{L}\big| \in \{0, 1\}$ measures whether site $\boldsymbol{r}$ is contained within the set $\tilde{v}_\mathcal{L}$ or not. Again, $\phi^{(\mathcal{L})}_{\boldsymbol{r}'\in\tilde{v}_\mathcal{L}} \in \{-1, +1\}$ is independent of $\boldsymbol{r}'$. The sum $\sum_\mathcal{L}$ extends over all loops $\mathcal{L}$ within the transition graph of a given dimer configuration. Rearranging the sums in Eq. (B.24) we obtain

$$\begin{aligned} \sum_\phi \phi\, \hat{Q}_\phi &= \sum_\mathcal{L} \phi^{(\mathcal{L})}_{\boldsymbol{r}'\in\tilde{v}_\mathcal{L}} \sum_{\boldsymbol{r}} (-1)^{r_x+r_y} \ \big|\{\boldsymbol{r}\} \cap \tilde{v}_\mathcal{L}\big|\ \hat{n}^{(h)}_{\boldsymbol{r}} = \\ &= \sum_\mathcal{L} \phi^{(\mathcal{L})}_{\boldsymbol{r}'\in\tilde{v}_\mathcal{L}} \big[N_A(\tilde{v}_\mathcal{L}) - N_B(\tilde{v}_\mathcal{L})\big] = \sum_\mathcal{L} \big[N_A(v_\mathcal{L}) - N_B(v_\mathcal{L})\big] = \hat{\mathcal{Q}}, \end{aligned} \tag{B.25}$$

where $N_{A/B}(s)$ denotes the number of A/B sublattice sites contained within a set $s \subset \mathbb{Z}^2$. From the first to the second line, we have used that an imbalance in the number of positive/negative charges $\hat{n}^{(h)}_{\boldsymbol{r}}$ on the sites within $\tilde{v}_\mathcal{L}$ is directly reflected in the imbalance of the number of A/B sublattice sites within $\tilde{v}_\mathcal{L}$. This is due to the fact that all loops $\mathcal{L}'$, which may potentially be contained within $\tilde{v}_\mathcal{L}$ for a given transition graph, are of even length and thus contain the same amount of A/B sublattice sites. From the second to the third line in Eq. (B.25), we have used that the system has even lengths L_x, L_y in both directions, which implies $N_A(V) - N_B(V) = 0$ for the entire lattice V under considerations. This completes our proof of Eq. (4.13).

B.5 Symmetry of $\hat{H}_J$

The Hamiltonian $\hat{H}_J = -J \sum_p \hat{h}_p$ of Eq. (4.2) can be demonstrated to have a symmetric spectrum: We define an operator

$$\hat{P} = (-1)^{\sum_{\{\boldsymbol{r}|\, r_x + r_y = 0 \bmod 2\}} \left(\hat{n}^{(d)}_{\boldsymbol{r},x} + \hat{n}^{(d)}_{\boldsymbol{r},z}\right)}, \tag{B.26}$$

which yieds the parity of the total number of dimers emerging into either x- or z-direction from lattice sites $\boldsymbol{r} = (r_x, r_y, r_z)$ that fulfill $r_x + r_y = 0 \bmod 2$. It can straightforwardly be verified that each plaquette of the lattice contains either one or three, i.e. an *odd* number of bonds that contribute to the parity of Eq. (B.26). Therefore, $\{\hat{P}, \hat{h}_p\} = 0$ for all plaquettes p and thus the operator $\hat{P}$ anticommutes with the Hamiltonian, $\{\hat{P}, \hat{H}_J\} = 0$. Hence, for every eigenstate $\hat{H}_J |\psi\rangle = E_\psi |\psi\rangle$ there exists a corresponding state $|\psi'\rangle = \hat{P} |\psi\rangle$ with opposite energy $\hat{H}_J |\psi'\rangle = -E_\psi |\psi'\rangle$. Note that this argument is independent of the spatial dimension of the dimer model.

As a consequence of the symmetric spectrum, each product state in the basis of dimer occupation numbers has energy expectation value zero, and thus formally corresponds to 'infinite temperature'.

References

[1] J. Feldmeier, F. Pollmann, and M. Knap. Emergent Glassy Dynamics in a Quantum Dimer Model. *Phys. Rev. Lett.*, 123:040601, 2019. doi:10.1103/PhysRevLett.123.040601.

[2] J. Feldmeier, P. Sala, G. de Tomasi, F. Pollmann, and M. Knap. Anomalous Diffusion in Dipole- and Higher-Moment-Conserving Systems. *Phys. Rev. Lett.*, 125:245303, 2020. doi:10.1103/PhysRevLett.125.245303.

[3] J. Feldmeier, W. Natori, M. Knap, and J. Knolle. Local probes for charge-neutral edge states in two-dimensional quantum magnets. *Phys. Rev. B*, 102:134423, 2020. doi:10.1103/PhysRevB.102.134423.

[4] J. Feldmeier, F. Pollmann, and M. Knap. Emergent fracton dynamics in a nonplanar dimer model. *Phys. Rev. B*, 103:094303, 2021. doi:10.1103/PhysRevB.103.094303.

[5] J. Feldmeier and M. Knap. Critically Slow Operator Dynamics in Constrained Many-Body Systems. *Phys. Rev. Lett.*, 127:235301, 2021. doi:10.1103/PhysRevLett.127.235301.

[6] A. G. Burchards, J. Feldmeier, A. Schuckert, and M. Knap. Coupled hydrodynamics in dipole-conserving quantum systems. *Phys. Rev. B*, 105:205127, 2022. doi:10.1103/PhysRevB.105.205127.

[7] J. Feldmeier, W. Witczak-Krempa, and M. Knap. Emergent tracer dynamics in constrained quantum systems. *Phys. Rev. B*, 106:094303, 2022. doi:10.1103/PhysRevB.106.094303.

[8] E. Schrödinger. Quantisierung als eigenwertproblem. *Annalen der physik*, 385(13): 437–490, 1926.

[9] P. W. Anderson. More is different: broken symmetry and the nature of the hierarchical structure of science. *Science*, 177(4047):393–396, 1972.

[10] L. D. Landau. On the theory of phase transitions. I. *Zh. Eksp. Teor. Fiz.*, 11:19, 1937.

[11] V. L. Ginzburg and L. D. Landau. *On the Theory of Superconductivity*, pages 113–137. Springer, Berlin, Heidelberg, 2009. doi:10.1007/978-3-540-68008-6_4.

[12] S. Sachdev. *Quantum Phase Transitions*. Cambridge University Press, 2nd edition, 2011. doi:10.1017/CBO9780511973765.

[13] D. C. Tsui, H. L. Stormer, and A. C. Gossard. Two-Dimensional Magnetotransport in the Extreme Quantum Limit. *Phys. Rev. Lett.*, 48:1559–1562, 1982. doi:10.1103/PhysRevLett.48.1559.

[14] J. G. Bednorz and K. A. Müller. Possible high T_c superconductivity in the Ba−La−Cu−O system. *Zeitschrift für Physik B Condensed Matter*, 64(2):189–193, 1986. doi:10.1007/BF01303701.

[15] X.-G. Wen. *Quantum field theory of many-body systems: from the origin of sound to an origin of light and electrons*. Oxford University Press, 2004.

[16] S. R. White. Density matrix formulation for quantum renormalization groups. *Phys. Rev. Lett.*, 69:2863–2866, 1992. doi:10.1103/PhysRevLett.69.2863.

[17] S. R. White. Density-matrix algorithms for quantum renormalization groups. *Phys. Rev. B*, 48:10345–10356, 1993. doi:10.1103/PhysRevB.48.10345.

[18] F. Verstraete, V. Murg, and J.I. Cirac. Matrix product states, projected entangled pair states, and variational renormalization group methods for quantum spin systems. *Advances in Physics*, 57(2):143–224, 2008. doi:10.1080/14789940801912366.

[19] Ulrich Schollwöck. The density-matrix renormalization group in the age of matrix product states. *Annals of Physics*, 326(1):96–192, 2011. doi:10.1016/j.aop.2010.09.012.

[20] X. G. Wen. Colloquium: Zoo of quantum-topological phases of matter. *Rev. Mod. Phys.*, 89:041004, 2017. doi:10.1103/RevModPhys.89.041004.

[21] L. D'Alessio, Y. Kafri, A. Polkovnikov, and M. Rigol. From quantum chaos and eigenstate thermalization to statistical mechanics and thermodynamics. *Advances in Physics*, 65(3):239–362, 2016. doi:10.1080/00018732.2016.1198134.

[22] J. M. Deutsch. Eigenstate thermalization hypothesis. *Reports on Progress in Physics*, 81(8):082001, 2018. doi:10.1088/1361-6633/aac9f1.

[23] M. Srednicki. Chaos and quantum thermalization. *Phys. Rev. E*, 50:888–901, 1994. doi:10.1103/PhysRevE.50.888.

[24] M. Srednicki. Thermal fluctuations in quantized chaotic systems. *Journal of Physics A: Mathematical and General*, 29(4):L75–L79, 1996. doi:10.1088/0305-4470/29/4/003.

[25] M. Srednicki. The approach to thermal equilibrium in quantized chaotic systems. *Journal of Physics A: Mathematical and General*, 32(7):1163–1175, 1999. doi:10.1088/0305-4470/32/7/007.

[26] M. Rigol, V. Dunjko, and M. Olshanii. Thermalization and its mechanism for generic isolated quantum systems. *Nature*, 452(7189):854–858, 2008. doi:10.1038/nature06838.

[27] D. M. Basko, I. L. Aleiner, and B. L. Altshuler. Metal–insulator transition in a weakly interacting many-electron system with localized single-particle states. *Annals of Physics*, 321(5):1126 – 1205, 2006. doi:10.1016/j.aop.2005.11.014.

[28] V. Oganesyan and D. A. Huse. Localization of interacting fermions at high temperature. *Phys. Rev. B*, 75:155111, 2007. doi:10.1103/PhysRevB.75.155111.

[29] M. Žnidarič, T. Prosen, and P. Prelovšek. Many-body localization in the Heisenberg XXZ magnet in a random field. *Phys. Rev. B*, 77:064426, 2008. doi:10.1103/PhysRevB.77.064426.

[30] R. Nandkishore and D. A. Huse. Many-Body Localization and Thermalization in Quantum Statistical Mechanics. *Annual Review of Condensed Matter Physics*, 6(1): 15–38, 2015. doi:10.1146/annurev-conmatphys-031214-014726.

[31] M. Schreiber, S. S. Hodgman, P. Bordia, H. P. Lüschen, M. H. Fischer, R. Vosk, E. Altman, U. Schneider, and I. Bloch. Observation of many-body localization of interacting fermions in a quasirandom optical lattice. *Science*, 349(6250):842–845, 2015. doi:10.1126/science.aaa7432.

[32] D. A. Abanin, E. Altman, I. Bloch, and M. Serbyn. Colloquium: Many-body localization, thermalization, and entanglement. *Rev. Mod. Phys.*, 91:021001, 2019. doi:10.1103/RevModPhys.91.021001.

[33] F. Alet and N. Laflorencie. Many-body localization: An introduction and selected topics. *Comptes Rendus Physique*, 19(6):498–525, 2018. doi:10.1016/j.crhy.2018.03.003.

[34] E. Altman and R. Vosk. Universal Dynamics and Renormalization in Many-Body-Localized Systems. *Annual Review of Condensed Matter Physics*, 6(1):383–409, 2015. doi:10.1146/annurev-conmatphys-031214-014701.

[35] M. Serbyn, Z. Papić, and D. A. Abanin. Local Conservation Laws and the Structure of the Many-Body Localized States. *Phys. Rev. Lett.*, 111:127201, 2013. doi:10.1103/PhysRevLett.111.127201.

[36] D. A. Huse, R. Nandkishore, and V. Oganesyan. Phenomenology of fully many-body-localized systems. *Phys. Rev. B*, 90:174202, 2014. doi:10.1103/PhysRevB.90.174202.

[37] M. Serbyn, M. Knap, S. Gopalakrishnan, Z. Papić, N. Y. Yao, C. R. Laumann, D. A. Abanin, M. D. Lukin, and E. A. Demler. Interferometric Probes of Many-Body Localization. *Phys. Rev. Lett.*, 113:147204, 2014. doi:10.1103/PhysRevLett.113.147204.

[38] J. Z. Imbrie. On Many-Body Localization for Quantum Spin Chains. *Journal of Statistical Physics*, 163(5):998–1048, 2016. doi:10.1007/s10955-016-1508-x.

[39] John Z. Imbrie. Diagonalization and many-body localization for a disordered quantum spin chain. *Phys. Rev. Lett.*, 117:027201, Jul 2016. doi:10.1103/PhysRevLett.117.027201. URL `https://link.aps.org/doi/10.1103/PhysRevLett.117.027201`.

[40] J. Z. Imbrie, V. Ros, and A. Scardicchio. Local integrals of motion in many-body localized systems. *Annalen der Physik*, 529(7):1600278, 2017. doi:10.1002/andp.201600278.

[41] R. P. Feynman. Simulating physics with computers. In *Feynman and computation*, pages 133–153. CRC Press, 2018.

[42] I. Bloch, J. Dalibard, and W. Zwerger. Many-body physics with ultracold gases. *Rev. Mod. Phys.*, 80:885–964, 2008. doi:10.1103/RevModPhys.80.885.

[43] C. Gross and I. Bloch. Quantum simulations with ultracold atoms in optical lattices. *Science*, 357(6355):995–1001, 2017. doi:10.1126/science.aal3837.

[44] H. Häffner, C.F. Roos, and R. Blatt. Quantum computing with trapped ions. *Physics Reports*, 469(4):155–203, 2008. doi:10.1016/j.physrep.2008.09.003.

[45] R. Blatt and C. F. Roos. Quantum simulations with trapped ions. *Nature Physics*, 8 (4):277–284, 2012. doi:10.1038/nphys2252.

[46] C. Monroe, W. C. Campbell, L.-M. Duan, Z.-X. Gong, A. V. Gorshkov, P. W. Hess, R. Islam, K. Kim, N. M. Linke, G. Pagano, P. Richerme, C. Senko, and N. Y. Yao. Programmable quantum simulations of spin systems with trapped ions. *Rev. Mod. Phys.*, 93:025001, 2021. doi:10.1103/RevModPhys.93.025001.

[47] M. H. Devoret, A. Wallraff, and J. M. Martinis. Superconducting Qubits: A Short Review. *arXiv:cond-mat/0411174*, 2004. doi:10.48550/arXiv.cond-mat/0411174.

[48] M. Kjaergaard, M. E. Schwartz, J. Braumüller, P. Krantz, J. I.-J. Wang, S. Gustavsson, and W. D. Oliver. Superconducting Qubits: Current State of Play. *Annual Review of Condensed Matter Physics*, 11(1):369–395, 2020. doi:10.1146/annurev-conmatphys-031119-050605.

[49] D. Loss and D. P. DiVincenzo. Quantum computation with quantum dots. *Phys. Rev. A*, 57:120–126, 1998. doi:10.1103/PhysRevA.57.120.

[50] A. Acín, I. Bloch, H. Buhrman, T. Calarco, C. Eichler, J. Eisert, D. Esteve, N. Gisin, S. J. Glaser, F. Jelezko, S. Kuhr, M. Lewenstein, M. F. Riedel, P. O. Schmidt, R. Thew, A. Wallraff, I. Walmsley, and F. K. Wilhelm. The quantum technologies roadmap: a European community view. *New Journal of Physics*, 20(8):080201, 2018. doi:10.1088/1367-2630/aad1ea.

[51] H. Bernien, S. Schwartz, A. Keesling, H. Levine, A. Omran, H. Pichler, S. Choi, A. S. Zibrov, M. Endres, M. Greiner, V. Vuletić, and M. D. Lukin. Probing many-body dynamics on a 51-atom quantum simulator. *Nature*, 551(7682):579–584, 2017. doi:10.1038/nature24622.

[52] C. J. Turner, A. A. Michailidis, D. A. Abanin, M. Serbyn, and Z. Papić. Weak ergodicity breaking from quantum many-body scars. *Nature Physics*, 14(7):745–749, 2018. doi:10.1038/s41567-018-0137-5.

[53] S. Choi, C. J. Turner, H. Pichler, W. W. Ho, A. A. Michailidis, Z. Papić, M. Serbyn, M. D. Lukin, and D. A. Abanin. Emergent SU(2) Dynamics and Perfect Quantum Many-Body Scars. *Phys. Rev. Lett.*, 122:220603, 2019. doi:10.1103/PhysRevLett.122.220603.

[54] W. W. Ho, S. Choi, H. Pichler, and M. D. Lukin. Periodic Orbits, Entanglement, and Quantum Many-Body Scars in Constrained Models: Matrix Product State Approach. *Phys. Rev. Lett.*, 122:040603, 2019. doi:10.1103/PhysRevLett.122.040603.

[55] C. J. Turner, A. A. Michailidis, D. A. Abanin, M. Serbyn, and Z. Papić. Quantum scarred eigenstates in a Rydberg atom chain: Entanglement, breakdown of thermalization, and stability to perturbations. *Phys. Rev. B*, 98:155134, 2018. doi:10.1103/PhysRevB.98.155134.

[56] S. Ok, K. Choo, C. Mudry, C. Castelnovo, C. Chamon, and T. Neupert. Topological many-body scar states in dimensions one, two, and three. *Phys. Rev. Research*, 1: 033144, 2019. doi:10.1103/PhysRevResearch.1.033144.

[57] M. Schecter and T. Iadecola. Weak Ergodicity Breaking and Quantum Many-Body Scars in Spin-1 XY Magnets. *Phys. Rev. Lett.*, 123:147201, 2019. doi:10.1103/PhysRevLett.123.147201.

[58] S. Mukerjee, V. Oganesyan, and D. Huse. Statistical theory of transport by strongly interacting lattice fermions. *Phys. Rev. B*, 73:035113, 2006. doi:10.1103/PhysRevB.73.035113.

[59] J. Lux, J. Müller, A. Mitra, and A. Rosch. Hydrodynamic long-time tails after a quantum quench. *Phys. Rev. A*, 89:053608, 2014. doi:10.1103/PhysRevA.89.053608.

[60] A. Bohrdt, C. B. Mendl, M. Endres, and M. Knap. Scrambling and thermalization in a diffusive quantum many-body system. *New Journal of Physics*, 19(6):063001, 2017. doi:10.1088/1367-2630/aa719b.

[61] A. Nahum, J. Ruhman, S. Vijay, and J. Haah. Quantum Entanglement Growth under Random Unitary Dynamics. *Phys. Rev. X*, 7:031016, 2017. doi:10.1103/PhysRevX.7.031016.

[62] T. Rakovszky, F. Pollmann, and C. W. von Keyserlingk. Sub-ballistic Growth of Rényi Entropies due to Diffusion. *Phys. Rev. Lett.*, 122:250602, 2019. doi:10.1103/PhysRevLett.122.250602.

[63] A. Nahum, S. Vijay, and J. Haah. Operator Spreading in Random Unitary Circuits. *Phys. Rev. X*, 8:021014, 2018. doi:10.1103/PhysRevX.8.021014.

[64] C. W. von Keyserlingk, T. Rakovszky, F. Pollmann, and S. L. Sondhi. Operator Hydrodynamics, OTOCs, and Entanglement Growth in Systems without Conservation Laws. *Phys. Rev. X*, 8:021013, 2018. doi:10.1103/PhysRevX.8.021013.

[65] V. Khemani, A. Vishwanath, and D. A. Huse. Operator Spreading and the Emergence of Dissipative Hydrodynamics under Unitary Evolution with Conservation Laws. *Phys. Rev. X*, 8:031057, 2018. doi:10.1103/PhysRevX.8.031057.

[66] T. Rakovszky, F. Pollmann, and C. W. von Keyserlingk. Diffusive Hydrodynamics of Out-of-Time-Ordered Correlators with Charge Conservation. *Phys. Rev. X*, 8: 031058, 2018. doi:10.1103/PhysRevX.8.031058.

[67] A. Chan, A. De Luca, and J. T. Chalker. Solution of a Minimal Model for Many-Body Quantum Chaos. *Phys. Rev. X*, 8:041019, 2018. doi:10.1103/PhysRevX.8.041019.

[68] A. J. Friedman, A. Chan, A. De Luca, and J. T. Chalker. Spectral Statistics and Many-Body Quantum Chaos with Conserved Charge. *Phys. Rev. Lett.*, 123:210603, 2019. doi:10.1103/PhysRevLett.123.210603.

[69] R. M. Nandkishore and M. Hermele. Fractons. *Annual Review of Condensed Matter Physics*, 10(1):295–313, 2019. doi:10.1146/annurev-conmatphys-031218-013604.

[70] M. Pretko, X. Chen, and Y. You. Fracton phases of matter. *International Journal of Modern Physics A*, 35(06):2030003, 2020. doi:10.1142/S0217751X20300033.

[71] J. M. Deutsch. Quantum statistical mechanics in a closed system. *Phys. Rev. A*, 43: 2046–2049, 1991. doi:10.1103/PhysRevA.43.2046.

[72] R. P. Feynman. *Statistical mechanics: a set of lectures*. CRC press, 2018.

[73] Y. G. Sinai. On the foundations of the ergodic hypothesis for a dynamical system of statistical mechanics. In *Doklady Akademii Nauk*, volume 153, pages 1261–1264. Russian Academy of Sciences, 1963.

[74] Y. G. Sinai. Dynamical systems with elastic reflections. *Russian Mathematical Surveys*, 25(2):137–189, 1970. doi:10.1070/rm1970v025n02abeh003794.

[75] L. A. Bunimovich. On the ergodic properties of nowhere dispersing billiards. *Communications in Mathematical Physics*, 65(3):295–312, 1979. doi:10.1007/BF01197884.

[76] N. Simányi. Proof of the Ergodic Hypothesis for Typical Hard Ball Systems. *Annales Henri Poincaré*, 5(2):203–233, 2004. doi:10.1007/s00023-004-0166-8.

[77] A. J. Lichtenberg and M. A. Lieberman. *Regular and chaotic dynamics*, volume 38. Springer Science & Business Media, 2013.

[78] M. L. Mehta. *Random matrices*. Elsevier, 2004.

[79] E. P. Wigner. Characteristic Vectors of Bordered Matrices with Infinite Dimensions. *Annals of Mathematics*, 62(2):548–564, 1955. doi:10.2307/1970079.

[80] E. P. Wigner. Characteristics vectors of bordered matrices with infinite dimensions ii. *Annals of Mathematics*, 65(2):203–207, 1957. doi:10.2307/1969956.

[81] Eugene P. Wigner. On the distribution of the roots of certain symmetric matrices. *Annals of Mathematics*, 67(2):325–327, 1958. doi:10.2307/1970008.

[82] F. J. Dyson. Statistical Theory of the Energy Levels of Complex Systems. I. *Journal of Mathematical Physics*, 3(1):140–156, 1962. doi:10.1063/1.1703773.

[83] O. Bohigas, M. J. Giannoni, and C. Schmit. Characterization of Chaotic Quantum Spectra and Universality of Level Fluctuation Laws. *Phys. Rev. Lett.*, 52:1–4, 1984. doi:10.1103/PhysRevLett.52.1.

[84] M. V. Berry and M. Tabor. Level clustering in the regular spectrum. *Proceedings of the Royal Society of London. A. Mathematical and Physical Sciences*, 356(1686):375–394, 1977. doi:10.1098/rspa.1977.0140.

[85] S. Müller, S. Heusler, P. Braun, F. Haake, and A. Altland. Semiclassical Foundation of Universality in Quantum Chaos. *Phys. Rev. Lett.*, 93:014103, 2004. doi:10.1103/PhysRevLett.93.014103.

[86] B. Bertini, P. Kos, and T. Prosen. Exact Spectral Form Factor in a Minimal Model of Many-Body Quantum Chaos. *Phys. Rev. Lett.*, 121:264101, 2018. doi:10.1103/PhysRevLett.121.264101.

[87] A. Chan, A. De Luca, and J. T. Chalker. Spectral Statistics in Spatially Extended Chaotic Quantum Many-Body Systems. *Phys. Rev. Lett.*, 121:060601, 2018. doi:10.1103/PhysRevLett.121.060601.

[88] E. J. Torres-Herrera and L. F. Santos. Dynamical manifestations of quantum chaos: correlation hole and bulge. *Philosophical Transactions of the Royal Society A: Mathematical, Physical and Engineering Sciences*, 375(2108):20160434, 2017. doi:10.1098/rsta.2016.0434.

[89] M. Schiulaz, E. J. Torres-Herrera, and L. F. Santos. Thouless and relaxation time scales in many-body quantum systems. *Phys. Rev. B*, 99:174313, 2019. doi:10.1103/PhysRevB.99.174313.

[90] M. V. Berry. Regular and irregular semiclassical wavefunctions. *Journal of Physics A: Mathematical and General*, 10(12):2083–2091, 1977. doi:10.1088/0305-4470/10/12/016.

[91] S. Lloyd. Pure state quantum statistical mechanics and black holes. *arXiv:1307.0378*, 2013. doi:10.48550/arXiv.1307.0378.

[92] S. Goldstein, J. L. Lebowitz, R. Tumulka, and N. Zanghì. Canonical Typicality. *Phys. Rev. Lett.*, 96:050403, 2006. doi:10.1103/PhysRevLett.96.050403.

[93] S. Popescu, A. J. Short, and A. Winter. Entanglement and the foundations of statistical mechanics. *Nature Physics*, 2(11):754–758, 2006. doi:10.1038/nphys444.

[94] P. Reimann. Typicality for Generalized Microcanonical Ensembles. *Phys. Rev. Lett.*, 99:160404, 2007. doi:10.1103/PhysRevLett.99.160404.

[95] J. Gemmer, M. Michel, and G. Mahler. *Quantum thermodynamics: Emergence of thermodynamic behavior within composite quantum systems*, volume 784. Springer, 2009.

[96] S. Sugiura and A. Shimizu. Canonical Thermal Pure Quantum State. *Phys. Rev. Lett.*, 111:010401, 2013. doi:10.1103/PhysRevLett.111.010401.

[97] T. Heitmann, J. Richter, D. Schubert, and R. Steinigeweg. Selected applications of typicality to real-time dynamics of quantum many-body systems. *Zeitschrift für Naturforschung A*, 75(5):421–432, 2020. doi:10.1515/zna-2020-0010.

[98] M. Kolodrubetz, D. Sels, P. Mehta, and A. Polkovnikov. Geometry and non-adiabatic response in quantum and classical systems. *Physics Reports*, 697:1–87, 2017. doi:10.1016/j.physrep.2017.07.001.

[99] M. Pandey, P. W. Claeys, D. K. Campbell, A. Polkovnikov, and D. Sels. Adiabatic Eigenstate Deformations as a Sensitive Probe for Quantum Chaos. *Phys. Rev. X*, 10: 041017, 2020. doi:10.1103/PhysRevX.10.041017.

[100] J. v. Neumann. Beweis des Ergodensatzes und desH-Theorems in der neuen Mechanik. *Zeitschrift für Physik*, 57(1):30–70, 1929. doi:10.1007/BF01339852.

[101] M. Rigol and M. Srednicki. Alternatives to Eigenstate Thermalization. *Phys. Rev. Lett.*, 108:110601, 2012. doi:10.1103/PhysRevLett.108.110601.

[102] H. Gharibyan, M. Hanada, S. H. Shenker, and M. Tezuka. Onset of random matrix behavior in scrambling systems. *Journal of High Energy Physics*, 2018(7):124, 2018. doi:10.1007/JHEP07(2018)124.

[103] S. Moudgalya, A. Prem, D. A. Huse, and A. Chan. Spectral statistics in constrained many-body quantum chaotic systems. *Phys. Rev. Research*, 3:023176, 2021. doi:10.1103/PhysRevResearch.3.023176.

[104] Singh, H. and Ware, B. A. and Vasseur, R. and Friedman, A. J. Subdiffusion and Many-Body Quantum Chaos with Kinetic Constraints. *Phys. Rev. Lett.*, 127:230602, 2021. doi:10.1103/PhysRevLett.127.230602.

[105] M. Winer and B. Swingle. Hydrodynamic Theory of the Connected Spectral form Factor. *Phys. Rev. X*, 12:021009, 2022. doi:10.1103/PhysRevX.12.021009.

[106] M. Rigol. Quantum quenches and thermalization in one-dimensional fermionic systems. *Phys. Rev. A*, 80:053607, 2009. doi:10.1103/PhysRevA.80.053607.

[107] L. F. Santos and M. Rigol. Onset of quantum chaos in one-dimensional bosonic and fermionic systems and its relation to thermalization. *Phys. Rev. E*, 81:036206, 2010. doi:10.1103/PhysRevE.81.036206.

[108] M. Rigol and L. F. Santos. Quantum chaos and thermalization in gapped systems. *Phys. Rev. A*, 82:011604, 2010. doi:10.1103/PhysRevA.82.011604.

[109] L. F. Santos and M. Rigol. Localization and the effects of symmetries in the thermalization properties of one-dimensional quantum systems. *Phys. Rev. E*, 82:031130, 2010. doi:10.1103/PhysRevE.82.031130.

[110] H. Kim, T. N. Ikeda, and D. A. Huse. Testing whether all eigenstates obey the eigenstate thermalization hypothesis. *Phys. Rev. E*, 90:052105, 2014. doi:10.1103/PhysRevE.90.052105.

[111] W. Beugeling, R. Moessner, and Masudul Haque. Finite-size scaling of eigenstate thermalization. *Phys. Rev. E*, 89:042112, 2014. doi:10.1103/PhysRevE.89.042112.

[112] W. Beugeling, R. Moessner, and M. Haque. Off-diagonal matrix elements of local operators in many-body quantum systems. *Phys. Rev. E*, 91:012144, 2015. doi:10.1103/PhysRevE.91.012144.

[113] R. Mondaini, K. R. Fratus, M. Srednicki, and M. Rigol. Eigenstate thermalization in the two-dimensional transverse field Ising model. *Phys. Rev. E*, 93:032104, 2016. doi:10.1103/PhysRevE.93.032104.

[114] G. Biroli, C. Kollath, and A. M. Läuchli. Effect of Rare Fluctuations on the Thermalization of Isolated Quantum Systems. *Phys. Rev. Lett.*, 105:250401, 2010. doi:10.1103/PhysRevLett.105.250401.

[115] S. Sorg, L. Vidmar, L. Pollet, and F. Heidrich-Meisner. Relaxation and thermalization in the one-dimensional Bose-Hubbard model: A case study for the interaction quantum quench from the atomic limit. *Phys. Rev. A*, 90:033606, 2014. doi:10.1103/PhysRevA.90.033606.

[116] T. Kinoshita, T. Wenger, and D. S. Weiss. A quantum Newton's cradle. *Nature*, 440: 900–3, 05 2006. doi:10.1038/nature04693.

[117] F. H. L. Essler and M. Fagotti. Quench dynamics and relaxation in isolated integrable quantum spin chains. *Journal of Statistical Mechanics: Theory and Experiment*, 2016(6):064002, 2016. doi:10.1088/1742-5468/2016/06/064002.

[118] J. Eisert, M. Friesdorf, and C. Gogolin. Quantum many-body systems out of equilibrium. *Nature Physics*, 11(2):124–130, 2015. doi:10.1038/nphys3215.

[119] L. Vidmar and M. Rigol. Generalized gibbs ensemble in integrable lattice models. *Journal of Statistical Mechanics: Theory and Experiment*, 2016(6):064007, 2016. doi:10.1088/1742-5468/2016/06/064007.

[120] P. W. Anderson. Absence of Diffusion in Certain Random Lattices. *Physical Review*, 109(5):1492–1505, 1958. doi:10.1103/PhysRev.109.1492.

[121] A. Lagendijk, B. Van Tiggelen, and D. S. Wiersma. Fifty years of Anderson localization. *Phys. Today*, 62(8):24–29, 2009.

[122] D. A. Huse, R. Nandkishore, V. Oganesyan, A. Pal, and S. L. Sondhi. Localization-protected quantum order. *Phys. Rev. B*, 88:014206, 2013. doi:10.1103/PhysRevB.88.014206.

[123] A. Chandran, V. Khemani, C. R. Laumann, and S. L. Sondhi. Many-body localization and symmetry-protected topological order. *Phys. Rev. B*, 89:144201, 2014. doi:10.1103/PhysRevB.89.144201.

[124] S. A. Parameswaran and R. Vasseur. Many-body localization, symmetry and topology. *Reports on Progress in Physics*, 81(8):082501, 2018. doi:10.1088/1361-6633/aac9ed.

[125] F. Wilczek. Quantum Time Crystals. *Phys. Rev. Lett.*, 109:160401, 2012. doi:10.1103/PhysRevLett.109.160401.

[126] D. V. Else, B. Bauer, and C. Nayak. Floquet Time Crystals. *Phys. Rev. Lett.*, 117: 090402, 2016. doi:10.1103/PhysRevLett.117.090402.

[127] V. Khemani, A. Lazarides, R. Moessner, and S. L. Sondhi. Phase Structure of Driven Quantum Systems. *Phys. Rev. Lett.*, 116:250401, 2016. doi:10.1103/PhysRevLett.116.250401.

[128] N. Y. Yao, A. C. Potter, I.-D. Potirniche, and A. Vishwanath. Discrete Time Crystals: Rigidity, Criticality, and Realizations. *Phys. Rev. Lett.*, 118:030401, 2017. doi:10.1103/PhysRevLett.118.030401.

[129] D. V. Else, C. Monroe, C. Nayak, and N. Y. Yao. Discrete Time Crystals. *Annual Review of Condensed Matter Physics*, 11(1):467–499, 2020. doi:10.1146/annurev-conmatphys-031119-050658.

[130] J. Randall, C. E. Bradley, F. V. van der Gronden, A. Galicia, M. H. Abobeih, M. Markham, D. J. Twitchen, F. Machado, N. Y. Yao, and T. H. Taminiau. Many-body-localized discrete time crystal with a programmable spin-based quantum simulator. *Science*, 374(6574):1474–1478, 2021. doi:10.1126/science.abk0603.

[131] R. Vosk, D. A. Huse, and E. Altman. Theory of the Many-Body Localization Transition in One-Dimensional Systems. *Physical Review X*, 5:031032, 2015. doi:10.1103/PhysRevX.5.031032.

[132] K. Agarwal, S. Gopalakrishnan, M. Knap, M. Müller, and E. Demler. Anomalous Diffusion and Griffiths Effects Near the Many-Body Localization Transition. *Physical Review Letters*, 114:160401, 2015. doi:10.1103/PhysRevLett.114.160401.

[133] A. C. Potter, R. Vasseur, and S. A. Parameswaran. Universal Properties of Many-Body Delocalization Transitions. *Physical Review X*, 5(3), 2015. doi:10.1103/PhysRevX.5.031033.

[134] Y. Bar Lev, G. Cohen, and D. R. Reichman. Absence of Diffusion in an Interacting System of Spinless Fermions on a One-Dimensional Disordered Lattice. *Phys. Rev. Lett.*, 114:100601, 2015. doi:10.1103/PhysRevLett.114.100601.

[135] D. J. Luitz, N. Laflorencie, and F. Alet. Extended slow dynamical regime close to the many-body localization transition. *Phys. Rev. B*, 93:060201, 2016. doi:10.1103/PhysRevB.93.060201.

[136] M. Žnidarič, A. Scardicchio, and V. K. Varma. Diffusive and Subdiffusive Spin Transport in the Ergodic Phase of a Many-Body Localizable System. *Physical Review Letters*, 117:040601, 2016. doi:10.1103/PhysRevLett.117.040601.

[137] S. Gopalakrishnan and S.A. Parameswaran. Dynamics and transport at the threshold of many-body localization. *Physics Reports*, 862:1–62, 2020. doi:10.1016/j.physrep.2020.03.003.

[138] W. De Roeck and F. Huveneers. Stability and instability towards delocalization in many-body localization systems. *Phys. Rev. B*, 95:155129, 2017. doi:10.1103/PhysRevB.95.155129.

[139] I.-D. Potirniche, S. Banerjee, and E. Altman. Exploration of the stability of many-body localization in $d > 1$. *Phys. Rev. B*, 99:205149, 2019. doi:10.1103/PhysRevB.99.205149.

[140] T. B. Wahl, A. Pal, and S. H. Simon. Signatures of the many-body localized regime in two dimensions. *Nature Physics*, 15(2):164–169, 2019. doi:10.1038/s41567-018-0339-x.

[141] J.-Y. Choi, S. Hild, J. Zeiher, P. Schauss, A. Rubio-Abadal, T. Yefsah, V. Khemani, D. A. Huse, I. Bloch, and C. Gross. Exploring the many-body localization transition in two dimensions. *Science*, 352(6293):1547–1552, 2016. doi:10.1126/science.aaf8834.

[142] M. H. Fischer, M. Maksymenko, and E. Altman. Dynamics of a Many-Body-Localized System Coupled to a Bath. *Phys. Rev. Lett.*, 116:160401, 2016. doi:10.1103/PhysRevLett.116.160401.

[143] E. Levi, M. Heyl, I. Lesanovsky, and J. P. Garrahan. Robustness of Many-Body Localization in the Presence of Dissipation. *Phys. Rev. Lett.*, 116:237203, 2016. doi:10.1103/PhysRevLett.116.237203.

[144] M. V. Medvedyeva, T. Prosen, and M. Žnidarič. Influence of dephasing on many-body localization. *Phys. Rev. B*, 93:094205, 2016. doi:10.1103/PhysRevB.93.094205.

[145] B. Everest, I. Lesanovsky, J. P. Garrahan, and E. Levi. Role of interactions in a dissipative many-body localized system. *Phys. Rev. B*, 95:024310, 2017. doi:10.1103/PhysRevB.95.024310.

[146] S. Gopalakrishnan, K. R. Islam, and M. Knap. Noise-Induced Subdiffusion in Strongly Localized Quantum Systems. *Phys. Rev. Lett.*, 119:046601, 2017. doi:10.1103/PhysRevLett.119.046601.

[147] I. Vakulchyk, I. Yusipov, M. Ivanchenko, S. Flach, and S. Denisov. Signatures of many-body localization in steady states of open quantum systems. *Phys. Rev. B*, 98: 020202, 2018. doi:10.1103/PhysRevB.98.020202.

[148] E. Wybo, M. Knap, and F. Pollmann. Entanglement dynamics of a many-body localized system coupled to a bath. *Phys. Rev. B*, 102:064304, 2020. doi:10.1103/PhysRevB.102.064304.

[149] J. P. Garrahan. Aspects of non-equilibrium in classical and quantum systems: Slow relaxation and glasses, dynamical large deviations, quantum non-ergodicity, and open quantum dynamics. *Physica A: Statistical Mechanics and its Applications*, 504: 130 – 154, 2018. doi:https://doi.org/10.1016/j.physa.2017.12.149.

[150] F. Ritort and P. Sollich. Glassy dynamics of kinetically constrained models. *Advances in Physics*, 52(4):219–342, 2003. doi:10.1080/0001873031000093582.

[151] G. H. Fredrickson and H. C. Andersen. Kinetic Ising Model of the Glass Transition. *Phys. Rev. Lett.*, 53:1244–1247, 1984. doi:10.1103/PhysRevLett.53.1244.

[152] J. Jäckle and S. Eisinger. A hierarchically constrained kinetic Ising model. *Zeitschrift für Physik B Condensed Matter*, 84(1):115–124, 1991. doi:10.1007/BF01453764.

[153] L. Berthier, G. Biroli, J.-P. Bouchaud, L. Cipelletti, and W. van Saarloos. *Dynamical heterogeneities in glasses, colloids, and granular media*, volume 150. Oxford University Press, 2011.

[154] D. Chandler and J. P. Garrahan. Dynamics on the Way to Forming Glass: Bubbles in Space-Time. *Annual Review of Physical Chemistry*, 61(1):191–217, 2010. doi:10.1146/annurev.physchem.040808.090405.

[155] V. Lubchenko and P. G. Wolynes. Theory of Structural Glasses and Supercooled Liquids. *Annual Review of Physical Chemistry*, 58(1):235–266, 2007. doi:10.1146/annurev.physchem.58.032806.104653.

[156] G. Parisi and F. Zamponi. Mean-field theory of hard sphere glasses and jamming. *Rev. Mod. Phys.*, 82:789–845, 2010. doi:10.1103/RevModPhys.82.789.

[157] P. Charbonneau, J. Kurchan, G. Parisi, P. Urbani, and F. Zamponi. Glass and Jamming Transitions: From Exact Results to Finite-Dimensional Descriptions. *Annual Review of Condensed Matter Physics*, 8(1):265–288, 2017. doi:10.1146/annurev-conmatphys-031016-025334.

[158] C. Castelnovo and C. Chamon. Topological quantum glassiness. *Philosophical Magazine*, 92(1-3):304–323, 2012. doi:10.1080/14786435.2011.609152.

[159] M. van Horssen, E. Levi, and J. P. Garrahan. Dynamics of many-body localization in a translation-invariant quantum glass model. *Phys. Rev. B*, 92:100305, 2015. doi:10.1103/PhysRevB.92.100305.

[160] Z. Lan, M. van Horssen, S. Powell, and J. P. Garrahan. Quantum Slow Relaxation and Metastability due to Dynamical Constraints. *Phys. Rev. Lett.*, 121:040603, Jul 2018. doi:10.1103/PhysRevLett.121.040603. URL `https://link.aps.org/doi/10.1103/PhysRevLett.121.040603`.

[161] N. Pancotti, G. Giudice, J. I. Cirac, J. P. Garrahan, and M. C. Bañuls. Quantum East Model: Localization, Nonthermal Eigenstates, and Slow Dynamics. *Phys. Rev. X*, 10:021051, 2020. doi:10.1103/PhysRevX.10.021051.

[162] T. Grover and M. P. A. Fisher. Quantum disentangled liquids. *Journal of Statistical Mechanics: Theory and Experiment*, 2014(10):P10010, 2014. doi:10.1088/1742-5468/2014/10/p10010.

[163] M. Schiulaz and M. Müller. Ideal quantum glass transitions: Many-body localization without quenched disorder. *AIP Conference Proceedings*, 1610(1):11–23, 2014. doi:10.1063/1.4893505.

[164] M. Schiulaz, A. Silva, and M. Müller. Dynamics in many-body localized quantum systems without disorder. *Phys. Rev. B*, 91:184202, 2015. doi:10.1103/PhysRevB.91.184202.

[165] W. De Roeck and F. Huveneers. Scenario for delocalization in translation-invariant systems. *Phys. Rev. B*, 90:165137, 2014. doi:10.1103/PhysRevB.90.165137.

[166] Z. Papić, E. Miles Stoudenmire, and Dmitry A. Abanin. Many-body localization in disorder-free systems: The importance of finite-size constraints. *Annals of Physics*, 362:714 – 725, 2015. doi:10.1016/j.aop.2015.08.024.

[167] F. Jin, R. Steinigeweg, F. Heidrich-Meisner, K. Michielsen, and H. De Raedt. Finite-temperature charge transport in the one-dimensional Hubbard model. *Phys. Rev. B*, 92:205103, 2015. doi:10.1103/PhysRevB.92.205103.

[168] N. Y. Yao, C. R. Laumann, J. I. Cirac, M. D. Lukin, and J. E. Moore. Quasi-many-body localization in translation-invariant systems. *Phys. Rev. Lett.*, 117:240601, 2016. doi:10.1103/PhysRevLett.117.240601.

[169] A. A. Michailidis, M. Žnidarič, M. Medvedyeva, D. A. Abanin, T. Prosen, and Z. Papić. Slow dynamics in translation-invariant quantum lattice models. *Phys. Rev. B*, 97:104307, 2018. doi:10.1103/PhysRevB.97.104307.

[170] J. Sirker. Exploration of the existence of a distinct quasi many-body localized phase: Numerical study of a translationally invariant system in the thermodynamic limit. *Phys. Rev. B*, 99:075162, 2019. doi:10.1103/PhysRevB.99.075162.

[171] T. Heitmann, J. Richter, T. Dahm, and R. Steinigeweg. Density dynamics in the mass-imbalanced Hubbard chain. *Phys. Rev. B*, 102:045137, 2020. doi:10.1103/PhysRevB.102.045137.

[172] N. D. Oppong, G. Pasqualetti, O. Bettermann, P. Zechmann, M. Knap, I. Bloch, and S. Fölling. Probing transport and slow relaxation in the mass-imbalanced Fermi-Hubbard model. *arXiv:2011.12411*, 2020. doi:10.48550/arXiv.2011.12411.

[173] Philip Zechmann, Alvise Bastianello, and Michael Knap. Tunable transport in the mass-imbalanced fermi-hubbard model, 2022. URL `https://arxiv.org/abs/2205.12970`.

[174] A. Smith, J. Knolle, D. L. Kovrizhin, and R. Moessner. Disorder-Free Localization. *Phys. Rev. Lett.*, 118:266601, 2017. doi:10.1103/PhysRevLett.118.266601.

[175] M. Brenes, M. Dalmonte, M. Heyl, and A. Scardicchio. Many-Body Localization Dynamics from Gauge Invariance. *Phys. Rev. Lett.*, 120:030601, 2018. doi:10.1103/PhysRevLett.120.030601.

[176] A. Smith, J. Knolle, R. Moessner, and D. L. Kovrizhin. Absence of Ergodicity without Quenched Disorder: From Quantum Disentangled Liquids to Many-Body Localization. *Phys. Rev. Lett.*, 119:176601, 2017. doi:10.1103/PhysRevLett.119.176601.

[177] A. Metavitsiadis, A. Pidatella, and W. Brenig. Thermal transport in a two-dimensional $\mathbb{Z}_2$ spin liquid. *Phys. Rev. B*, 96:205121, 2017. doi:10.1103/PhysRevB.96.205121.

[178] A. Smith, J. Knolle, R. Moessner, and D. L. Kovrizhin. Dynamical localization in $\mathbb{Z}_2$ lattice gauge theories. *Phys. Rev. B*, 97:245137, 2018. doi:10.1103/PhysRevB.97.245137.

[179] A. Russomanno, S. Notarnicola, F. M. Surace, R. Fazio, M. Dalmonte, and M. Heyl. Homogeneous Floquet time crystal protected by gauge invariance. *Phys. Rev. Research*, 2:012003, 2020. doi:10.1103/PhysRevResearch.2.012003.

[180] O. Hart, S. Gopalakrishnan, and C. Castelnovo. Logarithmic Entanglement Growth from Disorder-Free Localization in the Two-Leg Compass Ladder. *Phys. Rev. Lett.*, 126:227202, 2021. doi:10.1103/PhysRevLett.126.227202.

[181] B. Bertini, F. Heidrich-Meisner, C. Karrasch, T. Prosen, R. Steinigeweg, and M. Znidaric. Finite-temperature transport in one-dimensional quantum lattice models. *Reviews of Modern Physics*, 93(2):025003, 2021. doi:10.1103/RevModPhys.93.025003.

[182] O. A. Castro-Alvaredo, B. Doyon, and T. Yoshimura. Emergent Hydrodynamics in Integrable Quantum Systems Out of Equilibrium. *Phys. Rev. X*, 6:041065, 2016. doi:10.1103/PhysRevX.6.041065.

[183] B. Bertini, M. Collura, J. De Nardis, and M. Fagotti. Transport in Out-of-Equilibrium XXZ Chains: Exact Profiles of Charges and Currents. *Phys. Rev. Lett.*, 117:207201, 2016. doi:10.1103/PhysRevLett.117.207201.

[184] E. Leviatan, F. Pollmann, J. H. Bardarson, D. A. Huse, and E. Altman. Quantum thermalization dynamics with Matrix-Product States. *arXiv:1702.08894*, 2017. doi:10.48550/arXiv.1702.08894.

[185] H. Spohn. Nonlinear Fluctuating Hydrodynamics for Anharmonic Chains. *Journal of Statistical Physics*, 154(5):1191–1227, 2014. doi:10.1007/s10955-014-0933-y.

[186] C. D. White, M. Zaletel, R. S. K. Mong, and G. Refael. Quantum dynamics of thermalizing systems. *Phys. Rev. B*, 97:035127, 2018. doi:10.1103/PhysRevB.97.035127.

[187] B. Ye, F. Machado, C. D. White, R. S.K. Mong, and N. Y. Yao. Emergent Hydrodynamics in Nonequilibrium Quantum Systems. *Physical Review Letters*, 125(3), 2020. doi:10.1103/PhysRevLett.125.030601.

[188] B. Ye, F. Machado, J. Kemp, R. B. Hutson, and Y. Yao, N. Universal Kardar-Parisi-Zhang dynamics in integrable quantum systems. *arXiv:2205.02853*, 2022. doi:10.48550/arXiv.2205.02853.

[189] D. E. Parker, X. Cao, A. Avdoshkin, T. Scaffidi, and E. Altman. A Universal Operator Growth Hypothesis. *Phys. Rev. X*, 9:041017, 2019. doi:10.1103/PhysRevX.9.041017.

[190] T. K. Kvorning, L. Herviou, and J. H. Bardarson. Time-evolution of local information: thermalization dynamics of local observables. *arXiv:2105.11206*, 2021. doi:10.48550/arXiv.2105.11206.

[191] T. Rakovszky, C. W. von Keyserlingk, and F. Pollmann. Dissipation-assisted operator evolution method for capturing hydrodynamic transport. *Phys. Rev. B*, 105: 075131, 2022. doi:10.1103/PhysRevB.105.075131.

[192] C. von Keyserlingk, F. Pollmann, and T. Rakovszky. Operator backflow and the classical simulation of quantum transport. *Phys. Rev. B*, 105:245101, 2022. doi:10.1103/PhysRevB.105.245101.

[193] C. Cao, E. Elliott, J. Joseph, H. Wu, J. Petricka, T. Schäfer, and J. E. Thomas. Universal Quantum Viscosity in a Unitary Fermi Gas. *Science*, 331(6013):58–61, 2011. doi:10.1126/science.1195219.

[194] A. Sommer, M. Ku, G. Roati, and M. W. Zwierlein. Universal spin transport in a strongly interacting Fermi gas. *Nature*, 472(7342):201–204, 2011. doi:10.1038/nature09989.

[195] U. Schneider, L. Hackermüller, J. P. Ronzheimer, S. Will, S. Braun, T. Best, I. Bloch, E. Demler, S. Mandt, D. Rasch, and A. Rosch. Fermionic transport and out-of-equilibrium dynamics in a homogeneous Hubbard model with ultracold atoms. *Nature Physics*, 8(3):213–218, 2012. doi:10.1038/nphys2205.

[196] P. T. Brown, D. Mitra, E. Guardado-Sanchez, R. Nourafkan, A. Reymbaut, C.-D. Hébert, S. Bergeron, A.-M. S. Tremblay, J. Kokalj, D. A. Huse, P. Schauß, and W. S. Bakr. Bad metallic transport in a cold atom Fermi-Hubbard system. *Science*, 363 (6425):379–382, 2019. doi:10.1126/science.aat4134.

[197] E. Guardado-Sanchez, A. Morningstar, B. M. Spar, P. T. Brown, D. A. Huse, and W. S. Bakr. Subdiffusion and Heat Transport in a Tilted Two-Dimensional Fermi-Hubbard System. *Phys. Rev. X*, 10:011042, 2020. doi:10.1103/PhysRevX.10.011042.

[198] M. K. Joshi, F. Kranzl, A. Schuckert, I. Lovas, C. Maier, R. Blatt, M. Knap, and C. F. Roos. Observing emergent hydrodynamics in a long-range quantum magnet. *Science*, 376(6594):720–724, 2022. doi:10.1126/science.abk2400.

[199] D. Wei, A. Rubio-Abadal, B. Ye, F. Machado, J. Kemp, K. Srakaew, S. Hollerith, J. Rui, S. Gopalakrishnan, N. Y. Yao, I. Bloch, and J. Zeiher. Quantum gas microscopy of Kardar-Parisi-Zhang superdiffusion. *Science*, 376(6594):716–720, 2022. doi:10.1126/science.abk2397.

[200] P. N. Jepsen, J. Amato-Grill, I. Dimitrova, W. W. Ho, E. Demler, and W. Ketterle. Spin transport in a tunable Heisenberg model realized with ultracold atoms. *Nature*, 588 (7838):403–407, 2020. doi:10.1038/s41586-020-3033-y.

[201] D. A. Bandurin, I. Torre, R. Krishna Kumar, M. Ben Shalom, A. Tomadin, A. Principi, G. H. Auton, E. Khestanova, K. S. Novoselov, I. V. Grigorieva, L. A. Ponomarenko, A. K. Geim, and M. Polini. Negative local resistance caused by viscous electron backflow in graphene. *Science*, 351(6277):1055–1058, 2016. doi:10.1126/science.aad0201.

[202] J. Crossno, J. K. Shi, K. Wang, X. Liu, A. Harzheim, A. Lucas, S. Sachdev, P. Kim, T. Taniguchi, K. Watanabe, T. A. Ohki, and K. C. Fong. Observation of the Dirac fluid and the breakdown of the Wiedemann-Franz law in graphene. *Science*, 351 (6277):1058–1061, 2016. doi:10.1126/science.aad0343.

[203] P. J. W. Moll, P. Kushwaha, N. Nandi, B. Schmidt, and A. P. Mackenzie. Evidence for hydrodynamic electron flow in $PdCoO_2$. *Science*, 351(6277):1061–1064, 2016. doi:10.1126/science.aac8385.

[204] C. Zu, F. Machado, B. Ye, S. Choi, B. Kobrin, T. Mittiga, S. Hsieh, P. Bhattacharyya, M. Markham, D. Twitchen, A. Jarmola, D. Budker, C. R. Laumann, J. E. Moore, and N. Y. Yao. Emergent hydrodynamics in a strongly interacting dipolar spin ensemble. *Nature*, 597(7874):45–50, 2021. doi:10.1038/s41586-021-03763-1.

[205] J. Iaconis, S. Vijay, and R. Nandkishore. Anomalous subdiffusion from subsystem symmetries. *Phys. Rev. B*, 100:214301, 2019. doi:10.1103/PhysRevB.100.214301.

[206] A. Morningstar, V. Khemani, and D. A. Huse. Kinetically constrained freezing transition in a dipole-conserving system. *Phys. Rev. B*, 101:214205, 2020. doi:10.1103/PhysRevB.101.214205.

[207] J. Iaconis, A. Lucas, and R. Nandkishore. Multipole conservation laws and subdiffusion in any dimension. *Phys. Rev. E*, 103:022142, 2021. doi:10.1103/PhysRevE.103.022142.

[208] S. H. Shenker and D. Stanford. Black holes and the butterfly effect. *Journal of High Energy Physics*, 2014(3):67, 2014. doi:10.1007/JHEP03(2014)067.

[209] S. H. Shenker and D. Stanford. Multiple shocks. *Journal of High Energy Physics*, 2014 (12):46, 2014. doi:10.1007/JHEP12(2014)046.

[210] D. A. Roberts, D. Stanford, and L. Susskind. Localized shocks. *Journal of High Energy Physics*, 2015(3):51, 2015. doi:10.1007/JHEP03(2015)051.

[211] D. A. Roberts and D. Stanford. Diagnosing Chaos Using Four-Point Functions in Two-Dimensional Conformal Field Theory. *Phys. Rev. Lett.*, 115:131603, 2015. doi:10.1103/PhysRevLett.115.131603.

[212] A. Larkin and Y. N. Ovchinnikov. Quasiclassical method in the theory of superconductivity. *Sov Phys JETP*, 28(6):1200–1205, 1969.

[213] J. S. Cotler, D. Ding, and G. R. Penington. Out-of-time-order operators and the butterfly effect. *Annals of Physics*, 396:318–333, 2018. doi:https://doi.org/10.1016/j.aop.2018.07.020.

[214] I. L. Aleiner, L. Faoro, and L. B. Ioffe. Microscopic model of quantum butterfly effect: Out-of-time-order correlators and traveling combustion waves. *Annals of Physics*, 375:378–406, 2016. doi:https://doi.org/10.1016/j.aop.2016.09.006.

[215] D. Chowdhury and B. Swingle. Onset of many-body chaos in the $O(N)$ model. *Phys. Rev. D*, 96:065005, 2017. doi:10.1103/PhysRevD.96.065005.

[216] V. Khemani, D. A. Huse, and A. Nahum. Velocity-dependent Lyapunov exponents in many-body quantum, semiclassical, and classical chaos. *Phys. Rev. B*, 98:144304, 2018. doi:10.1103/PhysRevB.98.144304.

[217] A. Das, S. Chakrabarty, A. Dhar, A. Kundu, D. A. Huse, R. Moessner, S. S. Ray, and S. Bhattacharjee. Light-Cone Spreading of Perturbations and the Butterfly Effect in a Classical Spin Chain. *Phys. Rev. Lett.*, 121:024101, 2018. doi:10.1103/PhysRevLett.121.024101.

[218] C.-J. Lin and O. I. Motrunich. Out-of-time-ordered correlators in a quantum ising chain. *Phys. Rev. B*, 97:144304, 2018. doi:10.1103/PhysRevB.97.144304.

[219] Y. Huang, Y.-L. Zhang, and X. Chen. Out-of-time-ordered correlators in many-body localized systems. *Annalen der Physik*, 529(7):1600318, 2017.

[220] B. Swingle and D. Chowdhury. Slow scrambling in disordered quantum systems. *Phys. Rev. B*, 95:060201, 2017. doi:10.1103/PhysRevB.95.060201.

[221] D.-L. Deng, X. Li, J. H. Pixley, Y.-L. Wu, and S. Das Sarma. Logarithmic entanglement lightcone in many-body localized systems. *Phys. Rev. B*, 95:024202, 2017. doi:10.1103/PhysRevB.95.024202.

[222] X. Chen, T. Zhou, D. A. Huse, and E. Fradkin. Out-of-time-order correlations in many-body localized and thermal phases. *Annalen der Physik*, 529(7):1600332, 2017.

[223] David J. Luitz and Yevgeny Bar Lev. Information propagation in isolated quantum systems. *Phys. Rev. B*, 96:020406, 2017. doi:10.1103/PhysRevB.96.020406.

[224] A. Nahum, J. Ruhman, and D. A. Huse. Dynamics of entanglement and transport in one-dimensional systems with quenched randomness. *Phys. Rev. B*, 98:035118, 2018. doi:10.1103/PhysRevB.98.035118.

[225] C. Jonay, D. A. Huse, and A. Nahum. Coarse-grained dynamics of operator and state entanglement. *arXiv:1803.00089*, 2018. doi:10.48550/arXiv.1803.00089.

[226] M. Knap. Entanglement production and information scrambling in a noisy spin system. *Phys. Rev. B*, 98:184416, 2018. doi:10.1103/PhysRevB.98.184416.

[227] T. Rakovszky, C. W. von Keyserlingk, and F. Pollmann. Entanglement growth after inhomogenous quenches. *Phys. Rev. B*, 100:125139, 2019. doi:10.1103/PhysRevB.100.125139.

[228] Y. Huang. Dynamics of Rényi entanglement entropy in diffusive qudit systems. *IOP SciNotes*, 1(3):035205, 2020. doi:10.1088/2633-1357/abd1e2.

[229] M. Žnidarič. Entanglement growth in diffusive systems. *Communications Physics*, 3 (1):100, 2020. doi:10.1038/s42005-020-0366-7.

[230] S. Moudgalya, N. Regnault, and B. A. Bernevig. Entanglement of exact excited states of Affleck-Kennedy-Lieb-Tasaki models: Exact results, many-body scars, and violation of the strong eigenstate thermalization hypothesis. *Phys. Rev. B*, 98:235156, 2018. doi:10.1103/PhysRevB.98.235156.

[231] D. K. Mark, C.-J. Lin, and O. I. Motrunich. Unified structure for exact towers of scar states in the Affleck-Kennedy-Lieb-Tasaki and other models. *Phys. Rev. B*, 101: 195131, 2020. doi:10.1103/PhysRevB.101.195131.

[232] N. Shiraishi and T. Mori. Systematic Construction of Counterexamples to the Eigenstate Thermalization Hypothesis. *Phys. Rev. Lett.*, 119:030601, 2017. doi:10.1103/PhysRevLett.119.030601.

[233] S. Moudgalya, B. A. Bernevig, and N. Regnault. Quantum Many-Body Scars and Hilbert Space Fragmentation: A Review of Exact Results. *arXiv:2109.00548*, 2021. doi:10.48550/arXiv.2109.00548.

[234] Z. Papić. Weak ergodicity breaking through the lens of quantum entanglement. *arXiv:2108.03460*, 2021. doi:10.48550/arXiv.2108.03460.

[235] P. Sala, T. Rakovszky, R. Verresen, M. Knap, and F. Pollmann. Ergodicity Breaking Arising from Hilbert Space Fragmentation in Dipole-Conserving Hamiltonians. *Phys. Rev. X*, 10:011047, 2020. doi:10.1103/PhysRevX.10.011047.

[236] V. Khemani, M. Hermele, and R. Nandkishore. Localization from Hilbert space shattering: From theory to physical realizations. *Phys. Rev. B*, 101:174204, 2020. doi:10.1103/PhysRevB.101.174204.

[237] T. Rakovszky, P. Sala, R. Verresen, M. Knap, and F. Pollmann. Statistical localization: From strong fragmentation to strong edge modes. *Phys. Rev. B*, 101:125126, 2020. doi:10.1103/PhysRevB.101.125126.

[238] S. Moudgalya, A. Prem, R. Nandkishore, N. Regnault, and B. A. Bernevig. Thermalization and its absence within Krylov subspaces of a constrained Hamiltonian. *arXiv:1910.14048*, 2019. doi:10.48550/arXiv.1910.14048.

[239] S. Moudgalya and O. I. Motrunich. Hilbert Space Fragmentation and Commutant Algebras. *Phys. Rev. X*, 12:011050, 2022. doi:10.1103/PhysRevX.12.011050.

[240] S. Weinberg. *The quantum theory of fields*, volume 2. Cambridge University Press, 1995.

[241] A. Kitaev. Anyons in an exactly solved model and beyond. *Annals of Physics*, 321 (1):2 – 111, 2006. doi:10.1016/j.aop.2005.10.005.

[242] R. Moessner and K. S. Raman. *Quantum Dimer Models*, pages 437–479. Springer, Berlin, Heidelberg, 2011. doi:10.1007/978-3-642-10589-0_17.

[243] P. W. Anderson. The Resonating Valence Bond State in La_2CuO_4 and Superconductivity. *Science*, 235(4793):1196–1198, 1987. doi:10.1126/science.235.4793.1196.

[244] D. S. Rokhsar and S. A. Kivelson. Superconductivity and the Quantum Hard-Core Dimer Gas. *Phys. Rev. Lett.*, 61:2376–2379, 1988. doi:10.1103/PhysRevLett.61.2376.

[245] E. Fradkin and S. A. Kivelson. Short range resonating valence bond theories and superconductivity. *Modern Physics Letters B*, 04(03):225–232, 1990. doi:10.1142/S0217984990000295.

[246] R. Moessner, S. L. Sondhi, and Eduardo Fradkin. Short-ranged resonating valence bond physics, quantum dimer models, and Ising gauge theories. *Phys. Rev. B*, 65: 024504, 2001. doi:10.1103/PhysRevB.65.024504.

[247] J. Kogut and L. Susskind. Hamiltonian formulation of Wilson's lattice gauge theories. *Phys. Rev. D*, 11:395–408, 1975. doi:10.1103/PhysRevD.11.395.

[248] D. Horn. Finite matrix models with continuous local gauge invariance. *Physics Letters B*, 100(2):149–151, 1981. doi:10.1016/0370-2693(81)90763-2.

[249] P. Orland and D. Rohrlich. Lattice gauge magnets: Local isospin from spin. *Nuclear Physics B*, 338(3):647–672, 1990. doi:10.1016/0550-3213(90)90646-U.

[250] S. Chandrasekharan and U.-J Wiese. Quantum link models: A discrete approach to gauge theories. *Nuclear Physics B*, 492(1):455 – 471, 1997. doi:https://doi.org/10.1016/S0550-3213(97)80041-7.

[251] P. W. Leung, K. C. Chiu, and K. J. Runge. Columnar dimer and plaquette resonating-valence-bond orders in the quantum dimer model. *Phys. Rev. B*, 54:12938–12945, 1996. doi:10.1103/PhysRevB.54.12938.

[252] F. Alet, J. L. Jacobsen, G. Misguich, V. Pasquier, F. Mila, and M. Troyer. Interacting Classical Dimers on the Square Lattice. *Phys. Rev. Lett.*, 94:235702, 2005. doi:10.1103/PhysRevLett.94.235702.

[253] O. F. Syljuåsen. Plaquette phase of the square-lattice quantum dimer model: Quantum Monte Carlo calculations. *Phys. Rev. B*, 73:245105, 2006. doi:10.1103/PhysRevB.73.245105.

[254] C. Castelnovo, C. Chamon, C. Mudry, and P. Pujol. Zero-temperature Kosterlitz–Thouless transition in a two-dimensional quantum system. *Annals of Physics*, 322 (4):903 – 934, 2007. doi:10.1016/j.aop.2006.04.017.

[255] S. Wenzel, T. Coletta, S. E. Korshunov, and F. Mila. Evidence for Columnar Order in the Fully Frustrated Transverse Field Ising Model on the Square Lattice. *Phys. Rev. Lett.*, 109:187202, 2012. doi:10.1103/PhysRevLett.109.187202.

[256] D. Banerjee, M. Bögli, C. P. Hofmann, F.-J. Jiang, P. Widmer, and U.-J. Wiese. Interfaces, strings, and a soft mode in the square lattice quantum dimer model. *Phys. Rev. B*, 90:245143, 2014. doi:10.1103/PhysRevB.90.245143.

[257] T. Oakes, S. Powell, C. Castelnovo, A. Lamacraft, and J. P. Garrahan. Phases of quantum dimers from ensembles of classical stochastic trajectories. *Phys. Rev. B*, 98: 064302, 2018. doi:10.1103/PhysRevB.98.064302.

[258] L. Balents. Spin liquids in frustrated magnets. *Nature*, 464(7286):199–208, 2010. doi:10.1038/nature08917.

[259] L. Savary and L. Balents. Quantum spin liquids: a review. *Reports on Progress in Physics*, 80(1):016502, 2016. doi:10.1088/0034-4885/80/1/016502.

[260] Y. Zhou, K. Kanoda, and T.-K. Ng. Quantum spin liquid states. *Rev. Mod. Phys.*, 89: 025003, 2017. doi:10.1103/RevModPhys.89.025003.

[261] J. Knolle and R. Moessner. A Field Guide to Spin Liquids. *Annual Review of Condensed Matter Physics*, 10(1):451–472, 2019. doi:10.1146/annurev-conmatphys-031218-013401.

[262] C. Broholm, R. J. Cava, S. A. Kivelson, D. G. Nocera, M. R. Norman, and T. Senthil. Quantum spin liquids. *Science*, 367(6475), 2020. doi:10.1126/science.aay0668.

[263] G. Baskaran and P. W. Anderson. Gauge theory of high-temperature superconductors and strongly correlated fermi systems. *Phys. Rev. B*, 37:580–583, 1988. doi:10.1103/PhysRevB.37.580.

[264] I. Affleck, Z. Zou, T. Hsu, and P. W. Anderson. SU(2) gauge symmetry of the large-U limit of the Hubbard model. *Phys. Rev. B*, 38:745–747, 1988. doi:10.1103/PhysRevB.38.745.

[265] D. P. Arovas and A. Auerbach. Functional integral theories of low-dimensional quantum Heisenberg models. *Phys. Rev. B*, 38:316–332, 1988. doi:10.1103/PhysRevB.38.316.

[266] A.M. Polyakov. Quark confinement and topology of gauge theories. *Nuclear Physics B*, 120(3):429–458, 1977. doi:https://doi.org/10.1016/0550-3213(77)90086-4.

[267] N. Read and Subir Sachdev. Large-N expansion for frustrated quantum antiferromagnets. *Phys. Rev. Lett.*, 66:1773–1776, 1991. doi:10.1103/PhysRevLett.66.1773.

[268] X. G. Wen. Mean-field theory of spin-liquid states with finite energy gap and topological orders. *Phys. Rev. B*, 44:2664–2672, 1991. doi:10.1103/PhysRevB.44.2664.

[269] C. Chamon. Quantum Glassiness in Strongly Correlated Clean Systems: An Example of Topological Overprotection. *Phys. Rev. Lett.*, 94:040402, 2005. doi:10.1103/PhysRevLett.94.040402.

[270] J. Haah. Local stabilizer codes in three dimensions without string logical operators. *Phys. Rev. A*, 83:042330, 2011. doi:10.1103/PhysRevA.83.042330.

[271] B. Yoshida. Exotic topological order in fractal spin liquids. *Physical Review B*, 88: 125122, 2013. doi:10.1103/PhysRevB.88.125122.

[272] S. Vijay, J. Haah, and L. Fu. A new kind of topological quantum order: A dimensional hierarchy of quasiparticles built from stationary excitations. *Phys. Rev. B*, 92: 235136, 2015. doi:10.1103/PhysRevB.92.235136.

[273] S. Vijay, J. Haah, and L. Fu. Fracton topological order, generalized lattice gauge theory, and duality. *Phys. Rev. B*, 94:235157, 2016. doi:10.1103/PhysRevB.94.235157.

[274] M. Pretko. Subdimensional particle structure of higher rank $U(1)$ spin liquids. *Phys. Rev. B*, 95:115139, 2017. doi:10.1103/PhysRevB.95.115139.

[275] M. Pretko. The fracton gauge principle. *Phys. Rev. B*, 98:115134, 2018. doi:10.1103/PhysRevB.98.115134.

[276] M. Pretko. Higher-spin Witten effect and two-dimensional fracton phases. *Phys. Rev. B*, 96:125151, 2017. doi:10.1103/PhysRevB.96.125151.

[277] D. J. Williamson, Z. Bi, and M. Cheng. Fractonic matter in symmetry-enriched $U(1)$ gauge theory. *Physical Review B*, 100:125150, 2019. doi:10.1103/PhysRevB.100.125150.

[278] M. Pretko. Generalized electromagnetism of subdimensional particles: A spin liquid story. *Phys. Rev. B*, 96:035119, 2017. doi:10.1103/PhysRevB.96.035119.

[279] A. Gromov. Towards Classification of Fracton Phases: The Multipole Algebra. *Phys. Rev. X*, 9:031035, 2019. doi:10.1103/PhysRevX.9.031035.

[280] F. D. M. Haldane and E. H. Rezayi. Finite-Size Studies of the Incompressible State of the Fractionally Quantized Hall Effect and its Excitations. *Phys. Rev. Lett.*, 54: 237–240, 1985. doi:10.1103/PhysRevLett.54.237.

[281] S. A. Trugman and S. Kivelson. Exact results for the fractional quantum Hall effect with general interactions. *Phys. Rev. B*, 31:5280–5284, 1985. doi:10.1103/PhysRevB.31.5280.

[282] E. J. Bergholtz and A. Karlhede. Half-Filled Lowest Landau Level on a Thin Torus. *Phys. Rev. Lett.*, 94:026802, 2005. doi:10.1103/PhysRevLett.94.026802.

[283] A. Seidel, H. Fu, D.-H. Lee, J. M. Leinaas, and J. Moore. Incompressible Quantum Liquids and New Conservation Laws. *Phys. Rev. Lett.*, 95:266405, 2005. doi:10.1103/PhysRevLett.95.266405.

[284] M. Nakamura, Z.-Y. Wang, and E. J. Bergholtz. Exactly Solvable Fermion Chain Describing a $\nu = 1/3$ Fractional Quantum Hall State. *Phys. Rev. Lett.*, 109:016401, 2012. doi:10.1103/PhysRevLett.109.016401.

[285] B. Nachtergaele, S. Warzel, and A. Young. Low-complexity eigenstates of a $\nu = 1/3$ fractional quantum Hall system. *Journal of Physics A: Mathematical and Theoretical*, 54(1):01LT01, 2020. doi:10.1088/1751-8121/abca73.

[286] D. Bulmash and M. Barkeshli. Higgs mechanism in higher-rank symmetric U(1) gauge theories. *Phys. Rev. B*, 97:235112, 2018. doi:10.1103/PhysRevB.97.235112.

[287] H. Ma, M. Hermele, and X. Chen. Fracton topological order from the Higgs and partial-confinement mechanisms of rank-two gauge theory. *Phys. Rev. B*, 98:035111, 2018. doi:10.1103/PhysRevB.98.035111.

[288] M. Pretko and L. Radzihovsky. Fracton-Elasticity Duality. *Phys. Rev. Lett.*, 120: 195301, 2018. doi:10.1103/PhysRevLett.120.195301.

[289] A. Gromov. Chiral Topological Elasticity and Fracton Order. *Phys. Rev. Lett.*, 122: 076403, 2019. doi:10.1103/PhysRevLett.122.076403.

[290] A. Kumar and A. C. Potter. Symmetry-enforced fractonicity and two-dimensional quantum crystal melting. *Phys. Rev. B*, 100:045119, 2019. doi:10.1103/PhysRevB.100.045119.

[291] A. Prem, J. Haah, and R. Nandkishore. Glassy quantum dynamics in translation invariant fracton models. *Phys. Rev. B*, 95:155133, 2017. doi:10.1103/PhysRevB.95.155133.

[292] A. Browaeys and T. Lahaye. Many-body physics with individually controlled Rydberg atoms. *Nature Physics*, 16(2):132–142, 2020. doi:10.1038/s41567-019-0733-z.

[293] S. M. Winter, A. A. Tsirlin, M. Daghofer, J. van den Brink, Y. Singh, P. Gegenwart, and R. Valentí. Models and materials for generalized Kitaev magnetism. *Journal of Physics: Condensed Matter*, 29(49):493002, 2017. doi:10.1088/1361-648x/aa8cf5.

[294] M. Endres, H. Bernien, A. Keesling, H. Levine, E. R. Anschuetz, A. Krajenbrink, C. Senko, V. Vuletic, M. Greiner, and M. D. Lukin. Atom-by-atom assembly of defect-free one-dimensional cold atom arrays. *Science*, 354(6315):1024–1027, 2016. doi:10.1126/science.aah3752.

[295] H. Weimer, M. Müller, I. Lesanovsky, P. Zoller, and H. P. Büchler. A Rydberg quantum simulator. *Nature Physics*, 6(5):382–388, 2010. doi:10.1038/nphys1614.

[296] D. Jaksch, J. I. Cirac, P. Zoller, S. L. Rolston, R. Côté, and M. D. Lukin. Fast quantum gates for neutral atoms. *Phys. Rev. Lett.*, 85:2208–2211, 2000. doi:10.1103/PhysRevLett.85.2208.

[297] M. D. Lukin, M. Fleischhauer, R. Cote, L. M. Duan, D. Jaksch, J. I. Cirac, and P. Zoller. Dipole Blockade and Quantum Information Processing in Mesoscopic Atomic Ensembles. *Phys. Rev. Lett.*, 87:037901, 2001. doi:10.1103/PhysRevLett.87.037901.

[298] A. Keesling, A. Omran, H. Levine, H. Bernien, H. Pichler, S. Choi, R. Samajdar, S. Schwartz, P. Silvi, S. Sachdev, P. Zoller, M. Endres, M. Greiner, V. Vuletić, and M. D. Lukin. Quantum kibble–zurek mechanism and critical dynamics on a programmable rydberg simulator. *Nature*, 568(7751):207–211, 2019. doi:10.1038/s41586-019-1070-1.

[299] S. Ebadi, T. T. Wang, H. Levine, A. Keesling, G. Semeghini, A. Omran, D. Bluvstein, R. Samajdar, H. Pichler, W. W. Ho, S. Choi, S. Sachdev, M. Greiner, V. Vuletić, and M. D. Lukin. Quantum phases of matter on a 256-atom programmable quantum simulator. *Nature*, 595(7866):227–232, 2021. doi:10.1038/s41586-021-03582-4.

[300] A. Celi, B. Vermersch, O. Viyuela, H. Pichler, M. D. Lukin, and P. Zoller. Emerging Two-Dimensional Gauge Theories in Rydberg Configurable Arrays. *Phys. Rev. X*, 10:021057, 2020. doi:10.1103/PhysRevX.10.021057.

[301] M. C. Bañuls, R. Blatt, J. Catani, A. Celi, J. I. Cirac, M. Dalmonte, L. Fallani, K. Jansen, M. Lewenstein, S. Montangero, C. A. Muschik, B. Reznik, E. Rico, L. Tagliacozzo, K. Van Acoleyen, F. Verstraete, U.-J. Wiese, M. Wingate, J. Zakrzewski, and P. Zoller. Simulating lattice gauge theories within quantum technologies. *The European Physical Journal D*, 74(8):165, 2020. doi:10.1140/epjd/e2020-100571-8.

[302] R. Verresen, M. D. Lukin, and A. Vishwanath. Prediction of Toric Code Topological Order from Rydberg Blockade. *Phys. Rev. X*, 11:031005, 2021. doi:10.1103/PhysRevX.11.031005.

[303] G. Semeghini, H. Levine, A. Keesling, S. Ebadi, T. T. Wang, D. Bluvstein, R. Verresen, H. Pichler, M. Kalinowski, R. Samajdar, A. Omran, S. Sachdev, A. Vishwanath, M. Greiner, V. Vuletić, and M. D. Lukin. Probing topological spin liquids on a programmable quantum simulator. *Science*, 374(6572):1242–1247, 2021. doi:10.1126/science.abi8794.

[304] S. Ebadi, A. Keesling, M. Cain, T. T. Wang, H. Levine, D. Bluvstein, G. Semeghini, A. Omran, J.-G. Liu, R. Samajdar, X.-Z. Luo, B. Nash, X. Gao, B. Barak, E. Farhi, S. Sachdev, N. Gemelke, L. Zhou, S. Choi, H. Pichler, S.-T. Wang, M. Greiner, V. Vuletić, and M. D. Lukin. Quantum optimization of maximum independent set using rydberg atom arrays. *Science*, 376(6598):1209–1215, 2022. doi:10.1126/science.abo6587.

[305] T. Esslinger. Fermi-Hubbard Physics with Atoms in an Optical Lattice. *Annual Review of Condensed Matter Physics*, 1(1):129–152, 2010. doi:10.1146/annurev-conmatphys-070909-104059.

[306] A. Mazurenko, C. S. Chiu, G. Ji, M. F. Parsons, M. Kanász-Nagy, R. Schmidt, F. Grusdt, E. Demler, D. Greif, and M. Greiner. A cold-atom Fermi–Hubbard antiferromagnet. *Nature*, 545(7655):462–466, 2017. doi:10.1038/nature22362.

[307] M. H. Anderson, J. R. Ensher, M. R. Matthews, C. E. Wieman, and E. A. Cornell. Observation of Bose-Einstein Condensation in a Dilute Atomic Vapor. *Science*, 269 (5221):198–201, 1995. doi:10.1126/science.269.5221.198.

[308] K. B. Davis, M. O. Mewes, M. R. Andrews, N. J. van Druten, D. S. Durfee, D. M. Kurn, and W. Ketterle. Bose-Einstein Condensation in a Gas of Sodium Atoms. *Phys. Rev. Lett.*, 75:3969–3973, 1995. doi:10.1103/PhysRevLett.75.3969.

[309] M. Greiner, O. Mandel, T. Esslinger, T. W. Hänsch, and I. Bloch. Quantum phase transition from a superfluid to a Mott insulator in a gas of ultracold atoms. *Nature*, 415(6867):39–44, 2002. doi:10.1038/415039a.

[310] W. S. Bakr, J. I. Gillen, A. Peng, S. Fölling, and M. Greiner. A quantum gas microscope for detecting single atoms in a Hubbard-regime optical lattice. *Nature*, 462 (7269):74–77, 2009. doi:10.1038/nature08482.

[311] J. F. Sherson, C. Weitenberg, M. Endres, M. Cheneau, I. Bloch, and S. Kuhr. Single-atom-resolved fluorescence imaging of an atomic Mott insulator. *Nature*, 467(7311): 68–72, 2010. doi:10.1038/nature09378.

[312] R. Islam, R. Ma, P. M. Preiss, M. Eric Tai, A. Lukin, M. Rispoli, and M. Greiner. Measuring entanglement entropy in a quantum many-body system. *Nature*, 528 (7580):77–83, 2015. doi:10.1038/nature15750.

[313] A. M. Kaufman, M. E. Tai, A. Lukin, M. Rispoli, R. Schittko, P. M. Preiss, and M. Greiner. Quantum thermalization through entanglement in an isolated many-body system. *Science*, 353(6301):794–800, 2016. doi:10.1126/science.aaf6725.

[314] C. S. Chiu, G. Ji, A. Bohrdt, M. Xu, M. Knap, E. Demler, F. Grusdt, M. Greiner, and D. Greif. String patterns in the doped Hubbard model. *Science*, 365(6450):251–256, 2019. doi:10.1126/science.aav3587.

[315] A. Bohrdt, C. S. Chiu, G. Ji, M. Xu, D. Greif, M. Greiner, E. Demler, F. Grusdt, and M. Knap. Classifying snapshots of the doped Hubbard model with machine learning. *Nature Physics*, 15(9):921–924, 2019. doi:10.1038/s41567-019-0565-x.

[316] S. Trotzky, Y-A. Chen, A. Flesch, I. P. McCulloch, U. Schollwöck, J. Eisert, and I. Bloch. Probing the relaxation towards equilibrium in an isolated strongly correlated one-dimensional Bose gas. *Nature Physics*, 8(4):325–330, 2012. doi:10.1038/nphys2232.

[317] M. A. Nichols, L. W. Cheuk, M. Okan, T. R. Hartke, E. Mendez, T. Senthil, E. Khatami, H. Zhang, and M. W. Zwierlein. Spin transport in a Mott insulator of ultracold fermions. *Science*, 363(6425):383–387, 2019. doi:10.1126/science.aat4387.

[318] P. Bordia, H. Lüschen, S. Scherg, S. Gopalakrishnan, M. Knap, U. Schneider, and I. Bloch. Probing Slow Relaxation and Many-Body Localization in Two-Dimensional Quasiperiodic Systems. *Phys. Rev. X*, 7:041047, 2017. doi:10.1103/PhysRevX.7.041047.

[319] A. Lukin, M. Rispoli, R. Schittko, M. Eric Tai, A. M. Kaufman, S. Choi, V. Khemani, J. Léonard, and M. Greiner. Probing entanglement in a many-body-localized system. *Science*, 364(6437):256–260, 2019. doi:10.1126/science.aau0818.

[320] S. Scherg, T. Kohlert, P. Sala, F. Pollmann, B. Hebbe Madhusudhana, I. Bloch, and M. Aidelsburger. Observing non-ergodicity due to kinetic constraints in tilted Fermi-Hubbard chains. *Nature Communications*, 12(1):4490, 2021. doi:10.1038/s41467-021-24726-0.

[321] T. Kohlert, S. Scherg, P. Sala, F. Pollmann, B. H. Madhusudhana, I. Bloch, and M. Aidelsburger. Experimental realization of fragmented models in tilted Fermi-Hubbard chains. *arXiv:2106.15586*, 2021. doi:10.48550/arXiv.2106.15586.

[322] P. Zhang. Subdiffusion in strongly tilted lattice systems. *Phys. Rev. Research*, 2: 033129, 2020. doi:10.1103/PhysRevResearch.2.033129.

[323] E. van Nieuwenburg, Y. Baum, and G. Refael. From Bloch oscillations to many-body localization in clean interacting systems. *Proceedings of the National Academy of Sciences*, 116(19):9269–9274, 2019. doi:10.1073/pnas.1819316116.

[324] M. Schulz, C. A. Hooley, R. Moessner, and F. Pollmann. Stark Many-Body Localization. *Phys. Rev. Lett.*, 122:040606, 2019. doi:10.1103/PhysRevLett.122.040606.

[325] J. Smith, A. Lee, P. Richerme, B. Neyenhuis, P. W. Hess, P. Hauke, M. Heyl, D. A. Huse, and C. Monroe. Many-body localization in a quantum simulator with programmable random disorder. *Nature Physics*, 12(10):907–911, 2016. doi:10.1038/nphys3783.

[326] P. Jurcevic, H. Shen, P. Hauke, C. Maier, T. Brydges, C. Hempel, B. P. Lanyon, M. Heyl, R. Blatt, and C. F. Roos. Direct Observation of Dynamical Quantum Phase Transitions in an Interacting Many-Body System. *Phys. Rev. Lett.*, 119:080501, 2017. doi:10.1103/PhysRevLett.119.080501.

[327] W. Morong, F. Liu, P. Becker, K. S. Collins, L. Feng, A. Kyprianidis, G. Pagano, T. You, A. V. Gorshkov, and C. Monroe. Observation of stark many-body localization without disorder. *Nature*, 599(7885):393–398, 2021. doi:10.1038/s41586-021-03988-0.

[328] D. P. DiVincenzo. The physical implementation of quantum computation. *Fortschritte der Physik: Progress of Physics*, 48(9-11):771–783, 2000.

[329] F. Arute, K. Arya, R. Babbush, D. Bacon, J. C. Bardin, R. Barends, R. Biswas, S. Boixo, F. G. S. L. Brandao, D. A. Buell, B. Burkett, Y. Chen, Z. Chen, B. Chiaro, R. Collins, W. Courtney, A. Dunsworth, E. Farhi, B. Foxen, A. Fowler, C. Gidney, M. Giustina, R. Graff, K. Guerin, S. Habegger, M. P. Harrigan, M. J. Hartmann, A. Ho, M. Hoffmann, T. Huang, T. S. Humble, S. V. Isakov, E. Jeffrey, Z. Jiang, D. Kafri, K. Kechedzhi, J. Kelly, P. V. Klimov, S. Knysh, A. Korotkov, F. Kostritsa, D. Landhuis, M. Lindmark, E. Lucero, D. Lyakh, S. Mandrà, J. R. McClean, M. McEwen, Anthony Megrant, Xiao Mi, Kristel Michielsen, Masoud Mohseni, Josh Mutus, Ofer Naaman, Matthew Neeley, Charles Neill, Murphy Yuezhen Niu, Eric Ostby, Andre Petukhov, John C. Platt, Chris Quintana, Eleanor G. Rieffel, Pedram Roushan, Nicholas C. Rubin, Daniel Sank, Kevin J. Satzinger, Vadim Smelyanskiy, Kevin J. Sung, Matthew D. Trevithick, A. Vainsencher, B. Villalonga, T. White, Z. J. Yao, P. Yeh, A. Zalcman, H. Neven, and J. M. Martinis. Quantum supremacy using a programmable superconducting processor. *Nature*, 574(7779):505–510, 2019. doi:10.1038/s41586-019-1666-5.

[330] K. J. Satzinger, Y.-J Liu, A. Smith, C. Knapp, M. Newman, C. Jones, Z. Chen, C. Quintana, X. Mi, A. Dunsworth, C. Gidney, I. Aleiner, F. Arute, K. Arya, J. Atalaya, R. Babbush, J. C. Bardin, R. Barends, J. Basso, A. Bengtsson, A. Bilmes, M. Broughton, B. B. Buckley, D. A. Buell, B. Burkett, N. Bushnell, B. Chiaro, R. Collins, W. Courtney, S. Demura, A. R. Derk, D. Eppens, C. Erickson, L. Faoro, E. Farhi, A. G. Fowler, B. Foxen, M. Giustina, A. Greene, J. A. Gross, M. P. Harrigan, S. D. Harrington, J. Hilton, S. Hong, T. Huang, W. J. Huggins, L. B. Ioffe, S. V. Isakov, E. Jeffrey, Z. Jiang, D. Kafri, K. Kechedzhi, T. Khattar, S. Kim, P. V. Klimov, A. N. Korotkov, F. Kostritsa, D. Landhuis, P. Laptev, A. Locharla, E. Lucero, O. Martin, J. R. McClean, M. McEwen, K. C. Miao, M. Mohseni, S. Montazeri, W. Mruczkiewicz, J. Mutus, O. Naaman, M. Neeley, C. Neill, M. Y. Niu, T. E. O'Brien, A. Opremcak, B. Pató, A. Petukhov, N. C. Rubin, D. Sank, V. Shvarts, D. Strain, M. Szalay, B. Villalonga, T. C. White, Z. Yao, P. Yeh, J. Yoo, A. Zalcman, H. Neven, S. Boixo, A. Megrant, Y. Chen, J. Kelly, V. Smelyanskiy, A. Kitaev, M. Knap, F. Pollmann, and P. Roushan. Realizing topologically ordered states on a quantum processor. *Science*, 374(6572):1237–1241, 2021. doi:10.1126/science.abi8378.

[331] S. Choi, J. Choi, R. Landig, G. Kucsko, H. Zhou, J. Isoya, F. Jelezko, S. Onoda, H. Sumiya, V. Khemani, C. von Keyserlingk, N. Y. Yao, E. Demler, and M. D. Lukin. Observation of discrete time-crystalline order in a disordered dipolar many-body system. *Nature*, 543(7644):221–225, 2017. doi:10.1038/nature21426.

[332] E. Knill, R. Laflamme, and G. J. Milburn. A scheme for efficient quantum computation with linear optics. *Nature*, 409(6816):46–52, 2001. doi:10.1038/35051009.

[333] S. Trebst. Kitaev Materials. *arXiv:1701.07056*, 2017. doi:10.48550/arXiv.1701.07056.

[334] M. Hermanns, I. Kimchi, and J. Knolle. Physics of the Kitaev Model: Fractionalization, Dynamic Correlations, and Material Connections. *Annual Review of Condensed Matter Physics*, 9(1):17–33, 2018. doi:10.1146/annurev-conmatphys-033117-053934.

[335] H. Takagi, T. Takayama, G. Jackeli, G. Khaliullin, and S. E. Nagler. Concept and realization of Kitaev quantum spin liquids. *Nature Reviews Physics*, 1(4):264–280, 2019. doi:10.1038/s42254-019-0038-2.

[336] G. Jackeli and G. Khaliullin. Mott Insulators in the Strong Spin-Orbit Coupling Limit: From Heisenberg to a Quantum Compass and Kitaev Models. *Phys. Rev. Lett.*, 102:017205, 2009. doi:10.1103/PhysRevLett.102.017205.

[337] A. Banerjee, C. A. Bridges, J.-Q. Yan, A. A. Aczel, L. Li, M. B. Stone, G. E. Granroth, M. D. Lumsden, Y. Yiu, J. Knolle, and et al. Proximate Kitaev quantum spin liquid behaviour in a honeycomb magnet. *Nature Materials*, 15(7):733–740, 2016. doi:10.1038/nmat4604.

[338] A. Banerjee, J. Yan, J. Knolle, C. A. Bridges, M. B. Stone, M. D. Lumsden, D. G. Mandrus, D. A. Tennant, R. Moessner, and S. E. Nagler. Neutron scattering in the proximate quantum spin liquid α-RuCl3. *Science*, 356(6342):1055–1059, 2017. doi:10.1126/science.aah6015.

[339] J. A. Sears, M. Songvilay, K. W. Plumb, J. P. Clancy, Y. Qiu, Y. Zhao, D. Parshall, and Young-June Kim. Magnetic order in $\alpha - RuCl_3$: A honeycomb-lattice

quantum magnet with strong spin-orbit coupling. *Phys. Rev. B*, 91:144420, 2015. doi:10.1103/PhysRevB.91.144420.

[340] R. D. Johnson, S. C. Williams, A. A. Haghighirad, J. Singleton, V. Zapf, P. Manuel, I. I. Mazin, Y. Li, H. O. Jeschke, R. Valentí, and R. Coldea. Monoclinic crystal structure of $\alpha-\mathrm{RuCl_3}$ and the zigzag antiferromagnetic ground state. *Phys. Rev. B*, 92:235119, 2015. doi:10.1103/PhysRevB.92.235119.

[341] A. Banerjee, P. Lampen-Kelley, J. Knolle, C. Balz, A. A. Aczel, B. Winn, Y. Liu, D. Pajerowski, J. Yan, C. A. Bridges, and et al. Excitations in the field-induced quantum spin liquid state of $\alpha-\mathrm{RuCl_3}$. *npj Quantum Materials*, 3(1), 2018. doi:10.1038/s41535-018-0079-2.

[342] S. M. Winter, K. Riedl, D. Kaib, R. Coldea, and R. Valentí. Probing $\alpha-\mathrm{RuCl_3}$ Beyond Magnetic Order: Effects of Temperature and Magnetic Field. *Phys. Rev. Lett.*, 120: 077203, 2018. doi:10.1103/PhysRevLett.120.077203.

[343] Y. Kasahara, T. Ohnishi, Y. Mizukami, O. Tanaka, Sixiao Ma, K. Sugii, N. Kurita, H. Tanaka, J. Nasu, Y. Motome, and et al. Majorana quantization and half-integer thermal quantum Hall effect in a Kitaev spin liquid. *Nature*, 559(7713):227–231, 2018. doi:10.1038/s41586-018-0274-0.

[344] Y. Vinkler-Aviv and A. Rosch. Approximately Quantized Thermal Hall Effect of Chiral Liquids Coupled to Phonons. *Phys. Rev. X*, 8:031032, 2018. doi:10.1103/PhysRevX.8.031032.

[345] M. Ye, G. B. Halász, L. Savary, and L. Balents. Quantization of the Thermal Hall Conductivity at Small Hall Angles. *Phys. Rev. Lett.*, 121:147201, 2018. doi:10.1103/PhysRevLett.121.147201.

[346] B. Zhou, Y. Wang, G. B. Osterhoudt, P. Lampen-Kelley, D. Mandrus, R. He, K. S. Burch, and E. A. Henriksen. Possible structural transformation and enhanced magnetic fluctuations in exfoliated α-RuCl3. *Journal of Physics and Chemistry of Solids*, 128:291 – 295, 2019. doi:10.1016/j.jpcs.2018.01.026.

[347] Zhou, B. and Balgley, J. and Lampen-Kelley, P. and Yan, J.-Q. and Mandrus, D. G. and Henriksen, E. A. Evidence for charge transfer and proximate magnetism in graphene–$\alpha-\mathrm{RuCl_3}$ heterostructures. *Phys. Rev. B*, 100:165426, 2019. doi:10.1103/PhysRevB.100.165426.

[348] S. Mashhadi, Y. Kim, J. Kim, D. Weber, T. Taniguchi, K. Watanabe, N. Park, B. Lotsch, J. H. Smet, M. Burghard, and et al. Spin-Split Band Hybridization in Graphene Proximitized with α-RuCl3 Nanosheets. *Nano Letters*, 19(7):4659–4665, 2019. doi:10.1021/acs.nanolett.9b01691.

[349] M. Carrega, I. J. Vera-Marun, and A. Principi. Tunneling spectroscopy as a probe of fractionalization in two-dimensional magnetic heterostructures. *Phys. Rev. B*, 102: 085412, 2020. doi:10.1103/PhysRevB.102.085412.

[350] E. J. König, M. T. Randeria, and B. Jäck. Tunneling Spectroscopy of Quantum Spin Liquids. *Phys. Rev. Lett.*, 125:267206, 2020. doi:10.1103/PhysRevLett.125.267206.

[351] R. G. Pereira and R. Egger. Electrical Access to Ising Anyons in Kitaev Spin Liquids. *Phys. Rev. Lett.*, 125:227202, 2020. doi:10.1103/PhysRevLett.125.227202.

[352] S. T. Bramwell and M. J. P. Gingras. Spin Ice State in Frustrated Magnetic Pyrochlore Materials. *Science*, 294(5546):1495–1501, 2001. doi:10.1126/science.1064761.

[353] C. Castelnovo, R. Moessner, and S. L. Sondhi. Magnetic monopoles in spin ice. *Nature*, 451(7174):42–45, 2008. doi:10.1038/nature06433.

[354] E. Urban, T. A. Johnson, T. Henage, L. Isenhower, D. D. Yavuz, T. G. Walker, and M. Saffman. Observation of Rydberg blockade between two atoms. *Nature Physics*, 5(2):110–114, 2009. doi:10.1038/nphys1178.

[355] A. Gaëtan, Y. Miroshnychenko, T. Wilk, A. Chotia, M. Viteau, D. Comparat, P. Pillet, A. Browaeys, and P. Grangier. Observation of collective excitation of two individual atoms in the Rydberg blockade regime. *Nature Physics*, 5(2):115–118, 2009. doi:10.1038/nphys1183.

[356] T. Wilk, A. Gaëtan, C. Evellin, J. Wolters, Y. Miroshnychenko, P. Grangier, and A. Browaeys. Entanglement of Two Individual Neutral Atoms Using Rydberg Blockade. *Phys. Rev. Lett.*, 104:010502, 2010. doi:10.1103/PhysRevLett.104.010502.

[357] P. Schauß, M. Cheneau, M. Endres, T. Fukuhara, S. Hild, A. Omran, T. Pohl, C. Gross, S. Kuhr, and I. Bloch. Observation of spatially ordered structures in a two-dimensional Rydberg gas. *Nature*, 491(7422):87–91, 2012. doi:10.1038/nature11596.

[358] P. Schauss, J. Zeiher, T. Fukuhara, S. Hild, M. Cheneau, T. Macri, T. Pohl, I. Bloch, and C. Gross. Crystallization in Ising quantum magnets. *Science*, 347(6229):1455–1458, 2015. doi:10.1126/science.1258351.

[359] H. Labuhn, D. Barredo, S. Ravets, S. de Léséleuc, T. Macrì, T. Lahaye, and A. Browaeys. Tunable two-dimensional arrays of single Rydberg atoms for realizing quantum Ising models. *Nature*, 534(7609):667–670, 2016. doi:10.1038/nature18274.

[360] J. Zeiher, J. Y. Choi, A. Rubio-Abadal, T. Pohl, R. van Bijnen, I. Bloch, and C. Gross. Coherent Many-Body Spin Dynamics in a Long-Range Interacting Ising Chain. *Phys. Rev. X*, 7:041063, 2017. doi:10.1103/PhysRevX.7.041063.

[361] A. Chandran, Marc D. Schulz, and F. J. Burnell. The eigenstate thermalization hypothesis in constrained Hilbert spaces: A case study in non-Abelian anyon chains. *Phys. Rev. B*, 94:235122, 2016. doi:10.1103/PhysRevB.94.235122.

[362] V. Khemani, C. R. Laumann, and A. Chandran. Signatures of integrability in the dynamics of Rydberg-blockaded chains. *Phys. Rev. B*, 99:161101, 2019. doi:10.1103/PhysRevB.99.161101.

[363] C.-J. Lin and O. I. Motrunich. Exact Quantum Many-Body Scar States in the Rydberg-Blockaded Atom Chain. *Phys. Rev. Lett.*, 122:173401, 2019. doi:10.1103/PhysRevLett.122.173401.

[364] N. Chepiga and F. Mila. DMRG investigation of constrained models: from quantum dimer and quantum loop ladders to hard-boson and Fibonacci anyon chains. *SciPost Phys.*, 6(3):33, 2019. doi:10.21468/SciPostPhys.6.3.033.

[365] F. M. Surace, P. P. Mazza, G. Giudici, A. Lerose, A. Gambassi, and M. Dalmonte. Lattice Gauge Theories and String Dynamics in Rydberg Atom Quantum Simulators. *Phys. Rev. X*, 10:021041, 2020. doi:10.1103/PhysRevX.10.021041.

[366] Z. Lan and S. Powell. Eigenstate thermalization hypothesis in quantum dimer models. *Phys. Rev. B*, 96:115140, 2017. doi:10.1103/PhysRevB.96.115140.

[367] F. Alet, Y. Ikhlef, J. L. Jacobsen, G. Misguich, and V. Pasquier. Classical dimers with aligning interactions on the square lattice. *Phys. Rev. E*, 74:041124, 2006. doi:10.1103/PhysRevE.74.041124.

[368] C. Bartsch and J. Gemmer. Dynamical Typicality of Quantum Expectation Values. *Phys. Rev. Lett.*, 102:110403, 2009. doi:10.1103/PhysRevLett.102.110403.

[369] Markus Heyl. Dynamical quantum phase transitions: a review. *Reports on Progress in Physics*, 81(5):054001, 2018. doi:10.1088/1361-6633/aaaf9a.

[370] M. E. Fisher. Statistical Mechanics of Dimers on a Plane Lattice. *Phys. Rev.*, 124: 1664–1672, 1961. doi:10.1103/PhysRev.124.1664.

[371] M. Heyl, A. Polkovnikov, and S. Kehrein. Dynamical Quantum Phase Transitions in the Transverse-Field Ising Model. *Phys. Rev. Lett.*, 110:135704, 2013. doi:10.1103/PhysRevLett.110.135704.

[372] S. A. Weidinger, M. Heyl, A. Silva, and M. Knap. Dynamical quantum phase transitions in systems with continuous symmetry breaking. *Phys. Rev. B*, 96:134313, 2017. doi:10.1103/PhysRevB.96.134313.

[373] P. Karpov, R. Verdel, Y.-P. Huang, M. Schmitt, and M. Heyl. Disorder-Free Localization in an Interacting 2D Lattice Gauge Theory. *Phys. Rev. Lett.*, 126:130401, 2021. doi:10.1103/PhysRevLett.126.130401.

[374] M. Freedman, M. B. Hastings, C. Nayak, and X.-L. Qi. Weakly coupled non-Abelian anyons in three dimensions. *Phys. Rev. B*, 84:245119, 2011. doi:10.1103/PhysRevB.84.245119.

[375] G. Bednik. Hopfions in a lattice dimer model. *Phys. Rev. B*, 100:024420, 2019. doi:10.1103/PhysRevB.100.024420.

[376] G. Bednik. Probing topological properties of a three-dimensional lattice dimer model with neural networks. *Phys. Rev. B*, 100:184414, 2019. doi:10.1103/PhysRevB.100.184414.

[377] U.-J. Wiese. Ultracold quantum gases and lattice systems: quantum simulation of lattice gauge theories. *Annalen der Physik*, 525(10-11):777–796, 2013. doi:10.1002/andp.201300104.

[378] Alet, F. and Sørensen, E. S. Cluster Monte Carlo algorithm for the quantum rotor model. *Phys. Rev. E*, 67:015701, 2003. doi:10.1103/PhysRevE.67.015701.

[379] Alet, F. and Sørensen, E. S. Directed geometrical worm algorithm applied to the quantum rotor model. *Phys. Rev. E*, 68:026702, 2003. doi:10.1103/PhysRevE.68.026702.

[380] D. A. Huse, W. Krauth, R. Moessner, and S. L. Sondhi. Coulomb and Liquid Dimer Models in Three Dimensions. *Phys. Rev. Lett.*, 91:167004, 2003. doi:10.1103/PhysRevLett.91.167004.

[381] G. Chen, J. Gukelberger, S. Trebst, F. Alet, and L. Balents. Coulomb gas transitions in three-dimensional classical dimer models. *Phys. Rev. B*, 80:045112, 2009. doi:10.1103/PhysRevB.80.045112.

[382] A. W. Sandvik and R. Moessner. Correlations and confinement in non-planar two-dimensional dimer models. *Phys. Rev. B*, 73:144504, 2006. doi:10.1103/PhysRevB.73.144504.

[383] Syljuåsen, O. F. and Zvonarev, M. B. Directed-loop Monte Carlo simulations of vertex models. *Phys. Rev. E*, 70:016118, Jul 2004. doi:10.1103/PhysRevE.70.016118. URL `https://link.aps.org/doi/10.1103/PhysRevE.70.016118`.

[384] A. W. Sandvik. Computational Studies of Quantum Spin Systems. *AIP Conference Proceedings*, 1297(1):135–338, 2010. doi:10.1063/1.3518900.

[385] P. M. Chaikin and T. C. Lubensky. *Principles of Condensed Matter Physics*. Cambridge University Press, 1995. doi:10.1017/CBO9780511813467.

[386] S. Gopalakrishnan. Operator growth and eigenstate entanglement in an interacting integrable Floquet system. *Phys. Rev. B*, 98:060302, 2018. doi:10.1103/PhysRevB.98.060302.

[387] S. Gopalakrishnan and B. Zakirov. Facilitated quantum cellular automata as simple models with non-thermal eigenstates and dynamics. *Quantum Science and Technology*, 3(4):044004, 2018. doi:10.1088/2058-9565/aad759.

[388] J. Iaconis. Quantum State Complexity in Computationally Tractable Quantum Circuits. *PRX Quantum*, 2:010329, 2021. doi:10.1103/PRXQuantum.2.010329.

[389] A. Gromov, A. Lucas, and R. M. Nandkishore. Fracton hydrodynamics. *Phys. Rev. Research*, 2:033124, 2020. doi:10.1103/PhysRevResearch.2.033124.

[390] P. Fendley. Parafermionic edge zero modes in Z_n-invariant spin chains. *Journal of Statistical Mechanics: Theory and Experiment*, 2012(11):P11020, 2012. doi:10.1088/1742-5468/2012/11/p11020.

[391] P. Fendley. Strong zero modes and eigenstate phase transitions in the XYZ/interacting Majorana chain. *Journal of Physics A: Mathematical and Theoretical*, 49(30):30LT01, 2016. doi:10.1088/1751-8113/49/30/30lt01.

[392] J. Alicea and P. Fendley. Topological Phases with Parafermions: Theory and Blueprints. *Annual Review of Condensed Matter Physics*, 7(1):119–139, 2016. doi:10.1146/annurev-conmatphys-031115-011336.

[393] J. Kemp, N. Y. Yao, C. R. Laumann, and P. Fendley. Long coherence times for edge spins. *Journal of Statistical Mechanics: Theory and Experiment*, 2017(6):063105, 2017. doi:10.1088/1742-5468/aa73f0.

[394] D. V. Else, P. Fendley, J. Kemp, and C. Nayak. Prethermal Strong Zero Modes and Topological Qubits. *Phys. Rev. X*, 7:041062, 2017. doi:10.1103/PhysRevX.7.041062.

[395] L. M. Vasiloiu, F. Carollo, M. Marcuzzi, and J. P. Garrahan. Strong zero modes in a class of generalized Ising spin ladders with plaquette interactions. *Phys. Rev. B*, 100:024309, 2019. doi:10.1103/PhysRevB.100.024309.

[396] T. E. Harris. Diffusion with "Collisions" between Particles. *Journal of Applied Probability*, 2(2):323–338, 1965.

[397] D. G. Levitt. Dynamics of a Single-File Pore: Non-Fickian Behavior. *Phys. Rev. A*, 8: 3050–3054, 1973. doi:10.1103/PhysRevA.8.3050.

[398] H. van Beijeren, K. W. Kehr, and R. Kutner. Diffusion in concentrated lattice gases. III. Tracer diffusion on a one-dimensional lattice. *Phys. Rev. B*, 28:5711–5723, 1983. doi:10.1103/PhysRevB.28.5711.

[399] H. Hopf. Über die Abbildungen der dreidimensionalen Sphäre auf die Kugelfläche. *Selecta Heinz Hopf, Springer, Berlin, Heidelberg*, pages 38–63, 1964. doi:10.1007/978-3-662-25046-4_4.

[400] U. K. Rößler, A. N. Bogdanov, and C. Pfleiderer. Spontaneous skyrmion ground states in magnetic metals. *Nature*, 442(7104):797–801, 2006. doi:10.1038/nature05056.

[401] Mühlbauer, S. and Binz, B. and Jonietz, F. and Pfleiderer, C. and Rosch, A. and Neubauer, A. and Georgii, R. and Böni, P. Skyrmion Lattice in a Chiral Magnet. *Science*, 323(5916):915–919, 2009. doi:10.1126/science.1166767.

[402] J. E. Moore, Y. Ran, and X.-G. Wen. Topological Surface States in Three-Dimensional Magnetic Insulators. *Phys. Rev. Lett.*, 101:186805, 2008. doi:10.1103/PhysRevLett.101.186805.

[403] D.-L. Deng, S.-T. Wang, C. Shen, and L.-M. Duan. Hopf insulators and their topologically protected surface states. *Phys. Rev. B*, 88:201105, 2013. doi:10.1103/PhysRevB.88.201105.

[404] C. Liu, F. Vafa, and C. Xu. Symmetry-protected topological Hopf insulator and its generalizations. *Phys. Rev. B*, 95:161116, 2017. doi:10.1103/PhysRevB.95.161116.

[405] T. Oakes, J. P. Garrahan, and S. Powell. Emergence of cooperative dynamics in fully packed classical dimers. *Phys. Rev. E*, 93:032129, 2016. doi:10.1103/PhysRevE.93.032129.

[406] Théveniaut, H. and Lan, Z. and Meyer, G. and Alet, F. Transition to a many-body localized regime in a two-dimensional disordered quantum dimer model. *Phys. Rev. Research*, 2:033154, 2020. doi:10.1103/PhysRevResearch.2.033154.

[407] F. Pietracaprina and F. Alet. Probing many-body localization in a disordered quantum dimer model on the honeycomb lattice. *SciPost Phys.*, 10:44, 2021. doi:10.21468/SciPostPhys.10.2.044.

[408] F. Flicker, S. H. Simon, and S. A. Parameswaran. Classical Dimers on Penrose Tilings. *Phys. Rev. X*, 10:011005, 2020. doi:10.1103/PhysRevX.10.011005.

[409] F. Pollmann, J. J. Betouras, K. Shtengel, and P. Fulde. Correlated Fermions on a Checkerboard Lattice. *Phys. Rev. Lett.*, 97:170407, 2006. doi:10.1103/PhysRevLett.97.170407.

[410] N. Wilkins and S. Powell. Interacting double dimer model on the square lattice. *Phys. Rev. B*, 102:174431, 2020. doi:10.1103/PhysRevB.102.174431.

[411] N. Desai, S. Pujari, and K. Damle. Bilayer Coulomb phase of two-dimensional dimer models: Absence of power-law columnar order. *Phys. Rev. E*, 103:042136, 2021. doi:10.1103/PhysRevE.103.042136.

[412] Hsieh, D. and Qian, D. and Wray, L. and Xia, Y. and Hor, Y. S. and Cava, R. J. and Hasan, M. Z. A topological Dirac insulator in a quantum spin Hall phase. *Nature*, 452(7190):970–974, 2008. doi:10.1038/nature06843.

[413] V. Mourik, K. Zuo, S. M. Frolov, S. R. Plissard, E. P. A. M. Bakkers, and L. P. Kouwenhoven. Signatures of Majorana Fermions in Hybrid Superconductor-Semiconductor Nanowire Devices. *Science*, 336(6084):1003–1007, 2012. doi:10.1126/science.1222360.

[414] X-L. Qi and S.-C. Zhang. Topological insulators and superconductors. *Rev. Mod. Phys.*, 83:1057–1110, 2011. doi:10.1103/RevModPhys.83.1057.

[415] M. Z. Hasan and C. L. Kane. Colloquium: Topological insulators. *Rev. Mod. Phys.*, 82:3045–3067, 2010. doi:10.1103/RevModPhys.82.3045.

[416] S. H. Glarum, S. Geschwind, K. M. Lee, M. L. Kaplan, and J. Michel. Observation of fractional spin S=1/2 on open ends of S=1 linear antiferromagnetic chains: Nonmagnetic doping. *Phys. Rev. Lett.*, 67:1614–1617, 1991. doi:10.1103/PhysRevLett.67.1614.

[417] M. Kenzelmann, G. Xu, I. A. Zaliznyak, C. Broholm, J. F. DiTusa, G. Aeppli, T. Ito, K. Oka, and H. Takagi. Structure of End States for a Haldane Spin Chain. *Phys. Rev. Lett.*, 90:087202, 2003. doi:10.1103/PhysRevLett.90.087202.

[418] S. Chatterjee and S. Sachdev. Probing excitations in insulators via injection of spin currents. *Phys. Rev. B*, 92:165113, 2015. doi:10.1103/PhysRevB.92.165113.

[419] J. F. Rodriguez-Nieva, K. Agarwal, T. Giamarchi, B. I. Halperin, M. D. Lukin, and E. Demler. Probing one-dimensional systems via noise magnetometry with single spin qubits. *Phys. Rev. B*, 98:195433, 2018. doi:10.1103/PhysRevB.98.195433.

[420] S. Chatterjee, J. F. Rodriguez-Nieva, and E. Demler. Diagnosing phases of magnetic insulators via noise magnetometry with spin qubits. *Phys. Rev. B*, 99:104425, 2019. doi:10.1103/PhysRevB.99.104425.

[421] J. Aftergood and S. Takei. Probing quantum spin liquids in equilibrium using the inverse spin Hall effect. *Phys. Rev. Research*, 2:033439, 2020. doi:10.1103/PhysRevResearch.2.033439.

[422] K. S. Burch, D. Mandrus, and J.-G. Park. Magnetism in two-dimensional van der Waals materials. *Nature*, 563(7729):47–52, 2018. ISSN 1476-4687. doi:10.1038/s41586-018-0631-z.

[423] M. Gibertini, M. Koperski, A. F. Morpurgo, and K. S. Novoselov. Magnetic 2D materials and heterostructures. *Nature Nanotechnology*, 14(5):408–419, 2019. doi:10.1038/s41565-019-0438-6.

[424] M. Kim, P. Kumaravadivel, J. Birkbeck, W. Kuang, S. G. Xu, D. G. Hopkinson, J. Knolle, P. A. McClarty, A. I. Berdyugin, M. Ben Shalom, and et al. Micromagnetometry of two-dimensional ferromagnets. *Nature Electronics*, 2(10):457–463, 2019. doi:10.1038/s41928-019-0302-6.

[425] D. R. Klein, D. MacNeill, J. L. Lado, D. Soriano, E. Navarro-Moratalla, K. Watanabe, T. Taniguchi, S. Manni, P. Canfield, J. Fernández-Rossier, and P. Jarillo-Herrero. Probing magnetism in 2D van der Waals crystalline insulators via electron tunneling. *Science*, 360(6394):1218–1222, 2018. doi:10.1126/science.aar3617.

[426] O. Pietzsch, A. Kubetzka, M. Bode, and R. Wiesendanger. Observation of Magnetic Hysteresis at the Nanometer Scale by Spin-Polarized Scanning Tunneling Spectroscopy. *Science*, 292(5524):2053–2056, 2001. doi:10.1126/science.1060513.

[427] M. Bode, M. Heide, K. von Bergmann, P. Ferriani, S. Heinze, G. Bihlmayer, A. Kubetzka, O. Pietzsch, S. Blügel, and R. Wiesendanger. Chiral magnetic order at surfaces driven by inversion asymmetry. *Nature*, 447(7141):190–193, 2007. doi:10.1038/nature05802.

[428] J. Fernández-Rossier. Theory of Single-Spin Inelastic Tunneling Spectroscopy. *Phys. Rev. Lett.*, 102:256802, 2009. doi:10.1103/PhysRevLett.102.256802.

[429] J. Fransson, O. Eriksson, and A. V. Balatsky. Theory of spin-polarized scanning tunneling microscopy applied to local spins. *Phys. Rev. B*, 81:115454, 2010. doi:10.1103/PhysRevB.81.115454.

[430] T. Balashov, A. F. Takács, W. Wulfhekel, and J. Kirschner. Magnon Excitation with Spin-Polarized Scanning Tunneling Microscopy. *Phys. Rev. Lett.*, 97:187201, 2006. doi:10.1103/PhysRevLett.97.187201.

[431] A. Spinelli, B. Bryant, F. Delgado, J. Fernández-Rossier, and A. F. Otte. Imaging of spin waves in atomically designed nanomagnets. *Nature Materials*, 13(8):782–785, 2014. doi:10.1038/nmat4018.

[432] F. Delgado, C. D. Batista, and J. Fernández-Rossier. Local Probe of Fractional Edge States of $S = 1$ Heisenberg Spin Chains. *Phys. Rev. Lett.*, 111:167201, 2013. doi:10.1103/PhysRevLett.111.167201.

[433] A. T. Costa and D. L. R. Santos and N. M. R. Peres and J. Fernández-Rossier. Topological magnons in CrI_3 monolayers: an itinerant fermion description. *2D Materials*, 7(4):045031, 2020. doi:10.1088/2053-1583/aba88f.

[434] Y. Onose, T. Ideue, H. Katsura, Y. Shiomi, N. Nagaosa, and Y. Tokura. Observation of the Magnon Hall Effect. *Science*, 329(5989):297–299, 2010. doi:10.1126/science.1188260.

[435] M. Hirschberger, R. Chisnell, Y. S. Lee, and N. P. Ong. Thermal Hall Effect of Spin Excitations in a Kagome Magnet. *Phys. Rev. Lett.*, 115:106603, 2015. doi:10.1103/PhysRevLett.115.106603.

[436] R. Chisnell, J. S. Helton, D. E. Freedman, D. K. Singh, R. I. Bewley, D. G. Nocera, and Y. S. Lee. Topological Magnon Bands in a Kagome Lattice Ferromagnet. *Phys. Rev. Lett.*, 115:147201, 2015. doi:10.1103/PhysRevLett.115.147201.

[437] A. Roldán-Molina, A. S. Nunez, and J. Fernández-Rossier. Topological spin waves in the atomic-scale magnetic skyrmion crystal. *New Journal of Physics*, 18(4):045015, 2016. doi:10.1088/1367-2630/18/4/045015.

[438] B. Huang, G. Clark, E. Navarro-Moratalla, D. R. Klein, R. Cheng, K. L. Seyler, D. Zhong, E. Schmidgall, M. A. McGuire, D. H. Cobden, W. Yao, D. Xiao, P. Jarillo-Herrero, and X. Xu. Layer-dependent ferromagnetism in a van der Waals crystal down to the monolayer limit. *Nature*, 546(7657):270–273, 2017. doi:10.1038/nature22391.

[439] E. Aguilera, R. Jaeschke-Ubiergo, N. Vidal-Silva, Luis E. F. Foa Torres, and A. S. Nunez. Topological magnonics in the two-dimensional van der Waals magnet CrI_3. *Phys. Rev. B*, 102:024409, 2020. doi:10.1103/PhysRevB.102.024409.

[440] M. Bode. Spin-polarized scanning tunnelling microscopy. *Reports on Progress in Physics*, 66(4):523–582, 2003. doi:10.1088/0034-4885/66/4/203.

[441] H. Oka, O. O. Brovko, M. Corbetta, V. S. Stepanyuk, D. Sander, and J. Kirschner. Spin-polarized quantum confinement in nanostructures: Scanning tunneling microscopy. *Rev. Mod. Phys.*, 86:1127–1168, 2014. doi:10.1103/RevModPhys.86.1127.

[442] Katsura, H. and Nagaosa, N. and Lee, P. A. Theory of the Thermal Hall Effect in Quantum Magnets. *Phys. Rev. Lett.*, 104:066403, 2010. doi:10.1103/PhysRevLett.104.066403.

[443] L. Zhang, J. Ren, J.-S. Wang, and B. Li. Topological magnon insulator in insulating ferromagnet. *Phys. Rev. B*, 87:144101, 2013. doi:10.1103/PhysRevB.87.144101.

[444] D. Malz, J. Knolle, and A. Nunnenkamp. Topological magnon amplification. *Nature Communications*, 10(1), 2019. doi:10.1038/s41467-019-11914-2.

[445] F. J. Burnell and Chetan Nayak. SU(2) slave fermion solution of the Kitaev honeycomb lattice model. *Phys. Rev. B*, 84:125125, 2011. doi:10.1103/PhysRevB.84.125125.

[446] J. Knolle, D. L. Kovrizhin, J. T. Chalker, and R. Moessner. Dynamics of a Two-Dimensional Quantum Spin Liquid: Signatures of Emergent Majorana Fermions and Fluxes. *Phys. Rev. Lett.*, 112:207203, 2014. doi:10.1103/PhysRevLett.112.207203.

[447] Knolle, J. and Kovrizhin, D. L. and Chalker, J. T. and Moessner, R. Dynamics of fractionalization in quantum spin liquids. *Phys. Rev. B*, 92:115127, 2015. doi:10.1103/PhysRevB.92.115127.

[448] Knolle, J. *Dynamics of a Quantum Spin Liquid*. Springer, 2016.

[449] G. Baskaran, Saptarshi Mandal, and R. Shankar. Exact Results for Spin Dynamics and Fractionalization in the Kitaev Model. *Phys. Rev. Lett.*, 98:247201, 2007. doi:10.1103/PhysRevLett.98.247201.

[450] A. M. Tsvelik. Field-theory treatment of the Heisenberg spin-1 chain. *Phys. Rev. B*, 42:10499–10504, 1990. doi:10.1103/PhysRevB.42.10499.

[451] P. Fromholz and P. Lecheminant. Symmetry-protected topological phases in the SU(N) Heisenberg spin chain: A Majorana fermion approach. *Phys. Rev. B*, 102: 094410, 2020. doi:10.1103/PhysRevB.102.094410.

[452] F. L. Pedrocchi, S. Chesi, and D. Loss. Physical solutions of the Kitaev honeycomb model. *Phys. Rev. B*, 84:165414, 2011. doi:10.1103/PhysRevB.84.165414.

[453] F. Zschocke and M. Vojta. Physical states and finite-size effects in Kitaev's honeycomb model: Bond disorder, spin excitations, and NMR line shape. *Phys. Rev. B*, 92:014403, 2015. doi:10.1103/PhysRevB.92.014403.

[454] J. Hauschild and F. Pollmann. Efficient numerical simulations with Tensor Networks: Tensor Network Python (TeNPy). *SciPost Phys. Lect. Notes*, page 5, 2018. doi:10.21468/SciPostPhysLectNotes.5.

[455] F. Casola, T. van der Sar, and A. Yacoby. Probing condensed matter physics with magnetometry based on nitrogen-vacancy centres in diamond. *Nature Reviews Materials*, 3(1), 2018. doi:10.1038/natrevmats.2017.88.

[456] S. Gopalakrishnan and R. Vasseur. Kinetic Theory of Spin Diffusion and Superdiffusion in XXZ Spin Chains. *Phys. Rev. Lett.*, 122:127202, 2019. doi:10.1103/PhysRevLett.122.127202.

[457] A. Schuckert, I. Lovas, and M. Knap. Nonlocal emergent hydrodynamics in a long-range quantum spin system. *Phys. Rev. B*, 101:020416, 2020. doi:10.1103/PhysRevB.101.020416.

[458] D. Bulmash and M. Barkeshli. Generalized $U(1)$ Gauge Field Theories and Fractal Dynamics. *arXiv:1806.01855*, 2018. doi:10.48550/arXiv.1806.01855.

[459] Y. You, T. Devakul, S. L. Sondhi, and F. J. Burnell. Fractonic Chern-Simons and BF theories. *Phys. Rev. Research*, 2:023249, 2020. doi:10.1103/PhysRevResearch.2.023249.

[460] Y. You and F. von Oppen. Building fracton phases by Majorana manipulation. *Phys. Rev. Research*, 1:013011, 2019. doi:10.1103/PhysRevResearch.1.013011.

[461] H. Yan, O. Benton, L. D. C. Jaubert, and N. Shannon. Rank–2 $U(1)$ Spin Liquid on the Breathing Pyrochlore Lattice. *Phys. Rev. Lett.*, 124:127203, 2020. doi:10.1103/PhysRevLett.124.127203.

[462] S. Pai, M. Pretko, and R. M. Nandkishore. Localization in Fractonic Random Circuits. *Phys. Rev. X*, 9:021003, 2019. doi:10.1103/PhysRevX.9.021003.

[463] S. Moudgalya, B. A. Bernevig, and N. Regnault. Quantum many-body scars in a Landau level on a thin torus. *Phys. Rev. B*, 102:195150, 2020. doi:10.1103/PhysRevB.102.195150.

[464] S. R. Taylor, M. Schulz, F. Pollmann, and R. Moessner. Experimental probes of Stark many-body localization. *Phys. Rev. B*, 102:054206, 2020. doi:10.1103/PhysRevB.102.054206.

[465] M. Medenjak, K. Klobas, and T. Prosen. Diffusion in Deterministic Interacting Lattice Systems. *Phys. Rev. Lett.*, 119:110603, 2017. doi:10.1103/PhysRevLett.119.110603.

[466] J.-K. Yuan, S. A. Chen, and P. Ye. Fractonic superfluids. *Phys. Rev. Research*, 2:023267, 2020. doi:10.1103/PhysRevResearch.2.023267.

[467] B. Doyon. Lecture notes on Generalised Hydrodynamics. *SciPost Physics Lecture Notes*, 2020. doi:10.21468/SciPostPhysLectNotes.18.

[468] L. D. Landau and E. M. Lifshitz. Fluid mechanics. Volume 6 of Course of Theoretical Physics, 2nd English ed. Translated from the Russian by JB Sykes, WH Reid, 1987.

[469] D. Forster. *Hydrodynamic fluctuations, broken symmetry, and correlation functions*. CRC Press, 2018.

[470] M. Abramowitz and I. A. Stegun. *Handbook of Mathematical Functions*. Dover Publications Inc., 1965.

[471] H. van Beijeren. Transport properties of stochastic Lorentz models. *Rev. Mod. Phys.*, 54:195–234, 1982. doi:10.1103/RevModPhys.54.195.

[472] J. Lux. *Fluctuations in and out of Equilibrium: Thermalization, quantum measurements and Coulomb disorder*. PhD thesis, University of Cologne, 2016.

[473] A. Weiße, G. Wellein, A. Alvermann, and H. Fehske. The kernel polynomial method. *Rev. Mod. Phys.*, 78:275–306, 2006. doi:10.1103/RevModPhys.78.275.

[474] S. Bera, G. De Tomasi, F. Weiner, and F. Evers. Density Propagator for Many-Body Localization: Finite-Size Effects, Transient Subdiffusion, and Exponential Decay. *Phys. Rev. Lett.*, 118:196801, 2017. doi:10.1103/PhysRevLett.118.196801.

[475] S. Mandt, A. Rapp, and A. Rosch. Interacting Fermionic Atoms in Optical Lattices Diffuse Symmetrically Upwards and Downwards in a Gravitational Potential. *Phys. Rev. Lett.*, 106:250602, 2011. doi:10.1103/PhysRevLett.106.250602.

[476] M. Crossley, P. Glorioso, and H. Liu. Effective field theory of dissipative fluids. *Journal of High Energy Physics*, 2017(9):95, 2017. doi:10.1007/JHEP09(2017)095.

[477] P. Glorioso, M. Crossley, and H. Liu. Effective field theory of dissipative fluids (II): classical limit, dynamical KMS symmetry and entropy current. *Journal of High Energy Physics*, 2017(9):96, 2017. doi:10.1007/JHEP09(2017)096.

[478] H. Liu and P. Glorioso. Lectures on non-equilibrium effective field theories and fluctuating hydrodynamics. *PoS*, TASI2017:008, 2018. doi:10.22323/1.305.0008.

[479] P. Glorioso, J. Guo, J. F. Rodriguez-Nieva, and A. Lucas. Breakdown of hydrodynamics below four dimensions in a fracton fluid. *arXiv:2105.13365*, 2021. doi:10.48550/arXiv.2105.13365.

[480] A. Osborne and A. Lucas. Infinite families of fracton fluids with momentum conservation. *Phys. Rev. B*, 105:024311, 2022. doi:10.1103/PhysRevB.105.024311.

[481] K. T. Grosvenor, C. Hoyos, F. Peña Benitez, and P. Surówka. Hydrodynamics of ideal fracton fluids. *Phys. Rev. Research*, 3:043186, 2021. doi:10.1103/PhysRevResearch.3.043186.

[482] P. Sala, J. Lehmann, T. Rakovszky, and F. Pollmann. Dynamics in systems with modulated symmetries. *arXiv:2110.08302*, 2021. doi:10.48550/arXiv.2110.08302.

[483] O. Hart, A. Lucas, and R. Nandkishore. Hidden quasiconservation laws in fracton hydrodynamics. *Phys. Rev. E*, 105:044103, 2022. doi:10.1103/PhysRevE.105.044103.

[484] V. J. Minkiewicz, M. F. Collins, R. Nathans, and G. Shirane. Critical and Spin-Wave Fluctuations in Nickel by Neutron Scattering. *Phys. Rev.*, 182:624–631, 1969. doi:10.1103/PhysRev.182.624.

[485] E. Lake, M. Hermele, and T. Senthil. The dipolar Bose-Hubbard model. *arXiv:2201.04132*, 2022. doi:10.48550/arXiv.2201.04132.

[486] J. Berges. Introduction to Nonequilibrium Quantum Field Theory. *AIP Conference Proceedings*, 2004.

[487] J. Berges and J. Cox. Thermalization of quantum fields from time-reversal invariant evolution equations. *Physics Letters B*, 517(3):369–374, 2001. doi:10.1016/S0370-2693(01)01004-8.

[488] G. Aarts, D. Ahrensmeier, R. Baier, J. Berges, and J. Serreau. Far-from-equilibrium dynamics with broken symmetries from the 1 / N expansion of the 2PI effective action. *Phys. Rev. D*, 66(4), 2002. doi:10.1103/PhysRevD.66.045008.

[489] Gordon Baym. Self-Consistent Approximations in Many-Body Systems. *Physical Review*, 127(4):1391–1401, 1962. doi:10.1103/PhysRev.127.1391.

[490] N. Schluenzen, S. Hermanns, M. Scharnke, and M. Bonitz. Ultrafast Dynamics of Strongly Correlated Fermions – Nonequilibrium Green Functions and Self-energy Approximations. *Journal of Physics: Condensed Matter*, 32(10), 2020. doi:10.1088/1361-648X/ab2d32.

[491] J. Berges. Controlled nonperturbative dynamics of quantum fields out of equilibrium. *Nuclear Physics A*, 699(3-4):847–886, 2002. doi:10.1016/s0375-9474(01)01295-7.

[492] G. Aarts and A. Tranberg. Nonequilibrium dynamics in the O(N) model to next-to-next-to-leading order in the 1/N expansion. *Phys. Rev. D*, 74(2), 2006. doi:10.1103/PhysRevD.74.025004.

[493] S. A. Weidinger and M. Knap. Floquet prethermalization and regimes of heating in a periodically driven, interacting quantum system. *Scientific Reports*, 7(1), 2017. doi:10.1038/srep45382.

[494] M. Kronenwett and T. Gasenzer. Far-from-equilibrium dynamics of an ultracold Fermi gas. *Applied Physics B*, 102(3):469–488, 2011. doi:10.1007/s00340-011-4426-2.

[495] T. Gasenzer. Ultracold gases far from equilibrium. *The European Physical Journal Special Topics*, 168(1):89–148, 2009. doi:10.1140/epjst/e2009-00960-5.

[496] Thomas Gasenzer, Jürgen Berges, Michael G. Schmidt, and Marcos Seco. Nonperturbative dynamical many-body theory of a Bose-Einstein condensate. *Phys. Rev. A*, 72(6), 2005. doi:10.1103/PhysRevA.72.063604.

[497] M. Babadi, E. Demler, and M. Knap. Far-from-Equilibrium Field Theory of Many-Body Quantum Spin Systems: Prethermalization and Relaxation of Spin Spiral States in Three Dimensions. *Phys. Rev. X*, 5:041005, 2015. doi:10.1103/PhysRevX.5.041005.

[498] A. Schuckert, A. Piñeiro Orioli, and J. Berges. Nonequilibrium quantum spin dynamics from two-particle irreducible functional integral techniques in the schwinger boson representation. *Phys. Rev. B*, 98:224304, 2018. doi:10.1103/PhysRevB.98.224304.

[499] G. Aarts, N. Laurie, and A. Tranberg. Effective convergence of the two-particle irreducible $1/N$ expansion for nonequilibrium quantum fields. *Phys. Rev. D*, 78: 125028, 2008. doi:10.1103/PhysRevD.78.125028.

[500] J. Iaconis, A. Lucas, and X. Chen. Measurement-induced phase transitions in quantum automaton circuits. *Phys. Rev. B*, 102:224311, 2020. doi:10.1103/PhysRevB.102.224311.

[501] X. Feng and B. Skinner. Hilbert space fragmentation produces an effective attraction between fractons. *Phys. Rev. Research*, 4:013053, 2022. doi:10.1103/PhysRevResearch.4.013053.

[502] X. Chen, Y. Gu, and A. Lucas. Many-body quantum dynamics slows down at low density. *SciPost Phys.*, 9:71, 2020. doi:10.21468/SciPostPhys.9.5.071.

[503] S.-W. Liu, J. Willsher, T. Bilitewski, Jin-Jie Li, A. Smith, K. Christensen, R. Moessner, and J. Knolle. Butterfly effect and spatial structure of information spreading in a chaotic cellular automaton. *Phys. Rev. B*, 103:094109, 2021. doi:10.1103/PhysRevB.103.094109.

[504] D. Hahn, P. A. McClarty, and D. J. Luitz. Information Dynamics in a Model with Hilbert Space Fragmentation. *SciPost Phys.*, 11:74, 2021. doi:10.21468/SciPostPhys.11.4.074.

[505] W. Feller. *An introduction to probability theory and its applications, vol 2*. John Wiley & Sons, 2008.

[506] M. F. Shlesinger. Asymptotic solutions of continuous-time random walks. *Journal of Statistical Physics*, 10(5):421–434, 1974. doi:10.1007/BF01008803.

[507] J. Richter and A. Pal. Anomalous hydrodynamics in a class of scarred frustration-free Hamiltonians. *Phys. Rev. Research*, 4:L012003, 2022. doi:10.1103/PhysRevResearch.4.L012003.

[508] H. Spohn. *Large scale dynamics of interacting particles*. Springer Science & Business Media, 2012.

[509] G. De Tomasi, D. Hetterich, P. Sala, and F. Pollmann. Dynamics of strongly interacting systems: From Fock-space fragmentation to many-body localization. *Phys. Rev. B*, 100:214313, 2019. doi:10.1103/PhysRevB.100.214313.

[510] Z.-C. Yang, F. Liu, A. V. Gorshkov, and T. Iadecola. Hilbert-Space Fragmentation from Strict Confinement. *Phys. Rev. Lett.*, 124:207602, 2020. doi:10.1103/PhysRevLett.124.207602.

[511] L. Zadnik and M. Fagotti. The Folded Spin-1/2 XXZ Model: I. Diagonalisation, Jamming, and Ground State Properties. *SciPost Phys. Core*, 4:10, 2021. doi:10.21468/SciPostPhysCore.4.2.010.

[512] L. Zadnik, K. Bidzhiev, and M. Fagotti. The Folded Spin-1/2 XXZ Model: II. Thermodynamics and Hydrodynamics with a Minimal Set of Charges. *SciPost Phys.*, 10: 99, 2021. doi:10.21468/SciPostPhys.10.5.099.

[513] B. Pozsgay, T. Gombor, A. Hutsalyuk, Y. Jiang, L. Pristyák, and E. Vernier. Integrable spin chain with Hilbert space fragmentation and solvable real-time dynamics. *Phys. Rev. E*, 104:044106, 2021. doi:10.1103/PhysRevE.104.044106.

[514] K. Bidzhiev, M. Fagotti, and L. Zadnik. Macroscopic Effects of Localized Measurements in Jammed States of Quantum Spin Chains. *Phys. Rev. Lett.*, 128:130603, 2022. doi:10.1103/PhysRevLett.128.130603.

[515] S. Alexander and P. Pincus. Diffusion of labeled particles on one-dimensional chains. *Phys. Rev. B*, 18:2011–2012, 1978. doi:10.1103/PhysRevB.18.2011.

[516] R. G. Dias. Exact solution of the strong coupling $t-V$ model with twisted boundary conditions. *Phys. Rev. B*, 62:7791–7801, 2000. doi:10.1103/PhysRevB.62.7791.

[517] G. I. Menon, M. Barma, and D. Dhar. Conservation laws and integrability of a one-dimensional model of diffusing dimers. *Journal of Statistical Physics*, 86(5):1237–1263, 1997. doi:10.1007/BF02183622.

[518] K. Klobas, M. Medenjak, and T. Prosen. Exactly solvable deterministic lattice model of crossover between ballistic and diffusive transport. *Journal of Statistical Mechanics: Theory and Experiment*, 2018(12):123202, 2018. doi:10.1088/1742-5468/aae853.

[519] M. Kotrla. Energy spectrum of the Hubbard model with U=∞. *Physics Letters A*, 145(1):33 – 36, 1990. doi:10.1016/0375-9601(90)90272-P.

[520] J. De Nardis, D. Bernard, and B. Doyon. Diffusion in generalized hydrodynamics and quasiparticle scattering. *SciPost Phys.*, 6:49, 2019. doi:10.21468/SciPostPhys.6.4.049.

[521] C. Karrasch, J. E. Moore, and F. Heidrich-Meisner. Real-time and real-space spin and energy dynamics in one-dimensional spin-$\frac{1}{2}$ systems induced by local quantum quenches at finite temperatures. *Phys. Rev. B*, 89:075139, 2014. doi:10.1103/PhysRevB.89.075139.

[522] C. Karrasch. Hubbard-to-Heisenberg crossover (and efficient computation) of Drude weights at low temperatures. *New Journal of Physics*, 19(3):033027, 2017. doi:10.1088/1367-2630/aa631a.

[523] B. Pozsgay. A Yang–Baxter integrable cellular automaton with a four site update rule. *Journal of Physics A: Mathematical and Theoretical*, 54(38):384001, 2021. doi:10.1088/1751-8121/ac1dbf.

[524] Y. You, J. Bibo, F. Pollmann, and T. L. Hughes. Fracton Critical Point in Higher-Order Topological Phase Transition. *arXiv:2008.01746*, 2020. doi:10.48550/arXiv.2008.01746.

[525] N. Seiberg and S.-H. Shao. Exotic $U(1)$ Symmetries, Duality, and Fractons in 3+1-Dimensional Quantum Field Theory. *SciPost Phys.*, 9:46, 2020. doi:10.21468/SciPostPhys.9.4.046.

[526] P. Gorantla, H. T. Lam, N. Seiberg, and S.-H. Shao. Low-energy limit of some exotic lattice theories and UV/IR mixing. *Phys. Rev. B*, 104:235116, 2021. doi:10.1103/PhysRevB.104.235116.

[527] Y. You, J. Bibo, T. L. Hughes, and F. Pollmann. Fractonic critical point proximate to a higher-order topological insulator: How does UV blend with IR? *arXiv:2101.01724*, 2021. doi:10.48550/arXiv.2101.01724.

[528] O. Hart and R. Nandkishore. Spectroscopic fingerprints of gapless type-II fracton phases. *Phys. Rev. B*, 105:L180416, 2022. doi:10.1103/PhysRevB.105.L180416.

[529] S. Gopalakrishnan, A. Morningstar, R. Vasseur, and V. Khemani. Theory of anomalous full counting statistics in anisotropic spin chains. *arXiv:2203.09526*, 2022. doi:10.48550/arXiv.2203.09526.

[530] Ž Krajnik, J. Schmidt, V. Pasquier, E. Ilievski, and T. Prosen. Exact Anomalous Current Fluctuations in a Deterministic Interacting Model. *Phys. Rev. Lett.*, 128: 160601, 2022. doi:10.1103/PhysRevLett.128.160601.

[531] M. D. Grynberg. Revisiting Kawasaki dynamics in one dimension. *Phys. Rev. E*, 82 (5):051121, 2010. doi:10.1103/PhysRevE.82.051121.

[532] S. Vinet, G. Longpré, and W. Witczak-Krempa. Excitations and ergodicity of critical quantum spin chains from non-equilibrium classical dynamics. *arXiv: 2107.04615*, 2021. doi:10.48550/arXiv.2107.04615.

[533] J. De Nardis, S. Gopalakrishnan, R. Vasseur, and B. Ware. Subdiffusive hydrodynamics of nearly-integrable anisotropic spin chains. arXiv:2109.13251, 2021.

[534] T. Thiery, F. Huveneers, M. Müller, and W. De Roeck. Many-Body Delocalization as a Quantum Avalanche. *Phys. Rev. Lett.*, 121:140601, 2018. doi:10.1103/PhysRevLett.121.140601.

[535] J. Wildeboer, A. Seidel, N. S. Srivatsa, A. E. B. Nielsen, and O. Erten. Topological quantum many-body scars in quantum dimer models on the kagome lattice. *Phys. Rev. B*, 104:L121103, 2021. doi:10.1103/PhysRevB.104.L121103.

[536] S. Biswas, D. Banerjee, and A. Sen. Scars from protected zero modes and beyond in $U(1)$ quantum link and quantum dimer models. *SciPost Phys.*, 12:148, 2022. doi:10.21468/SciPostPhys.12.5.148.

[537] K. Klocke, D. Aasen, R. S. K. Mong, E. A. Demler, and J. Alicea. Time-domain anyon interferometry in kitaev honeycomb spin liquids and beyond. *Phys. Rev. Lett.*, 126: 177204, 2021. doi:10.1103/PhysRevLett.126.177204.

[538] Y. Li, X. Chen, and M. P. A. Fisher. Quantum zeno effect and the many-body entanglement transition. *Phys. Rev. B*, 98:205136, 2018. doi:10.1103/PhysRevB.98.205136.

[539] Y. Li, X. Chen, and M. P. A. Fisher. Measurement-driven entanglement transition in hybrid quantum circuits. *Phys. Rev. B*, 100:134306, 2019. doi:10.1103/PhysRevB.100.134306.

[540] B. Skinner, J. Ruhman, and A. Nahum. Measurement-Induced Phase Transitions in the Dynamics of Entanglement. *Phys. Rev. X*, 9:031009, 2019. doi:10.1103/PhysRevX.9.031009.

[541] A. Chan, R. M. Nandkishore, M. Pretko, and G. Smith. Unitary-projective entanglement dynamics. *Phys. Rev. B*, 99:224307, 2019. doi:10.1103/PhysRevB.99.224307.

[542] S. Choi, Y. Bao, X.-L. Qi, and E. Altman. Quantum Error Correction in Scrambling Dynamics and Measurement-Induced Phase Transition. *Phys. Rev. Lett.*, 125:030505, 2020. doi:10.1103/PhysRevLett.125.030505.

[543] S. C. Morampudi, A. Chandran, and C. R. Laumann. Universal Entanglement of Typical States in Constrained Systems. *Phys. Rev. Lett.*, 124:050602, 2020. doi:10.1103/PhysRevLett.124.050602.

[544] S. Aaronson and D. Gottesman. Improved simulation of stabilizer circuits. *Phys. Rev. A*, 70:052328, 2004. doi:10.1103/PhysRevA.70.052328.

[545] R. Orús. A practical introduction to tensor networks: Matrix product states and projected entangled pair states. *Annals of Physics*, 349:117–158, 2014. doi:10.1016/j.aop.2014.06.013.

[546] M. B. Hastings. An area law for one-dimensional quantum systems. *Journal of Statistical Mechanics: Theory and Experiment*, 2007(08):P08024–P08024, 2007. doi:10.1088/1742-5468/2007/08/p08024.

[547] G. Vidal. Efficient Simulation of One-Dimensional Quantum Many-Body Systems. *Phys. Rev. Lett.*, 93:040502, 2004. doi:10.1103/PhysRevLett.93.040502.

[548] J. Haegeman, J. I. Cirac, T. J. Osborne, I. Pižorn, H. Verschelde, and F. Verstraete. Time-Dependent Variational Principle for Quantum Lattices. *Phys. Rev. Lett.*, 107: 070601, 2011. doi:10.1103/PhysRevLett.107.070601.

[549] J. Haegeman, C. Lubich, I. Oseledets, B. Vandereycken, and F. Verstraete. Unifying time evolution and optimization with matrix product states. *Phys. Rev. B*, 94:165116, 2016. doi:10.1103/PhysRevB.94.165116.

[550] lp_solve, Open source (Mixed-Integer) Linear Programming system, http://lpsolve.sourceforge.net/5.5/.

This thesis was typeset using LaTeX, originally developed by Leslie Lamport and based on Donald Knuth's TeX. The body text is set in 11 point Palatino, designed by Hermann Zapf. A template that can be used to format a PhD thesis with this look and feel has been released under the permissive mit (x11) license, and can be found online at github.com/suchow/Dissertate or from its author, Jordan Suchow, at suchow@post.harvard.edu.